Advances in Vanadium-Based Catalyst Research for the Selective Catalytic Reduction of NO_x by NH_3

THÈSE N^{O} 8233 (2017)

PRÉSENTÉE LE 14 DÉCEMBRE 2017
À LA FACULTÉ DES SCIENCES DE BASE
GROUPE KRÖCHER
PROGRAMME DOCTORAL EN CHIMIE ET GÉNIE CHIMIQUE

ÉCOLE POLYTECHNIQUE FÉDÉRALE DE LAUSANNE

POUR L'OBTENTION DU GRADE DE DOCTEUR ÈS SCIENCES

PAR

Adrian MARBERGER

acceptée sur proposition du jury:

Prof. G. Laurenczy, président du jury
Prof. O. Kröcher, Dr D. Ferri, directeurs de thèse
Prof. A. Trovarelli, rapporteur
Dr D. Peitz, rapporteur
Prof. W. L. Queen, rapporteuse

ÉCOLE POLYTECHNIQUE
FÉDÉRALE DE LAUSANNE
Suisse
2017

„In den Wissenschaften ist viel Gewisses, sobald man sich von den Ausnahmen nicht irre machen lässt und die Probleme zu ehren weiss.“

Johann Wolfgang von Goethe

Abstract

The most efficient after-treatment technology for reducing harmful NO_x emissions from stationary and mobile sources of diesel exhaust is the selective catalytic reduction (SCR) of NO_x with ammonia (NH_3). Vanadium-based SCR catalysts reduce NO_x selectively between ca. 200 and 500°C. Low temperature activity and high temperature stability are important for the automotive sector because of the large temperature fluctuations in the exhaust gas. Additionally, SCR catalysts need to be resistant to water vapor, sulfur and potentially poisoning elements. To date, V-based SCR catalysts of type $V_2O_5/WO_3/TiO_2$ (VWT) are the most widespread systems because of their activity over a broad temperature range, high sulfur tolerance and moderate production cost. Drawbacks are the moderate hydrothermal stability, poor low temperature activity and potential vanadium volatility which are the main research topics for V-based SCR catalysts.

Exposure to different aging procedures of a V-loading optimized VWT catalyst (2 wt% V_2O_5) revealed that a hydrothermal environment affects the aging much more severely compared to a dry environment. Before deactivation, VWT catalysts have the capability to activate, which was correlated to changes in V and W surface coverage, the increased fraction of Lewis acid sites and SCR active vanadyl sites. The VWT catalyst with optimized V-loading was further investigated by means of transient experimentation, which revealed important insights into the mechanism of the SCR reaction: The active site was assigned to mono-oxo V^{5+} Lewis acid species, which were reduced only in presence of both NO and NH_3. The formation of the nitrosamide intermediate, which is formed simultaneously to V^{5+} reduction, was also verified.

The addition of 2 - 4 wt% SiO_2 during the VWT catalyst synthesis increased the stability up to 650°C because it prevented anatase TiO_2 particles from sintering by inhibiting their inter-particle contact. Using a SiO_2 stabilized TiO_2 support material, the potential of $FeVO_4$ as a source of active redox centers

was explored as a novel class of hydrothermally stable SCR catalyst. A loading of 4.5 wt% $FeVO_4$ was found to be the optimum trade-off between stability and activity. Remarkable catalyst activation was observed after calcination at 600°C, which was correlated to the decomposition of $FeVO_4$. Similar to $FeVO_4$, it was shown that the catalytic activity of supported $CeVO_4$, $AlVO_4$ and $ErVO_4$ is closely correlated to their degree of decomposition. The decomposition of metal vanadates generates dispersed VO_x domains, which resemble those of VWT catalysts.

This thesis demonstrates that research on V-based SCR catalysts is still crucial because their modification and optimization can result in enhanced performance and temperature stability. Metal vanadates can be envisaged as a reservoir for active V-species as they decompose once supported on TiO_2. Transient experimentation allowed in-depth mechanistic studies on V-based catalysts. This encourages further exploration of SCR catalysts in order to improve the fundamental knowledge of such systems that will assist the discovery of highly active and stable catalysts for the abatement of NO_x.

Keywords

SCR, Vanadium, V_2O_5, Metal Vanadates, WO_3, TiO_2, SiO_2, Diffuse reflectance spectroscopy, transient experimentation, Lewis acid sites, catalyst aging

Kurzfassung

Die effizienteste Technologie zur Reduzierung von schädlichen Stickoxidemissionen aus stationären und mobilen Dieselabgasen ist die selektive katalytische Reduktion (SCR) von NO_x mit Ammoniak (NH_3). Vanadium-basierte SCR-Katalysatoren reduzieren NO_x selektiv zu H_2O und N_2 zwischen ca. 200°C und 500°C. Niedrige Temperaturaktivität und hohe Temperaturstabilität sind wichtig für den Automobilsektor wegen den grossen Temperaturschwankungen im Abgas. Zusätzlich müssen SCR-Katalysatoren gegen Wasserdampf, Schwefel und potentielle Vergiftungselemente resistent sein. V-basierte Katalysatoren vom Typ $V_2O_5/WO_3/TiO_2$ (VWT) sind aufgrund ihrer Aktivität über ein breites Temperaturfenster, hohen Schwefel-Toleranz und moderaten Herstellungskosten die am weitesten verbreiteten Systeme. Nachteile sind die mässige hydrothermale Stabilität, die schlechte Tieftemperaturaktivität und die potentielle Vanadium-Volatilität, welches die Hauptforschungsthemen für V-basierte SCR-Katalysatoren sind.

Die Aktivität und Stabilität eines VWT-Katalysatoren (2.0 Gew.% V_2O_5) war stark von der Zugabe von Wasserdampf im Alterungsprozess abhängig. Bevor VWT deaktivierte, wurde der Katalysator aktiver als in seinem Grundzustand, was mit Änderungen der V- und W-Oberflächenbedeckung, dem erhöhten Anteil an Lewis-Säuren und SCR-aktiven Vanadylzentren korreliert werden konnte. Der VWT-Katalysator mit optimierter V-Beladung wurde durch transiente Experimente weiter untersucht, was wichtige Einblicke in den Mechanismus der SCR-Reaktion zeigte. Die aktive Stelle wurde mono-oxo V^{5+} Lewis-Säuren zugeordnet, welche sich nur in Gegenwart von NO und NH_3 reduzierten. Die Bildung von Nitrosamid als Zwischenprodukt, welches gleichzeitig zur V^{5+}-Reduktion gebildet wird, konnte ebenfalls identifiziert werden.

Die Zugabe von 2 - 4 Gew.% SiO_2 während der VWT Synthese erhöhte die Stabilität auf bis zu 650°C, da der Kontakt von Anatas-TiO_2 Partikeln verhindert wurde und so das Sintern inhibierte. Unter Verwendung eines SiO_2-stabilisierten TiO_2 Trägermaterials wurde das Potential von $FeVO_4$ als Quelle

für aktive Redoxzentren als neuartige Klasse von hydrothermisch stabilem SCR-Katalysator untersucht. Eine Beladung von 4.5 Gew.% $FeVO_4$ stellte das Optimum Stabilität und Aktivität dar. Nach der Kalzinierung bei 600°C wurde eine bemerkenswerte Katalysatoraktivierung beobachtet, die mit der Zersetzung von $FeVO_4$ korreliert werden konnte. Ähnlich wie bei $FeVO_4$ konnte nachgewiesen werden, dass die katalytische Aktivität von geträgertem $CeVO_4$, $AlVO_4$ und $ErVO_4$ eng mit deren Zersetzungsgrad korreliert. Die Zersetzung von Metallvanadaten erzeugt dispergierte VO_x-Spezies, die denen von herkömmlichen VWT-Katalysatoren ähneln.

Diese Dissertation zeigt, dass die Erforschung von V-basierten SCR-Katalysatoren nach wie vor wichtig ist, weil ihre Modifikation und Optimierung zu einer verbesserten Katalysatoraktivität und Temperaturstabilität führt. Geträgerte Metallvanadate sollten als Reservoir für aktive V-Spezies in Betracht gezogen werden, weil sie sich bei erhöhten Temperaturen zersetzen. Transiente Experimente erlaubten eingehende mechanistische Untersuchungen an V-basierten Katalysatoren. Die hier gefundenen Resultate zeigen die Notwendigkeit für die weitere Erforschung von SCR-Katalysatoren, um das grundlegende Wissen über solche Systeme zu erweitern, damit der Industrie in Zukunft stabile und aktive Katalysatoren zur Verringerung von NO_x zur Verfügung stehen.

Acknowledgements

First of all, I would genuinely like to thank Prof. Dr. Oliver Kröcher for giving me the opportunity to conduct this work in the framework of a doctoral research study, for his continuous optimism, sharing the profound knowledge in the field of SCR and setting the right research focus with regard to my thesis and the industry collaboration.

I am deeply grateful to Dr. Davide Ferri for the daily support and supervision. His personal enthusiasm for catalysis research and spectroscopy is infectious. His deep knowledge in chemistry, a vast variety of characterization methods and even history, the insightful and sometimes crazy discussions (on and off topic) and the instantaneous detailed corrections of my reports and manuscripts made it possible to finalize this work.

I owe my deep gratitude to Martin Elsener who is the "catalytic soul" in our laboratories. I truly admire his knowledge about chemistry, catalysis, SCR, mushrooms and beyond and his creativity in constructing appropriate and feasible research set-ups. Thanks to him, my areal comfort zone at Paul Scherrer Institut increased to ca. 100 km^2 over lunchtimes.

I would like to thank Prof. Alessandro Trovarelli, Prof. Wendy Lee Queen and Dr. Daniel Peitz for accepting to be the co-examiners for this thesis and Prof. Gabor Laurenczy for acting as the Jury President.

My sincerest thanks go to my current PhD comrade-in-arms, namely Patrick "Simon" Steiger, Andrey "Putin" Petrov and Thibault "Tibo" Fovanna, for the daily help, ideas, support, wanted and unwanted distractions and simply letting me know when I was way in over my head. You all heavily contributed in creating a charming working and lunchtime atmosphere.

My thanks also go to the former and current members of the Catalysis for Energy group, namely Dr. Anastasios "Tasos" Kambolis, Dr. Katarzyna Anna "Kasia" Michalow-Mauke, Dr. Manasa Sridhar, Dr. Valentina "Vale" Marchionni, Dr. Arnim "Amrin" Eyssler, Dr. Christian Proff, Dr. Ivo Alxneit,

Gisela Herlein Schmutz and all not mentioned members for all the guidance, assistance and rememberable memories and over the years.

A thank goes to the interns and apprentices who helped preparing and characterizing countless catalysts over the years.

A big credit goes to Marcel Hottiger who fulfilled all my wishes when it came to special polymeric or metal parts of my set-up and to Dr. Maarten Nachtegaaal and Dr. Olga Safonova for allocating multiple (unscheduled) beamtimes and the constant support.

I would also acknowledge other lab members I have met in these years. Rene, Franky, Gael, Dominik, Susy, Niv, Sebastian, Daniel and all those I forgot. You all helped in making the institute livelier with e.g. nice chats, coffee breaks, lunches, Aare/NPP swimming or barbeques.

Gratitude goes to the industry research partner Treibacher Industrie AG in Althofen, Austria. Among others, Dr. K. Schermanz, A. Deutsch, Dr. A. Sagar and Dr. C. Artner-Wallner all contributed for this successful collaboration.

A huge thank goes to all my friends: To Öme and our UJ team who restored my mood to 100% every Thursday evening; To the Höusinki T8 team (Vinz and Cédi (+ Saalschutz, remember?), Sam, Schrom, Clau, Dave, Joe, Urs, Dario and Mareischen) and their better halves for countless (non)sense discussions in the Total-Bar and after it; To my very old friend Bruno and Family for still being one; To Manu and Ilan for showing me how to be man AND Dad; To Jess for being the true friend at UZH and beyond, believing in me and now proofreading the presented thesis; And to all those I forgot, you know that I can be oblivious.

Last but not least, I owe my deepest gratitude to my family: Ma and Pa, you are the ones who always believed in me, even when it seemed that I lost track. Your support, love, guidance and understanding is overwhelming; My siblings Ju and Bär (with Family) who know how to bring me down to earth; And my Parents-in-law JeJe for being very supportive during stressful times.

One last most special thank goes to my small family, Lisa and Elin. Lisa, thank you for being you, full of love, energy, passion and some craziness! You

introduced me to your world of literature, theater and film, you are holding our family together and you make my life complete. Das Beste kommt zum Schluss: Elin, deine Geburt hat mein Leben gewaltig verändert und bereichert. Dein Lachen, deine Mimik und deine „Redekunst“ kann eine schlechte Laune oder einen gestressten Tag am PSI sofort vergessen machen.

Contents

Abstract ..... **v**

Kurzfassung ..... **vii**

Acknowledgements ..... **ix**

Contents ..... **xiii**

Chapter 1 ..... **21**

Introduction **21**

1.1 Exhaust emissions of internal combustion engines 21

1.2 Diesel exhaust gas after-treatment 23

1.2.1 Legislations 23

1.2.2 Diesel exhaust gas after-treatment systems 24

1.2.3 Diesel exhaust gas after-treatment systems in the media 26

1.3 Selective catalytic reduction (SCR) of NO_x with NH_3 27

1.3.1 NH_3 sources 27

1.3.2 Essential SCR related chemical reactions 27

1.3.3 SCR technology application range 28

1.3.4 SCR catalysts 29

1.4 Vanadium-based SCR catalysts 30

1.4.1 Support Material - TiO_2 30

1.4.2 Promoter - WO_3 31

1.4.3 Promoter - SiO_2 32

1.4.4 Commercial TiO_2-based support materials 32

1.4.5 Other promoters 33

1.4.6 Vanadium oxides - active sites 34

1.4.7 Proposed mechanisms 35

1.5 Vanadate-based SCR catalysts 37

1.6 Challenges for V-based SCR catalysts 39
1.7 Background of the thesis 40
1.8 Scope of the thesis 40
Chapter 2 43
Methods 43
2.1 Preparation of catalysts 43
2.1.1 Vanadia-based SCR catalysts 43
2.1.2 Metal vanadate-based SCR catalysts 43
2.1.3 Preparation of monoliths 44
2.2 Catalytic tests 44
2.2.1 Aging of catalysts 46
2.3 Characterization techniques 46
2.3.1 Powder X-ray diffraction spectroscopy 46
2.3.2 BET surface area 47
2.3.3 Diffuse reflectance infra-red Fourier transform (DRIFT) spectroscopy 48
2.3.4 Diffuse reflectance ultra-violet visible spectroscopy (DRUV) . 48
2.3.5 Raman spectroscopy 48
2.3.6 X-ray absorption spectroscopy 49
Chapter 3 51
Optimizing the vanadium loading on a tungsta-titania support for activity and stability 51
3.1 Introduction 51
3.2 Catalyst preparation 53
3.3 Characterization 53
3.4 Results and Discussion 53
3.4.1 Catalytic activity 53

3.5 Physico-chemical characterization 57
3.5.1 VO_x surface coverage 62
3.5.2 WO_x surface coverage 64
3.6 Conclusions 64
Chapter 4 67
Differences of thermally and hydrothermally aged VWT catalysts . 67
4.1 Introduction 67
4.2 Experimental 69
4.2.1 Catalyst preparation 69
4.2.2 Aging procedure 69
4.2.3 Characterization methods 69
4.2.4 Vanadium volatility 70
4.3 Results and discussion 70
4.3.1 Catalytic activity 70
4.3.2 Vanadium volatility 73
4.3.3 X-ray diffraction 74
4.3.4 Surface area and k_{BET} 75
4.3.5 Spectroscopic investigations 77
4.4 Conclusion 80
Chapter 5 83
Mechanistic details of a state-of-the-art vanadia-tungsta-titania catalyst 83
5.1 Introduction 83
5.2 Methods 85
5.3 Results and discussion 87
5.3.1 Catalytic activity 87
5.3.2 Single transient experiments 89

5.3.3 Influence of H_2O 93

5.3.4 Multiple transient experiments 97

5.4 Conclusion 102

Chapter 6 103

Silicon for the stabilization of an optimized V-based SCR catalyst 103

6.1 Introduction 103

6.2 Experimental section 104

6.2.1 Catalyst preparation 104

6.2.2 Physico-chemical characterization methods 105

6.3 Results and discussion 106

6.3.1 Benefits and limitations of co-impregnated VW-Ti catalysts 106

6.3.2 Catalytic activity of Si-stabilized vanadia-tungsta-titania catalysts 107

6.4 Physico-chemical characterization 111

6.4.1 XRD results 111

6.4.2 TEM/STEM 118

6.4.3 ^{29}Si MAS NMR 120

6.5 Conclusions 122

Chapter 7 123

Introducing metal vanadate-based SCR catalysts 123

7.1 Introduction 123

7.2 Experimental section 124

7.3 Results and discussion 125

7.3.1 Loading dependent catalytic activity 125

7.3.2 Composition dependent catalytic activity 126

7.3.3 Calcination dependent catalytic activity 128

7.3.4 Physico-chemical characterization - BET and XRD 131

7.3.5 DRIFT and XANES 134
7.4 Conclusion 140
Chapter 8 141
Supported rare earth metal vanadates as SCR catalysts 141
8.1 Introduction 141
8.2 Experimental section 142
8.2.1 Catalyst preparation 142
8.2.2 Catalytic Measurements 143
8.2.3 Characterization methods 143
8.3 Results and discussion 143
8.3.1 Catalytic activity 143
8.4 Material characterization 147
8.4.1 XRD results 147
8.4.2 BET surface area and surface coverage of V 158
8.4.3 H_2-TPR 159
8.4.4 Diffuse reflectance UV-vis spectroscopy 161
8.4.5 NH_3 adsorption - DRIFT spectroscopy 168
8.5 Conclusions 173
Chapter 9 175
Summary and Outlook 175
9.1 Summary 175
9.2 Outlook 177
References 179
List of publications 193
Curriculum vitae 195

„Liegt die Wahrheit in den Hirnen?
Oder in den Gestirnen?
In den Genen? In den Systemen?
Oder zwischen zwei Extremen?“
Saalschutz

Chapter 1

Introduction

1.1 Exhaust emissions of internal combustion engines

Internal combustion engines generate mechanical power and heat from the combustion of a fuel [1]. The most common used gaseous and liquid fuels for off-road, on-road and marine applications are natural gas, gasoline and fuel oil (e.g. diesel or heavy oil) [2]. In an ideal combustion, the hydrocarbons (HC) are reacted with oxygen to produce carbon dioxide (CO_2) and water vapor (H_2O) according to eq. (1-1) [2].

$$C_nH_m + \left(n + \frac{m}{4}\right) O_2 \rightarrow nCO_2 + \frac{m}{2} H_2O \qquad \textbf{(1-1)}$$

Together with dinitrogen (N_2) from air, these components make up for more than 99% of the exhaust composition [3]. However, the exothermic combustion reaction normally occurs in an incomplete manner, producing a mixture of different potentially harmful compounds. High temperature and pressure during the combustion further promote the formation of undesired products because reactant components, lubricating oil, fuel and oil additives/contaminants can react with each other. The exhaust gas composition, therefore, heavily depends on the engine, the fuel and the working conditions [3].

The major exhaust emissions (apart from N_2, H_2O and CO_2) from internal combustion engines fall into two categories, gaseous compounds and solid particulates. The gaseous pollutants of greatest consequence for the environment and health are, however, unburned hydrocarbons (HC), carbon monoxide (CO), nitrogen oxides (NO_x), nitrous oxide (N_2O) and sulfur oxides (SO_x). Solid particulate matter (PM) mainly comprises of carbon, HC, sulfur and heavy

metal elements. The gaseous and solid pollutants affect the human health, the climate, generate tropospheric ozone air pollution and are harmful to the environment [4-6].

The two most common types of internal combustion engines, the gasoline engine and the diesel engine, inherently operate under different air/fuel ratios (λ)[7]. **Figure 1-1** schematically shows that the maximum power output falls approximately together with the maximum emission NO_x levels and that the various emissions are not minimized at one specific λ. It is therefore not possible to run an internal combustion engine completely emission free [5].

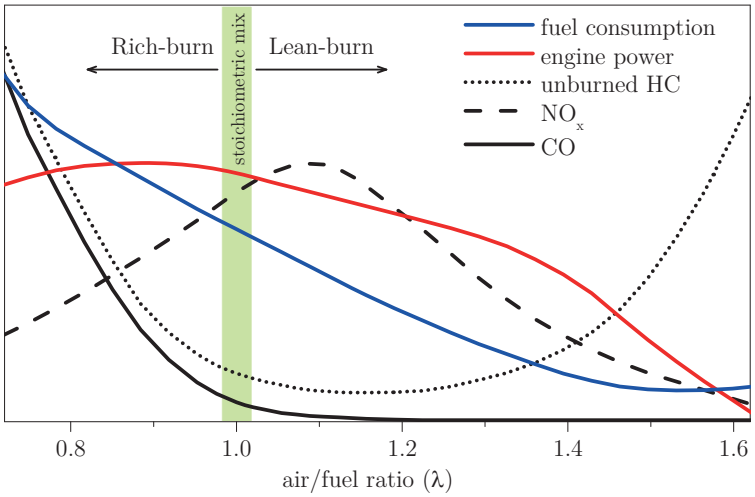

Figure 1-1. The main exhaust emissions, fuel consumption and engine power of internal combustion engines as a function of operation condition (λ = air/fuel ratio, adapted from ref. [5])

The gasoline engine works under stoichiometric conditions (λ=1, **Figure 1-1**), thereby also generating an exhaust gas composition with a 1:1 ratio of reductive and oxidative compounds. In the downstream exhaust gas abatement system, CO/HC and H_2 can thus react stoichiometrically with O_2 and NO_x over a three-way catalyst to CO_2, H_2O and N_2. In contrast, diesel engines operate with an excess of O_2 (λ>1, lean-burn) in the air-fuel mixture, which also leaves a surplus of O_2 in the exhaust gas. In this environment, CO and HC can oxidize to CO_2 over a catalyst, but the reduction of NO_x is impossible. NO_x abatement is thus preferentially done over a separate catalyst and an additionally injected NO_x selective reducing agent.

Diesel engines are widespread in the stationary power-generation applications and are the main energy source for marine and road transport. The lean engine operation is more economical compared to the gasoline engine ($\lambda = 1$), making them irreplaceable to date. To that end, more stringent regulations towards CO_2 emissions pose advantages to diesel engines because of their inherently higher thermodynamic efficiency. Their disadvantages are mainly the higher emissions of NO_x and PM [8].

1.2 Diesel exhaust gas after-treatment

1.2.1 Legislations

Before the Second World War, various European countries already established laws for limiting smoke, grit and dust from industrial plants [9]. After the war, air pollution was of limited interest to the public and was considered as an inevitable byproduct of economic growth. Due to the increasing smog problematics in major cities in Europe and North America, first clean air legislations were enforced in the late 1950s (UK) and late 1960s (US) [9-10]. For motor vehicle emissions, regulations focused first on visible smoke, then CO and later HC and NO_x [11].

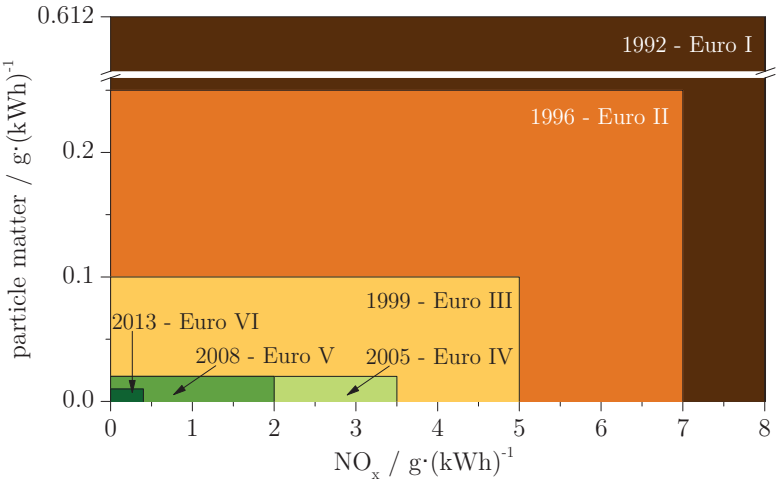

Figure 1-2. Regulations of European emission standards for NO_x and PM (Euro I - VI) for diesel heavy-duty engines.

With the increased awareness of health and environmental issues caused by the exhaust gas of the combustion engines, governmental agencies throughout the

world ratified more stringent regulations to reduce exhaust gas emissions [11-13]. After 1992 and the establishment of the first European Union emission standard for on-road vehicles ("Euro 1" for light-duty and "Euro I" for heavy-duty engines), five more standards were defined, each with increasingly stringent levels of PM, NO_x, HC and CO. The largest changes were thereby implemented for PM and NO_x as presented in **Figure 1-2**. Starting from 1997, legislations were also introduced for off-highway applications and have been reinforced multiple times for e.g. rail, marine and stationary power generation applications [8, 14].

Because emissions of NO_x and PM are unavoidable for diesel engines (**Figure 1-1**), various approaches and developments have tackled this issue in the last decades. The engine-out emissions were lowered considerably by engine development, e.g. improved engine design, fuel injection equipment or implementing turbo-charging [7-8, 15]. Due to the regulations, however, an exhaust gas after-treatment system became unavoidable, opening an entire research field in diesel emission control in the 1980s.

1.2.2 Diesel exhaust gas after-treatment systems

Nowadays, a diesel after-treatment system consists of various components, commonly installed according to **Figure 1-3** for on-road vehicles, which can however deviate depending on the application [16]. Diesel oxidation catalysts (DOC) were already introduced after the first governmental regulations had been enforced and are mainly used for oxidizing CO, PM, gas phase HC and soluble organic fractions (SOF) to CO_2, but also for generating exotherms for the downstream after-treatment components [17]. The DOC is also used to partly oxidize NO to NO_2, which is necessary for the efficient abatement of NO_x that is implemented downstream of the DOC [18]. The catalyst is usually a Pt/Pd-based material washcoated on a honeycomb structure. It is the first exhaust component after the engine, although different configurations and coupled systems can be found on the market as well [17-18].

Traditionally, the second component is a diesel particulate filter (DPF), which is essential to filtering out the harmful PM. New designs and modifications of diesel engines and their partial oxidation over the DOC have contributed sig-

nificantly to lower PM levels, but do not eliminate their emission completely [17, 19]. The DPF generally consists of a wall flow filter that is either blocked up- or downstream of the filter opening in such a way that the gas is forced to diffuse through the filter wall. PM accumulates in the DPF over time and requires regeneration by burning off PM. Depending on the application and DPF, this can be done continuously with NO_2 or periodically with O_2 [20]. In the last years, formulations were found that could incorporate the DOC in the DPF which improved the thermal efficiency of these systems [17].

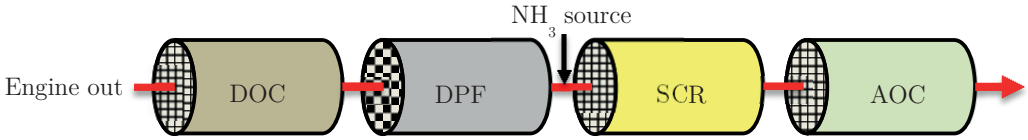

Figure 1-3. Typical diesel exhaust gas system with the different components for cleaning the exhaust gas.

To meet the newer regulation standards, a NO_x abatement system is also needed. Two major technologies are on the market to date, namely lean NO_x trap (LNT, also called NO_x storage and reduction (NSR)) and selective catalytic reduction (SCR) of NO_x with an additional reducing agent. Because the performance of these technologies improves if NO is partly oxidized to NO_2, these systems are located downstream of the DOC [20]. In the LNT/NSR technology, NO_2 is stored in the form of nitrates on a barium containing catalyst during lean operation, which are then reduced over a noble metal to N_2 in a periodically induced rich atmosphere [21-22]. In the SCR system, the NO_x is continuously removed over a catalyst by exploiting HC, H_2 or most commonly a source of NH_3 as the reductant [8]. NH_3 is thereby the only reductant that operates with 1:1 stoichiometric ratio and can completely and selectively reduce NO_x. For low temperature NO_x removal (below 200°C, e.g. for light-duty applications) a combined LNT-SCR system can be beneficial, especially during short city drives [16]. Because focus is laid on the NH_3-SCR technology in this thesis, it is introduced in greater detail in section 1.3.

The last catalyst in a diesel exhaust gas after-treatment system is the ammonia oxidation catalyst (AOC, also referred to as ammonia slip catalyst, ASC). The AOC oxidizes potentially unreacted NH_3 after the SCR system which depends

on the accuracy of the control system. Ideally, the catalyst oxidizes NH_3 to N_2 and water vapor selectively without forming unwanted oxidation products such as N_2O or NO_x [8, 23]. Advances have been made to directly incorporate the ASC in the rear part of an SCR monolith as a second catalyst beneath the SCR coating or at the monolith outlet [24].

1.2.3 Diesel exhaust gas after-treatment systems in the media

In September 2015, the Environmental Protection Agency's (EPA) announced that Volkswagen (VW) implemented a software in some of their models to alter their diesel emission control system [25]. Because of the clear and serious evidences originally found by researchers at West Virginia University and the International Council on Clean Transportation [26-28], the VW company admitted that a special software was installed, which lowered the NO_x emissions only during dynamometer tests. During normal driving, the vehicles had up to ca. 35 times greater NO_x emissions than the legally allowed limit. By averaging over different on-road emission tests, the NO_x levels were 7 times higher than the limit for Euro 6 vehicles [28]. The software could distinguish between real driving and test driving conditions, thereby switching between the operation modes. This resulted in NO_x levels below the emission legislation limits when tested on the dynamometer. During on-road driving, however, the software altered fuel pressure, injection timing and exhaust-gas recirculation. For NO_x abatement systems using NH_3-SCR technology, also the urea injection amount/rate was lowered. The software was most likely implemented to save fuel and to improve the vehicle's acceleration, both valid selling points for higher mileage and power [29]. More than 11 million VW cars were affected worldwide and recent developments of the scandal brought to light that also other manufactures modified the NO_x emissions artificially under laboratory testing [30]. The market share of diesel vehicles decreased from 2016 onwards and it is probable that the scandal changed the entire light-duty vehicle landscape. Governments around the world are starting to discuss regulations and banning of diesel vehicles, thereby moving towards more eco-friendly automobiles [30]. For heavy-duty and off-road applications, the diesel engine is, however, still irreplaceable as power source due to its obvious advantages.

1.3 Selective catalytic reduction (SCR) of NO_x with NH_3

The SCR reaction converts gaseous NO_x with NH_3 to water and N_2 over a solid catalyst. The technology was first introduced in Japan in the 1970s for stationary exhaust gas after-treatment systems [31-32]. In Europe, the first SCR systems were installed in 1985 and the SCR technology is nowadays known as the most efficient and established posttreatment for reducing NO_x [8]. The term "selective" is used because NH_3 is selectively reacted with NO_x and is ideally not consumed by side reactions such as oxidation to N_2, N_2O or NO.

1.3.1 NH_3 sources

In the NH_3-SCR technology, a source of NH_3 has to be provided to the exhaust gas in order to reduce the NO_x to N_2 and H_2O. During the 1970 and 1980s, mainly gaseous or aqueous NH_3 was used as NH_3 source in stationary applications, but its toxicity and storage safety problems were unsuitable for mobile applications. In the late 1980s, urea ($CO(NH_2)_2$) was introduced as the safest and easiest to handle NH_3-precursor [33-34]. With the introduction of the SCR system in mobile applications, aqueous urea (most common trade name AdBlue®, 32.5 wt% urea [35]) became the most used NH_3-precursor worldwide, especially for heavy-duty engines [36-37]. Historically, as alternatives or for niche markets, cyanuric acid, ammonium formate, ammonium carbamate, metal ammine chlorides, methanamide or guanidinium salts can also be used as NH_3 sources [37].

1.3.2 Essential SCR related chemical reactions

There are three main types of SCR reactions that lead to the reduction of NO_x, depending on the NO/NO_2 ratio in the exhaust feed as well as the reaction temperature. The engine out NO_x emissions typically consist of ca. 90% NO and 10% NO_2 [8] but depend on the engine, the temperature and the exhaust gas after treatment systems installed upstream of the SCR system (e.g. DOC). In the "standard SCR reaction" (eq. (1-2)), one equivalent of NO and NH_3 are reacted together with O_2 to H_2O and N_2. The much quicker "fast SCR reaction" reduces one equivalent of NO and NO_2 together with two equivalents of NH_3 to N_2 and H_2O (eq. (1-3)). NO_2 can also react directly with NH_3 in the

generally called "NO_2-SCR reaction" (eq. (1-4)) [38-40]. At low temperature (<200°C) and an excess of NO_2, ammonium nitrate can be formed that can cause temporary deactivation due to catalyst pore blocking (eq. (1-5)) [41].

$$4NH_3 + 4NO + O_2 \rightarrow 4N_2 + 6H_2O \quad \textbf{(1-2)}$$

$$2NH_3 + NO + NO_2 \rightarrow 2N_2 + 3H_2O \quad \textbf{(1-3)}$$

$$8NH_3 + 6NO_2 \rightarrow 7N_2 + 12H_2O \quad \textbf{(1-4)}$$

$$2NH_3 + 2NO_2 \rightarrow N_2 + \ NH_4NO_3 + H_2O \quad \textbf{(1-5)}$$

Mainly reaction (1-2) and (1-3) are at work for the NO_x abatement above 200°C because of the inherently higher reaction rates and the fact that NO is the main component of the NO_x mixture. The selectivity for these reactions is generally high at temperatures below 400°C under dry model exhaust gas conditions and is enhanced at higher temperatures in presence of the inherently present H_2O in real exhaust gases [42]. However, at high reaction temperatures, side reactions start competing with the SCR reaction. The oxidation of ammonia with O_2 generates byproducts, namely N_2, N_2O, NO and NO_2 (eq. (1-6) - eq. (1-10)) [43].

$$4NH_3 + 3O_2 \rightarrow 2N_2 + 6H_2O \quad \textbf{(1-6)}$$

$$4NH_3 + 4O_2 \rightarrow 2N_2O + 6H_2O \quad \textbf{(1-7)}$$

$$4NH_3 + 5O_2 \rightarrow 4NO + 6H_2O \quad \textbf{(1-8)}$$

$$4NH_3 + 7O_2 \rightarrow 4NO_2 + 6H_2O \quad \textbf{(1-9)}$$

$$4NH_3 + 4NO + 3O_2 \rightarrow 4N_2O + 6H_2O \quad \textbf{(1-10)}$$

The most notable byproduct is nitrous oxide (N_2O), a significant greenhouse gas with a 310 time larger global warming potential than CO_2 [44]. Depending on the fuel quality, the reaction temperature and the catalyst used for the SCR applications, also NH_4NO_3 or sulfur containing species (e.g. $(NH_4)_2SO_4$) can form and alter the performance of the SCR catalyst [45-46].

1.3.3 SCR technology application range

Diesel engines are commonly separated into two categories, the on-road applications (e.g. passenger car, trucks or busses) and non-road applications

(e.g. mining trucks, harvesters, trains, container ships or power generating applications) [47]. While the size of the diesel engines is limited for on-road applications, the non-road applications encompass a great variety of engine sizes and designs. Due to the worldwide increasingly stringent NO_x exhaust regulations, both categories require NO_x abatement, most commonly by means of the NH_3-SCR technology. The NH_3-SCR technology installed in non-road applications differs from the on-road counterpart mainly in the outline, the volume of the SCR catalyst, the catalyst composition and the NH_3 source. This is because the engine size, typical engine working speed, quality of fuel and field of application are different [8, 47].

1.3.4 SCR catalysts

The core of the NH_3-SCR system is the catalyst which is generally installed as a monolithic unit. The last four decades of research yielded different classes of catalysts with a vast amount of diverse formulations. The most prominent classes are vanadia-titania and copper/iron-zeolite systems [8, 32, 48-51]. Vanadium or copper/iron is the active redox center while titania/zeolite acts as the support material. These types of catalysts have different main characteristics with advantages and disadvantages depending on the usage.

Due to the early industrial implementation, vanadium-based SCR catalysts were investigated thoroughly in the past decade [31]. To date, they are the choice for non-road applications. Major advantages are the high sulfur tolerance and the reasonable price for the integrated metal-oxides. Drawbacks are the moderate thermal/hydrothermal stability up to ca. 600°C, which rules out the installation of a DPF with active regeneration [8]. Their performance at low temperature is further dependent on the NO/NO_2 gas mixture (section 1.3.2) and only the "fast SCR" reaction provides an acceptable low-temperature activity [8, 39]. The vanadia-titania catalyst system is described in detail in section 1.4.

At low temperatures, Cu/Fe-exchanged zeolite catalysts exhibit a higher NO_x conversion efficiency than V-based catalysts [52]. These catalysts are also more thermally/hydrothermally stable, are less dependent on the NO_2 concentration (Cu-based catalysts) and are, therefore, more suited for systems with high

temperature excursions such as on-road applications [53]. Potential drawbacks are hydrocarbon poisoning, limited sulfur tolerance for most of these systems and high production costs. To that end, applicability issues with regard to the NH_3 dosage can arise because of the high NH_3 storage capacity of zeolites [8, 54-55].

1.4 Vanadium-based SCR catalysts

V-based catalysts typically consist of anatase TiO_2 as support material, WO_3 as a promoter for activity and stability and ca. 1 - 3 wt% V_2O_5 as the active redox species [8, 39, 56]. Various promoters, such as Mo, Fe, Ce or Mn are occasionally implemented [8, 57-60]. Despite the conventional V_2O_5 notation, vanadium is actually dispersed as VO_x species over the high surface area support due to the high interaction strength between V and Ti [61-64]. Extensive research has been undertaken to understand the different aspects of standard V-based catalysts. Amongst others, the efforts were aimed at understanding the influence of preparation methods [65-66], the nature of the active centers and the rate determining step [67-74], the origin of catalyst aging [75-76], the electronic interactions between the various catalyst components [77] or poisoning phenomena [78-80]. In the following, oxides of Ti, W, V, Si and other elements used in V-based catalysts are presented in detail.

1.4.1 Support Material - TiO_2

Support materials play the crucial role of dispersing the catalytically active species over their porous structure, thereby stabilizing the active metal(oxide) centers, hindering their sintering and decreasing the loading of costly elements (e.g. noble metals) [81-82]. A vast variety of support materials is used, ranging from carbon based materials to zeolites and to a large range of metal oxides. Some oxide based systems can generate difficulties because of undesired phase transitions under operating conditions. A good example is TiO_2 because of its three polymorphs, anatase, rutile and brookite, which are all naturally occurring at atmospheric pressure [83]. TiO_2 is nevertheless broadly utilized due to its tunable porous surface, thermal and chemical stability, acid-base properties and mechanical strength [81]. In contrast to SiO_2, TiO_2 interacts with the active metal phase and is, therefore, most often used for V-based SCR catalysts

[84]. TiO_2 further ensures a homogenous dispersion of the supported metal oxide such as vanadium oxide, which results in improved SCR activity [46].

The anatase modification is used the most as support material, as it is thermodynamically stable up to ca. 700 - 800°C where the irreversible anatase-rutile transition occurs [84]. The rutile modification is most often disadvantageous as SCR catalyst support because of its much lower surface area. The transition temperature can be adjusted by adding dopants in the synthesis process or by subsequent addition of cationic components. More than 30 cationic materials are known to inhibit or to promote the phase transformation [83]. TiO_2 can interact structurally or electronically with the additives, thereby changing its properties such as morphology, surface coverage, reducibility, acid sites strength and band gap [57, 77, 85-88].

1.4.2 Promoter - WO_3

Oxides of tungsten (also recognized as wolfram [89]) are the most common additives to the TiO_2 support. For instance, dispersed WO_3 is proposed to have multiple promotional effects including the prevention of V island formation [62, 76], the increase of the number of NH_3 adsorption sites [87] or the improvement of thermal stability of the thermodynamically unfavorable anatase phase [39]. Most frequently, WO_3 is introduced by impregnation using ammonium meta- or paratungstate as precursor. WO_3 induces and preserves high levels of TiO_2 lattice distortions that limit particle growth. The onset of the anatase to rutile phase transition can thus be delayed from ca. 700 to 900°C by adding 3 - 9 wt% WO_3 [90-92]. The specific surface area mirrors the effect of anatase particles growth and the phase transition upon an increased calcination temperature. For example, the surface area of TiO_2 calcined at 600 and 700°C dropped from 70 m^2/g to ca. 20 m^2/g, respectively, while it decreased from 90 to only 54 m^2/g in the case of 6 wt% WO_3-TiO_2 [90]. The dispersion of WO_3 on TiO_2 is also crucial for its promotional effects and depends on the preparation method [93]. WO_3 remains amorphous on TiO_2 up to a loading of ca. 7 wt% after impregnation in basic conditions [91]. By careful control of the W concentration and the pH in the impregnation procedure, one can regulate the nuclearity of adsorbed WO_x species on TiO_2. The adsorption process of WO_x is driven elec-

trostatically and involves bridging and terminal neighboring (hydr)oxo groups [94].

Another important promoting effect is gained by increasing the surface acidity [95], which guarantees the NH_3 supply for the SCR reaction. With the addition of WO_3, the weak basic sites of titania disappear and WO_3-TiO_2 becomes much more acidic. The type of acidity (Brønsted or Lewis sites) thereby depends on the loading as well as the surrounding atmosphere [96]. In the absence of water and with a moderate W-loading, surface tungstate species are present as Brønsted and Lewis acid sites [92], while in the presence of water, the Lewis acid sites can convert into Brønsted sites [97-98].

Additional promotional effects include the broadening of the SCR temperature window, the poisoning resistance to alkali metal and arsenious oxides and the lower ammonia and SO_2 oxidation at elevated reaction temperature [92, 99-100].

1.4.3 Promoter - SiO_2

Silicon is proposed to be a valuable promoter for tackling the stability of TiO_2 because it delays sintering [101-108]. The stabilization effect can origin from the distortion of the anatase lattice, the formation of solid solutions, the substitution of Ti^{4+} by Si^{4+} or from the inhibition of molecule diffusion and the reduction of anatase inter-particle contact [83]. All these phenomena possibly hinder the growth of anatase crystallites and the subsequent phase transformation to rutile [109]. Except for the stabilization effect, SiO_2 lowers the activity of an SCR catalyst. It is thus of importance to carefully choose and design the synthesis of Si-stabilized V-based SCR catalysts [101, 103, 105-107, 110-111]. The effect of SiO_2 as a promoter of V-based catalysts is addressed thoroughly in Chapter 6.

1.4.4 Commercial TiO_2-based support materials

With the research and development of the SCR technology for the transportation and off-road sector during the 1990s, tailored TiO_2-based support materials with different promoters appeared on the market. To date, these supports are produced by many suppliers and are commercially and academi-

cally widely used in the SCR community. The materials used in this work (**Table 1-1)** are prepared by a co-precipitation method where WO_3 and/or SiO_2 are added as promoters as described in section 1.4.2 and section 1.4.3 and the TiO_2 is synthesized from the sulfate process [101].

Table 1-1. Commercially available support materials used in this work for the preparation of V-based SCR catalysts [112].

tradename [a]	DT-51	DT-51D	DT-52	DT-58	DT-S10
abbreviation	TiO_2	TiO_2	WTi	SiWTi	SiTi
TiO_2	100 wt%	100 wt%	90 wt%	81 wt%	90 wt%
TiO_2 modification	anatase	anatase	anatase	anatase	anatase
WO_3			10 wt%	9 wt%	
SiO_2				10 wt%	10 wt%
SO_3	1.25 wt%	0.6 wt%	1.35 wt%	0.3 wt%	0.3 wt%
surface area (m^2/g)	90	85	90	110	110

[a] Cristal Global company

1.4.5 Other promoters

Molybdenum oxide has a similar effect on V_2O_5/TiO_2 as WO_3. It prevents TiO_2 from sintering, increases the acidity of the catalyst, is advantageous in the NO_x conversion and NO and SO_2 oxidation [39], alters the electronic interaction between V and the support [57] and prevents catalyst deactivation by As [113].

Cerium oxide addition can improve the NO_x conversion of V-based catalyst in a broad temperature regime due to enhanced NO_x adsorption and synergetic interactions among the Ce and V, W species [59]. Ce can also act as a redox center, thereby acting as the active site which can produce active SCR catalysts without V, thus being considered an SCR active component [114-115]. The redox properties of the Ce^{4+}/Ce^{3+} pair and the propensity of Ce to form solid solutions with other oxides increases the amount of active sites and improves the (hydro)-thermal stability [59, 116-122]. Ce-modified V-based SCR catalysts show enhanced thermal stability because of the formation of cerium vanadate which decreases the propensity of anatase to sinter [123].

The addition of manganese oxide is especially useful to generate low-temperature SCR catalysts because it readily provides oxygen for the re-oxidation of the active sites [124-125]. Because of its high activity, Mn-based catalysts can be prepared without V but often lack hydrothermal and SO_2 resistance. By modifying the composition with Ce, progress towards higher stability and resistance to SO_2 was made [126].

1.4.6 Vanadium oxides - active sites

Vanadium (V) is a Group 5 transition element and is the 23rd element of the Periodic table. It is the 22nd most abundant element in the earth's crust and in its metallic form it is bright sliver-white, soft and ductile. At first, it was of interest for nutritionists because it was found to be an essential element for marine mammal species. With time the element was found to be useful for a broad variety of applications, such as stainless steel fabrication, catalysis and batteries [127-129].

Especially for catalysis, supported vanadium-oxide is nowadays essential for the production of chemicals by selective oxidation as well as for NH_3-SCR [130-131]. Supported vanadium-oxide SCR catalysts (V-Ti) are commonly labelled V_2O_5-TiO_2, even though vanadium is not present as such. Depending on its loading, V is highly dispersed over the large surface area of TiO_2 and is present as tetrahedral VO_4 units in monomeric or polymeric form [132-133]. An estimate surface density of ca. 8 VO_x/nm^2 is used for monolayer coverage on TiO_2 [134-135]. For the sake of comparison between catalysts, the composition of V-based SCR catalysts is normally given in wt% of metal oxide (e.g. WO_3 or V_2O_5). Vanadium is typically impregnated on anatase together with WO_3 for the purposes discussed in section 1.4.2. Typical compositions include ca. 1 - 3 wt% V_2O_5, depending on the application [40, 46]. More details on the loading of vanadium on a TiO_2-based support are discussed in Chapter 3.

The formal oxidation state of supported vanadium oxide is either V^{5+} or V^{4+}, but catalysts generally contain both oxidized and reduced vanadium cations. The V^{5+}/V^{4+} redox couple is crucial for the SCR reaction, but also for oxidation catalysts or vanadium redox batteries [61, 136]. In aqueous solutions, V^{5+} ions form yellow complexes, while V^{4+} generates blue aquo-complexes. For the

synthesis of SCR catalysts, the vanadium oxide is impregnated with a vanadium precursor such as ammonium metavanadate. The formal V oxidation state of the precursor is V^{5+}, the corresponding aqueous solution is yellow and so are the synthesized V_2O_5-(WO_3)-TiO_2 catalysts.

The exact nature of the active VO_x species on TiO_2 is an ongoing debate and has been the subject of extensive spectroscopic investigations [137-143]. The performance of a V-based SCR catalyst depends on V-loading, support and promoter material as well as on its preparation method, making it unlikely that all catalysts exhibit the same VO_x species as active sites. To that end, different characterization methods are used, which have diverse strengths and limitations towards, e.g., the vanadium visibility, the surface sensitivity or the oxidation state detection [134, 139, 144-149]. Despite the ambiguities, it is now generally accepted that below monolayer coverage, monomeric or polymeric VO_x species are strongly anchored to the TiO_2 surface [143]. However, vanadium oxide supported on TiO_2 can become mobile under SCR conditions or high temperatures, resulting in geometrical structure transformations of VO_x [64, 150]. More recently, various theoretical studies based on DFT calculations targeted the nature of monomeric and polymeric VO_x species on TiO_2 more precisely. For instance, the surface oxygen atoms, the terminal oxygen atoms (e.g. V=O), surface acid sites or the TiO_2 anchoring planes were explored in order to understand the synergetic effect of V and Ti on an atomic level [68, 150-153]. Because of the strong interaction between Ti and V, theoretical studies using a bulk V_2O_5 model have to be read with caution [67, 154-155]. Studies using a set of monomeric and polymeric VO_x units on a model TiO_2 surface concluded that different VO_x structures may coexist on the surface [68, 150, 156-158]. After hydration of the model system, the V=O bonds remained stable and interacted weakly with surface TiO_2. The structures of the VO_x units are, however, heavily V loading and reaction condition dependent.

1.4.7 Proposed mechanisms

During the 1980s and 1990s, the reaction mechanism on V-based catalysts was heavily investigated as summarized by Busca et al. and Forzatti [39, 140]. It is now generally accepted that the standard SCR reaction proceeds accord-

ing to the stoichiometry of eq. (1-2) and each nitrogen atom of the N_2 product originates from NO and NH_3. The first popular proposal was an Eley-Rideal type mechanism, where gaseous NO reacted with adsorbed NH_4^+ to form N_2 and H_2O [159]. The ammonium ion is thereby adsorbed on a V-OH Brønsted acid site and an adjacent V^{5+}=O species acts as the redox active site. In the following, studies confirmed this reaction scheme with slight modifications and alterations [160-161].

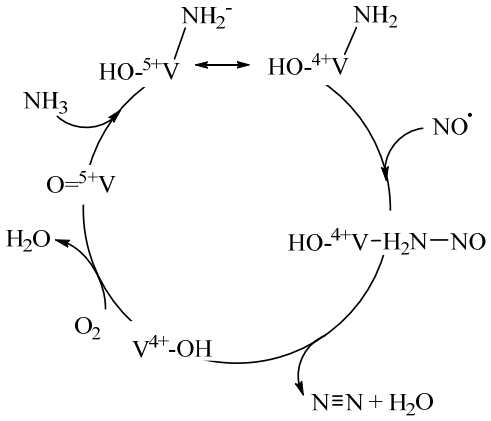

Figure 1-4. Proposed reaction mechanism with Lewis acid centers as NH_3 adsorbing sites.

In the early 1990s, the "amide-nitrosamide" mechanism was proposed, which utilized a Lewis acid site for the adsorption of NH_3 instead of a Brønsted acid site (**Figure 1-4**) [69, 140, 162]. This mechanism was more detailed especially because of the introduction of the nitrosamide (H_2N-NO) intermediate which readily decomposes into N_2 and H_2O.

A combination of the reaction including both mechanisms, the adjacent V species and the "amide-nitrosamide" mechanism was proposed by Topsøe et al. [70, 163]. NH_3 adsorbs on a Brønsted acid site and is activated by an adjacent V^{5+}=O site acting as the redox center according to **Figure 1-5**. To date, it is still debated whether the Brønsted and Lewis acid sites are the important adsorption sites for the SCR reaction and it remains unclear whether it is essential that the active V site is in close proximity to a second VO_x center. Chapter 5 is dedicated to disentangle this ambiguity using advanced spectroscopic methods and experimental design. Advances in the spectroscopic techniques,

computational and *in situ*/*operando* studies continuously provide new aspects concerning the SCR reaction [67-68, 74, 154-155, 164-166].

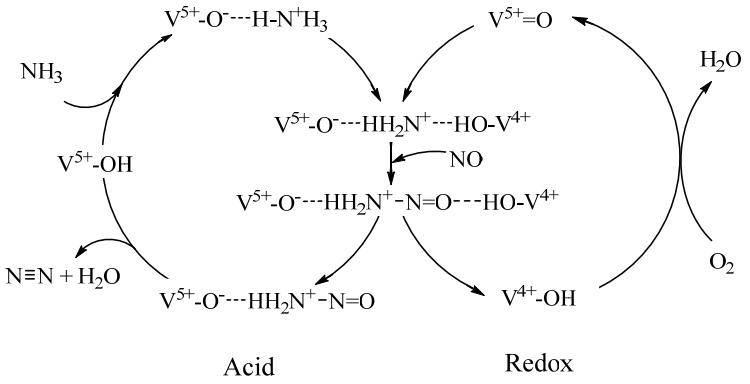

Figure 1-5. Proposed reaction mechanism with Brønsted acid centers as NH_3 adsorbing sites [70].

The exhaust gas composition, loading/surface covering of V-species and promoters are, however, different for most mechanistic studies. It is therefore plausible that not only one mechanism is correct on V-based SCR systems. Some key factors are nonetheless generally accepted [8, 140, 153]:

- The SCR reaction proceeds according to eq. (1-2) and N_2 is formed from the nitrogen atoms of NO and NH_3.
- NO and NH_3 are reacting according to an Eley-Rideal type mechanism (NH_3 is adsorbed on the catalysts).
- N_2O is not an intermediate.
- V species are the active redox sites, reduction occurs upon the reaction of NO and NH_3, while the re-oxidation is done by O_2.

1.5 Vanadate-based SCR catalysts

SCR catalysts in mobile sources have to operate under dynamic conditions and in extreme cases, such as low temperature due to cold starts or short city driving. As explained in section 1.2.2, the catalysts can also be exposed to high temperature (> 600°C) due to the coupled particulate filter, which is often located upstream of the SCR catalyst and undergoes periodical regeneration. Therefore, such catalysts have to exhibit both high N_2 selectivity and high-temperature stability over a broader operation temperature window [8, 64, 167-

168]. A possible solution to the limited thermal stability of V_2O_5-based SCR catalyst was proposed by Casanova et al. [169]. Modification of a V_2O_5-based catalyst with rare earth metals resulted in increased SCR activity and improved surface area stability after aging at 750°C. The formation of metal vanadates ($MeVO_4$) was considered as the driving force for the enhanced performance. Based on this study, $MeVO_4$ were introduced as a new class of SCR active materials. Their potential is further amplified by their high melting temperatures, lower V volatility and no toxicity compared to V_2O_5-based catalysts [170].

Table 1-2. Melting points and corresponding Tamman temperatures of selected metal oxides and metal vanadates [168, 171-173].

metal oxide	melting point (K)	Tamman temperature (K)
V_2O_5	963	482
WO_3	1745	873
TiO_2	2120	1060
Fe_2O_3	1838	919
$FeVO_4$	1123	562
$CeVO_4$	1373	687
$TbVO_4$	above 1400	-
$ErVO_4$	above 1400	-

Mobile V and W-containing species on the support are most often the origin for the onset of catalyst activation/deactivation, TiO_2 phase transition and V volatility [64]. The theoretical starting temperature of diffusion can be rationalized on the base of the Tamman temperature, the half melting point of the oxides in K. It reflects the temperature at which the molecules of the solid phase have acquired enough energy for their start of bulk mobility and reactivity due to thermal generation of defects [174]. While it is below 250°C for V_2O_5, the Tamman temperature for, e.g., TiO_2 is ca. 780°C, making it understandable why vanadium species on a TiO_2 surface are more readily prone to diffuse on the support compared to other oxide phases present in the catalysts. The Tamman temperature of all metal vanadates is higher compared to V_2O_5 (**Table 1-2**), making the metal vanadates inherently more stable.

Unsupported bulk $MeVO_4$ materials exhibit some SCR activity [175-177]. When supported on a TiO_2-based material, the SCR activity of various $MeVO_4$ such as $FeVO_4$, $ErVO_4$ or $TbVO_4$ can be greatly enhanced [58, 168, 170, 178-182]. Rare earth metal vanadates supported on SiWTi (**Table 1-1**) exhibit a high thermal stability up to 750°C while remaining SCR active [167, 169]. The stability is proposed to originate from the ability of the rare earth metals to suppress the undesired anatase to rutile phase transition of the support. Since vanadium is locked in the vanadate structure, no free V_2O_5 that promotes sintering is dispersed on the catalyst surface [167].

1.6 Challenges for V-based SCR catalysts

The location of the SCR catalyst in mobile diesel exhaust gas after treatment systems (**Figure 1-3**) heavily affects the exhaust gas temperature and composition and generates challenges for vanadium-based catalysts. As stated in section 1.3.4, V-based catalysts are not as thermally stable as Cu/Fe-exchanged zeolite catalysts. In addition, the low-temperature activity is not as high as that of zeolite-based materials [52]. It is therefore essential to chemically modify V-based catalysts by altering the composition of the support material or by changing the active vanadium redox center. They further bear potential risk to human health and the environment when V is released to the atmosphere because the thermal stability of V-based catalysts is not given above ca. 550°C [183]. The Occupational Safety and Health Administration have listed V_2O_5 as a contaminant with limits of 0.5 mg/m^3 for dust and 0.1 mg/m^3 for fumes [184] and the U.S. Environmental Protection Agency has listed V_2O_5 as a harmful pollutant [185]. An ideal V-based SCR catalyst should therefore be free of V_2O_5 or WO_3 emissions even at high reaction temperature. A last challenge that is especially prominent for this type of catalyst is the dependence on NO_2 at low temperature because only with a sufficient amount of NO_2 in the gas feed, the low temperature acidity is competitive with Cu-exchanged zeolite catalysts.

Summarizing, an ideal vanadium-based SCR catalyst should withstand high temperatures up to ca. 650°C without releasing V and W, should be low-

temperature active (<200°C) and should not be affected by any contaminants such as alkali metals, mercury or sulfur.

1.7 Background of the thesis

This work was initiated by Treibacher Industrie AG (TIAG), a chemical industry company located in Althofen, Austria. The presented work is thus part of a research collaboration between TIAG and the Paul Scherrer Institute (PSI). The original title of the research plan was "Entwicklung temperaturstabiler Vanadium-basierter SCR-Katalysatoren, insbesondere mit Vanadaten als Aktiv-Komponente". Therefore, the main focus of the collaboration was the exploration of the potential of metal vanadates as SCR catalysts. After benchmarking the state-of-the-art V-based SCR catalysts, it was the aim to generate highly active $MeVO_4$-based SCR catalysts with improved thermal stability compared to conventional V_2O_5-based catalysts.

1.8 Scope of the thesis

The thesis is divided in two parts. The first part (Chapter 3 - Chapter 5) focuses on the assessment and characterization of standard $V_2O_5/WO_3/TiO_2$ (VWT) catalysts. Although the last 30 years of research on the SCR technology has produced a vast amount of knowledge, it is necessary to deepen this knowledge in order to advance the catalyst performance and durability. Due to progress in the characterization equipment technology, the data quality has greatly enhanced and it is nowadays possible to monitor the behavior of a catalyst under relevant working conditions with high time resolution. After testing different V_2O_5 loadings and preparation methods, an optimized VWT catalyst was investigated by means of transient experimentation, which revealed important insights into the mechanism of the SCR reaction. The three chapters are based on publications in "Catalysts" [186] and in "Angewandte Chemie International Edition" [187] as well as one manuscript in preparation [188].

The second part (Chapter 6 - Chapter 8) is dedicated to the improvement of the thermal stability and durability of VWT catalysts. To gain stability, either different sources of SiO_2 were incorporated and/or the vanadium source was changed to metal vanadates, a novel class of SCR materials. Different metal

vanadates were investigated in order to optimize the performance and stability and physico-chemical characterization methods were applied to gain insights into the behavior of metal vanadates. The three chapters are based on publications in “ACS Catalysis” [189], in “Applied Catalysis B: Environmental” [190] and in “Catalysis Today” [191].

Chapter 2

Methods

2.1 Preparation of catalysts

2.1.1 Vanadia-based SCR catalysts

Unless otherwise stated, the catalytic powders were prepared by wet impregnation of a commercial titania-based support (**Table 1-1**) with NH_4VO_3 (AMV, Simga Aldrich). AMV was dissolved in water and added to an aqueous slurry of the support material. After the slurry was sonicated for 10 min in an ultrasonic bath, homogenized with a disperser (Miccra D-8, 20,000 rpm, 5 min) and stirred for ca. 30 min, water was evaporated under reduced pressure and the sample was dried at 120°C for ca. 3 h. Finally, the sample was grinded thoroughly and was calcined at 450°C or 550°C in a muffle oven for 3 h or 10 h (fresh catalyst).

2.1.2 Metal vanadate-based SCR catalysts

The bulk metal vanadates ($CeVO_4$, $FeVO_4$, $ErVO_4$) were provided by Treibacher Industrie AG and were obtained from co-precipitation of metals nitrate and AMV. The powders were dried at 120°C and calcined at 700°C if needed. SiWTi ("Tiona DT-58", 10 wt% SiO_2, 9 wt% WO_3, and 81 wt% TiO_2, Cristal Global, **Table 1-1**) was used as the catalyst support. After mixing $CeVO_4$, $FeVO_4$, $ErVO_4$, CeO_2 (Sigma-Aldrich) with SiWTi in 5 eq. of H_2O at RT for 1 h, the slurry was sonicated for 10 min, homogenized with a disperser (30'000 rpm, 5 min) and stirred at 50°C for 30 min. The solvent was removed under reduced pressure and the resulting powder was dried at 120°C and calcined at 450°C for 3 h in a muffle oven. For the sake of comparison, the metal vanadate loading was calculated based on the amount of nominal V_2O_5.

2.1.3 Preparation of monoliths

For washcoating, the powders were suspended in a mixture of water (2-3 eq. of sample), homogenized with a disperser (30,000 rpm, 5 min) sonicated for 10 min in an ultrasonic bath. The honeycomb monoliths (cordierite, 400 cpsi, ca. 12 × 17 × 50 mm) were dip coated by repeated immersion in the slurry and drying with an air blower until a loading of the active material of ca. 1.25 - 1.35 g was obtained. The monoliths and the remaining slurry were dried overnight at 120°C and calcined at 450°C for 10 h in a muffle oven.

2.2 Catalytic tests

The washcoated monoliths were tested on a laboratory test reactor (**Figure 2-1**, [192-193]) under a feed of 10 vol% O_2, 5 vol% H_2O, 500 ppm NO, 0 - 600 ppm NH_3 with balance N_2 (ca. 500 L_n/h), in order to mimic realistic exhaust gas composition. The gas hourly space velocity (GHSV = volumetric gas flow/coated monolith volume) was 50,000 h^{-1}, which is typical of SCR converters of diesel vehicles [192]. The NO_x conversion was estimated according to (2-1) [56, 194]:

$$NO_x\ conversion = \frac{C^{in}_{NO_x} - C^{out}_{NO_x}}{C^{in}_{NO}} \cdot 100\% \qquad \textbf{(2-1)}$$

where C^{in}_{NOx} is the NO concentration upstream of the catalyst and C^{out}_{NOx} the sum of the NO and NO_2 concentrations downstream of the catalyst. Online gas analysis of the exhaust gas was performed with a Fourier transform infrared spectrometer (Nexus 670 ThermoNicolet, ThermoFisher) equipped with a heated gas cell. The maximum NO_x conversion was measured by dosing NH_3 in excess, i.e. at $NH_3/NO_x = 1.2$. The excess of NH_3 is exploited to achieve a maximum NO_x conversion that is not affected by possible side reactions of NH_3. It further ensures a maximum NH_3 surface coverage at elevated reaction temperatures [195]. Since the standard SCR-reaction (1-2) is zeroth order with respect to NH_3, NH_3 does not influence the equilibrium.

For the screening of potential catalysts, not the whole reaction temperature regime was measured but only 250, 350 and 550°C. 250°C represents the low temperature regime and provides data for the calculation of the reaction rate con-

stants. At 350°C, V-based catalysts often exhibit their optimal working conditions. The high temperature activity and selectivity were tested at 550°C.

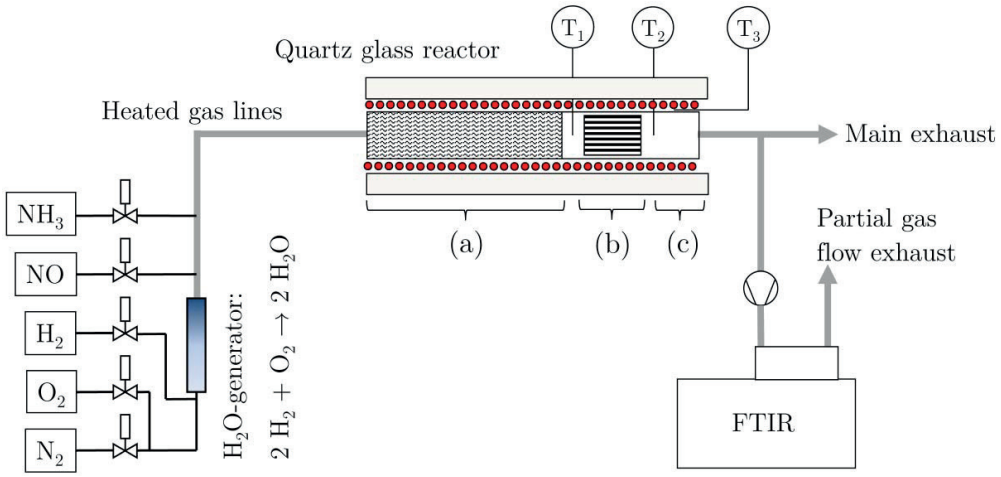

Figure 2-1. Laboratory test rig with a gas mixing set up, heated gas lines, H_2O-generator, quartz glass reactor and an FT-IR spectrometer. To ensure uniform temperature along the reactor bed, the reactor was divided into three heating zones: (a) pre-heating with ceramic beads and temperature control at T_1, (b) length of the catalyst bed with the temperature control at T_2 in the center of the reactor and (c) reactor outlet the temperature control at T_3. A partial gas flow was actively let through the gas analysis, a Fourier transform infrared spectrometer with a 2.0 m gas cell.

In order to obtain a more practice-oriented value for SCR systems, the NO_x conversion at 10 ppm NH_3 slip was measured as well [40, 193, 196]. The mass specific rate constant (k_{mass}) for the maximum NO_x conversion was calculated according to (2-2), under the assumption of a pseudo-first order of the SCR reaction with respect to NO and zeroth order with respect to NH_3 (full surface coverage with ammonia) [40, 194-195],

$$k_{mass} = -\frac{V^*}{A} \cdot ln(1 - X_{NO_x}) \qquad \textbf{(2-2)}$$

where V^* is the total flow rate at reaction condition, A the loading of the active component and X_{NOx} the fractional NO_x conversion. Although adsorption of both NH_3 and NO occurs at low temperature [40], NH_3 adsorption dominates on acidic SCR catalysts so that the first order SCR reaction with respect to NO is justified. The rate constant is independent of the active component loading, which is particularly important for coated monoliths where small loading

deviations are unavoidable. It should be noted that k_{mass} is a parameter used for the sake of comparison of the catalysts and not for quantitative kinetic studies. Only k_{mass} values at 200 - 300°C were used for the comparison. Above 300°C, diffusion limitations, NH_3 desorption and high NO_x conversion hinder the usage of this parameter. The k_{mass} normalized by the BET specific surface area is provided as k_{BET}.

The N_2O, NO and NO_2 selectivities were obtained from the direct NH_3 oxidation in an NO-free feed consisting of 500 ppm NH_3, 10 vol% O_2 + 5 vol% H_2O in N_2 according to

$$S_i = \frac{v_{NH_3} \cdot product\ (i) formed}{v_i \cdot NH_3\ consumed} \qquad \left[\frac{mol\ N}{mol\ N}\right] \qquad \textbf{(2-3)}$$

where v_{NH3} and i are the stoichiometric coefficients of ammonia and product i (NO or NO_2). For N_2O, the coefficient is ½.

2.2.1 Aging of catalysts

The type of aging has a great influence to structure and the activity of the catalytic material and is therefore always addressed accordingly. Two main aging procedures were applied, namely thermal and hydrothermal aging. Unless stated otherwise, the thermal aging of washcoated monoliths was performed in a muffle oven at ambient pressure and gas environment by ramping the temperature to the set-point within two hours. The hydrothermal aging of the washcoated monoliths was performed in a lab scale flow reactor (analogous set up to that shown in **Figure 2-1**) in 20 vol% O_2 and 10 vol% H_2O with balance N_2 at GHSV = 10,000 h^{-1}. Generally, the set-point temperature (e.g. 550, 600, 650, 700 or 750°C) was reached after 30 min and the dwelling time was 16 h.

2.3 Characterization techniques

2.3.1 Powder X-ray diffraction spectroscopy

Powder X-ray diffraction (XRD) patterns were collected on a D8 ADVANCE (Bruker AXS GmbH, Karlsruhe, Germany) diffractometer using Cu kα1 radiation (λ = 1.5406 Å). Data were recorded from 10° to 65° 2Θ using a step size of 0.03°/1 s acquisition time. The phases were identified with the

X'Pert HighScore Plus software. The average crystallite size ($D_{p,XRD}$) of TiO_2 was determined by the Scherrer equation (eq. (2-4)) using the peaks at 25.4 and at 48.0° [197],

$$D_{p,XRD} = \frac{K\lambda}{\beta \cos\Theta} \qquad \textbf{(2-4)}$$

where λ is the wavelength of X-ray, Θ the diffraction Bragg angle and β is the corrected peak width at half maximum.

2.3.2 BET surface area

Based on the theory of Brunauer-Emmett-Teller (BET, [198]), the specific surface area (SSA) was measured by N_2 adsorption at –196°C on a Quantachrome Autosorb I instrument. Prior to the measurement, the samples were outgassed at 300 - 350°C for 5 - 10 h. For the calculation of the BET-SSA, 11 points in the pressure range of 0.05 - 0.3 P/P_0 were chosen as generally applied for mesoporous materials.

The surface density (ρ_o, atoms/nm^2, eq. (2-5) of the metal oxides covering the TiO_2 surface are calculated as follows [199]:

$$\rho_o = \frac{\frac{N_A \cdot x_o}{MW}}{SSA \cdot 10^{18}} \qquad \textbf{(2-5)}$$

$$f_{m,o} = \frac{\rho_o}{\rho_{m,o}} \qquad \textbf{(2-6)}$$

$$Tf_m = \sum\nolimits_o f_{m,o} \qquad \textbf{(2-7)}$$

where N_A is Avogadro's number, x_o the weight fraction of the supported metal oxide (SiO_2, WO_3, V_2O_5) and MW the corresponding molecular weight. The fractional monolayer coverage ($f_{m,o}$) and the total fractional monolayer coverage (Tf_m) were calculated from the surface density (ρ_o) and the theoretical monolayer coverage ($\rho_{m,o}$, e.g. 7.9 VO_x nm^{-2} and 4.2 WO_x nm^{-2} [135]) according to eq. (2-6) and (2-7), respectively [102]. In Chapter 3, 4 and 8, the monolayer coverage is given as $\Upsilon = f_{m,o} \cdot 100\%$.

2.3.3 Diffuse reflectance infra-red Fourier transform (DRIFT) spectroscopy

Diffuse reflectance Fourier transform infrared (DRIFT) spectra were measured using a Bruker Vertex 70 spectrometer (Bruker) equipped with a liquid N_2 cooled MCT detector and a Praying Mantis mirror unit (Harrick). The homemade DRIFT cell was equipped with a flat CaF_2 window (d = 25 mm; 2 mm thick) and was connected to gas supply lines. The catalyst powder was finely ground and softly pressed in the sample holder of the cell. Prior to the experiments, the samples were dried *in situ* in 10 vol% O_2 (100 mL/min, bal. N_2) at 400°C for 1 h. After cooling to 250°C, a background spectrum was collected prior to admittance of NH_3. NH_3 adsorption was followed during exposure of 500 ppm of NH_3 - 5 vol% O_2 flow (100 mL/min, bal. N_2) at 250°C for 15 min. All spectra were collected by accumulating 100 scans at 4 cm^{-1} resolution and a scanner velocity of 80 kHz.

2.3.4 Diffuse reflectance ultra-violet visible spectroscopy (DRUV)

The diffuse reflectance ultraviolet visible (DRUV) spectra were measured using a Carry 4000 spectrometer (Agilent) equipped with the same set of mirrors used for DRIFT. The spectra were recorded in the range 200 - 800 nm and are presented in Kubelka-Munk units [200]:

$$\mathrm{F(R)} = \frac{(1-R)^2}{2R} \qquad \textbf{(2-8)}$$

where R is the absolute reflectance of the sampled layer. The catalyst samples were background corrected using a spectrum of the corresponding support material, while $BaSO_4$ was used as background for all reference samples. The Fityk software [201] was exploited for the deconvolution of the DRIFT and DRUV data using Gaussian functions for all features.

2.3.5 Raman spectroscopy

Raman spectra were recorded with a Raman spectrometer (CW Raman RXN1-PhAT-785-D-laser Invictus, Kaiser Optical Systems SARL) equipped with a 785 nm diode laser (Invictus 785 nm NIR Laser) and a PhAT-system probe-head (Kaiser Optical Systems) with collimated incident radiation and a sampling spot-size diameter of ca. 3 mm. The average laser power on the sam-

ple was ca. 300 mW and the detector was a charge-coupled device (CCD, 1024×256 EEC MPP Type, Kaiser Optical Systems) cooled to −40°C. The spectra were collected at ambient conditions by averaging 100 scans with each an exposure length of 2 s and a spectral resolution of 1 cm^{-1}.

2.3.6 X-ray absorption spectroscopy

X-ray absorption near edge structure (XANES) spectra were recorded at beamline SuperXAS of the Swiss Light Source (SLS, Villigen, Switzerland). The spectra were collected around the V K-edge (5.465 keV) in fluorescence mode using double Si(111) crystal monochromator and a 10 µm V foil to calibrate the monochromator position. Samples were diluted with cellulose and pressed into pellets. The data were aligned, background corrected, and normalized using Athena (IFFEFIT software package [202]).

Chapter 3

Optimizing the vanadium loading on a tungsta-titania support for activity and stability

3.1 Introduction

The amount of vanadium used to promote the SCR activity of WO_3-TiO_2 (WTi) is a crucial aspect for the activity and stability of the catalyst. Despite the conventional V_2O_5 notation, vanadium is mainly present as dispersed monomeric or polymeric VO_x species [61-63]. A V_2O_5 content of 0.5 - 1.5 wt% is often chosen for stationary applications, where the volume of the catalytic converter and the activity are not key properties. Instead, sulfur resistance and longevity, which lower the overall production costs, are of higher significance [99]. In mobile applications, V-based catalysts need to be highly active due to the limited available space for the exhaust gas treatment system. Hence, the V_2O_5 content is increased to 2 - 3 wt%. Moreover, these catalysts have to operate in a broader temperature window ranging from cold start conditions to full engine load. Finally, the SCR catalyst may experience severe temperature surges because of the regeneration of the upstream diesel particulate filter.

The V-loading has been investigated on various support materials such as Al_2O_3, ZrO_2, SiO_2 or TiO_2 [56, 62, 133, 143, 203]. Among these, WTi has often been used for catalyst preparation. Madia et al. examined the thermal stability of 1, 2 and 3 wt% V_2O_5/WTi [75]. The most active and thermally stable catalyst at 600°C was found at 2 wt% V_2O_5. The structural investigation revealed

This chapter is based on the postprint version of the publication: A. Marberger, M. Elsener, D. Ferri, O. Kröcher, VO_x Surface Coverage Optimization of V_2O_5/WO_3/TiO_2 Catalysts by Variation of the V Loading and by Aging, *Catalysts* **2015**, *5(4)*, 1704-1720. A. Marberger performed most experiments, analyzed and interpreted the data together with the coauthors and wrote the manuscript.

that the enhanced SCR performance is related to the amount of polymeric vanadyl surface species generated by the thermal aging. The decrease in the SCR performance for the high V-loaded catalyst upon aging was related to the loss of surface area and to the growth of three-dimensional vanadia species. Went et al. [133] investigated the different V species by varying the V_2O_5 loading on TiO_2 from 1.3, 2.5, 3.0, 6.1 and 9.8 wt%. It was shown that both monomeric and polymeric VO_x species are present up to 3 wt% V_2O_5, while crystalline V_2O_5 was also detected above 6 wt% V_2O_5. Lee et al. [204] investigated V_2O_5/WTi with a V_2O_5 loading of 1, 3, 5, 7 and 10 wt% and different preparation methods. The 3 wt% V_2O_5/WTi exhibited the highest NO_x conversion in the fresh state at 450°C and after aging at 650°C. The V loading of V_2O_5/WTi has been the object of attention of other authors as well, e.g. Putluru et al. [205] (1.5 and 3.0 wt% V_2O_5/WTi), Amiridis et al. [206] (1.0, 2.0, 3.5, 3.9, 6.6, 8.5, 11.1, 15.9 wt% V_2O_5/WTi) Kompio et al. [62] (0.5, 1.5, 3.0, 5.0 wt% V_2O_5/WTi) and Djerad et al. [56] (3 and 8 wt% V_2O_5/WTi). All these studies emphasize the importance of an optimal V loading on a TiO_2-based SCR catalyst. However, the adjustment of the loading only slightly around 2 - 3 wt% V_2O_5, the concentration range relevant for real-world applications, is missing.

The calcination and aging of V_2O_5/WTi catalysts cause a change of the surface area that is directly linked to the surface density of vanadyl species and as a consequence also the catalytic performance. As Kwon et al. [207] pointed out, one can determine the optimal surface density of the vanadyl species that is crucial for a high catalytic activity. By variation of the V loading (0, 0.5, 1.0, 1.5 and 2.0 wt% V_2O_5) in these V_2O_5/TiO_2 catalysts, a VO_x surface density of 4.5 VO_x nm^{-2} was found to be optimal for high NO_x conversion. This corresponds to a surface coverage of 55 - 60%, based on the theoretical maximum VO_x surface density of 7.9 VO_x nm^{-2} [135].

The objective of this chapter is the fine-tuning of V_2O_5 on a commercial WTi support, thereby clarifying the importance of this parameter for the optimum performance. The catalyst composition was systematically altered with 1.7, 2.0, 2.3, 2.6, 2.9, 3.2 and 3.5 wt% V_2O_5. Additionally, the catalysts were hydrothermally aged in order to mimic a long term use.

3.2 Catalyst preparation

The general preparation of V-based catalysts is described in detail in section 2.1.1. For this investigation, a commercial WO_3-TiO_2 (WTi, 12 g, **Table 1-1**) support was impregnated with NH_4VO_3 (eq. to 1.7 - 3.5 wt% V_2O_5, Sigma Aldrich). For washcoating the monoliths, the powders were suspended in a mixture of water (2 eq. of sample) and colloidal silicate (Ludox, 40 wt% in H_2O, Sigma Aldrich, 0.1 eq. of TiO_2) was used as binder material.

3.3 Characterization

Catalytic measurements and characterization methods (BET, XRD and XANES) are described in detail in the sections 2.2 and 2.3, respectively.

3.4 Results and Discussion

3.4.1 Catalytic activity

The NO_x conversion of fresh and the hydrothermally aged V_2O_5/WO_3-TiO_2 (V_2O_5/WTi) catalysts with increasing V_2O_5 is reported in **Figure 3-1a** and **Figure 3-1b**, respectively. Since hydrothermal aging is more practice-relevant compared to thermal aging, the washcoated monoliths were aged at 600°C for 16 h (GHSV= 10'000 h^{-1}) under a continuous flow of 10 vol% O_2 and 5 vol% H_2O in a flow reactor. All curves of **Figure 3-1a** show a characteristic steep increase in activity between 200 and 300°C. In the 350 - 450°C temperature regime the catalysts exhibited a NO_x conversion that was often higher than 95%. Between 500 and 550°C, the NO_x conversion always decreased due to a selectivity loss (NH_3 oxidation to N_2 or NO).

Below 300°C, the fresh catalysts showed increasing NO_x conversion under NH_3 excess (maximum NO_x conversion) with increasing V_2O_5 loading from 1.7 wt% to 3.5 wt%. The NO_x conversion measured at 250°C are reported in **Table 3-1** for comparison. As an example, the maximum NO_x conversion for 2.0 wt% V_2O_5 at 250 and 300°C was 37% and 78%, respectively, while it was 75% (250°C) and 96% (300°C) for the highest loading of 3.5 wt%. At 550°C, the trend was reversed and high loading was no longer beneficial for a high NO_x conversion. The catalyst with 3.5 wt% V_2O_5 showed severe selectivity losses so

that the originally broad operation window narrowed significantly. All catalysts had NO_x conversions higher than 95% in the temperature regime of 350 - 450°C.

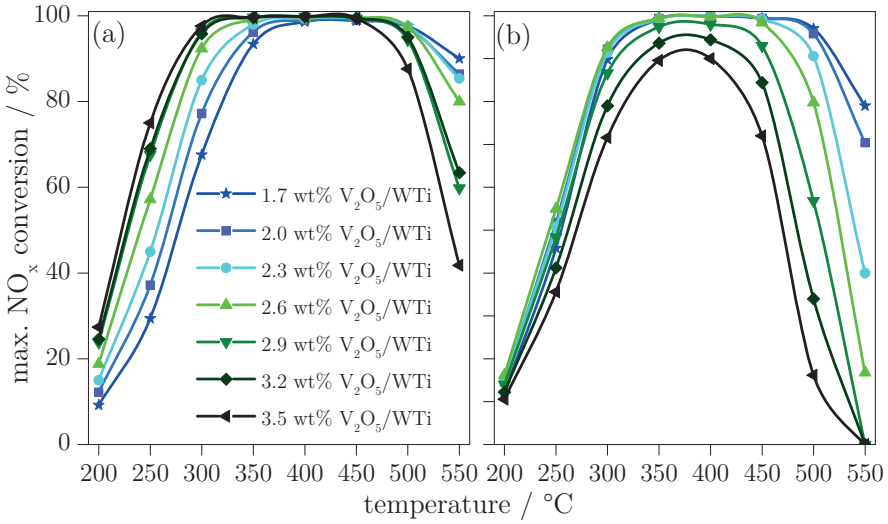

Figure 3-1. Maximum NO_x conversion of 1.7 - 3.5 wt% V_2O_5/TWi (a) in the fresh state and (b) in the aged state (hydrothermal aging at 600°C for 16 h).

The aged catalysts (**Figure 3-1b**) showed deactivation tendencies for high V_2O_5 loading which is recognizable in the decreased NO_x conversion in the low temperature regime and above ca. 400°C. Below 300°C, the catalysts with a loading up to 2.3 wt% V_2O_5 benefited from the aging and became more active than in the fresh state. This was especially evident for the samples with 2.0 and 2.3 wt% V_2O_5, whose NO_x conversions were higher than 50% at 250°C and 90% at 300°C, respectively (**Table 3-1**). While for 2.6 wt% V_2O_5 the NO_x conversion was comparable to that in the fresh state, the deactivation was more pronounced at higher loadings.

In the medium temperature regime, the catalysts with a loading higher than 2.6 wt% V_2O_5 suffered from deactivation. In the high temperature regime, the NO_x conversion was below 60% for catalysts with more than 2.6 wt% V_2O_5. It is important to mention that the entire temperature range of 200 - 550°C is required for a complete performance test. If the catalysts are tested only up to 450°C or 500°C, the negative effect of a high V content cannot be perceived. The hydrothermal aging at 600°C is not very severe but high enough to reveal

that the V_2O_5 loading on WTi should not exceed 2.6 wt% to guarantee sufficient catalyst stability. Below 2.0 wt% V_2O_5/WTi, the aging did not affect the catalyst negatively but on the other side the activity in the low temperature regime was too low for these catalysts. A good compromise between low temperature activity, stability and high temperature selectivity was found for a loading between 2.0 and 2.6 wt% V_2O_5 on WTi.

Table 3-1. NO_x conversion (%) at 250°C for the fresh and the aged catalysts as function of V_2O_5 loading. Data are from Figure 3-1.

V_2O_5 (wt%)	1.7	2.0	2.3	2.6	2.9	3.2	3.5
fresh-450°C	29.4	37.2	45.0	57.2	67.6	69.0	75.0
aged-600°C	45.8	51.8	50.8	55.0	48.4	41.2	35.6

Similar trends to the maximum NO_x conversion of **Figure 3-1** were observed for the NO_x conversion at 10 ppm NH_3 slip, which is shown in **Figure 3-2**. The main difference is that the effect of loading and aging were more pronounced. With a maximum permissible NH_3 slip of 10 ppm, which is relevant for practical applications, often lower NO_x conversions are obtained than for equimolar dosing conditions or for NH_3 dosage in excess [40, 193, 196].

While a high V loading was advantageous for high NO_x conversion in the fresh state (**Figure 3-2a**), a low loading was beneficial after aging (**Figure 3-2b**). The catalysts with low V loading exhibited an activation, i.e. an improved NO_x conversion compared to the fresh state. An additional feature of the highly V-loaded catalysts in the fresh state is the late NH_3 slip during NO_x conversion at 10 ppm NH_3 slip. This is observable by comparing e.g. 3.2 wt% V_2O_5 in **Figure 3-2a** and **Figure 3-1a**. The catalyst exhibited similar NO_x conversion, evidencing that the NH_3 slip is not critical; in the aged state, however, the NH_3 slip was more pronounced for higher V_2O_5 loadings. Hence, the difference between maximum NO_x conversion and NO_x conversion at 10 ppm NH_3 slip became larger. Therefore, the impact of aging can be better evaluated when the NO_x conversion at 10 ppm NH_3 slip is considered. The reason for the enhanced significance of the deactivation is likely related to the fact that the surface acidity is indirectly included in the information delivered by the NH_3 slip

measurement. If a catalyst loses surface acidity, e.g. by sintering of the support, the NH_3 uptake decreases while the NH_3 slip increases. Therefore, the deactivation of high V-loaded catalysts in the aged state (**Figure 3-2b**) demonstrates that these catalysts possess lower surface acidity compared to the fresh catalysts.

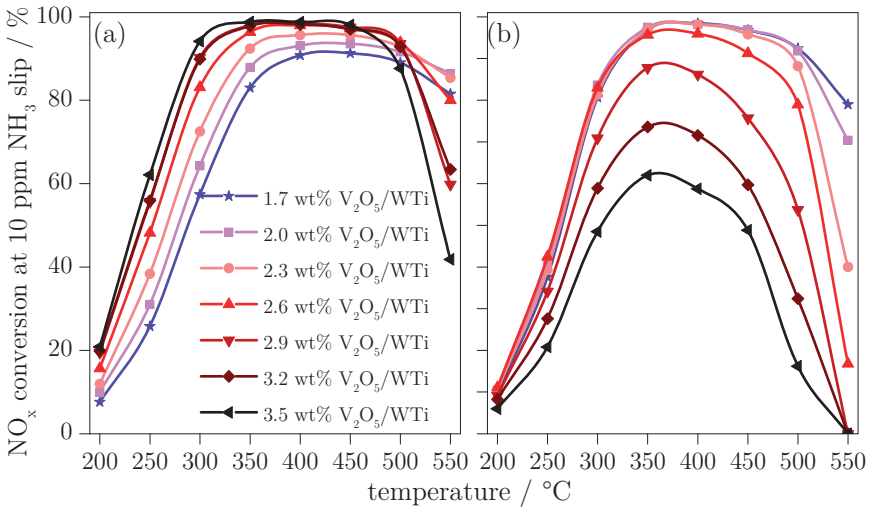

Figure 3-2. NO_x conversion at 10 ppm NH_3 slip of 1.7 - 3.5 wt% V_2O_5/WTi (a) in the fresh state and (b) in the aged state (hydrothermal aging at 600°C for 16 h).

In the low temperature regime of 200 - 300°C where NO_x conversion is determined by the catalyst activity and mass transfer limitations are negligible [45, 208], the reaction rate constant k_{mass} (**Figure 3-3**) was calculated according to eq. (2-2). With this value, the catalysts can be compared irrespective of the small loading deviations of the washcoat. It is evident that k_{mass} of the fresh catalysts increased from 1.7 to 2.9 wt% V_2O_5, whereas it only slightly increased from 2.9 to 3.5 wt% V_2O_5. This behaviour is common to all temperatures in **Figure 3-3a** - **Figure 3-3c**. A higher loading than 2.9 wt% V_2O_5 was, therefore, no longer beneficial for catalysts in the fresh state. In the aged state, the catalysts with 2.0 - 2.6 wt% V_2O_5 exhibited a k_{mass} of around 30, 150 and 550 $cm^3g^{-1}s^{-1}$ at 200, 250 and 300°C, respectively. At the lowest loading of 1.7 wt% V_2O_5, k_{mass} was lower compared to the loadings around 2.3 wt% V_2O_5. At higher loading than 2.6 wt% V_2O_5, k_{mass} linearly decreased to about half of the maximum rate constant for 2.6 wt% V_2O_5/WTi. By comparing the fresh and the aged catalysts, it is apparent that they were only deactivated

above 2.6 wt% V_2O_5. For 1.7 - 2.0 wt% V_2O_5, k_{mass} increased upon aging, while no effect of aging was observed for loadings between 2.3 wt% and 2.6 wt% V_2O_5.

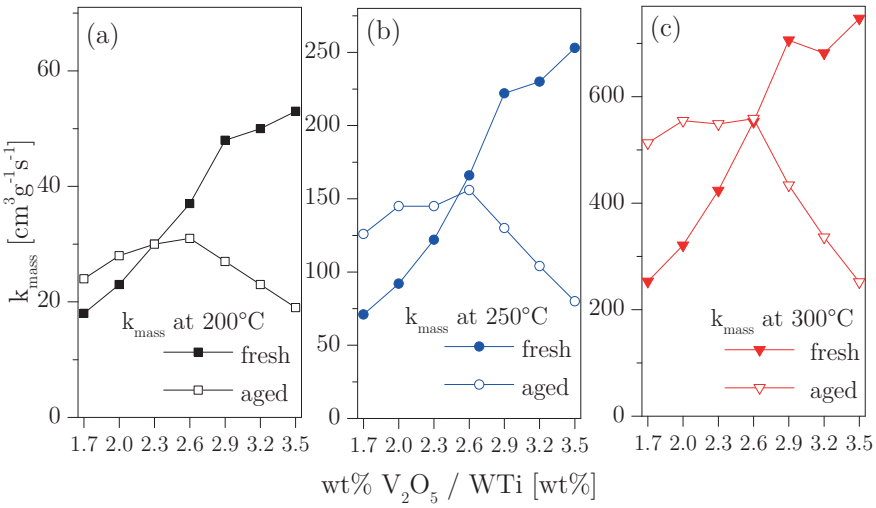

Figure 3-3. Reaction rate constant k_{mass} determined at (a) 200°C, (b) 250°C and (c) 300°C as a function of V_2O_5 loading in the fresh and the aged state.

The performance tests in the fresh and the aged state clearly indicate that the V_2O_5 loading should be adjusted between 2.0 and 2.6 wt% for a WO_3/TiO_2 support material. Only in this range, a compromise between good activity and hydrothermal aging resistance was obtained. The determination of the NO_x conversion at 10 ppm NH_3 slip is an important performance test, which reveals the deactivation effect more markedly than the measurement of the maximum NO_x conversion.

3.5 Physico-chemical characterization

The washcoat material remaining from the slurries was dried and calcined at 550, 600, 650 and 700°C for 10 h and analyzed using BET, XRD and XANES.

The change of the BET specific surface area (SSA) of 2.0, 2.9 and 3.5 wt% V_2O_5/WTi upon calcination is displayed in **Figure 3-4a**. These three samples were chosen to adequately represent the V loading range. After calcination at 550°C, the SSA of all V-loaded catalysts was lower (by ca. 15 m^2/g) than that

of the WTi support material irrespective of V_2O_5 loading. In contrast, by increasing the calcination temperature to 600°C, it becomes evident that a high V loading negatively affected the SSA. For 2.0 wt% V_2O_5/WTi, the SSA decreased only by 5 m^2/g (-7%), while it decreased from 64 m^2/g to 38 m^2/g (-41%) for 3.5 wt% V_2O_5/WT. The increase in calcination temperature from 600 to 650°C had a similar effect on all catalysts, i.e. the SSA decreased by further 25 m^2/g. While 2.0 wt% V_2O_5/WTi still had a residual SSA of 35 m^2/g, the SSA of 3.5 wt% V_2O_5/WTi decreased to 13 m^2/g.

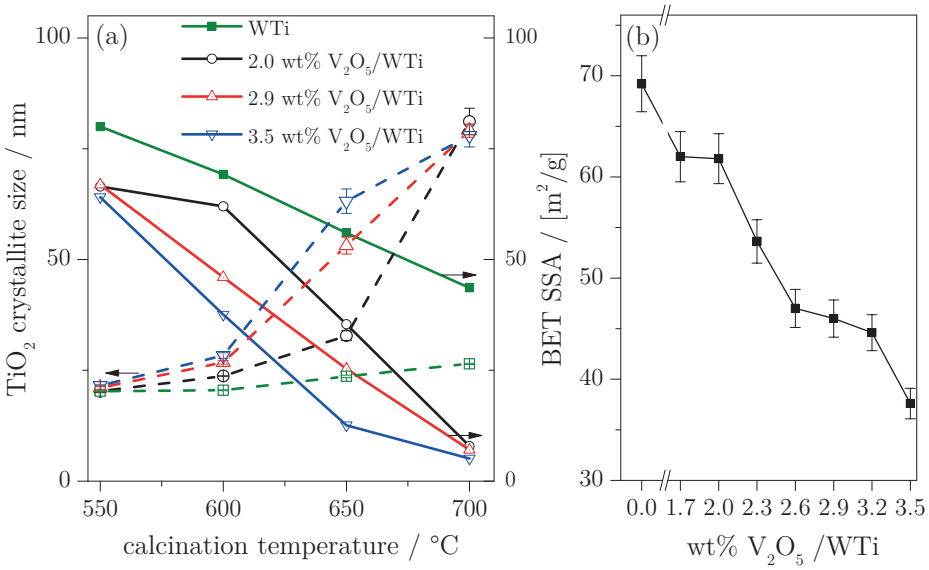

Figure 3-4. Calcination temperature dependence of (a) specific surface area (lines) and crystallite size (dashed lines) of WTi, 2.0, 2.9 and 3.5 wt% V_2O_5/WTi. The crystallite size was obtained from the XRD reflections of anatase at 2Θ 25.4 and 48.0° using the Scherrer equation. (b) Specific surface area of all catalysts calcined at 600°C.

At 700°C, the loading did not play a role anymore and the SSA of all V_2O_5/WTi was reduced to below 10 m^2/g. For a loading of 2.9 wt% V_2O_5, the SSA linearly decreased by 15 - 20 m^2/g with each 50°C increase in temperature. In contrast to the V-loaded samples, the support material WTi exhibited a SSA of 44 m^2/g after calcination at 700°C. This confirms the observation that vanadium assists the sintering of the support material [75]. It is also evident that a high vanadium content accelerates sintering, i.e. sintering can start already at lower calcination temperatures. The low melting point of V_2O_5 is

typically considered responsible for the undesired effect of V on the dispersion of the W-containing phase. [171]

The impact of loading on SSA is further demonstrated in **Figure 3-4b**, where the SSA of 1.7 - 3.5 wt% V_2O_5/WTi catalysts calcined at 600°C is shown. The change of SSA between the support material WTi and up to 2.0 wt% V_2O_5 was below 10 m^2/g but decreased by about 5 m^2/g with every additional 0.3 wt% V_2O_5. It should be noticed that by comparing maximum NO_x conversion and SSA at 600°C, only loadings of 2.0 and 2.3 wt% V_2O_5/WTi seem to be optimal. Both samples have a SSA above 50 m^2/g and their activity/selectivity did not decrease upon aging.

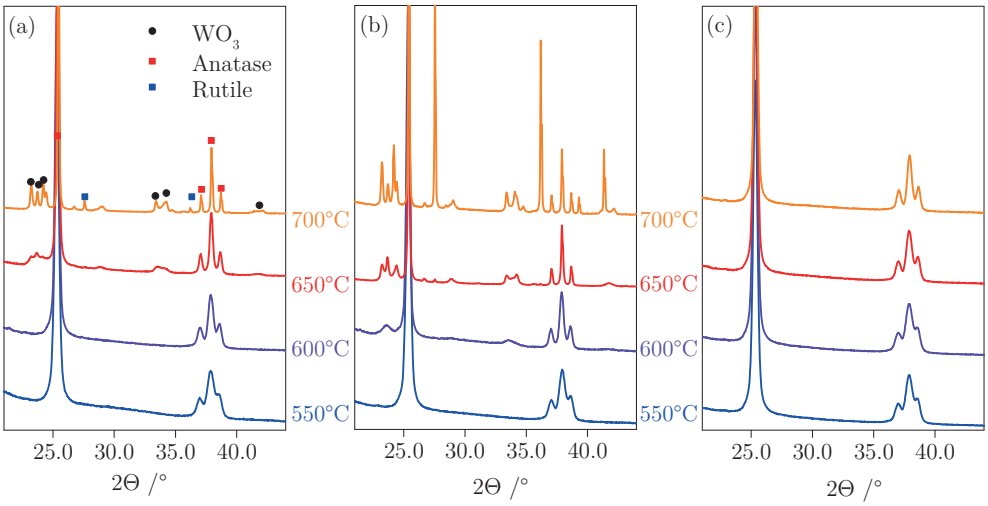

Figure 3-5. XRD patterns of (a) 2.0 wt% V_2O_5/WTi, (b) 3.5 wt% V_2O_5/WTi and (c) WTi calcined at the indicated temperatures. All diffractograms are normalized using the anatase peak at 25.4°.

The XRD patterns of 2.0, 3.5 wt% V_2O_5/WTi and WTi are shown for various calcination temperatures in **Figure 3-5**. **Figure 3-6** further displays the patterns of all catalysts calcined at 600°C with an additional inset for the WO_3 reflection at 2Θ 23.5°. In all diffractograms, the anatase peaks are visible at 2Θ 25.4° and between 37 - 40°.

For 2.0 wt% V_2O_5 (**Figure 3-5a**), calcination up to 600°C did not cause formation of any other visible phase. Hence, it can be assumed that the vanadium and tungsten species are well dispersed or that their crystallite size is below the

detection limit of XRD. At 650°C, WO_3 was detected, which became more prominent at 700°C together with the beginning of the anatase to rutile phase transformation. The crystallinity of the anatase phase visibly increased (2Θ 37.8°) with increasing calcination temperature. The XRD patterns of 3.5 wt% V_2O_5/WTi in **Figure 3-5b** revealed the same phase evolution as in **Figure 3-5a**. However, phase changes occurred already at lower calcination temperatures than in the case of 2.0 wt% V_2O_5/WTi. The WO_3 crystallites were already detected at 600°C and the anatase to rutile phase transformation started at 650°C. Despite structural changes, no V-containing phase was detected and the VO_x species seemed to remain well dispersed. The changes in the speciation of the WO_3 phase are associated with the presence of V in agreement with the BET observations (**Figure 3-4**). At identical calcination temperatures, WTi did not present any evidence of WO_3 sintering.

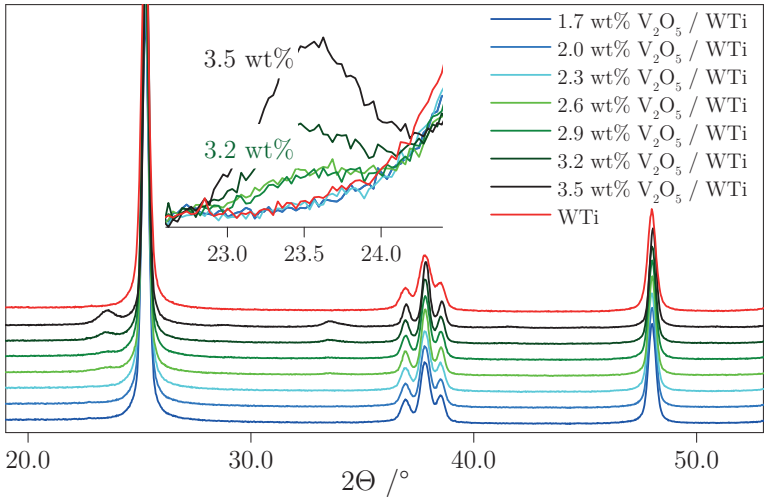

Figure 3-6. XRD patterns of 1.7 - 3.5 wt% V_2O_5/WTi calcined at 600°C. The inset shows a magnification around the WO_3 peak at 23.5°. All diffractograms are normalized using the anatase peak at 25.4°.

The crystallite size of anatase TiO_2 was determined using the Scherrer equation (2-4) from the XRD patterns of **Figure 3-5** and the values are reported in **Figure 3-4a**. At 550°C, the crystallite size was around 20 nm irrespective of the V loading. It increased already at 600°C for catalysts with high V loading. At 650°C, the deviation between low and high V loading was more pronounced and varied from 33 (± 1) to 63 (± 3) nm, respectively. At 700°C, no significant

size difference between low and high V loading was found (around 80 nm) in agreement with the similar SSA values. Both, the SSA and the crystallite size showed that the catalysts sintered with increasing V loading and increasing calcination temperature. To that end, an increasing V-loading affected the WO_3 crystallite formation after calcination at 600°C (**Figure 3-6**). WO_3 was not visible below 2.3 wt% V_2O_5 and the diffractograms matched that of the support material, WTi. The contribution of WO_3 appeared first for 2.6 wt% V_2O_5/WTi and became more prominent with increasing V loading.

Since XRD was not able to provide information on V because of its low loading and low aggregation state, two catalysts were selected for an element specific characterization. The local environment of the VO_x species supported on WTi was studied using XANES.

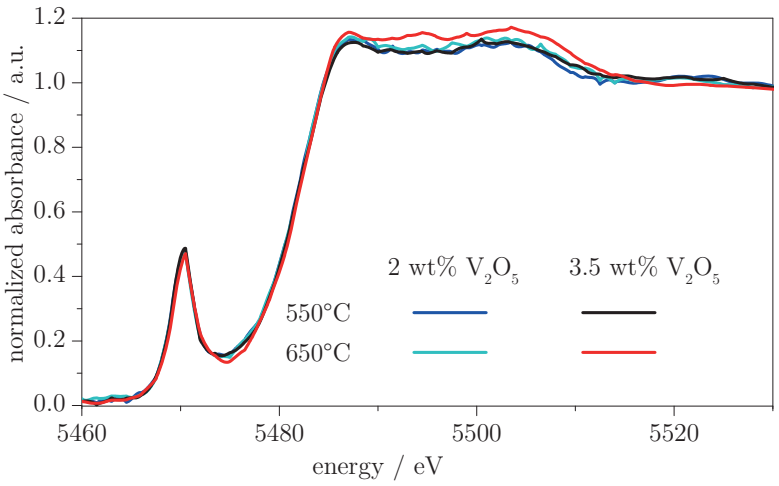

Figure 3-7. Normalized V K-edge XANES spectra of selected catalysts in the fresh and the aged state.

The normalized XANES spectra of 2.0 and 3.5 wt% V_2O_5 /WTi calcined at 550 and 650°C recorded at the V K-edge are shown in **Figure 3-7**. Without attempting a quantitative assessment of both oxidation state and coordination of the VO_x species represented by these spectra, a qualitative discussion is sufficient to support the interpretation of the loading and sintering effects. The spectra of 2.0 and 3.5 wt% V_2O_5/WTi calcined at 550°C are comparable, suggesting a similar local environment of V. This is in agreement with the XRD data of **Figure 3-5**, where no formation of any VO_x phase was observed be-

cause the agglomerates were not crystalline enough or below the detection limit. Upon calcination at 650°C, an obvious change in the XANES region is observed for 3.5 wt% V_2O_5/WTi. The whiteline region (up to 5.52 keV) develops three features characteristic of V_2O_5, suggesting that the VO_x species evolved to form V_2O_5-like agglomerates [106]. This change is correlated with the increase of VO_x surface coverage from 46% in 2.0 wt% V_2O_5/WTi to 232% in 3.5 wt% V_2O_5/WTi that is discussed in the next section. Hence, VO_x started to adopt a different local environment when the VO_x surface coverage exceeded the theoretical monolayer value.

3.5.1 VO_x surface coverage

The surface coverage of VO_x and WO_x provides additional insight for structure - activity relationships. The VO_x and WO_x surface coverages (Υ) were calculated according to equation (2-5) and (2-6) considering that the theoretical saturation values for the monolayer coverage are 7.9 VO_x nm^{-2} and 4.2 WO_x nm^{-2}, respectively [135]. As a result, **Figure 3-8** shows the surface coverage of a low, medium and high loaded V_2O_5/WTi catalyst at various calcination temperatures.

For both high SCR activity and selectivity, the VO_x coverage should be below the monolayer level [205]. The VO_x coverage in **Figure 3-8a** was below 50% for a calcination at 550°C and below 100% for all catalysts at 600°C. At 650°C, 3.5 wt% V_2O_5/WTi exceeds the monolayer coverage and at 700°C, all catalysts theoretically exhibit a multilayer of VO_x species. This was not observable by XRD (**Figure 3-5**) but only in the XANES spectra (**Figure 3-7**), which revealed polymeric VO_x with a vanadium environment similar to that of V_2O_5. **Figure 3-8c** further displays the VO_x coverage of all catalysts calcined at 600°C, which varies from Υ = 24 - 78%. This corresponds well with the XRD observation and the absence of V_2O_5. A Υ = 27%, 36% and 46% was calculated for 2.0, 2.3 and 2.6 wt% V_2O_5/WTi calcined at 600°C, respectively. By comparing Υ with k_{mass} in **Figure 3-3a** - **Figure 3-3c**, it can be concluded that an optimized VO_x coverage should be between 25 - 50%. Below this value, the catalysts seem to have not enough active sites for the SCR reaction, while above 50%, the catalysts showed strong selectivity issues. This is evident from

Figure 3-8a. The fresh 3.5 wt% V_2O_5/WTi catalyst had a surface coverage of 46% and was very active. Upon aging at 600°C, the coverage increased to 78% and the catalyst experienced strong deactivation. Similar considerations apply for the activation of catalysts with a low V loading. After increasing the calcination from 550 to 650°C, the VO_x coverage of e.g. 2.0 wt% V_2O_5/WTi increased from below 25% to roughly 50% (**Figure 3-8a**), which is a plausible explanation for the activation.

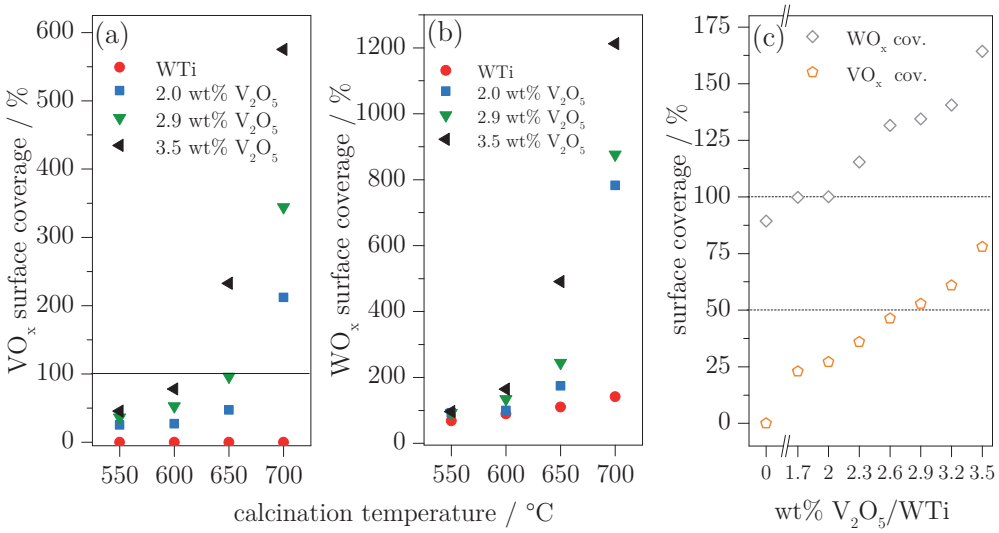

Figure 3-8. Surface coverage (ϒ) of (a) VO_x and (b) WO_x for the support material WTi and three different catalysts as function of calcination temperature. (c) Surface coverage of VO_x and WO_x as function of V_2O_5 loading at 600°C. Surface coverage calculated from the fractional surface coverage according to eq. (2-5) and (2-6).

A study of Amiridis et al. [206] estimated an optimum V_2O_5 coverage of around 2 µmol/m² (2.4 VO_x/nm² = 30% surface coverage) for V_2O_5/TiO_2 doped with around 0.8 wt% WO_3. The optimum catalyst was chosen from the activation energy of the catalysts, which only slightly decreased with further increasing the V content. Kwon et al. [207] have shown that VO_x coverage of 55 - 60% is optimal for the catalytic activity of V_2O_5/TiO_2. In the present system, the optimum coverage seems to be lower, which can be explained by the enhanced surface acidity induced by WO_3 [39]. Adsorbed NH_3 becomes more readily available for the SCR reaction, hence a lower VO_x coverage is sufficient for optimizing the catalyst performance in the presence of WO_3.

3.5.2 WO_x surface coverage

In the case of WO_x (**Figure 3-8b**), only calcination at 550°C produced a sub-monolayer coverage for all catalysts. Already at 600°C, the catalysts with high V content exceeded the theoretical WO_x monolayer as shown in greater detail in **Figure 3-8c**. Up to 2.0 wt% V_2O_5, the WO_x coverage remained below one monolayer, while it was slightly above ($\Upsilon = 115\%$) for 2.3 wt% V_2O_5. For higher V contents, the WO_x surface coverage increased in agreement with the XRD observation of **Figure 3-6**. At 2.6 wt% V_2O_5 or higher, WO_3 crystallites were detected and the WO_x surface coverage was noticeably above one monolayer.

Comparison of the surface coverage with the NO_x conversion of **Figure 3-1b** and **Figure 3-2b** suggests that the aging at 600°C and catalyst activation/deactivation can be correlated with the increase in surface coverage of WO_x. Tungsten oxide provides acid sites to the catalyst where the NH_3 is supposed to adsorb and be readily available for the SCR reaction [39]. Upon calcination at increasing temperature, the available WO_x species and hence the surface acidity decrease and the catalyst increasingly loses activity. This is clearly visible from the NO_x conversion at 10 ppm NH_3 slip (**Figure 3-2**). The decrease in acidity caused by crystallization of WO_3 reduces the potential adsorption sites for NH_3 thus enhancing the 10 ppm NH_3 slip.

3.6 Conclusions

This chapter focused on the activity and stability of V_2O_5/WO_3-TiO_2 SCR catalysts upon systematic variation of the vanadium content. Only V_2O_5 loadings between 2.0 and 2.6 wt% withstand a moderate hydrothermal aging at 600°C for 16 h and are in fact activated upon aging, which is examined more thoroughly in Chapter 4. Below 2.0 wt% V_2O_5, sufficient activity cannot be guaranteed, while above 2.6 wt% V_2O_5 deactivation upon aging increasingly occurs. Based on NO_x conversion at 10 ppm NH_3 slip, it was shown that the aging at high V_2O_5 loading is in fact more severe than one could anticipate from a standard measurement of the SCR activity with equimolar dosage of NH_3 and NO_x. The early NH_3 slip is a practical and direct indicator of the loss of surface acidity caused by the sintering of WO_3, which is confirmed by the

XRD data. In the case of VO_x species at the loadings studied in this work, XRD is not able to yield any information. The evolution from highly dispersed VO_x species to a polymeric VO_x environment similar to that of V_2O_5 upon aging of the catalyst with a high V loading was qualitatively captured by V K-edge XANES.

The catalytic performance was further correlated with the surface coverage of WO_x and VO_x. An optimum surface VO_x coverage between 25 - 50% was estimated, which can be adjusted by either the V loading or the specific surface area (calcination temperature). For the WO_x surface coverage, it was shown that above one WO_x monolayer, WO_3 crystallites are formed, thus diminishing the NH_3 uptake and hence the activity of the catalyst. It can be concluded that a V_2O_5 loading not higher than 2.6 wt% should be used in SCR catalysts composed of V_2O_5, 10 wt% WO_3 and TiO_2 in order to maintain the activity and stability of the catalyst.

Chapter 4

Differences of thermally and hydrothermally aged VWT catalysts

4.1 Introduction

Besides the harmful NO_x, the combustion of diesel fuel generates mainly CO_2 and H_2O. Especially the ca. 10 vol% water that is present in the diesel exhaust influences directly the performance of the SCR catalysts because of its inhibiting character in the low temperature regime [140, 209] and because it generates higher selectivity at higher reaction temperature [75, 140]. When exposed to very high temperatures (above 600°C), a VWT catalyst generally starts to be deactivated, an effect which can be investigated under either thermal [75-76, 210-211] or hydrothermal [211-214] conditions.

Recently, Kompio et al. [76] investigated the time and temperature impact upon thermal aging. It was shown that a VWT catalyst (V_2O_5 loading of 0.5 - 1.5 wt%) can be thermally activated/deactivated at aging temperatures between 600 - 750°C, depending on the aging time. For 600°C, the VWT catalysts were found to be more active with longer aging times. At higher aging temperatures, VWT deactivated heavily after 1000 min. An increase of SCR activity upon thermal or hydrothermal aging for low V-loaded VWT catalyst was also observed in Chapter 3 and by others [75, 210]. With higher V loading, this effect vanished and a decreasing selectively at higher temperature for the SCR reaction was observed. The increased activity upon aging of the catalyst

This chapter is based on the manuscript: A. Marberger, D. Ferri, M. Elsener, O. Kröcher, The Influence of Water to the Aging of V-based Catalysts for the Selective Catalytic Reduction of NO with NH_3, *Manuscript in preparation*, **2017**. A. Marberger performed the experiments, analyzed and interpreted the data together with the co-authors and wrote the manuscript.

was explained by the morphology change and the formation of bulk WO_3 units and polymeric VO_x species which are often reported as inherently more active than isolated VO_x sites [62, 133, 142, 206].

A crucial and disadvantageous parameter of V-based SCR catalyst is the potential vanadium volatility because of its hazard to human health and the environment [215]. While vanadium itself, as well as metal vanadates, are not considered as toxic, vanadium pentoxide (V_2O_5) is listed as carcinogenic. The classification as an environmental risk is complicated by the redox properties of vanadium. Nevertheless, the Occupational Safety and Health Administration have listed V_2O_5 as a contaminant with limits of 0.5 mg/m^3 for dust and 0.1 mg/m^3 for fumes [184] and the U.S. Environmental Protection Agency has listed V_2O_5 as a harmful pollutant [185]. Chapman et al. [64] studied the release of V and W from V-based SCR catalysts after thermal and hydrothermal aging. While no V was recovered in dry conditions after 750°C aging temperature, an increasing amount of volatile V was found for hydrothermally aged catalysts at increasing temperatures. The overall small amount of released V was justified by the strong V interaction with titania. Similar results were also found on engine-based V volatility tests with the difference that aging at 500°C already resulted in small amounts of volatile V, which increased with increasing temperature [183].

In this Chapter, the focus was put on the influence of H_2O on the aging of VWT (2 wt% V_2O_5-10 wt% WO_3-TiO_2) using a static and a dynamic aging procedure, both in absence and presence of water. Because aging of VWT catalysts is not a defined procedure in literature and industry, it is important to systematically address the impact of this parameter. With the comparison between the procedures, the impact of a constant gas flow on the aging of a VWT catalyst was also considered. After comparing the performance of the thermally and hydrothermally aged catalysts and measuring the corresponding V volatility, the catalysts were physico-chemically characterized by means XRD, BET, DRIFT and Raman spectroscopy.

4.2 Experimental

4.2.1 Catalyst preparation

The general preparation of V-based catalysts is described in detail in section 2.1.1. For this investigation, the optimized catalyst from Chapter 3 was used where a commercial WO_3-TiO_2 (WTi, **Table 1-1**) support was impregnated with NH_4VO_3 (eq. to 2.0 wt% V_2O_5, Sigma Aldrich).

4.2.2 Aging procedure

Identically washcoated monoliths were aged with four different aging procedures, namely static thermal, static hydrothermal, dynamic thermal and dynamic hydrothermal aging. The static aging was performed in a calibrated muffle oven (volume ca. 4 dm^3). For the hydrothermal measurement, water was introduced into the muffle oven by means of a saturated N_2 flow (ca. 10 vol% H_2O). The reactor for the dynamic aging was a glass tube of 28 mm internal diameter, similar to that reported by Kleemann et al. [193], with a preheating unit filled with steatite pellets followed by a unit comprising the catalyst sample. The aging reactor was divided in three heating sections independently controlled by separate heating coils. This ensured that the temperature remained constant over the entire length of the monolith. Dynamic aging was carried out by passing a constant flow of 10 vol% O_2 (and 10 vol% H_2O for hydrothermally aging) in N_2 (GHSV= 10'000 h^{-1}) over the catalyst. For both procedures, the same temperature ramps (10°C / min) and identical dwell times (16 h) was used. Both aging set-ups were calibrated at each aging temperature beforehand in order to ensure that the two procedures were comparable.

4.2.3 Characterization methods

Catalytic measurements and characterization methods are described in detail in the sections 2.2 and 2.3, respectively. The catalysts were characterized using BET, XRD, DRIFT and Raman spectroscopy.

4.2.4 Vanadium volatility

For the measurement of volatile V-species, a dedicated laboratory test-rig was used with identical dimensions to that of the catalytic measurements described in section 2.2. The model gas composition contained 10 vol% O_2, 10 vol% H_2O, 500 ppm of NO, 500 ppm of NH_3 with balance N_2 at GHSV = 30'000 h^{-1}. For the extraction of the volatile V-species, a portion of the gas flow (ca. 2 L/min) was sucked off the main exhaust with a sampling tube attached to a pump and a controlling gas meter. The sampling tube was filled with γ-Al_2O_3 as adsorbing material (200 mg, ca. 0.5 mm, Alfa Aesar), which was fixed in between quartz wool plugs. After a sampling time of 24 h (ca. 3.0 m^3 of sampling gas), the entire sampling bed was removed and digested with aqueous HNO_3/HCl/HF and analyzed by inductively coupled plasma optical emission spectrometry (ICP-OES) with a V detection limit of ca. 0.05 µg V/m^3_N (0.75 µg V/g Al_2O_3). The V concentration obtained from ICP-OES was normalized to the gas flow for the sake of comparison.

4.3 Results and discussion

4.3.1 Catalytic activity

Figure 4-1a shows the NO_x conversion of 2 wt% V_2O_5 WO_3/TiO_2 (V-WTi) after dynamic hydrothermal aging at 700°C for 0 h, 5 h, 10 h and 16 h. The temperature was chosen to ensure that V-WTi deactivated heavily [75]. In the fresh state (0 h, calcination at 450°C), the activity sharply increased from 200 to 300°C. Over 90% NO_x conversion was found between 350 - 500°C. Above 500°C, the NO_x conversion started diminishing, which is typically a sign of loss of selectivity due to NH_3 oxidation events in V-based catalysts [76, 210].

Aging for 5 h deactivated the catalyst severely at high reaction temperatures (> 400°C), whereas activation was observed in the low temperature regime. The activation is more evident in **Figure 4-1b** where the k_{mass} value for the 5 h aged catalyst was larger than the one in the fresh state, a phenomenon that has recently been described in detail [76]. It was proposed that the formation of polymeric V-O-V from isolated VO_x species is the reason for the higher activity. Aging affected the NO_x conversion at 10 ppm NH_3 slip more than the max-

imum NO_x conversion. This is an indication that the overall NH_3 storage capacity and the related surface acidity were lowered, thus decreasing the delivery of NH_3 for the SCR reaction (see also Chapter 3). Longer aging (10 h) deactivated the catalyst severely in the entire temperature regime, an effect that was intensified by extending the aging to 16 h. It is evident from **Figure 4-1** that the aging time should be selected carefully because a short aging time may not represent the real activity of an aged V-WTi catalyst at a given temperature. Therefore, an aging time of 16 h was chosen for all catalyst aging events.

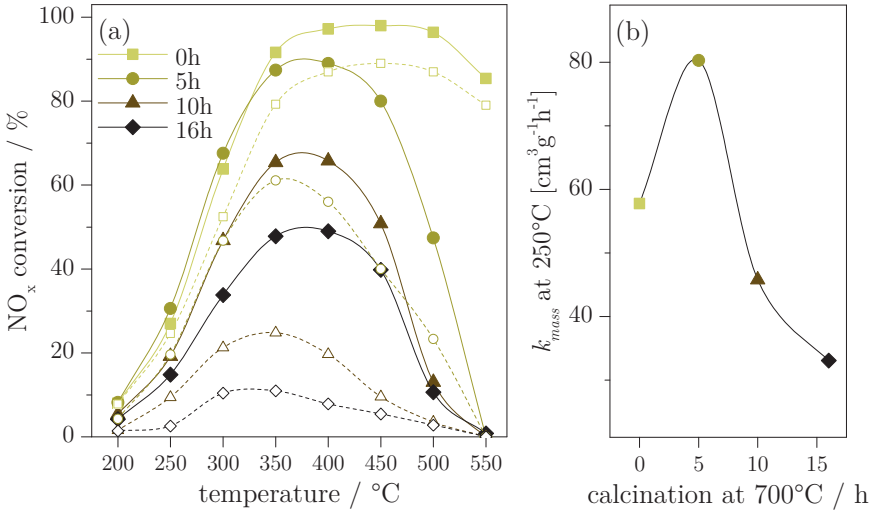

Figure 4-1. (a) Maximum NO_x conversion (—) and NO_x conversion at 10 ppm NH_3 slip (---) of V-WTi after time dependent dynamic hydrothermal aging and (b) the corresponding rate constants k_{mass} calculated at reaction temperature of 250°C.

The impact of four different aging procedures on the catalytic activity of V-WTi is compared in **Figure 4-2**. The four identically prepared monolithic catalysts exhibited virtually the same NO_x conversion in the fresh state (**Figure 4-2a**). The catalysts show typical NO_x reduction curves where the activity is sharply enhanced between 200 and 300°C and full NO_x conversion is achieved above 350°C. Due to the identical preparation, the similarity of the performance is indicative of the consistency and reproducibility of the monolithic laboratory test rig as well as the washcoat procedure. The NO_x conversion of V-WTi after aging at 550, 600 and 650°C (**Figure 4-2b**, **4-2c** and **4-2d**, respectively) was repeated for the four different aging procedures. The corre-

sponding k_{mass} and k_{mass} after calcination at 700°C are presented in **Figure 4-2e**. It is obvious from **Figure 4-2b** and **Figure 4-2e** that irrespective of the aging procedure, the catalysts were greatly activated after aging at 550°C, as indicated by the values of maximum NO_x conversion as well as the NO_x conversion at 10 ppm NH_3 slip. The addition/presence of water during aging activated the catalyst to a greater extent than in the corresponding aging in dry environment. The activity profile suggests that the effect of hydrothermal aging is equal to V-WTi aged under static or dynamic conditions. The effect of the presence or absence of H_2O in the gas environment during aging appears to be more critical for catalyst activation. From **Figure 4-2e** it is evident that aging at 550°C in dry conditions activated the catalyst only to a certain extent. The dynamic thermal aging was thereby slightly less activating than the static thermal aging. One reason could be that static thermal aging in an oven is performed in air, thus in the presence of small amounts of water vapor while a water-free O_2/N_2 feed was mixed to carry out the dynamic thermal aging.

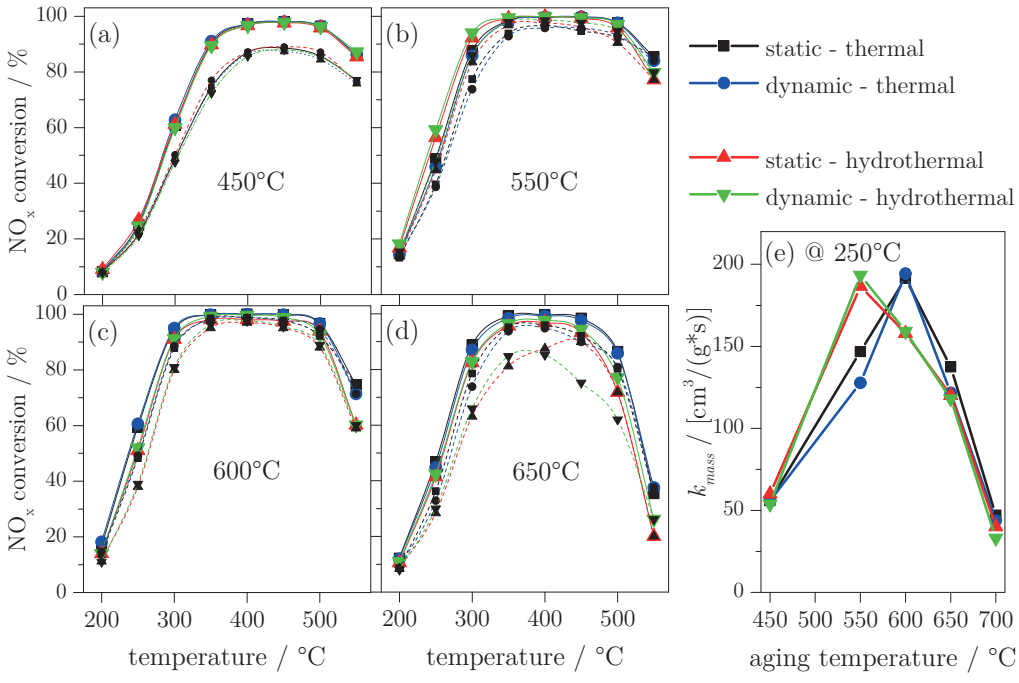

Figure 4-2. Maximum NO_x conversion (—) and NO_x conversion at 10 ppm NH_3 slip (---) of V-WTi in the fresh (a) state and after aging at (b) 550°C, (c) 600°C and (c) 650°C with the indicated aging procedure. (d) Corresponding k_{mass} at 250°C of the catalysts aged at different temperatures and with the indicated aging procedures.

After aging at 600°C (**Figure 4-2c**), the trend was opposite to that after aging at 550°C and the thermally aged V-WTi were more active than the hydrothermally aged ones. Aging in dry conditions further activated the catalyst and both the dynamic and static procedure reached the same rate constants of the hydrothermally aged samples after aging at 550°C (**Figure 4-2e**). The hydrothermally aged samples started to deactivate after aging at 600°C, irrespective of the aging procedure. It seems plausible that water vapor in the gas environment during aging accelerates the activation as well as the deactivation process of V-WTi. One reason for this is the enhanced diffusion of V and W species on the catalyst surface [64], which generates initially activated catalysts at 550°C but causes deactivation tendencies at 600°C.

Finally, aging at 650°C (**Figure 4-2d**) and 700°C (**Figure 4-1a** for hydrothermal aging, not shown for thermal aging) in presence and absence of H_2O deactivated V-WTi to a comparable extent. The catalysts started deactivating in the low and the high temperature regime. Also, the NO_x conversion at 10 ppm NH_3 slip started to be reduced significantly, indicating the onset of loss of surface acidity [192]. From **Figure 4-2** it is obvious that no difference between static and dynamic aging could be found. It was therefore concluded that a constant gas flow does not influence the aging process and that no active carrier gas is needed to simulate the diffusion of V and W containing species.

4.3.2 Vanadium volatility

The V volatility of V-WTi was measured on a dedicated laboratory set up where emissions were continuously collected upon trapping by Al_2O_3 for 24 h at 550, 600 and 650°C in a continuous feed of 10 vol% O_2 500 ppm NH_3, 500 ppm NO in N_2. H_2O (10 vol%) was added in the case of wet conditions. The V release of V-WTi at these three temperatures in presence and absence of H_2O is presented in **Table 4-1**. At 550°C, the V release was slightly higher for wet conditions than for the dry conditions after gas feed normalization. The V release at 600°C was still very low in dry conditions, but increased to ca. 50 $\mu g/m^3$ V in wet conditions. It suggests that a H_2O containing gas feed has a tremendous effect on the V release. This is even more evident at 650°C, where VW-Ti in wet conditions released more than 200 $\mu g/m^3$ V, ca. 6 times more

than in dry conditions. Because of the enhanced mobility of V induced by H_2O in the gas feed [64], it is not surprising that the V release is much higher in presence of H_2O. The absolute loss of vanadium from the catalyst is however very limited and is always below 0.8% of the overall V content. Hence, the V release is not the reason for the change in the catalytic activity upon aging. The effect of activation and deactivation upon aging the catalyst thermally and hydrothermally was, therefore, further investigated physico-chemically by means of XRD, BET and Raman spectroscopy.

Table 4-1. Gas feed normalized V emissions of V-WTi at 550, 600 and 650°C.

Aging temperature	Gas feed	450°C	550°C	600°C	650°C
V release [µg/m^3]	dry	-	1.0 ± 0.1	1.4 ± 0.1	34.2 ± 5.1
	wet	-	2.1 ± 0.2	49.3 ± 7.2	201 ± 30
Υ [%][b]	dry	17	24	32	42
	wet	17[a]	27	37	44

[a] V-WTi calcined at 450°C was studied in dry conditions because it is the catalyst in the fresh state (as calcined), [b] VO_x surface coverage (Υ) calculated according to equation (2-5) and (2-6).

4.3.3 X-ray diffraction

The XRD patterns of the support material WTi (**Figure 4-3a**), of V-WTi after thermal aging (**Figure 4-3b**) and after hydrothermal aging (**Figure 4-3c**) clearly show the anatase TiO_2 reflections, which sharpen with increasing aging temperature as a result of crystallite size growth. The samples aged at 700°C also exhibited a small fraction of rutile TiO_2, with more intense reflections in the case of the thermally aged sample. As observed in Chapter 3, V is a known promoter of the growth of anatase particles and of the subsequent phase transformation from anatase to rutile [83, 109].

The anatase crystallite size increased continuously up to 650°C, irrespective of the gas composition (**Figure 4-4a**), while more intense increase was detected after thermal aging than for hydrothermal aging of V-WTi at 700°C. Besides the TiO_2 reflections, also a WO_3 phase appeared above 550°C after thermal and hydrothermal aging of V-WTi (**Figure 4-3b** and **Figure 4-3c**). Similar to

TiO_2, larger WO_3 crystallites formed after 700°C in case of the thermally aged catalyst. It is plausible that water partly hinders the WO_3 crystallite growth because of continuous formation of mobile WO_x species such as $WO_2(OH)_2$ [64]. No WO_3 reflections were detected in case of WTi even after aging at 700°C, which is a clear indication that V promotes sintering of the support material.

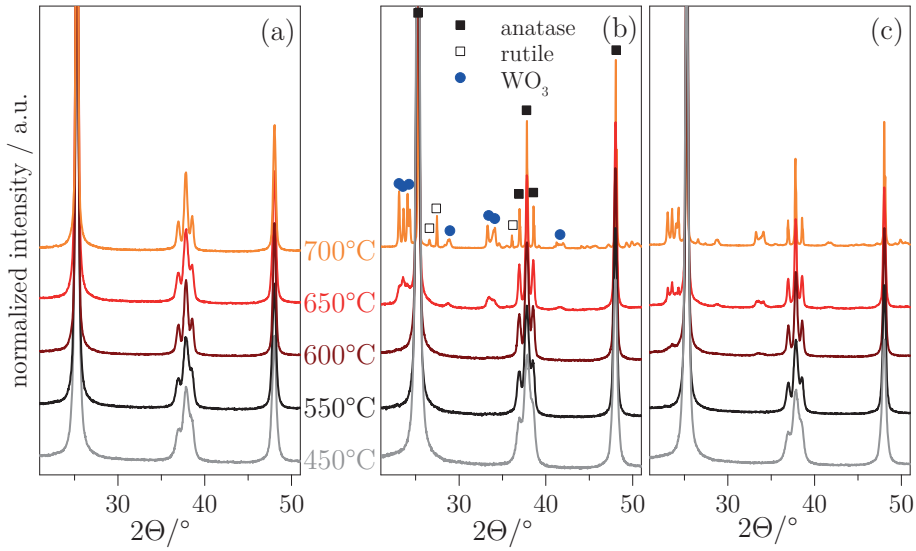

Figure 4-3. XRD patterns of (a) WTi and V-WTi after (b) thermal and (c) hydrothermal aging at various temperatures.

No reflections of a vanadium containing phase were detected, suggesting that the VO_x species are either finely dispersed, have an amorphous character or have crystallite sizes below the XRD detection limit. This is generally the case for VWT catalysts because of the high interaction potential between V and TiO_2, which leads to highly dispersed species on WO_3-TiO_2 [46, 84].

4.3.4 Surface area and k_{BET}

The BET surface area of thermally and hydrothermally aged V-WTi decreased steadily with increasing aging temperature (**Figure 4-4a**). Already aging at 550°C had a distinct impact and at 600°C, the surface area dropped to roughly half of that obtained for the fresh state. Hydrothermal aging had a more pronounced effect on the BET values retrieved after aging at 550 and 600°C. The surface area of V-based SCR catalysts is directly linked to the surface density of VO_x species and, as a consequence, to the catalytic performance

[207]. As proposed in Chapter 3, V-WTi catalysts display optimal performance at a VO_x surface coverage of 25 - 50%. The calculated VO_x coverage for V-WTi in the fresh state was 17% (**Table 4-1**) and upon aging, it increased to 24% and 27% for thermally and hydrothermally treated samples. After aging at 600°C, the VO_x surface coverage increased to 32% (thermal) and 37% (hydrothermal), hence in the optimal coverage range, which was reflected by the increased activity at this aging temperature.

The correlation between SCR activity and BET surface area is represented by k_{BET} (see section 2.2), the surface independent k_{mass} plotted in **Figure 4-4b**. It is obvious that hydrothermally aged V-WTi activated to a greater extent than thermally aged V-WTi at 550°C. At 600°C, k_{BET} increased for both aging gas compositions, but more for thermally aged V-WTi. It is interesting to compare k_{mass} (**Figure 4-2e**) and k_{BET} (**Figure 4-4b**) of hydrothermally aged V-WTi because its values decrease for the former and increase for the latter. Because the k_{BET} values increased, it was concluded that the loss of activity after aging at 600°C mainly originates from the loss of surface area.

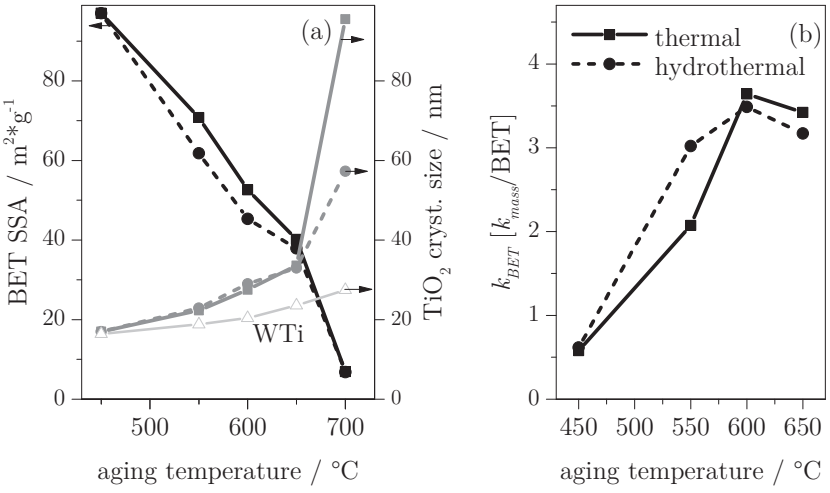

Figure 4-4. (a) BET surface area of WTi (△), V-WTi after thermal (■) and hydrothermal (●) aging and (b) k_{BET} at the temperatures indicated.

However, it cannot be excluded that other factors such as loss of surface acidity, V and W polymerization or changes the catalyst morphology contribute to changes in the activity as well. At 650°C, also the k_{BET} values decrease, making it impossible to identify the exact origin of the decrease in catalytic activity.

The activation event of V-WTi after aging at 550 and 600°C could conclusively be correlated to the increase in VO_x surface coverage and was further spectroscopically investigated by means of diffuse reflectance infra-red and Raman spectroscopy.

4.3.5 Spectroscopic investigations

In situ DRIFT spectra of WTi after aging at 550°C and V-WTi in the fresh state and after hydrothermal aging at 550°C were recorded during the adsorption of 500 ppm NH_3 at 250°C in O_2/N_2 (**Figure 4-5**). While adsorbed NH_3 produced positive signals, negative features were observed from the perturbation of the catalyst surface by NH_3. The signals were assigned according to literature [71, 78, 123, 135, 216-218].

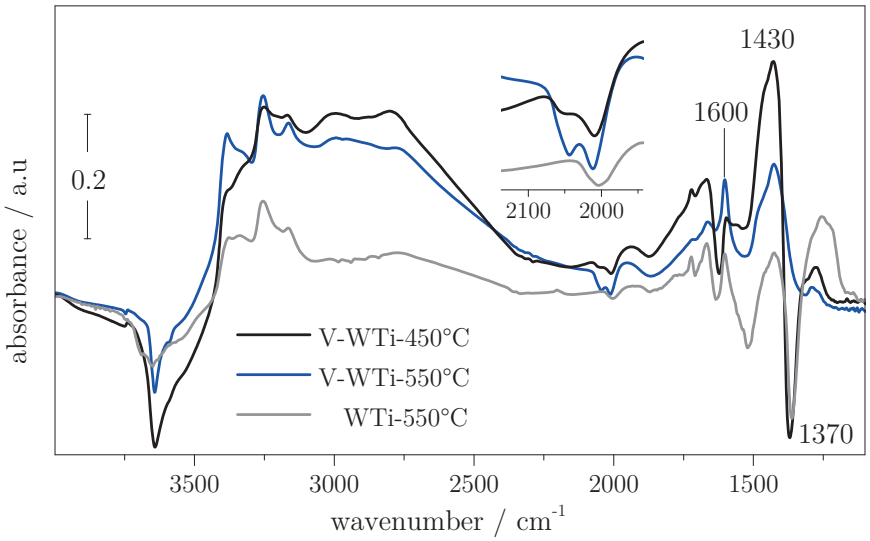

Figure 4-5. *In situ* DRIFT spectra of WTi aged at 550°C and V-WTi in the fresh state and hydrothermally aged at 550°C recorded during adsorption of 500 ppm NH_3 at 250°C in O_2/N_2 after 30 min. Catalysts were dried *in situ* at 350°C in O_2/N_2 for 1 h prior to NH_3 admittance.

The stretch mode of W-OH groups of WTi was vaguely visible at ca. 3650 cm^{-1} and was absent in V-WTi. Instead, an intense negative feature at 3640 cm^{-1} appeared, which was assigned to ν(V-OH) [219]. It could not be decided whether the absence of W-OH is due to interaction with VO_x species or due to signal overlap. The inset in **Figure 4-5** reveals the presence of vanadyl (2050 cm^{-1} - 2044 cm^{-1} for 2ν(V=O)) and wolframyl groups (2011 cm^{-1} - 2000 cm^{-1} for

2ν(W=O)) in V-WTi and only the 2ν(W=O) in WTi. Protonated NH_4^+ and N-H stretch frequencies from the coordination of NH_3 to Brønsted and Lewis acid sites of WTi and V-WTi are visible at 3380, 3255 and 3165 cm^{-1}. The corresponding deformation modes of NH_3 adsorbed on Brønsted (B_{NH3}, 1670 and 1430 cm^{-1}) and Lewis acid sites ($L_{NH3,}$ 1600 and 1270 cm^{-1}) are more distinctly visible.

Major differences between V-WTi in the fresh state and after hydrothermal aging are noticeable in the intensity of the acid sites (increase of 1600 cm^{-1} and decreased of 1430 cm^{-1}) and the loss of the negative peak at 1370 cm^{-1}. This suggests that more NH_3 adsorbed on Lewis acid sites and less to Brønsted acid sites after hydrothermal aging of V-WTi at 550°C. Since the DRIFT spectra were collected in dry conditions, it is not possible that water vapor altered the acid sites ratio. The increased amount of Lewis acid sites was tentatively associated with the activation of the catalyst upon hydrothermal aging at 550°C (**Figure 4-2e**) [162]. The importance of Lewis acid sites for V-based SCR catalyst is presented in Chapter 5.

The negative peak at ca. 1370 cm^{-1} was assigned to NH_3 adsorbed on residual sulfate (S=O) species [220-221] and was only detected for V-WTi calcined at 450°C and WTi aged at 550°C. The absence of this signal in the hydrothermally aged V-WTi reveals that the sulfates can be removed in presence of H_2O at 550°C. This modifies the surface of the catalyst and consequently the interaction with NH_3 since sulfated TiO_2 improves the NH_3 adsorption [221] and can modify the activity of V-based SCR catalysts [222]. Gas phase SO_2 was proposed to increase the SCR activity of low V-loaded VWT catalysts but has no positive effect at high V loading [206]. Upon hydrothermal aging, also the features of the mono-oxo vanadyl (ca. 2044 cm^{-1}) and the mono-oxo wolframyl (ca. 2010 cm^{-1}) groups were perturbed to a greater extend by NH_3 compared to V-WTi in the fresh state. The higher VO_x surface coverage at 550°C (**Table 4-1**) is a plausible explanation for the intensification of the signal of the vanadyl species. Since they are known to be involved in the SCR mechanism (see section 1.4.7), it is likely that they contribute to the catalyst activation observed in **Figure 4-2e**.

From the DRIFT result it can be concluded that structural changes such as increased density of Lewis acid sites and vanadyl species and loss of sulfates are likely responsible for the catalyst activation upon hydrothermal aging of V-WTi at 550°C.

The Raman spectra of thermally and hydrothermally aged V-WTi, as well as WTi, are shown in **Figure 4-6**. The intense TiO_2 features at 639, 518 and 397 cm^{-1} (E_g, A_{1g} and B_{1g} mode, respectively [223]) are visible in all spectra together with a weak TiO_2 signal at ca. 800 cm^{-1} [224-225] that is covered by a more intense band of crystalline WO_3 at ca. 806 cm^{-1} (ν(O-W-O), [226]) in the catalyst aged at 650°C. The decreased intensity of the signals at 518 and 397 cm^{-1} with increasing aging temperature is a consequence of the higher surface coverage of V and W and the decrease in surface area [227]. The signals between 950 and 1040 cm^{-1} were assigned to WO_x and VO_x species and are highlighted in the insets of **Figure 4-6**. The signal at ca. 983 cm^{-1}, which was present in WTi and V-WTi, was assigned to the W=O stretch mode of hydrated WO_x [99]. The weak blue-shift of this signal for V containing samples at higher aging temperature indicates the presence of hydrated V=O species [99, 228].

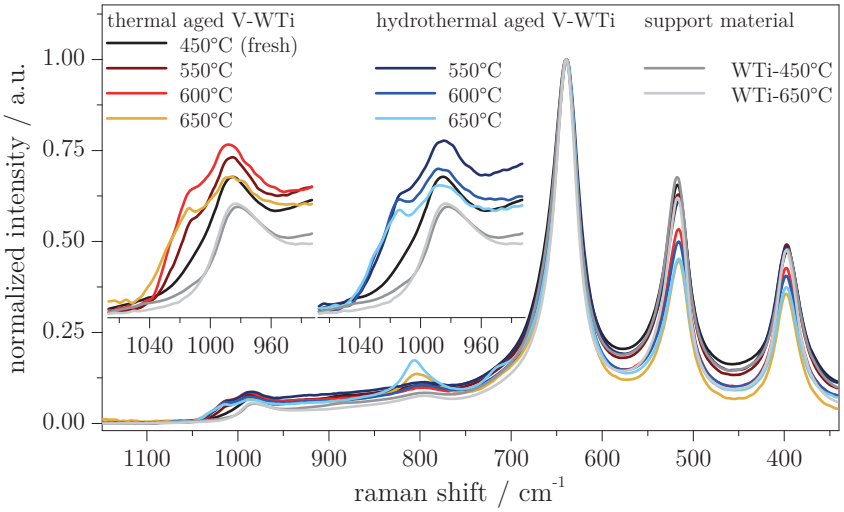

Figure 4-6. Raman spectra of WTi and V-WTi in the fresh state and after static-thermally and static-hydrothermally aged at 550, 600 and 650°C.

The most prominent difference between WTi and V-WTi aged at 550°C and above, is the band at ca. 1015 cm^{-1} with a shoulder at ca. 1030 cm^{-1}. These fea-

tures only appeared after aging at 550°C and could be assigned to the fundamental W=O and V=O stretch vibrations in the dehydrated state [99, 224, 228]. Catalyst aging thus generates WO_x and VO_x units, which are less prone to hydration under ambient conditions. It is likely that the formation of these species is related to the activation of the catalyst upon aging. This is in agreement with the DRIFT results of **Figure 4-5** where an increased amount of Lewis acid sites was observed in hydrothermally aged V-WTi. Conclusively, an increased amount of dehydrated surface sites (Lewis acid sites) increases the NH_3 adsorption potential and generates highly SCR active V=O sites [70, 162].

The intensity of the W=O and V=O signals is different for hydrothermally and thermally aged V-WTi at a given temperature. At 550 and 600°C, these features are more prominent in the case of the hydrothermally aged sample. Similar to the DRIFT data, it seems that water vapor in the aging environment is capable of producing more W=O and V=O Lewis acid sites. Aging at 650°C generated very similar features for both aging procedures, in agreement with the similar activity and the onset of catalyst deactivation (**Figure 4-2** and **Figure 4-4**).

4.4 Conclusion

Static and dynamic aging procedures in presence and absence of water were tested on a $V_2O_5/WO_3/TiO_2$ catalyst. While the two procedures did not demonstrate any major difference, water heavily affected the structure of the catalyst. Catalytic tests showed that the hydrothermally aged catalyst activated more readily than the thermally treated sample at 550°C. The hydrothermal treatment also produced deactivation tendencies at 600°C, while the activity of the thermally aged catalyst increased. Above this temperature, all catalysts aged similarly, which was especially visible in the NO_x conversion at 10 ppm NH_3 slip and the reaction rate constant. Due to the presence of vanadium, the support material was heavily affected by aging, which was illustrated by the increased TiO_2 crystallite size and the formation of crystalline WO_3. The activation of the catalysts could be correlated to the increased VO_x surface coverage calculated from the surface area. To that end, the spectroscopic data showed that the activity upon aging correlates to an increased presence of Lew-

is acid sites and SCR active vanadyl sites. Catalyst aging thus generates WO_x and VO_x units, which are less prone to hydration under ambient conditions. The presence of water during the aging process generated these features at lower temperature compared to dry aging. Conclusively, it is important to stress that water in the aging process, which is always present in real-world applications, is an essential additive because it heavily affects the morphology and catalytic activity of V-based SCR catalysts.

Chapter 5

Mechanistic details of a state-of-the-art vanadia-tungsta-titania catalyst

5.1 Introduction

Based on the findings in Chapter 3 and Chapter 4, a VWT catalyst with a V_2O_5 loading of 2 wt% was chosen for a mechanistic study. Despite the widespread use of SCR, molecular aspects of its mechanism remain controversial in literature [32, 140, 159, 162, 229-230]. The current understanding of the NH_3-SCR mechanism on V-based catalysts was briefly discussed in section 1.4.7. The reaction proceeds according to the stoichiometry of eq. (1-2) and the two nitrogen atoms of the N_2 product originate one each from NO and NH_3. It is generally accepted that the mechanism comprises an acid site where NH_3 is activated and a redox site that requires oxygen to be regenerated. The Brønsted and Lewis acid sites are responsible for the adsorption of NH_3 and have thus been anticipated to be essential for the reaction mechanism. While Brønsted acid sites bind NH_3 to form NH_4^+ (B_{NH3}), Lewis acid sites coordinate NH_3 directly with a metal atom (L_{NH3}). NO reacts on the acid sites according to an Eley-Rideal mechanism accompanied by the reduction of V^{5+} to V^{4+}. It is also recognized that the role of oxygen is to restore the $V^{5+}O_x$ active center. Various experimental and theoretical studies have tackled the crucial issue of the involvement of either B_{NH3} or L_{NH3} sites in the standard SCR reaction without reaching unequivocal conclusions. Ramis et al. [162] reported a mechanism

This chapter is based on the postprint version of the publication: A. Marberger, D. Ferri, M. Elsener, O. Kröcher, The Significance of Lewis Acid Sites for the Selective Catalytic Reduction of Nitric Oxide on Vanadium-Based Catalysts, *Angew. Chem. Int. Ed.* **2016**, 55, 11989-11994**.** A. Marberger performed the experiments, analyzed and interpreted the data together with the co-authors and wrote the manuscript.

based on L_{NH3} active species that encompasses the formation of a NH_2NO reaction intermediate. B_{NH3} was later proposed by Topsøe [229] as the active center. Given their large excess compared to L_{NH3} species, especially with the introduction of tungsta in the catalyst formulation, the SCR activity was correlated with the change of B_{NH3} coverage [78, 87, 231]. However, two considerations seem to complicate the Brønsted acid mechanism. Ammonia must lose all protons to form the N_2 product, thus making the initial protonation to NH_4^+ an apparently superfluous step. The energy barrier for the reaction involving a Brønsted acid site is also higher than that comprising a Lewis acid site [68]. On its turn, L_{NH3} is more resistant to desorption at given temperature [232] and demonstrates higher heat of adsorption than B_{NH3} [233]. Although the two reaction pathways may probably not exclude each other, it is essential to understand whether either or both species are relevant.

Spectroscopy contributed considerably to the formulation of the proposed reaction mechanisms [162-163, 229-230]. However, it should be noted that this precious mechanistic information was derived under steady state conditions, thus under less suitable experimental conditions and inappropriate time scales to observe active and intermediate species and to describe the working catalyst. Also the widely used temperature programmed desorption method can only predict the amount and stability of acid sites, but is intrinsically ambiguous with respect to the nature and reactivity of the acid site(s) directly involved in the reaction. Important mechanistic details were obtained on V-based catalysts also by the transient-response method [234], but without implementation of spectroscopic measurements. Transient experiments are more suitable to disclose the nature of active centers on a catalyst surface. From a spectroscopic perspective, second to sub-second time-resolution is required to capture relevant structural changes while the catalytic system is perturbed. So far, little time-resolved examination of this kind has been reported for a state-of-the-art V_2O_5-WO_3-TiO_2 SCR catalyst.

In this chapter, time-resolved IR and visible spectroscopy was used to demonstrate the unambiguous involvement of NH_3 bonded to Lewis acid sites in the SCR mechanism. At low temperature, the B_{NH3} species barely contribute to the

activity of a V-based catalyst and solely L_{NH3} species participate in the standard SCR reaction. It was further possible to associate the V^{5+}/V^{4+} redox pair with the Lewis acid site. The striking experimental observations provide a new perspective on the mechanism based on Lewis acid sites that may encourage the use of this experimental approach as tool to support the design of SCR catalysts. This holds for V-based catalysts but due to the general applicability of the method, the development of other types of catalysts should profit too.

5.2 Methods

The catalyst was prepared by consecutive impregnation of commercial TiO_2 (DT-51-D, **Table 1-1**) with ammonium metatungstate hydrate ($(NH_4)_6H_2W_{12}O_{40} \cdot xH_2O$), Sigma-Aldrich) and ammonium vanadate (NH_4VO_3, Fluka) to obtain a nominal composition of 2 wt% V_2O_5-10 wt% WO_3-TiO_2 (V-W-Ti), a commonly used composition for state-of-the-art V-based SCR catalysts [75]. Calcination in air at 550°C for 5 h was performed after impregnation with the tungsten precursor, while after introduction of vanadium, the material was calcined in air at 450°C for 10 h.

Catalytic activity data for NH_3-SCR over the selected catalyst was obtained in a fixed bed reactor (6 mm internal diameter) operating at atmospheric pressure. The catalyst (40 mg, 100 - 200 μm) was mixed with cordierite (150 mg, 100 - 200 μm) and placed between quartz wool plugs in the quartz tube reactor. After pre-treatment in 5 vol% O_2/N_2 at 450°C for 1 h, a mixture of 500 ppm NO, 500 ppm NH_3 in 5 vol% O_2/N_2 (1 vol% H_2O if used) was fed into the reactor at a gas hourly space velocity (GHSV) of 60,000 mL $g^{-1}s^{-1}$ (100 mL min^{-1}). The SCR activity was recorded at 150, 175, 200, 225, 250, 275, 300 and 350°C after a waiting time of 15 min. The NO_x conversion was calculated according to equation (2-1). Feed and reaction products were analyzed by transmission FTIR using a Thermo Scientific Antaris IGS FTIR spectrometer equipped with a multiple-pass gas cell (180 mm path length). The same catalytic tests was performed with the spectroscopic cell that was used to obtain the DRIFT and DR-vis data.

Diffuse reflectance Fourier transform infrared (DRIFT) spectra were measured using a Bruker Vertex 70 spectrometer equipped with a Praying Mantis mirror unit (Harrick) and a liquid-N_2 cooled HgCdTe detector. The diffuse reflectance visible (DR-vis) spectra were measured using an Agilent Carry 4000 spectrometer equipped with an identical set of mirrors for diffuse reflectance. The homemade spectroscopy cell based on the commercial Harrick cell but with reduced dead volume, was equipped with a flat CaF_2 window (d= 25 mm; 2 mm thick) and was connected to heated stainless steel gas supply lines. The cell exhibited 95% gas exchange level after 15 s at 50 mL/min. In order to follow the kinetics of consumption and formation of adsorbed species the following integrals were taken: for δ_{as}(N-H) of L_{NH3}, normalized integral between 1610 - 1590 cm^{-1}; for δ_{as}(N-H) of B_{NH3}, normalized integral between 1480 - 1395 cm^{-1}, and for ν(NO) of NO^+, normalized integral between 2240 - 2140 cm^{-1}. The outlet of the cell was connected to a mass spectrometer (InProcess Instruments GAM 400) and an FTIR spectrometer (Bruker Alpha equipped with a 70 mm pathlength gas cell heated to 150°C). The sample was finely ground and placed in the sample cup of the cell (100 mm^3, ca. 40 mg). Prior to the experiments, the sample was dried *in situ* in 5 vol% O_2/N_2 (100 mL/min) at 400°C for 2 h. For all the experiments the overall flow was kept at 100 mL/min (60,000 h^{-1}) and the temperature at 250°C, if not otherwise specified. In the single transient experiments, NH_3 (500 ppm in 5 vol% O_2/N_2) was adsorbed for 15 min followed by desorption (5 vol% O_2/N_2) for 15 min. Then, 500 ppm NO was admitted to the catalyst in 5 vol% O_2/N_2 for 15 min. Both DRIFT and DR-vis measurements were performed using the same setup. In case of experiments with water, 1 vol% of H_2O was added to the feed continuously during NH_3 adsorption/desorption and NO admittance.

All DRIFT spectra were obtained by accumulating 10 interferograms at 4 cm^{-1} resolution and 80 kHz scanner velocity (0.9 s/spectrum). The DR-vis data were obtained by measuring continuously the absorbance at fixed wavelength (e.g. 400 or 700 nm) at 1 point/s time-resolution. The DR-vis spectra collected in the 350 - 800 nm spectral range were obtained at 1 nm resolution. All DRIFT and DR-vis data are represented in absorbance units [235].

For the concentration modulation excitation experiments, the solenoid valves were used to automatically switch between gases and were operated by the OPUS software (Bruker). The concentration of NH_3 and NO was always 500 ppm when added. The following pulse sequences were used for **Figure 5-12**:

(i) NO pulses in NH_3: NO/N_2 vs. N_2, constant NH_3/5 vol% O_2/N_2
(ii) alternated NO and NH_3 pulses: NO/N_2 vs. NH_3/N_2, constant 5 vol% O_2/N_2
(iii) NH_3 pulses in NO: NH_3/N_2 vs. N_2, constant NO/5 vol% O_2/N_2
(iv) NH_3 pulses in N_2: NH_3/N_2 vs. N_2, constant 5 vol% O_2/N_2
(v) N_2 pulses in NH_3: N_2 vs. N_2, constant NH_3/5 vol% O_2/N_2.

The sets of time-resolved spectra (DRIFT and DR-vis) obtained from the modulation experiments were converted into phase-resolved spectra using phase sensitive detection (PSD) [236]:

$$I(\varphi^{PSD}) = \frac{2}{T}\int_0^T I(t)\, sin(k\omega t + \varphi^{PSD})dt \qquad \textbf{(5-1)}$$

where *I(t)* is the set of time-resolved data, ω the stimulation frequency, k the demodulation index ($k = 1$ is the fundamental harmonics and was used in this Chapter), T the modulation period and φ^{PSD} the phase angle. Matlab was used to process the time-resolved data using PSD. The modulation period ($T = 220$ s and $T = 36$ s) is defined as the time required to conclude one full sequence. A single modulation period with T = 220 s thus consisted of 240 consecutive time-resolved DRIFT spectra. In the case of DR-vis spectroscopy, identical modulation sequences consisted of 10 consecutive spectra collected from 350 to 800 nm at 1 nm resolution. Ten modulation periods were carried out.

5.3 Results and discussion

5.3.1 Catalytic activity

The NH_3-SCR activity in dry and wet conditions (1 vol% H_2O) in the quartz reactor and in the spectroscopic DRIFT cell at constant GHSV is compared in **Figure 5-1**. The relatively low vanadium loading guaranteed on the one hand sub-monolayer coverage of oxo-species (ca. 25%, see Chapter 3), providing high selectivity and stability, and on the other hand sufficiently high

activity in the SCR reaction for most commercial applications. The NO reduction behavior measured in the spectroscopic cell in the temperature range 150 - 350°C was comparable to that obtained in a tubular quartz reactor, thus ensuring transferability of the spectroscopic data. For example at 250°C, the NO_x conversion in absence of H_2O attained 97% in the quartz reactor and 90% in the spectroscopic cell. A reaction temperature of 250°C could lead to diffusion limitations that may affect the rate constants and the spectroscopic measurements. However, the high activity is related to the whole catalyst bed in the cell and is needed in order to achieve a reasonable conversion at the top of the bed where the infrared and UV-vis radiations probe the sample (ca. 200 μm depth).

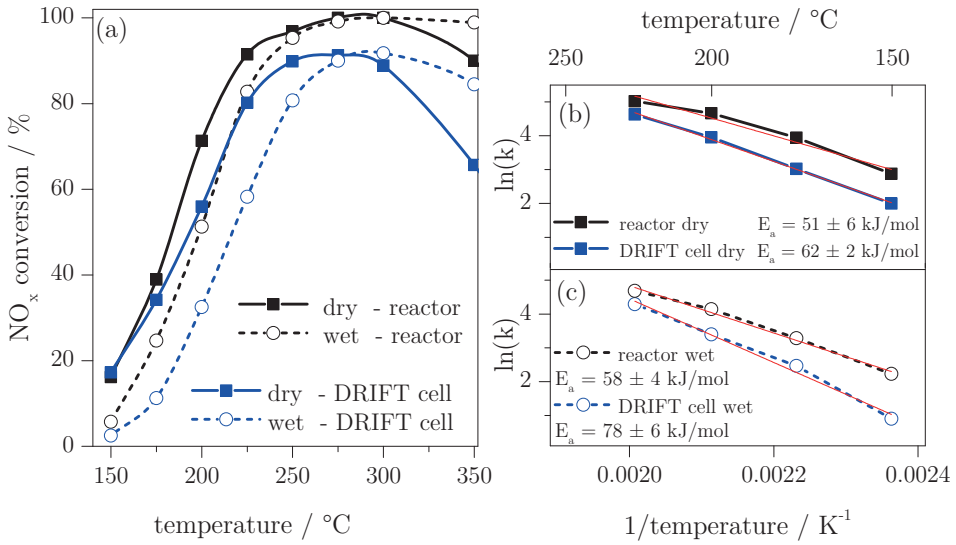

Figure 5-1. Comparison of NH_3-SCR activity on V-W-Ti measured in the quartz reactor and in the spectroscopic cell. The experiments were performed in dry conditions and with addition of 1 vol% H_2O. The space velocity was kept constant between all experiments (GHSV= 60,000 mL $g^{-1}s^{-1}$). (a) NO_x conversion as function of temperature in the dry and wet state, (b) and (c) corresponding Arrhenius plots in the temperature range 150 - 225°C.

Addition of 1 vol% H_2O caused a decrease of the catalytic activity in both reactors, especially below 250°C. The inhibiting effect of H_2O on the NH_3-SCR reaction is well-known and has its origin in the competitive adsorption between H_2O and NH_3 [237-238]. The apparent activation energies in the dry state, cal-

culated from the Arrhenius plot in **Figure 5-1c** are comparable within the given error.

5.3.2 Single transient experiments

When examined by DRIFT spectroscopy, NH_3 adsorption on V-W-Ti at 250°C followed by desorption in 5 vol% O_2/N_2 (**Figure 5-2a**) left the characteristic features of ammonium ions (NH_4^+) adsorbed on Brønsted acid sites (B_{NH3}, 3200 - 2700, 1670 and 1423 cm^{-1}) and of NH_3 coordinated to Lewis acid sites (L_{NH3}, 3250, 1603 and 1250 cm^{-1}), which were easily assigned on the base of existing literature [162, 239-240]. The coverage of both species was only slightly diminished upon desorption. Various negative peaks were associated with the coordination of NH_3 to Ti and W hydroxyl groups, vanadyl (V=O) and wolframyl (W=O) groups and residual sulfate (S=O) species. It is obvious from the perspective of infrared spectroscopy that NH_3 adsorption on Brønsted acid sites was dominant and that tungsta played a major role in this respect.

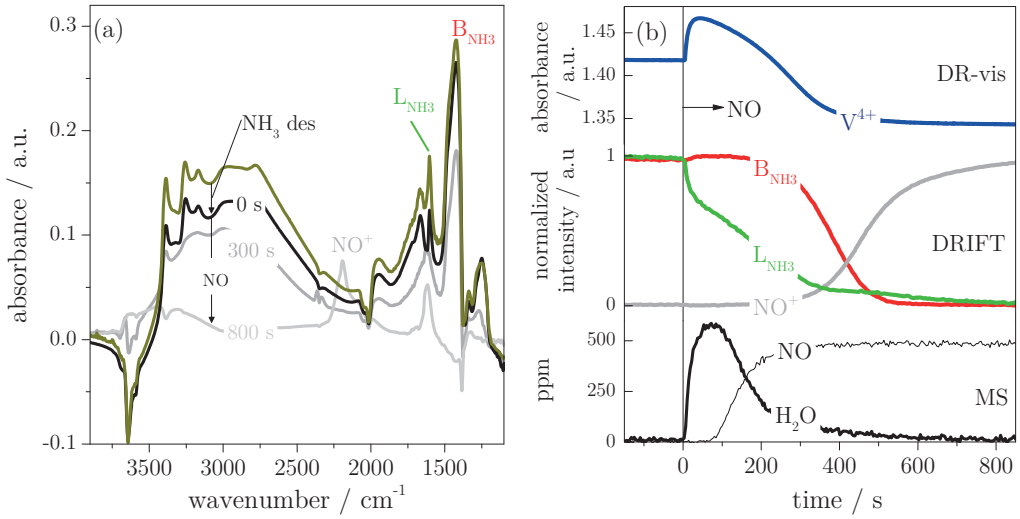

Figure 5-2. Transient infrared and visible spectra of NO reaction on NH_3-equilibrated V-W-Ti. (a) DRIFT spectra of V-W-Ti after 500 ppm NH_3 adsorption (15 min), desorption (15 min) followed by 500 ppm NO addition. (b) Temporal evolution of selected signals during addition of NO from identical DRIFT and DR-vis measurements and from online gas analysis by mass spectrometry. DRIFT: δ_{as}(N-H) of L_{NH3}, δ_{as}(N-H) of B_{NH3}, and ν(NO) of NO^+. DR-vis: V^{4+} (700 nm, d-d transition). Negative and positive absorbance values indicate consumption and formation of species, respectively. Conditions: 5 vol% O_2/N_2; 250°C.

When the residual adsorbed NH_3 after desorption at 250°C was reacted with 500 ppm $NO/O_2/N_2$ while recording DRIFT spectra at 0.9 s/spectrum, the first evident effect was that these species were consumed before nitrosyl species (NO^+) and water started to populate the surface of the catalyst (**Figure 5-2a**). Only a deeper inspection of the time-resolved spectra demonstrated that the consumption rates of L_{NH3} and B_{NH3} were not identical upon exposure to NO. This is best seen from the temporal evolution of the two species and NO^+ (**Figure 5-2b**). Consumption of L_{NH3} occurred in two stages, which could be distinguished by the time evolution of L_{NH3} rather than for the presence of two distinct spectroscopic signatures. An instantaneous removal of ca. 30% of L_{NH3} ($L_{NH3}(1)$) was followed by a slower consumption of L_{NH3} ($L_{NH3}(2)$). Only when L_{NH3} had been almost completely consumed, the signal of NO^+ started intensifying. B_{NH3} coverage at this point was still ca. 70%. B_{NH3} only started declining long after reaction of L_{NH3}. The simultaneous mass spectrometric data undoubtedly demonstrated that the water product of standard SCR evolved parallel to the consumption of L_{NH3} thus reflecting the occurrence of the SCR reaction in the early stages of NO admittance. This is further supported by the very similar ratio between consumed NO and evolved water (1.53) to the stoichiometry of the standard SCR reaction (1.5).

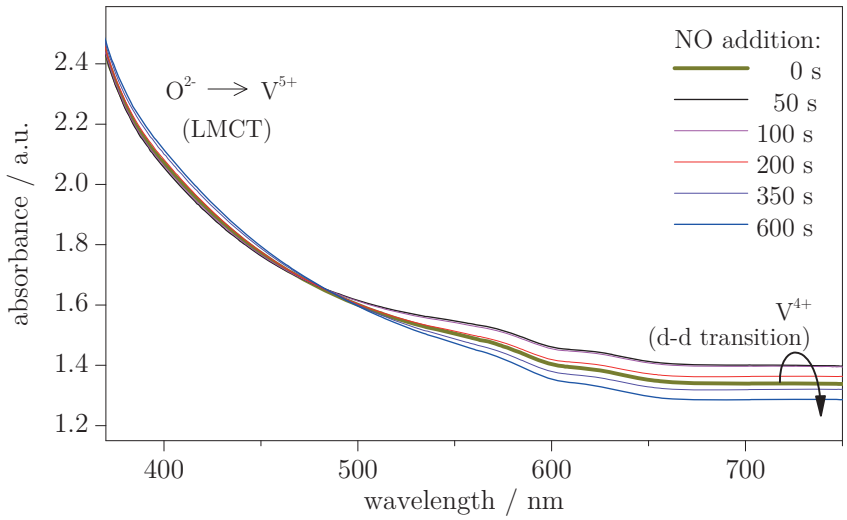

Figure 5-3. Selected time-resolved DR-vis spectra of V-W-Ti obtained while flowing 500 ppm NO, 5 vol% O_2 in N_2 at 250°C. Prior to reaction, the catalyst was submitted to NH_3 adsorption (500 ppm, 15 min) and desorption (N_2, 15 min) at 250°C.

Exposure to NO had an immediate impact also on the oxidation state of vanadium (**Figure 5-2b**) in an identical diffuse reflectance visible (DR-vis) spectroscopy experiment (**Figure 5-3**). NO caused a rapid initial reduction, which was monitored using the d-d transition at 700 nm as the fingerprint of V^{4+} [241-242]. Reduction was followed by a slower re-oxidation before returning to a constant (and on average higher) oxidation state after all adsorbed NH_3 had been consumed. Hence, the time-resolved measurement of **Figure 5-2** clearly demonstrates that NO reacted primarily with L_{NH3} and simultaneously enhanced reduction of V^{5+} to V^{4+} compared to NH_3 adsorption. After the fast initial reaction of NO with L_{NH3}, the SCR reaction slowed down due to the decreasing L_{NH3} coverage and the increasing levels of V^{5+}. B_{NH3} started declining only after consumption of $L_{NH3}(2)$. Although it cannot be excluded that B_{NH3} converts into L_{NH3} before reacting, it demonstrates that at low temperature only the Lewis acid sites are SCR active. Moreover, NO is activated on a Lewis acid site occupied by NH_3 simultaneously to the reduction of V^{5+} to V^{4+}. As long as L_{NH3} is available, NO cannot adsorb as NO^+ and gradually consumes the remaining NH_3 species.

The rates of initial consumption of L_{NH3} and of the parallel initial reduction to V^{4+} were independent of temperature (200 - 250°C) and presence of oxygen (**Figure 5-4**), suggesting that $L_{NH3}(1)$ is not involved in the rate determining step. On the contrary, the fraction of $L_{NH3}(2)$ increased with decreasing temperature, while its consumption rate decreased. $L_{NH3}(2)$ was yet susceptible to the absence of oxygen. Admittance of NO in absence of oxygen (**Figure 5-4c**) consumed only $L_{NH3}(1)$ that could react faster at all temperatures, but no further L_{NH3} consumption was observed once that of $L_{NH3}(1)$ had occurred. This observation suggests that $L_{NH3}(1)$ does not require gas phase oxygen to complete the SCR reaction. The absence of oxygen further discards the possibility for NO_2 to be the source of the initial fast decay of L_{NH3} (fast SCR) [45, 72]. When the catalyst was equilibrated with NH_3 in absence of oxygen after reaction with NO (**Figure 5-4d**), no fast L_{NH3} consumption was detected.

This measurement demonstrates decisively that $L_{NH3}(1)$ does not need oxygen to react but cannot be regenerated if oxygen is absent. Therefore, this active

site is an oxidized center. The reaction of $L_{NH3}(2)$ can be instead associated with the slower re-oxidation that was clearly temperature dependent in agreement with oxygen being involved in the rate determining step [72].

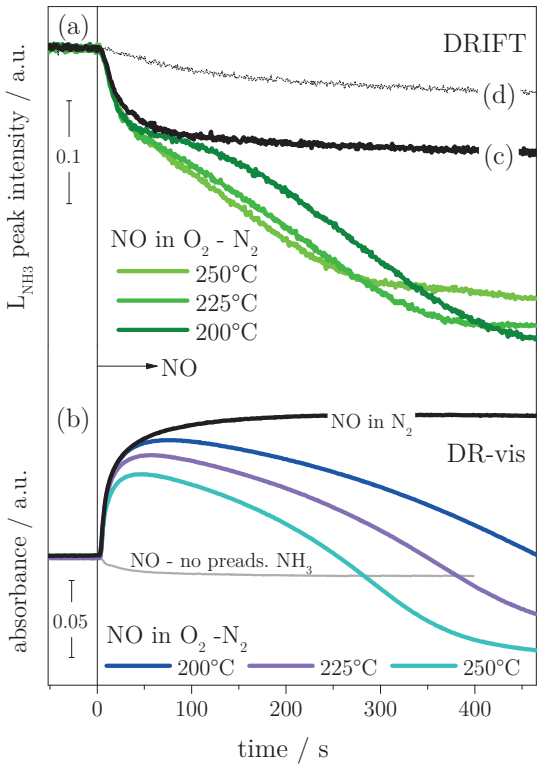

Figure 5-4. Temperature dependence of NO reaction on NH_3-equilibrated V-W-Ti. Temporal evolution of selected (a) DRIFT and (b) DR-vis signals during NO addition at 200, 225 and 250°C (with and without O_2) in identical measurements to that of Figure 5-2. (c) and (d) traces correspond to temporal evolution of L_{NH3} in two consecutive runs in absence of oxygen and intervalled by NH_3 adsorption/desorption. DRIFT: δ_{as}(N-H) of L_{NH3}; DR-vis: V^{4+} (700 nm).

Without oxygen, re-oxidation did not occur and a constant V^{4+} content was obtained over time on stream. This data encourages proposing the existence of $V^{5+}O_x$ Lewis acid sites that are already arranged in an optimum configuration to react with NO after NH_3 adsorption. The structure of these sites will be addressed below [63, 132, 243]. Once these sites have been reduced by the reaction of coordinated NH_3 with NO, they need to be regenerated by oxidation of V^{4+}.

5.3.3 Influence of H_2O

Water adsorption on V-W-Ti was also followed by DRIFT (**Figure 5-5**) prior to the single transient experiment. Water physisorption can be characterized by the δ(O-H) at 1626 cm^{-1} and by the perturbation of the OH groups with formation of a broad signal extending between 3600 and 2500 cm^{-1} characteristic of hydrogen bonded molecules. The negative peak at 1380 cm^{-1} corresponds to the coordination of water to the sulfate species present on TiO_2. It is also evident that water adsorption causes a general slight decrease of transmittance in the whole spectral region.

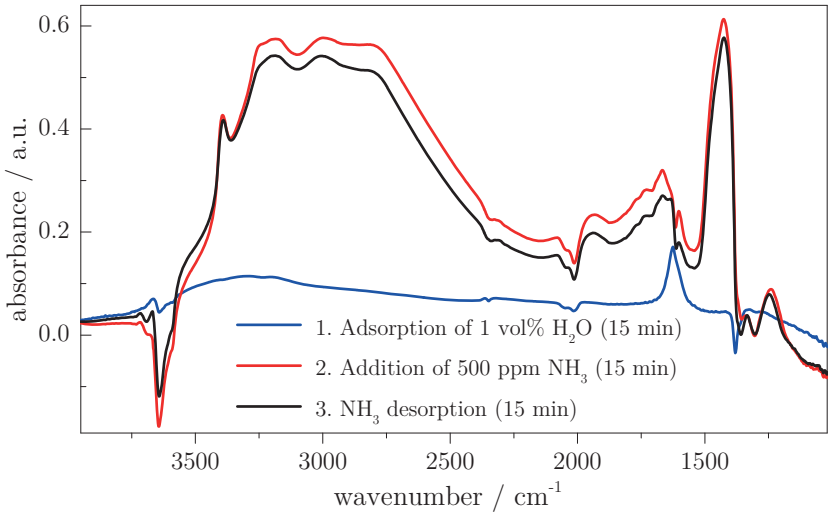

Figure 5-5. DRIFT spectra of V-W-Ti at 250°C in 5 vol% O_2/N_2 with 1 vol% H_2O adsorption for 15 min followed by NH_3 adsorption (500 ppm, 15 min) and desorption (15 min) in continuous feed of 1 vol% H_2O.

After NH_3 addition, the signal at 1626 cm^{-1} gradually disappeared and the L_{NH3} and B_{NH3} formed showing the typical features of adsorbed NH_3 described in **Figure 5-2**. Since the signal at 1626 cm^{-1} was consumed upon NH_3 addition, it can be concluded that NH_3 adsorbed more strongly to the surface acid sites compared to water. However, the intensity of the L_{NH3} signal was lower than in the absence of water. Therefore, water competes with adsorbed NH_3 for adsorption or partly converts Lewis acid sites into Brønsted acid sites.

The NO addition to pre-adsorbed NH_3 with 1 vol% H_2O in the gas feed throughout the whole measurement on V-W-Ti was repeated in **Figure 5-6**

and **Figure 5-7** in an identical sequence to that shown in dry conditions (**Figure 5-2** and **Figure 5-4**, respectively). Online MS in **Figure 5-6b** showed the evolution of H_2O in coincidence with the consumption of L_{NH3} (ratio formed H_2O: consumed NO = 1.26). The ΔH_2O was obtained by subtracting the 10'000 ppm H_2O present in the feed, hence this corresponds only to water formed by reaction of NO with adsorbed NH_3. This also explains the greater noise in this MS signal compared to the one in **Figure 5-2b**.

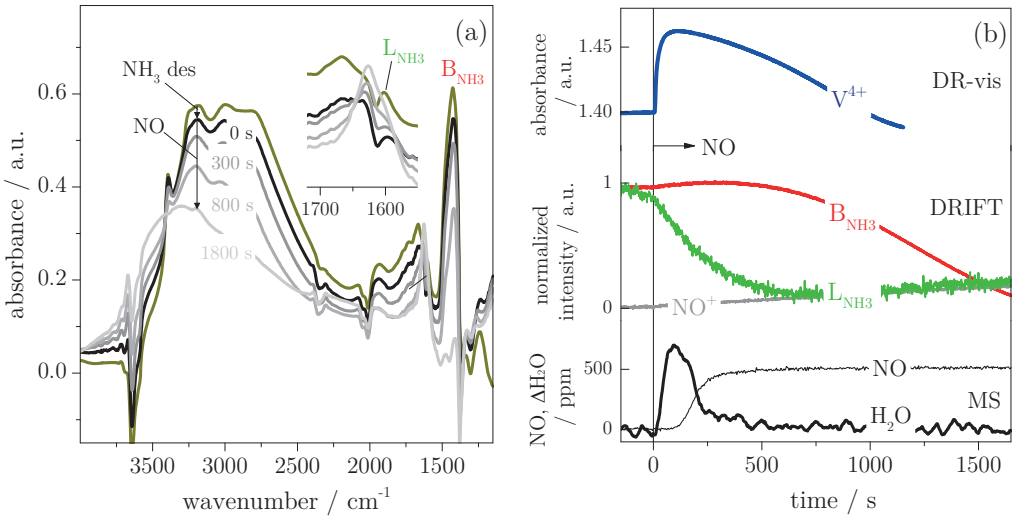

Figure 5-6. (a) DRIFT spectra of V-W-Ti after 500 ppm NH_3 adsorption (1 vol% H_2O, 5 vol% O_2 in N_2, 15 min), NH_3 desorption (1 vol% H_2O, 5 vol% O_2 in N_2, 15 min) followed by 500 ppm NO addition in 1 vol% H_2O, 5 vol% O_2 in N_2 at 250°C. (b) Temporal evolution of selected signals during addition of NO from DRIFT and DR-vis spectra of (a) and online gas analysis by mass spectrometry.

L_{NH3} species started decaying immediately after exposure to NO, similar to the measurements without H_2O, while the attenuation of B_{NH3} started only after 500 s. Differences with and without water in the feed are, that the L_{NH3} signals were smaller after NH_3 desorption in presence of water and L_{NH3} consumption did not occur in two steps as derived from the temporal evolution of the signal at 1603 cm^{-1}. The overall time needed for the consumption of all adsorbed NH_3 increased (e.g. note the x-axis scales in **Figure 5-7** and **Figure 5-4**) in agreement with the decreased NH_3-SCR activity (**Figure 5-1**) and NO^+ formation was suppressed. The data in **Figure 5-5** - **Figure 5-7** suggests that

the reason for this inhibition and the lower NO_x conversion possibly correlate mainly with the loss of L_{NH3}.

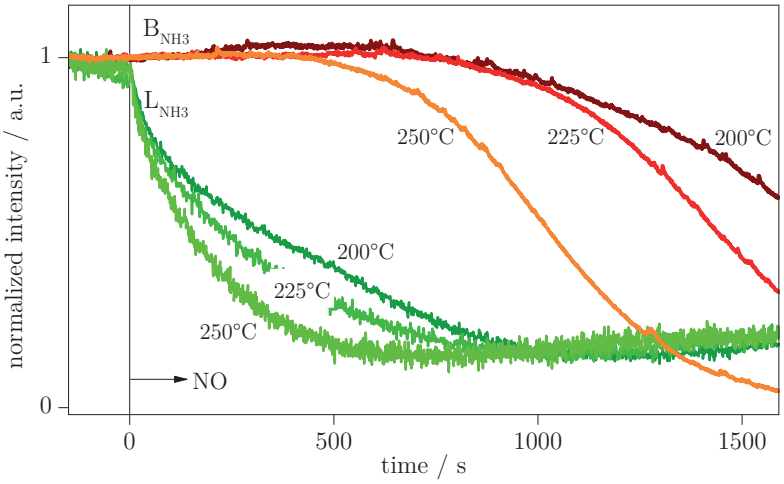

Figure 5-7. Temperature dependence of NO reaction on NH_3-equilibrated V-W-Ti in a continuous 1 vol% H_2O- 5 vol% O_2 - N_2 gas feed. Temporal evolution of selected DRIFT signals (δ_{as}(N-H) of L_{NH3} and δ_{as}(N-H) of B_{NH3}) during NO addition at 200, 225 and 250°C (with and without O_2), conducted identically to those in Figure 5-4.

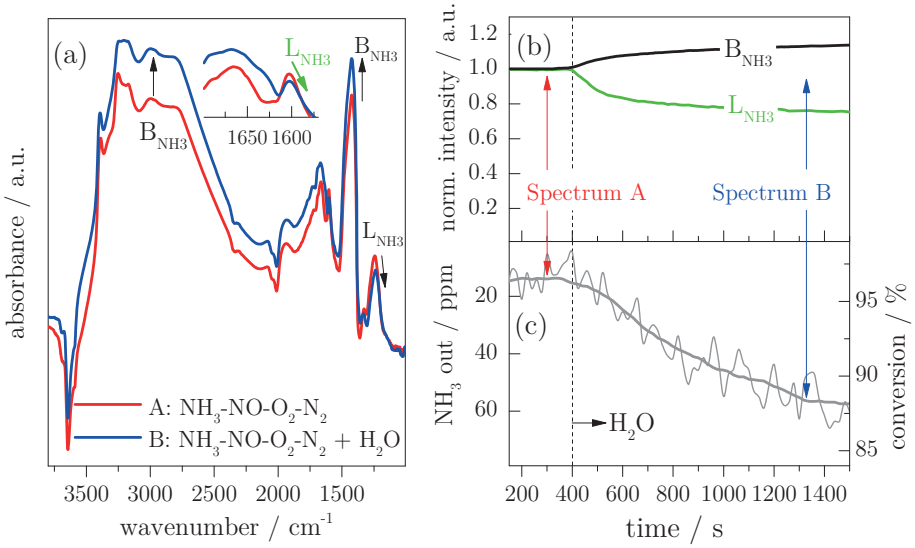

Figure 5-8. DRIFT spectra (a) of V-W-Ti at 250°C after equilibration in 500 ppm NO, 500 ppm NH_3 5 vol% O_2/N_2 (spectrum A) and 20 min after addition of 1 vol% H_2O (spectrum B). (b) Temporal evolution of L_{NH3} (1603 cm^{-1}) and B_{NH3} (1423 cm^{-1}) of DRIFT spectra in (a) and online NH_3 analysis (c) by FT-IR before and during water dosage. Water was added at time 0 s. Vertical arrows indicate the time at which spectra A and B were acquired.

The influence of water under SCR conditions was further studied by addition of water under steady state conditions. For this purpose, a constant feed of 500 ppm NH_3, 500 ppm NO, 5 vol% O_2 in N_2 was admitted to the catalyst till equilibration (**Figure 5-8**). The DRIFT spectrum was similar to that of adsorbed NH_3 in O_2-N_2 in **Figure 5-5**. The online gas analysis (**Figure 5-8c**) indicated ca. 96% NO_x conversion. Addition of water to the feed (at time 0 s) caused a slow adjustment of conversion at ca. 87%, confirming the inhibiting effect of H_2O and the data of **Figure 5-1**. The temporal evolution of the major signals in the DRIFT spectra upon water dosage (**Figure 5-8b**) revealed a slight increase of B_{NH3} intensity and a decay of L_{NH3}. Steady state under the new feed conditions was attained after 20 min (**Figure 5-8a**, spectrum B). At this point, the L_{NH3} signal was reduced by ca. 30% indicating that L_{NH3} remains on the catalyst surface despite the 1 vol% H_2O in the feed. The slight increase of B_{NH3} was tentatively associated with the conversion of Lewis to Brønsted acid sites. This experiment verifies that the Lewis acid sites did not vanish and remain at a significant level in presence of NO, NH_3, O_2 and water.

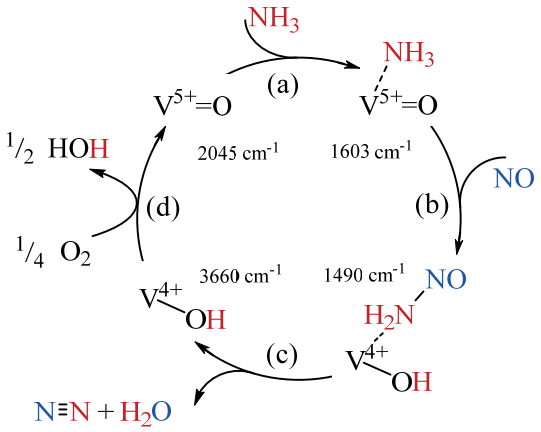

Figure 5-9. Proposed reaction mechanism of standard NH_3-SCR.

The experiments in section 5.3.2 and 5.3.3 undoubtedly demonstrate two crucial steps of the standard SCR reaction mechanism on V-W-Ti: i) the direct involvement of the V^{5+} Lewis acid site and ii) the rate determining step, the oxidation of V^{4+} by oxygen. This is represented for clarity in steps (a) and (d) of **Figure 5-9**, respectively within the paradigm of the catalytic cycle proposed by Ramis et al. [162] based on Lewis acid sites.

5.3.4 Multiple transient experiments

It was possible to obtain an even more complete picture of the reaction mechanism under more realistic reaction conditions than those of **Figure 5-2** and **Figure 5-4** by periodically perturbing the atmosphere around the catalyst while acquiring time-resolved spectroscopic data. This approach mimics better the SCR conditions than the single transient experiment of **Figure 5-2**. The short time-scale inspection of the SCR reaction using modulated excitation spectroscopy [236, 244-245] can trace the surface changes with additional precision due to phase sensitive analysis.

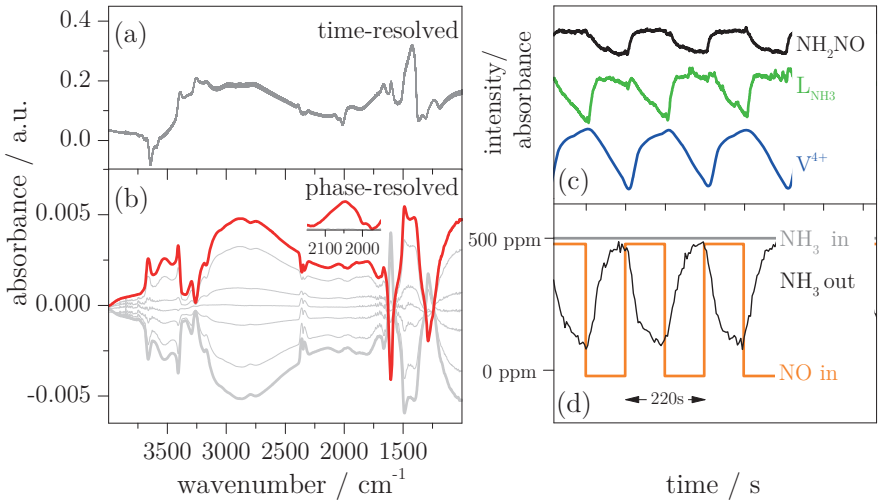

Figure 5-10. Concentration modulation approach: NO pulses in NH_3. (a) Time-resolved DRIFT spectra of V-W-Ti during a full NO+NH_3+O_2/NH_3+O_2 modulation experiment at 250°C (T= 220 s). (b) Corresponding set of selected phase-resolved data (φ^{PSD}= 150 - 320°); in red the in-phase spectra. (c) Temporal evolution of selected signals from the time-resolved DRIFT and DR-vis spectra over multiple periods. (d) Representation of the pulse sequence (NH_3 in and NO in) and experimental FTIR gas analysis (NH_3 out). Conditions: 500 ppm NH_3, 500 ppm NO, 5 vol% O_2 in N_2.

The most valuable modulation sequence consisted of NO pulses in a continuous flow of NH_3/O_2 (**Figure 5-10**), thus on a catalyst surface permanently covered by adsorbed NH_3. Other relevant sequences for the discussion are presented in **Figure 5-12**. Only the phase-resolved spectra were able to reveal the subtle, but important changes as the SCR reaction was switched on and off repeatedly by NO pulses. These changes mirrored those observed in the single transient

experiment of **Figure 5-2**. Despite their dominant presence in the time-resolved spectra (**Figure 5-10a**), none of the changes could be associated with B_{NH3} confirming its extraneousness to SCR. On the contrary, L_{NH3} played a major role in the spectra. It exhibited signals of opposite sign to that of two signals at 1490 and 1400 cm^{-1}, which were otherwise hidden in the time-resolved spectra by the persistent B_{NH3} signals. These two signals were slightly phase shifted, suggesting that they did not belong to the same species.

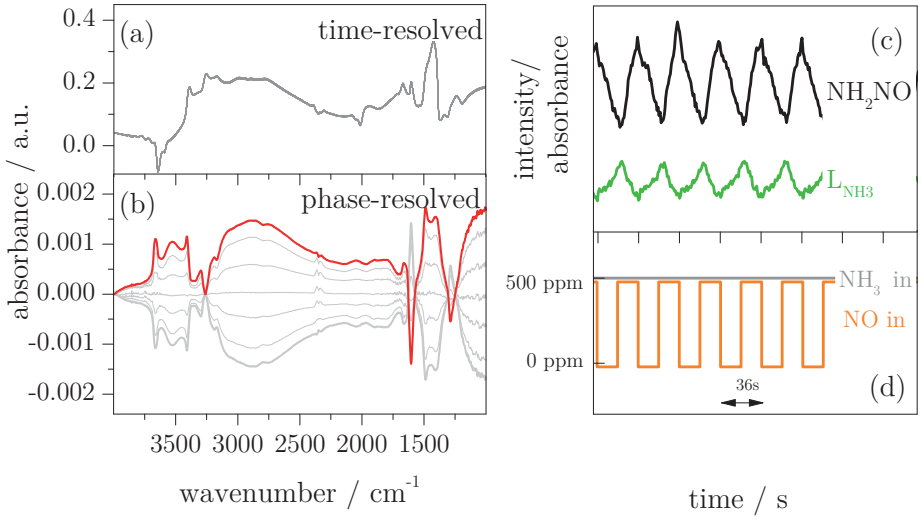

Figure 5-11. Concentration modulation approach: short NO pulses in NH_3. (a) Time-resolved DRIFT spectra of V-W-Ti during a full $NO+NH_3+O_2/NH_3+O_2$ modulation experiment at 250°C (T= 36 s). (b) Corresponding set of selected phase-resolved data (φ^{PSD}= 70 - 250°); the in-phase spectrum is red. (c) Temporal evolution of selected signals from the time-resolved spectra over multiple periods. (d) Representation of the pulse sequence.

The modulation experiment was repeated with the identical modulation sequence (NO pulses in NH_3) but shorter modulation period (T= 36 s; 60 periods) in **Figure 5-11**. This time-scale is in the same range of $L_{NH3}(1)$ consumption as in **Figure 5-2**, thus omitting the involvement of the more slowly reacting $L_{NH3}(2)$. All the features that were visible in the long experiment of **Figure 5-12** were also detected using the short modulation period. A major difference between the two experiments is the lower intensity of the dynamic signals in the PSD of the short pulse sequence (compare scales of the absorbance y-axis). This is also visible in **Figure 5-11c** where the peak intensity of the time-

resolved spectra was less pronounced. Nonetheless, the same evolution of species was observed for both, the short and longer modulation period.

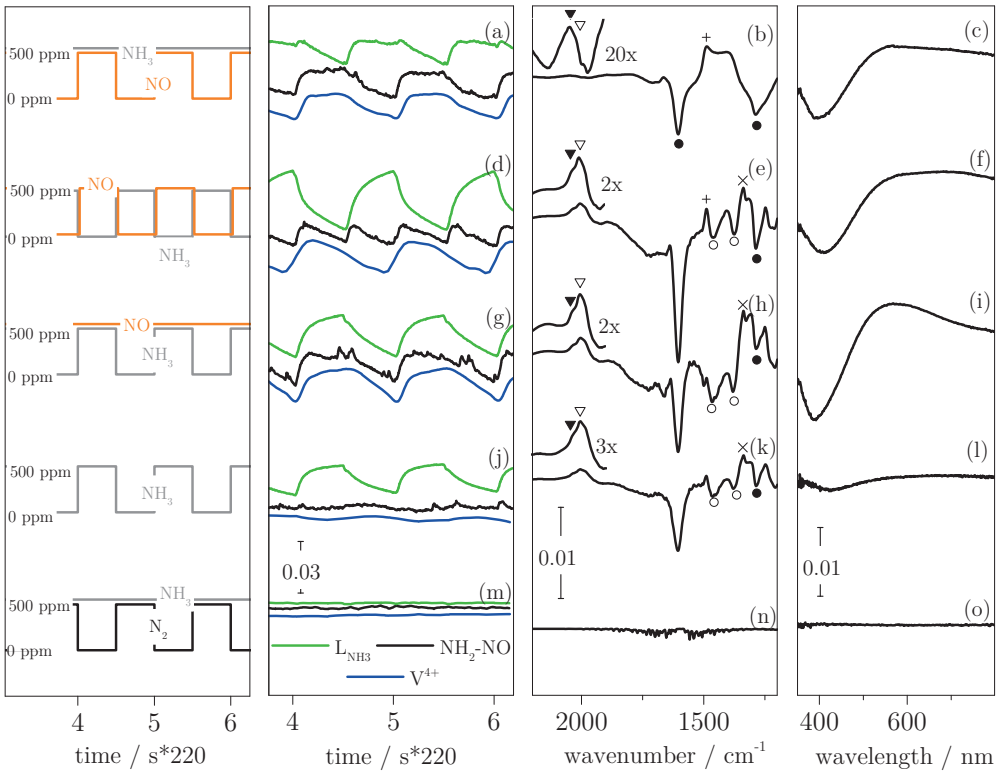

Figure 5-12. Concentration modulation sequences. Representation of the modulation sequences performed with DRIFT and DR-vis (T= 220 s): (a-c) NO pulses in NH_3, (d-f) alternated NO and NH_3 pulses, (g-i) NH_3 pulses in NO, (j-l) NH_3 pulses in inert, and (m-o) pulses of inert in NH_3. (a, d, g, j, m) NH_2NO and L_{NH3} peak intensity of the time-resolved DRIFT spectra and absorbance of V^{4+} of time-resolved DR-vis spectra. Corresponding phase-resolved (b, e, h, k, n) DRIFT and (c, f, i, l, o) DR-vis data; only the in-phase spectra are displayed. Min. and max. NO and NH_3 concentration values are 0 ppm and 500 ppm. (●) L_{NH3}; (+) NH_2NO; (○) B_{NH3}; (×) S=O; (▼) V=O; (▽) W=O. Conditions: 500 ppm NH_3, 500 ppm NO, 5 vol% O_2 in N_2; 250°C.

The features at 1603 and 1490 cm^{-1} did not reflect NH_3 adsorption/desorption because of their opposite sign. This process was rather mimicked by the sequence in **Figure 5-12j-l**, where a minor fraction of B_{NH3} was also seen to contribute to the phase-resolved spectra and with the same sign as L_{NH3}. The signal at 1490 cm^{-1} was assigned to the nitrosamide intermediate (NH_2NO, ν(NO) [162]. The assignment was confirmed by the temporal evolution of the feature in this sequence and in that obtained by alternating NO and NH_3 pulses. In the

NH_3/O_2 pulse (**Figure 5-10c** and **Figure 5-11c**), the replenishment of L_{NH3} consumed in the previous $NO+NH_3+O_2$ pulse was accompanied by the disappearance of nitrosamide due to the absence of NO. This corresponds to interrupting the catalytic cycle at step (b) in **Figure 5-9**. Nitrosamide sharply intensified again when NO was admitted concomitantly to the consumption of L_{NH3}. Hence, L_{NH3} reacted repeatedly with NO as in the experiment of **Figure 5-2**, which was confirmed by the loss of gas phase NH_3 (**Figure 5-10d**).

When NO pulses were alternated to NH_3 pulses (**Figure 5-12d**), the SCR reaction occurred only briefly at the valve switch. Consistently with its nature of being an intermediate, nitrosamide was formed rapidly at each pulse before returning to lower levels because the gas composition was either only NO or only NH_3. The need of both NH_3 and NO for V^{5+} reduction was confirmed by the DR-vis data of this sequence (**Figure 5-12f**). The V^{4+} level increased only at the beginning of the $NO+O_2$ pulse since Lewis acids were covered by NH_3 reacting with NO at the V^{5+} center. V^{4+} slowly re-oxidized already in the NO pulse, due to oxygen and the slight oxidative character of NO (compare with **Figure 5-4b**). The change in L_{NH3} was larger in this sequence because of the continuous addition and removal of gas phase NH_3 and was thus complemented by minor variations of the B_{NH3} coverage as a result of adsorption/desorption.

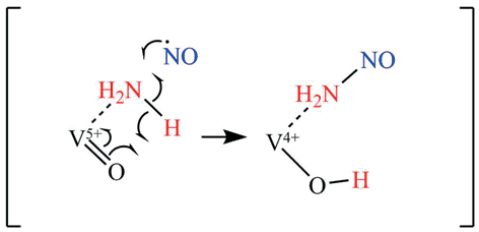

Figure 5-13. Proposed intermediate of the NH_3-SCR mechanism.

The molecular level information on the vanadium reduction/oxidation present in the phase-resolved DRIFT data was enriched by important details on the V=O and V-OH groups involved in this chemistry. The spectra allowed distinguishing between the reactivity of isolated V=O and the NH_3 adsorption capacity of WO_3 [234]. The sequence of **Figure 5-10** and **Figure 5-12a-c** was the only one where only the signature of mono-oxo V=O groups at 2045 cm^{-1} was observed [219]. In all other cases, perturbation of W=O wolframyl species

(2005 cm^{-1}) always masked the contribution of V=O, which is reasonable based on the above observation that NH_3 adsorption/desorption was present in those sequences. The appearance of V=O species simultaneous to L_{NH3} consumption confirmed that NH_3 dissociated on V=O in the presence of NO, thus producing a V-OH group (3660 cm^{-1}). The V-OH group in turn was oxidized by oxygen and restored to unoccupied V=O (steps (c) and (d) in **Figure 5-9**). This observation is consistent with a concerted transfer of a hydrogen atom to the coordinating vanadium mono-oxo group simultaneous to the formation of the N-N bond of the nitrosamide (NH_2NO) intermediate (**Figure 5-13**). The exact formation mechanism of NH_2NO can only be described tentatively with the available data. When NO reacts with adsorbed NH_3 on a Lewis acid site (L_{NH3}), the N-N bond is formed with the simultaneous reduction of V^{5+} to V^{4+} and the loss of a hydrogen atom of NH_3 to the vanadyl oxygen atom. This concerted pathway allows both nitrogen atoms of NO and NH_3 to remain in the -III and +III oxidation state, respectively, which is advantageous for reaction towards the N_2 product according to the cycle of **Figure 5-9**.

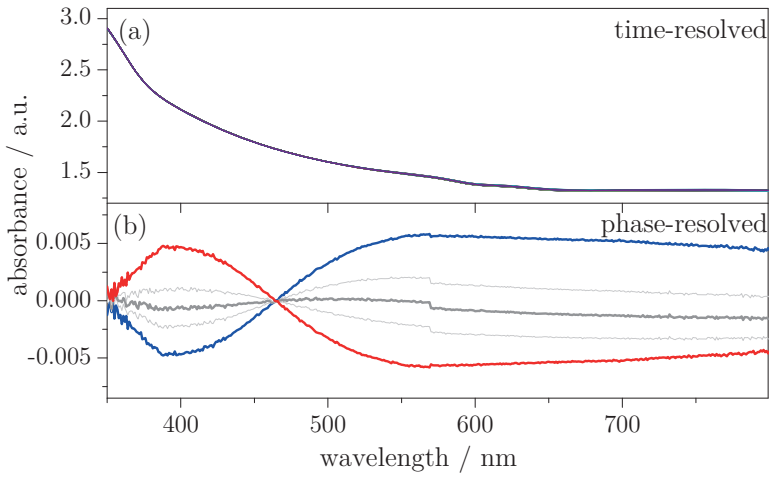

Figure 5-14. (a) Time-resolved DR-vis spectra of V-W-Ti during the $NO+NH_3+O_2/NH_3+O_2$ modulation sequence at 250°C (T= 220 s). Note that due to the very small differences all spectra overlap. (b) Corresponding set of selected phase-resolved data (φ^{PSD}= 20 - 200°); in-phase spectra (red and blue), out-of-phase spectrum (green). The isosbestic point at 460 nm is rather evident, which suggests interconversion between V^{5+} and V^{4+}.

The statement that NO does not adsorb directly on the vanadyl group to further react with NH_3 was proven by the experiment of **Figure 5-2**, where it was shown that NO only adsorbs and forms NO^+ after all the L_{NH3} were consumed. B_{NH3} were still present on the surface when NO^+ appeared, indicating that NO^+ was formed predominantly at the Lewis acid sites. On the contrary, the NO immediately forms NO^+ and nitrates on the surface in absence of NH_3. As long as NH_3 is present on the surface, NO remains in the gas phase and is involved in the V^{5+} reduction. The direct involvement of the V^{4+}/V^{5+} pair in the sequence of NO pulses in NH_3 was disclosed by the phase-resolved data (**Figure 5-14b**), while virtually no change in the oxidation state of vanadium was visible in time-resolved DR-vis (**Figure 5-14a**). The fraction of vanadium changing repeatedly between V^{5+} reducing in presence of both NO and NH_3 and V^{4+} that was more slowly restored in the subsequent NH_3+O_2 pulse was clearly visible, in agreement with the single transient experiment of **Figure 5-2**.

5.4 Conclusion

The combined transient time-resolved DRIFT and DR-vis study adds a new perspective to the SCR mechanism over VWT catalysts, using a time scale pertinent to the observation of active, intermediate and spectator species. Using tailored time-resolved pulse experiments, the entire mechanism of standard NH_3-SCR could be described. NO reacts predominantly with NH_3 adsorbed on Lewis acid sites at low temperature. Despite their abundance, Brønsted acid sites hardly contribute to the SCR activity and mainly serve as a NH_3 pool to replenish the Lewis sites. The active Lewis acid site consists of mono-oxo V^{5+}, which reduces only in presence of both NO and NH_3. On top of this, verification of the formation of the nitrosamide intermediate, which is formed simultaneously to V^{5+} reduction, was achieved. Once consumed, the active Lewis sites must be regenerated upon re-oxidation, which is the rate determining step.

Chapter 6

Silicon for the stabilization of an optimized V-based SCR catalyst

6.1 Introduction

Silicon was proposed to be a valuable promoter (section 1.4.3) [64, 101-108] for tackling the stability concerns of VWT catalyst as described in section 1.6 and presented in Chapter 3 and 4. The stabilization effect is considered to origin from the distortion of the anatase lattice, the formation of solid solutions, the substitution of Ti^{4+} by Si^{4+} or from the inhibition of molecule diffusion and the reduction of anatase inter-particle contact [83]. All these phenomena possibly hinder the growth of anatase crystallites and the subsequent phase transformation to rutile [109].

Chapman et al. tested the stability of various SiO_2-WO_3-TiO_2 materials using various precursors and loadings of SiO_2 and WO_3 [101]. After impregnation with 2 wt% V_2O_5, a support with ca. 5 wt% SiO_2 and 6 - 8 wt% WO_3 was found to be optimal for the catalyst stability. A sol-gel and co-precipitation approach used in other studies and the effect of SiO_2 loading in V_2O_5-SiO_2-TiO_2 catalysts were tested [103, 105]. The catalysts, stabilized by 10 - 20 wt% SiO_2, exhibited higher overall stability, lower SO_2 oxidation activity and increased vanadia dispersion reflecting the enhanced SCR activity. Similar observations were also found for catalysts prepared by co-precipitation of V, Mo, Ti and 7 - 13 wt% SiO_2. Due to the high V loading (8 wt% V_2O_5), the catalyst was active

This chapter is based on the preprint version of the publication: A. Marberger, D. Ferri, D. Rentsch, F. Krumeich, M. Elsener, O. Kröcher, Effect of SiO_2 on Co-impregnated $V_2O_5/WO_3/TiO_2$ Catalysts for the Selective Catalytic Reduction of NO with NH_3, *Catal. Today*, **2017**, doi.org/10.1016/j.cattod.2017.11.037. A. Marberger performed the experiments, analyzed and interpreted the data together with the co-authors and wrote the manuscript.

at low temperature and the vanadia species were in polymeric form [110]. Co-impregnation of V and W on SiO_2-TiO_2 and TiO_2 showed that both the presence of SiO_2 and the preparation method have a significant effect on activity and stability [106]. In presence of SiO_2, the support sintering as well as the formation of crystalline WO_3 and V_2O_5 started at higher temperatures. Incipient wetness impregnation of Si and V (1 wt% V_2O_5) on TiO_2 revealed a limited interaction between the two elements, hence the structure of the surface vanadium oxide was not altered by the presence of SiO_2 [111]. SiO_2 in flame-made VWT did not only exhibit improved thermal stability but also prevented the crystallization of tungsten oxide and increased the NO_x conversion at high temperatures. The low temperature SCR activity was, however, inferior compared to that of the SiO_2 free catalyst [107]. Summarizing, SiO_2 plays a major role in changing the properties of SCR catalysts such as stability and activity. Additionally, selection of the appropriate preparation method is crucial to resolve the issues of stability and low temperature activity [66, 205, 224, 246-248].

In this chapter, a co-impregnation method of W and V is used to optimize the low temperature activity of VWT catalysts. Because the hydrothermal stability of VWT is not guaranteed above 600°C, the main focus is to induce stability to the co-impregnated VWT catalysts upon addition of SiO_2. Thereby, the SiO_2 loading as well as the SiO_2 precursor type is optimized and the best performing catalyst is investigated physico-chemically using XRD, BET, transmission electron microscopy (TEM) and ^{29}Si nuclear magnetic resonance (NMR) spectroscopy.

6.2 Experimental section

6.2.1 Catalyst preparation

The catalysts were prepared following a wet co-impregnation procedure approach [59, 106, 204, 249], thereby using commercial low sulfate containing TiO_2 (DT-51-D, 0.6 wt% SO_3, **Table 1-1**), ammonium vanadate (AMV, NH_4VO_3, Sigma Aldrich) and ammonium metatungstate hydrate (AMT, $(NH_4)_6H_2W_{12}O_{40} \cdot xH_2O$, Sigma Aldrich). For the Si-containing catalysts, tetra-

methylammonium silicate (TMA-Si, 17 wt% SiO_2 in aqueous solution, Sigma Aldrich), tetraethyl orthosilicate (TEOS, Sigma Aldrich), colloidal silica (Ludox AS30, ca. 200 m^2/g, Sigma Aldrich) or fumed SiO_2 (particle size 7 nm, Sigma Aldrich) were used as precursors. The resulting samples are abbreviated as SiVW-Ti (TMA-Si), Si-TEOS-VW-Ti (TEOS), Si-col-VW-Ti (colloidal silica) and Si-fumed-VW-Ti (fumed SiO_2). AMV (eq. to 2.0 wt% V_2O_5, dissolved in 20 ml H_2O) and AMT (eq. to 10 wt% WO_3, dissolved in 10 ml H_2O) were added to an aqueous slurry of TiO_2 (H_2O/TiO_2 ratio 5/1) and stirred for 30 min, followed by addition of the Si precursor (according to **Table 6-2**). Reference catalysts 2 wt% V_2O_5-WO_3/TiO_2 (V-WTi), 2 wt% V_2O_5-$SiO_2/WO_3/TiO_2$ (V-SiWTi) and 2 wt% V_2O_5-SiO_2/TiO_2 (V-SiTi) were obtained from commercial DT-52, DT-58 and DT-S10 (**Table 1-1**) by impregnation with AMV, respectively. Their general preparation and the washcoating of monoliths are described in detail in section 2.1. After the catalytic test in the fresh state, the catalysts were consecutively hydrothermally aged at 600, 650 and 700°C for 16 h and tested on a lab scale reactor described in section 2.2.

6.2.2 Physico-chemical characterization methods

The methodology for XRD and BET measurements are described in detail in section 2.3. TEM and scanning transmission electron microscopy (STEM) images were taken with a Talos F200X (FEI) microscope operated at an acceleration voltage of 200 kV. Elemental mappings were recorded by four energy-dispersive X-ray spectrometers (EDX) mounted on this microscope. Magic angle spinning (MAS) solid-state ^{29}Si NMR spectra were recorded on a Bruker 400 NMR spectrometer using a 7 mm CP/MAS probe. The single pulse experiments were recorded at 79.5 MHz using the following parameters: 4500 Hz MAS rate, ca. 10,000 scans, 10 s relaxation delays applying high powered SPINAL 64 proton decoupling during the data acquisition. The ^{29}Si chemical shifts were referenced to an external sample of tetramethylsilane (TMS). The observed resonances were analyzed using the Q^n classification, where a SiO_4 tetrahedron is connected to n neighboring SiO_4 tetrahedra (n= 0 - 4) [250].

6.3 Results and discussion

6.3.1 Benefits and limitations of co-impregnated VW-Ti catalysts

The activity of two different catalysts comprising both 2 wt% V_2O_5 and 10 wt% WO_3 on a commercial TiO_2 support was compared after different aging temperatures in **Figure 6-1**. For V-WTi, a commercial tungsta-titania support (DT-52, **Table 1-1**) was impregnated with V, while for VW-Ti, commercial TiO_2 (DT-51-D, **Table 1-1**) was co-impregnated with V and W (**Table 6-2**).

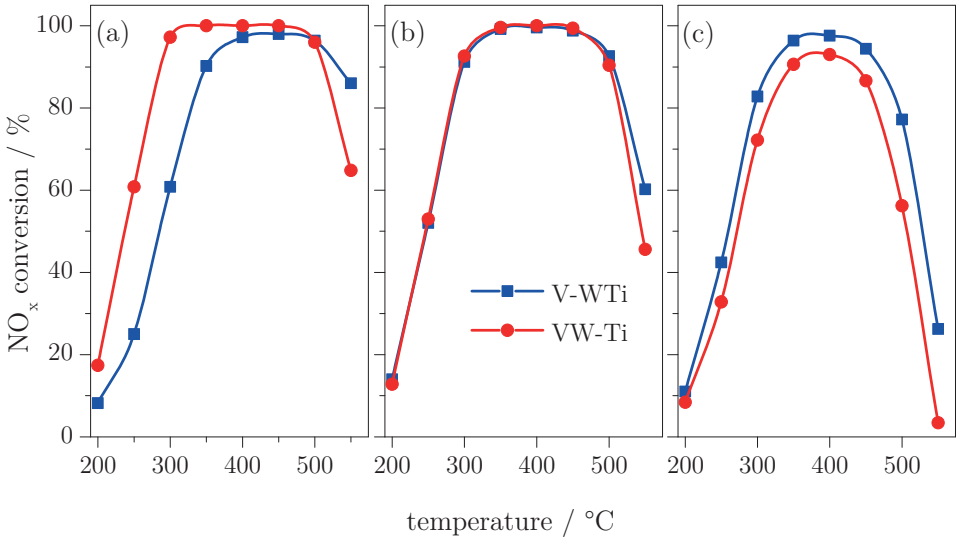

Figure 6-1. NO_x conversion of V-WTi (impregnation of V on WTi) and VW-Ti (co-impregnation of V and W on Ti) after calcination at (a) 450°C for 10 h and after hydrothermal aging at (b) 600°C and (c) 650°C for 16 h.

It is evident that the co-impregnated catalyst (VW-Ti) exhibited a much higher activity compared to the reference catalyst (V-WTi), especially in the lower temperature regime (below 300°C). At 250°C the conversion difference was ca. 35% in the fresh state (catalyst calcined at 450°C for 10 h). After hydrothermal aging at 600°C (**Figure 6-1b**), the NO_x conversion of both catalysts was nearly identical (ca. 53% at 250°C), hence VW-Ti was slightly deactivated while V-WTi was activated by aging. The activation of V-based catalysts with such a support is a known phenomenon [76] and has been addressed in Chapter 3 and Chapter 4. By increasing the aging temperature to 650°C (**Figure 6-1c**), the co-impregnated catalyst showed more pronounced aging tendencies over the whole temperature range, while V-WTi mainly deactivated at high reaction

temperatures (> 400°C). It appears that co-impregnation of V and W on TiO_2 is advantageous to obtain a highly active catalyst after moderate calcination at 450°C. To this end, the synthetic route is simple and less time consuming, which brings advantages in lowering the production cost of potential applications. However, the co-impregnated VW-Ti catalyst already started deactivating after hydrothermal aging at 600°C and even more severely at 650°C compared to V-WTi. In order to preserve the benefit of the low temperature activity of co-impregnated VW-Ti but to gain temperature stability, VW-Ti was modified by SiO_2 (SiVW-Ti), because of its known promotion effect towards increasing the temperature stability of VWT catalysts [64, 83, 101-108, 110-111]. Various co-impregnated SiVW-Ti catalysts with different SiO_2 contents and precursors were synthesized according to **Table 6-2** and were investigated with respect to the effect and the origin of their thermal stabilization.

6.3.2 Catalytic activity of Si-stabilized vanadia-tungsta-titania catalysts

The SiVW-Ti catalysts were synthesized identically to VW-Ti but additionally comprised various loadings of SiO_2 (0 - 10 wt%, precursors TMA-Si) added during the co-impregnation process (e.g. 5 wt% SiO_2, 2 wt% V_2O_5, 10 wt% WO_3 on TiO_2 is labelled as 5SiVW-Ti, **Table 6-2**). To simplify the comparison of the activity of all catalysts with different SiO_2 contents and aging temperatures (450, 600, 650 and 700°C), only three crucial temperatures for each catalyst, i.e. 250, 350 and 550°C were tested and are shown in **Figure 6-2a** - **Figure 6-2c**, respectively. The activity of the catalyst after calcination at 450°C in the low temperature regime (**Figure 6-2a**) reveals that a higher amount of SiO_2 is increasingly detrimental for the activity. Already with 5 wt% SiO_2 (5SiVW-Ti), the NO_x conversion decreased from 60% to ca. 40%. At 350°C (**Figure 6-2b**), the activity decreased only for SiO_2 contents larger than 5 wt%, while for the high temperature activity (**Figure 6-2c**) the increasing SiO_2 content increased the NO_x conversion.

After aging at 600°C, a small deactivation of the catalyst without SiO_2 was obvious at 250 and 550°C. The low temperature activity in **Figure 6-2a** reveals that the addition of 3 - 10 wt% SiO_2 produced a slightly more active catalyst than its corresponding fresh state. At the reaction temperature of 350°C,

all catalysts showed full conversion (**Figure 6-2b**) after aging at 600°C. At high reaction temperature (**Figure 6-2c**), the NO_x conversion increased up to a loading of 4 wt% SiO_2. Comparison of the fresh and aged catalysts with different SiO_2 loadings revealed that the optimal SiO_2 content is around 3 - 4 wt%. **Figure 6-2** demonstrates that this amount of SiO_2 guarantees high catalytic activity already in the fresh state and aging resistance up to 600°C.

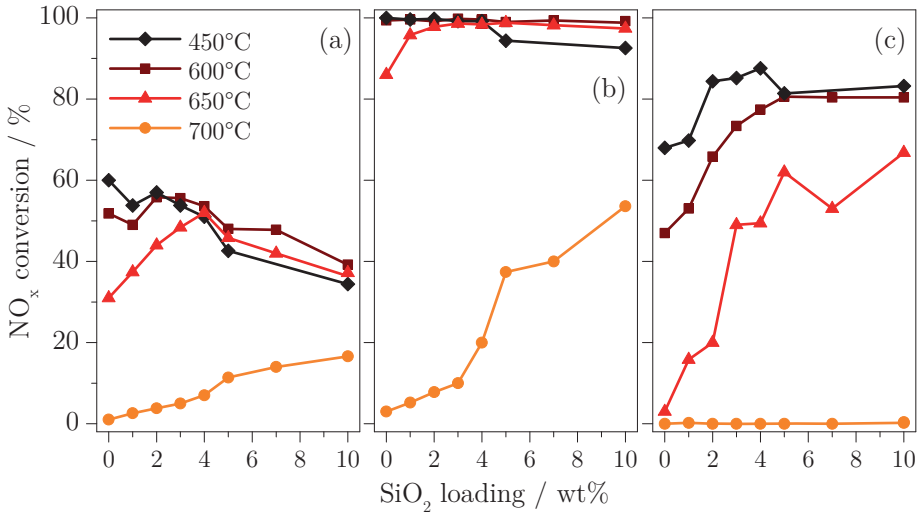

Figure 6-2. NO_x conversion of co-impregnated SiVW-Ti catalysts with different SiO_2 loadings using a TMA-silicate as precursor at (a) 250°C, (b) 350°C and (c) 550°C in the fresh state (calcination at 450°C) and after consecutive hydrothermal aging at 600, 650 and 700°C. All catalysts comprise 2 wt% V_2O_5 and 10 wt% WO_3.

Major differences between the co-impregnated catalysts with and without SiO_2 stabilization can be observed after hydrothermal aging at 650°C. VW-Ti heavily deactivated in the low and high temperature regime (see also **Figure 6-1c**) but a low amount of SiO_2 contributed to stabilize the catalyst. The low temperature activity of VW-Ti could be fully preserved with a loading of 4wt% SiO_2 (4SiVW-Ti). The NO_x conversion at intermediate temperatures was only affected for SiO_2 loadings up to 2 wt%, while a higher SiO_2 content was beneficial for the conversion in the high temperature regime.

Summarizing, the optimized 4SiVW-Ti showed high NO_x conversion at low temperature in the fresh state, similar to the catalyst without TMA-Si stabilization (VW-Ti). While the SCR activity of VW-Ti and the V-WTi were considerably affected by aging at 650°C over the entire reaction temperature re-

gime (**Figure 6-1c**), it was not affected for 4SiVW-Ti in the low and medium temperature regime (**Figure 6-2** and **Figure 6-4b**) and was only partly lost in the high temperature regime. The reaction rate constant k_{mass} (**Table 6-2**) is a useful parameter to compare the activity of different catalysts and is a suitable descriptor of the effect of SiO_2 loading. The highest k_{mass} value after calcination at 650°C was found for 4SiVW-Ti (142 $cm^3g^{-1}s^{-1}$) while a lower or higher SiO_2 content decreased the k_{mass} values. **Figure 6-3** additionally displays the k_{mass} values as a function of SiO_2 loading and all aging temperature. It is clear that k_{mass} decreases with increasing aging temperature and that 4SiVW-Ti preserves the highest k_{mass} value after aging at 650°C.

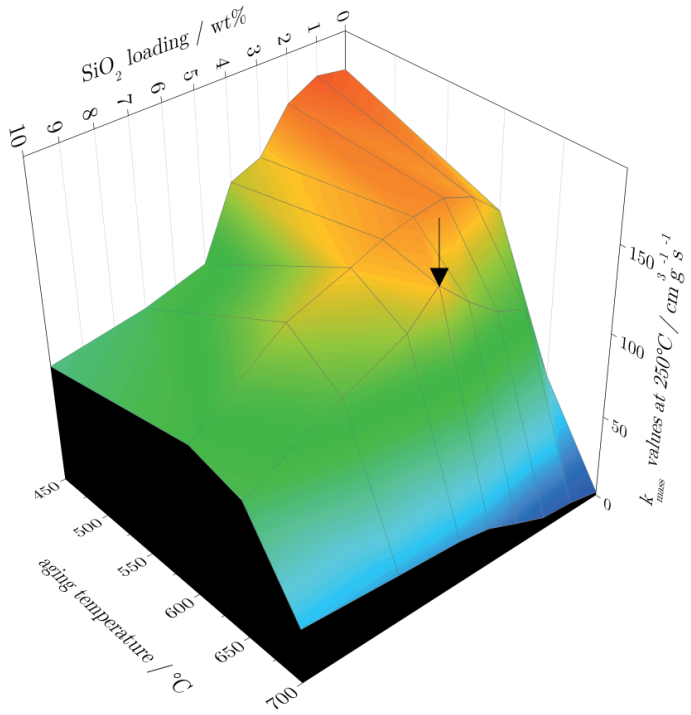

Figure 6-3. Mass specific reaction rate constants (k_{mass}) of SiVW-Ti for the maximum NO_x conversion at 250°C as a function of aging temperature and SiO_2 loading. The arrow indicates the catalyst with the highest k_{mass} obtained after aging at 650°C.

Based on the loading study using TMA-Si, three additional SiO_2 precursors (TEOS (4Si-TEOS-VWT), fumed silica (4Si-fumed-VWT) and colloidal silica (4Si-col-VWT)) were also tested at a fixed loading of 4 wt% SiO_2 (**Table 6-2**) in order to investigate the influence of the nuclearity of the silicon precursor on the activity and stability of the catalysts. While TEOS is a molecular silicon

precursor, the silicon nuclearity increases from TMA-Si to fumed silica and colloidal silica. SiO_2 in TMA-Si is mainly structured as cubic octamer nuclei, which can, however, slightly vary depending on the concentration and alkylammonia used [251-252]. The mean particle size of fumed silica and colloidal silica used in this work is ca. 7 nm and 20 nm, respectively [253].

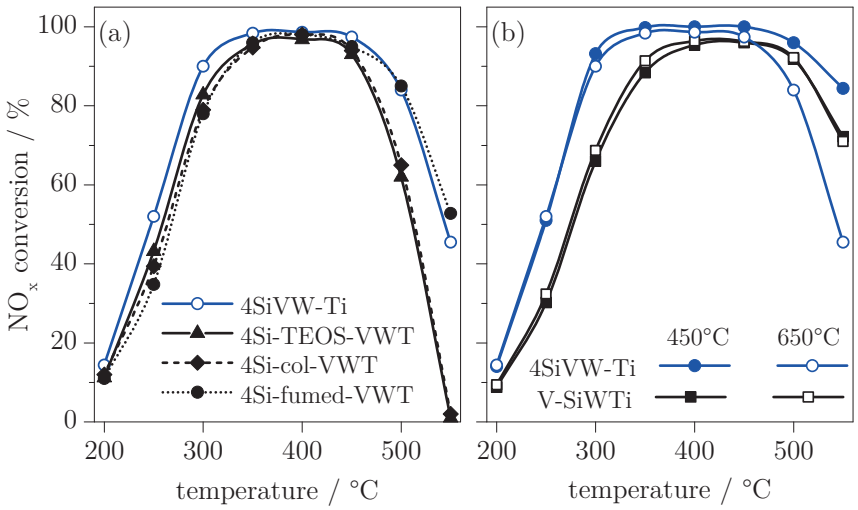

Figure 6-4. (a) NO_x conversion of co-impregnated Si stabilized catalyst with each 4 wt% SiO_2 after hydrothermal aging at 650°C for 16 h. (b) Performance comparison of the optimized 4SiVW-Ti (SiO_2 from TMA-Si) catalyst with the V-SiWTi (commercial Si-stabilized tungsta-titania support) in the fresh state and after hydrothermal aging at 650°C. All catalysts comprise 2 wt% V_2O_5 and 10 wt% WO_3.

Figure 6-4a shows that hydrothermal aging at 650°C affected all tested catalysts more significantly compared to that prepared from TMA-Si. There was no noticeable correlation between catalyst aging and nuclearity of the silicon precursors and the highest k_{mass} value was obtained with TMA-Si (4SiVW-Ti), followed by 4Si-TEOS-VWT, 4Si-fumed-VWT and 4Si-col-VWT (**Table 6-2**). Hence, the best SiO_2-stabilized catalyst was obtained from the TMA-Si precursor and with a loading of ca. 4 wt% SiO_2. **Figure 6-4b** compares the NO_x conversion of the optimized 4SiVW-Ti catalyst with that of a silica stabilized reference catalyst (V-SiWTi, support with 10% SiO_2, 9 wt% WO_3 and TiO_2, DT58 from Cristal Global) with identical vanadium loading. It is evident that 4SiVW-Ti is more active in the fresh state and, below 450°C, also after hydrothermal aging at 650°C. A co-impregnated catalyst using a commercial Si-

stabilized Ti support VW-SiTi (**Figure 6-5**, 10 wt% SiO_2, DT-S10 see **Table 1-1**) also exhibited a lower NO_x conversion and a lower k_{mass} value (**Table 6-2**) than 4SiVW-Ti. This was not the case after hydrothermal aging of 4SiVW-Ti at 700°C (**Figure 6-2**). Nevertheless, 4SiVW-Ti seems to be the best catalyst with respect to simultaneous low temperature activity and hydrothermal stability up to 650°C.

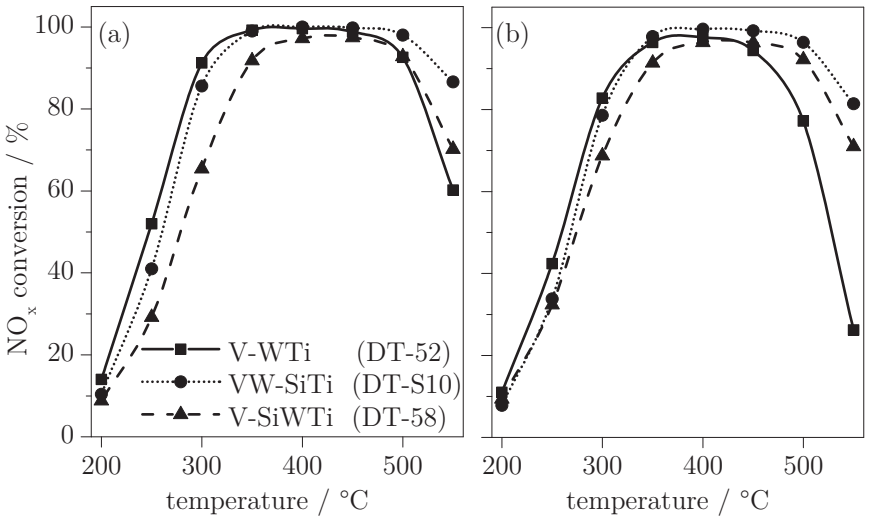

Figure 6-5. NO_x conversion of V-WTi (2 wt% V_2O_5 on DT-52), VW-SiTi (2 wt% V_2O_5, 10 wt% WO_3 on DT-S10, V-SiWTi (2 wt% V_2O_5 on DT-58) hydrothermally aged at (a) 600°C and (b) 650°C. See Table 1-1 for specifications of the support materials.

In the following section, the co-impregnated catalysts stabilized with TMA-Si, which showed improved hydrothermal stability, was characterized by means of powder XRD, BET, TEM, high-angle annular dark-field imaging TEM (HAADF-TEM) and ^{29}Si MAS NMR.

6.4 Physico-chemical characterization

6.4.1 XRD results

The XRD patterns of SiVW-Ti catalysts and TiO_2 after aging at 450, 600, 650 and 700°C are displayed in **Figure 6-6a** - **Figure 6-6d**, respectively. Up to an aging at 650°C, all catalysts exhibited the anatase phase but the peaks broadened with increasing SiO_2 loading due to smaller anatase crystallites. Low Si-loaded catalysts aged at 700°C also showed reflections of rutile. The median

size of the anatase crystallites after aging at 650°C was calculated by the Scherrer equation (**Table 6-2**). The anatase crystallite size of commercial TiO_2 after calcination at 450 and 650°C was ca. 20 and 30 nm, respectively (**Table 6-1**).

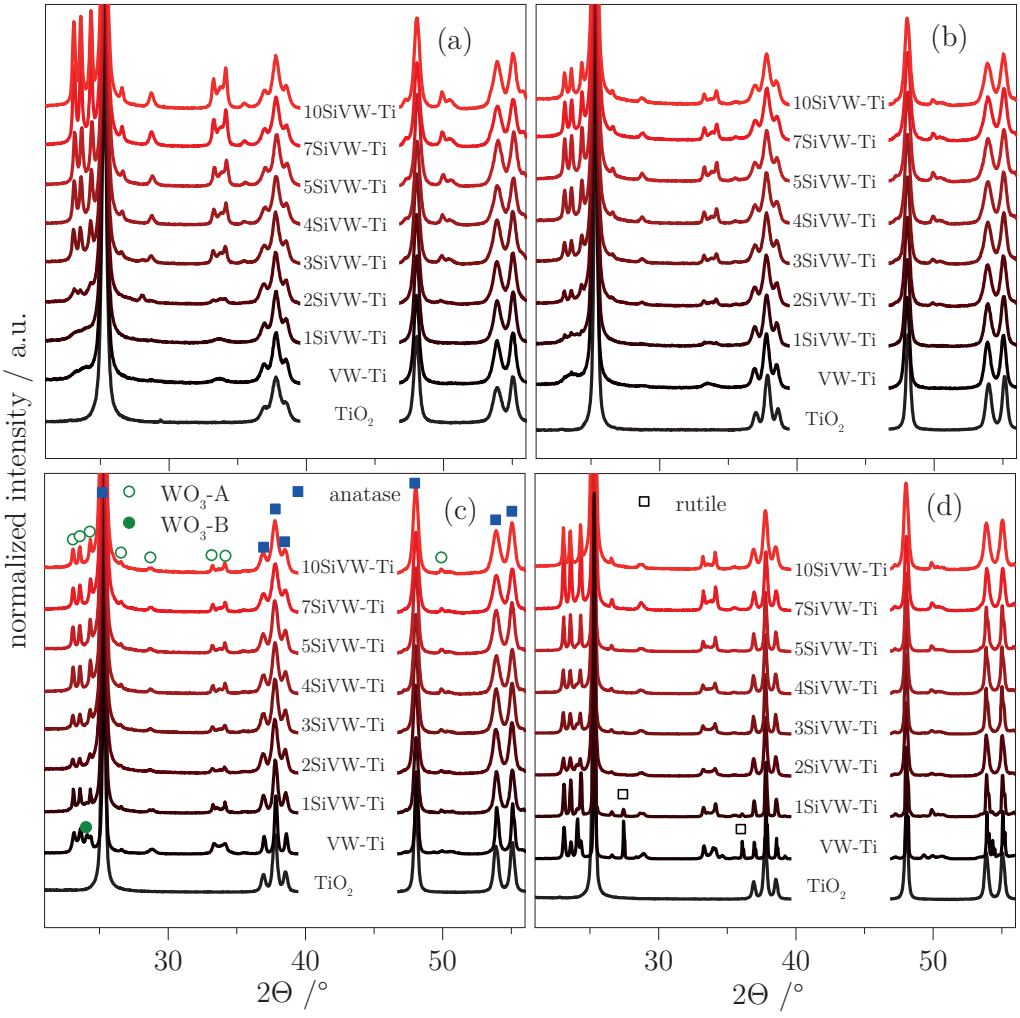

Figure 6-6. XRD patterns of TiO_2, VW-Ti and SiVW-Ti after aging at (a) 450°C, (b) 600°C, (c) 650°C and (d) 700°C.

After impregnation of 10 wt% WO_3 on TiO_2 (W-Ti), the crystallite size remained identical in the fresh state but was only ca. 25 nm after aging at 650°C. Therefore, WO_3 assisted the retardation of the sintering of the anatase phase [90-92]. By co-impregnating V and W (VW-Ti), the TiO_2 particle size grew to ca. 44 nm after aging at 650°C, confirming the promoting effect of V

towards anatase particle growth as shown in Chapter 3 and Chapter 4. Already 1 wt% SiO_2 could hinder particle growth to some extent (ca. 29 nm for 1SiVW-Ti). SiO_2 loadings of 2 to 5 wt% resulted in crystallite sizes of around 24 nm, which decreased to ca. 22 nm by increasing the SiO_2 loading to 7 and 10 wt%. SiO_2 in SiVW-Ti with loadings of 7 - 10 wt% is thus capable of preserving the crystallite size of TiO_2 after calcination at 450°C. Summarizing, a correlation between TiO_2 particle size and SiO_2 loading upon aging could be confirmed [105, 107].

Table 6-1. Calculated anatase TiO_2 crystallite sizes from XRD peak at 25.4° of TiO_2 (DT-51-D), W-Ti (10 wt% WO_3 on TiO_2) and WTi (DT-52) after calcination at 450 and 650°C. See Table 1-1 for specifications of the support materials.

Calc. temp.	450°C [nm]	650°C [nm]
TiO_2	20.3	30.0
W-Ti	20.5	24.3
WTi	16.4	24.8

No reflection was found at all SiO_2 loadings that could be attributed to SiO_2 or V_2O_5 crystallites, suggesting that VO_x and SiO_2 remained dispersed/amorphous or formed crystallites below the XRD detection limit. Besides TiO_2, clear WO_3 reflections were observed. The region at 23 - 24° comprehending the WO_3 reflections is enlarged in **Figure 6-7** for all catalysts and aging temperatures.

From **Figure 6-7a** it is obvious that the addition of SiO_2 promotes the formation of crystalline WO_3 after calcination at 450°C. The WO_3 peaks already became visible with 2 wt% SiO_2 and were attributed to a monoclinic crystal structure with $P2_1/n$ space group [254]. By increasing the SiO_2 loading, this WO_3 phase became more prominent. After aging at 600 and 650°C (**Figure 6-7b** and **Figure 6-7c**, respectively), these reflections lost intensity with increasing SiO_2 contents. This suggests that crystalline WO_3 in e.g. 10SiVW-Ti calcined at 450°C partly decomposes with increasing aging temperature. Due to the increased surface diffusion, it is plausible that SiO_2 and WO_3 compete for anchoring positions on TiO_2. Because WO_3 is favored due to its higher acid strength [255-256], WO_3 crystallites partly decompose with increasing aging

temperature. For low loaded SiO_2 catalysts, no WO_3 was detected in the fresh state, however, the WO_3 reflections appeared with increasing aging temperature. The WO_3 crystallite formation of these catalysts is therefore dependent on the aging temperature. Because the WO_3 formation/decomposition upon aging is also influenced by the SiO_2 loading, an intermediate SiO_2 loading of 3 - 5 wt% results in WO_3 reflections that are similar at all aging temperatures.

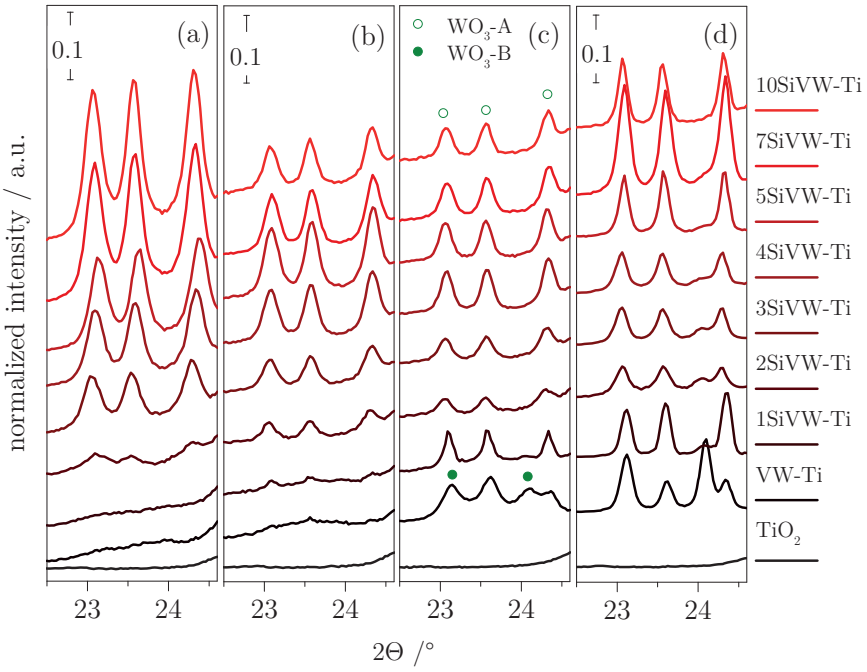

Figure 6-7. XRD patterns of the 2Θ region between 22.5 and 24.6° of TiO_2 , VW-Ti and SiVW-Ti catalysts after aging at (a) 450°C, (b) 600°C, (c) 650°C and (d) 700°C. The full XRD patterns of a-d are shown in Figure 6-6.

It should be noted that VW-Ti and 1SiVW-Ti aged at 650°C displayed an additional WO_3 reflection at 23.1 and 24.1° from a different WO_3 phase (WO_3-B, **Figure 6-7b**). This phase was tentatively assigned to a monoclinic crystal structure with Pc space group [254]. This phase became more prominent at 700°C (**Figure 6-7d**), where a clear SiO_2 loading dependence was observed: VW-Ti exhibited a major fraction of the WO_3-B phase, which decreased with increasing SiO_2 content and was no longer detectable in 7SiVW-Ti and 10SiVW-Ti.

The XRD data reveals that SiO_2 hinders the dispersion of WO_3 on the TiO_2 surface and consequently promotes the formation of crystalline WO_3 for SiVW-

Ti catalysts. On the contrary, SiO_2 does not interact with vanadium species [111]. The observation that WO_3 crystallite formation depends on SiO_2 loading can be explained with the fractional surface coverages of VO_x, WO_x and SiO_x (**Figure 6-8a** - **Figure 6-8c**), which were calculated according to eq. (2-6) using the BET surface area and the theoretical saturation values for the monolayer coverage, i.e. 7.9 VO_x nm^{-2}, 4.2 WO_x nm^{-2} and 10.5 SiO_x nm^{-2} [102, 135, 257].

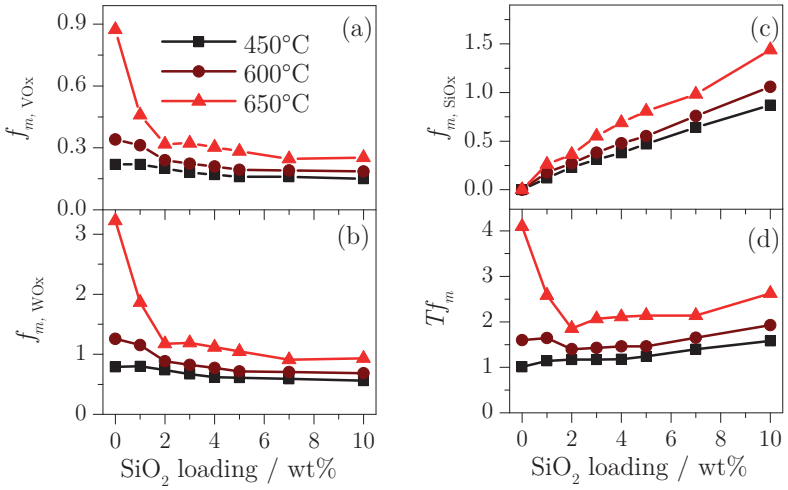

Figure 6-8. Calculated fractional monolayer coverage ($f_{m,o}$) from eq. (2-6) of (a) VO_x, (b) WO_x, (c) SiO_x and (d) total fractional monolayer coverage (Tf_m) from eq. (2-7) of VW-Ti and SiVW-Ti catalysts after calcination at 450, 600 and 650°C.

For VW-Ti, a fractional monolayer coverage of 0.22 VO_x and 0.79 WO_x was obtained in the fresh state, which yields a total fractional monolayer of ca. one (Tf_m, eq. (2-7)). Tf_m exceeded the monolayer value already for a loading of ca. 3 - 4 wt% SiO_2 (ca. 1.2, **Figure 6-8d**) in the fresh catalysts, which most likely accounted for the formation of the crystalline WO_3 units observed by XRD (**Figure 6-7a**). Tf_m was ca. 1.6 for 10SiVW-Ti, thus the formation of WO_3 crystallites was facilitated to a greater extend due to blocking SiO_x units on TiO_2 interaction sites. Because of the multiple total monolayer fractions at all loadings (Tf_m = 2 - 4), the presence of WO_3 crystallites was less dependent on the SiO_2 content (**Figure 6-7c**) after aging at 650°C. The catalysts with low SiO_2 content started sintering severely at this temperature, which was reflected by the decrease of the BET surface area (**Table 6-2**) and Tf_m above 2.5. It is

likely that sintering induced the formation of the second WO_3 phase, which was mainly observed for VW-Ti and 1SiVW-Ti.

Table 6-2. BET surface area, TiO_2 XRD crystallite size, reaction rate constant k_{mass} measured at 250°C, calculated fractional V surface coverage ($f_{m,VOx}$) of Si-stabilized VWT catalysts with different SiO_2 loadings and precursors after aging at 650°C. All catalysts comprise 2 wt% V_2O_5 and 10 wt% WO_3.

			After aging at 650°C			
Name	Si-pr.[a]	SiO_2 [wt%]	BET [m^2g^{-1}]	XRD [nm]	k_{mass} [$cm^3g^{-1}s^{-1}$]	$f_{m,VOx}$[b]
VW-Ti	-	0	19	44.6 ± 0.3	54	0.88
1SiVW-Ti	TMA-Si	1	37	28.9 ± 0.6	104	0.45
2SiVW-Ti	TMA-Si	2	52	24.3 ± 0.3	111	0.32
3SiVW-Ti	TMA-Si	3	52	24.8 ± 0.0	126	0.32
4SiVW-Ti	TMA-Si	4	55	23.6 ± 0.1	143	0.30
5SiVW-Ti	TMA-Si	5	59	24.0 ± 0.2	126	0.28
7SiVW-Ti	TMA-Si	7	68	22.5 ± 0.8	109	0.25
10SiVW-Ti	TMA-Si	10	66	21.3 ± 0.1	83	0.25
4Si-TEOS-VWT	TEOS	4	37	30.5 ± 0.9	115	0.45
4Si-col-VWT	Coll. silica	4	33	34.8 ± 0.4	102	0.51
4Si-fumed-VWT	Fumed silica	4	50	26.9 ± 0.5	84	0.34
10Si-fumed-VWT	Fumed silica	10	65	25.0 ± 0.5	75	0.26
V-WTi[c]	-	0	35	32.8 ± 0.3	118	0.48
VW-SiTi[c]	-	10	78	15.3 ± 0.5	84	0.21
V-SiWTi[c]	-	10	90	14.5 ± 0.6	82	0.19
Support TiO_2	-	-		30.0 ± 0.3	-	-
Support W-Ti	-	-		24.8 ± 0.8	-	-

[a]Si-precursors: TMA-Si (tetramethyl ammonium silicate, 17 wt% SiO_2, Sigma Aldrich), TEOS (Tetraethyl ortho silicate, Sigma Aldrich), colloidal silica (Ludox AS30, Sigma Aldrich), fumed SiO_2 (silica, 7 nm, Sigma Aldrich). [b]calculated according to eq. 2-6 [c]Commercial supports according to Table 1-1.

It should be mentioned that it is difficult to find a correlation between the WO_3 crystallite formation and the corresponding activity/stability of the catalysts. 2SiVW-Ti, 3SiVW-Ti and 10SiVW-Ti revealed lower WO_3 diffraction intensities than 4SiVW-Ti (**Figure 6-7c**) but their k_{mass} values (**Table 6-2**)

were lower than that of 4SiVW-Ti after aging at 650°C. Also, catalysts with the identical composition and activity after aging at 600°C, i.e. V-WTi and VW-Ti (**Figure 6-1b**), exhibited very different XRD reflections of WO_3 (**Figure 6-9** and **Figure 6-6b**, respectively).

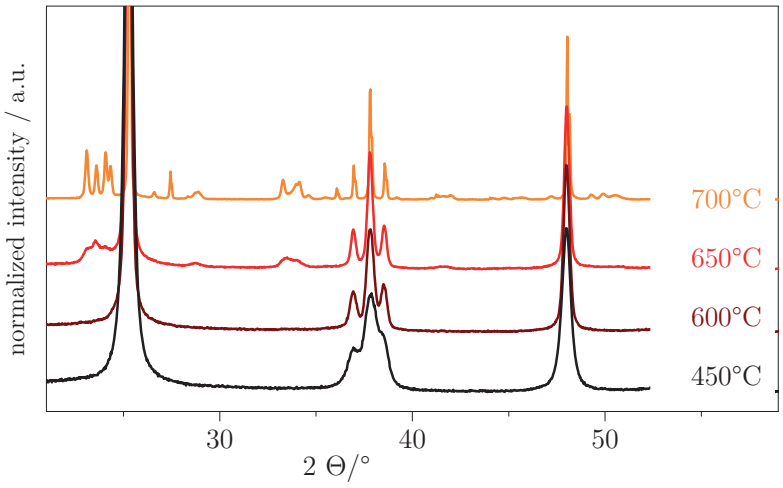

Figure 6-9. XRD patterns of V-WTi calcined at the indicated temperatures.

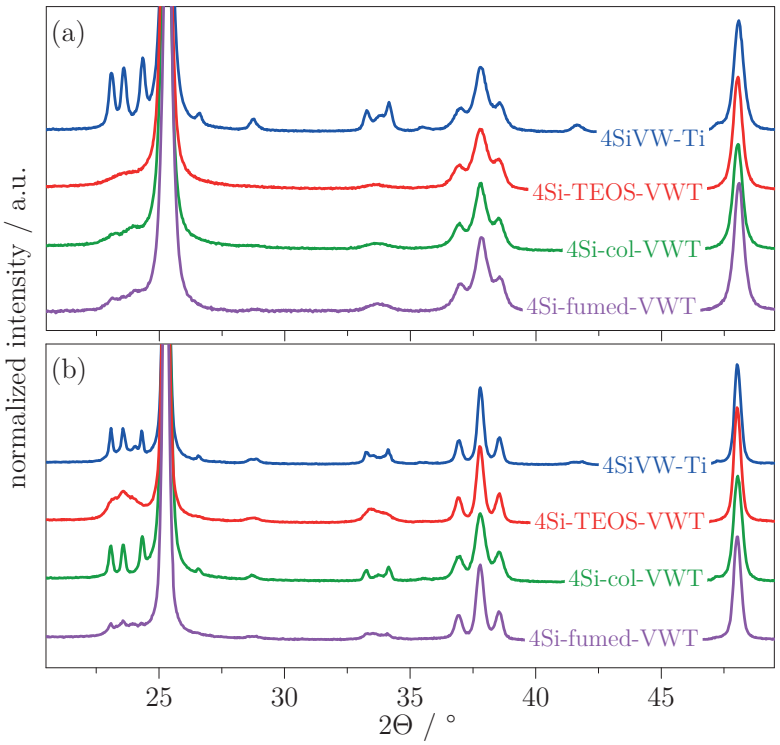

Figure 6-10. XRD diffractograms of 4SiVW-Ti, 4Si-TEOS-VWT, 4Si-col-VWT and 4Si-fumed-VWT (specification of precursors see Table 6-2) after aging at (a) 450°C and (b) 650°C.

The comparison of the different SiO_2 precursors at fixed loading (4 wt% SiO_2, **Figure 6-10**) revealed that crystalline WO_3 was formed in all samples. In the fresh state, the largest amount of crystalline WO_3 was detected in 4SiVW-Ti, while it was only poorly visible for other catalysts. After aging at 650°C (**Figure 6-10b**), 4Si-fumed-VWT and 4Si-TEOS-VWT showed smaller WO_3 reflections than 4SiVW-Ti and 4Si-col-VWT. Similar to the SiO_2 loading study, no obvious correlation between the stability of the catalyst and the formation of WO_3 could be found. In order to address the origin of the stabilization effect by SiO_2 in SiVW-Ti more specifically, the optimized catalyst 4SiVW-Ti was further characterized by electron microscopy and NMR.

6.4.2 TEM/STEM

Figure 6-11 displays the transmission electron microscope images of VW-Ti and 4SiVW-Ti after aging at 600 and 650°C. In all images, TiO_2 particles are visible, which mainly differ in size depending on the catalyst and the aging temperature. Similar particle sizes of VW-Ti (**Figure 6-11a**) and 4SiVW-Ti (**Figure 6-11c**) after aging at 600°C are evident from TEM. In contrast, the TEM images of the same catalysts after aging at 650°C (**Figure 6-11b** and **Figure 6-11d**, respectively) showed a clear difference. The TiO_2 particles grew to a larger extent for VW-Ti than for 4SiVW-Ti, which was also evident from the exponential growth of TiO_2 crystallites for VW-Ti observed by XRD (**Table 6-2**). A further observation from the TEM data is that the addition of TMA-Si created regions of amorphous SiO_2 (**Figure 6-11d**). The formation of amorphous SiO_2 possibly reduced the contact between anatase particles, which is a possible explanation for the stabilizing effect of SiO_2 at elevated temperatures [258]. Since TMA-Si is not a molecular SiO_2 precursor [251, 259], it is likely that large SiO_2 agglomerates can be formed once supported on TiO_2 and that they serve as spacer between the TiO_2 particles thus preventing their coalescence.

HAADF-STEM images and the corresponding elemental mappings from EDX spectroscopy of 4SiVW-Ti after aging at 650°C are shown in **Figure 6-12**.

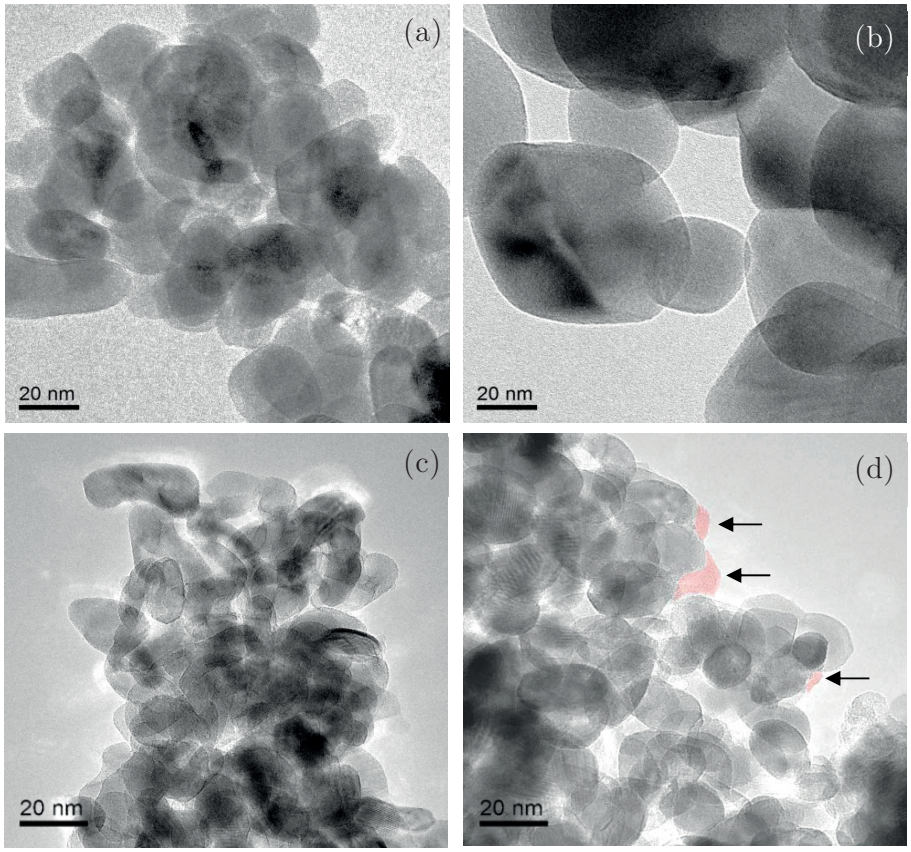

Figure 6-11. TEM images of VW-Ti (no SiO_2) calcined at (a) 600°C and (b) 650°C and 4SiVW-Ti (4 wt% SiO_2) calcined at (c) 600°C and (d) 650°C. The red colored area next to the arrows in (d) indicates the presence of amorphous SiO_2 particles.

The elemental mapping revealed that the particles displayed in the HAADF image in **Figure 6-12a** mainly consist of Ti (**Figure 6-12b**), have uniformly distributed W (**Figure 6-12c**) but inhomogeneously dispersed Si (**Figure 6-12d**). Vanadium could not be detected due to its overall low concentration and because the main V peak overlaps with the second line of Ti in the EDX spectrum. The extended SiO_2 agglomerates cannot be solely responsible for the suppression of the TiO_2 sintering because of their limited dispersion. To that end, the fractional monolayer coverage of SiO_2 in SiVW-Ti catalyst with a loading up to 4 wt% SiO_2 was below 0.7 (**Figure 6-8**), making it even more unlikely to suppress the contact between all TiO_2 particles. By close inspection of the elemental map in **Figure 6-12d** it is evident that beside large SiO_2 agglomerates, Si is dispersed over the whole region of TiO_2. Similar to W, Si covered all TiO_2 particles but with a higher degree of inhomogeneity. This sug-

gests that finely dispersed Si units are also partly responsible for the delay in TiO_2 particle sintering at elevated aging temperatures. It may explain why already 1 - 2 wt% SiO_2 had a major effect on the inhibition of the TiO_2 particle growth after aging at 650°C (**Table 6-2**).

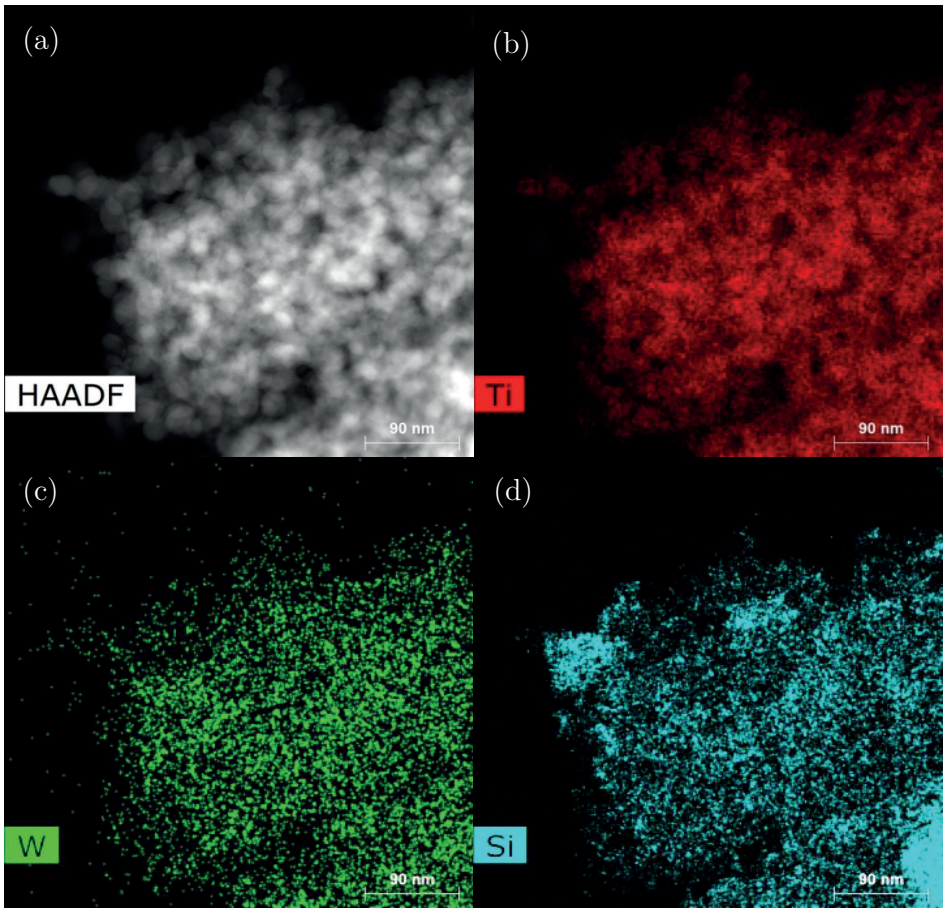

Figure 6-12. (a) HAADF-STEM image of 4SiVW-Ti calcined at 650°C and the corresponding elemental mapping of (b) Ti, (c) W and (d) Si.

6.4.3 ^{29}Si MAS NMR

In order to investigate the nature of the silicate at a molecular level, ^{29}Si MAS NMR was applied to selected SiVW-Ti catalysts, namely 4SiVW-Ti and 10SiVW-Ti (**Figure 6-13**). The local structure of the tetrahedral SiO_2 units (Q^n, n is the number of Si-O-Si bonds) could be followed because the chemical shift is highly sensitive to the local environment [250].

Figure 6-13a shows the ^{29}Si MAS NMR of 10SiVW-Ti calcined at 450, 600 and 650°C, respectively. In the fresh state, ca. 65% of SiO_2 was associated with the presence of three dimensional silicates (Q^4), while layered/surface (Q^3) and chain silicate (Q^2) accounted for 25% and 10%, respectively. No isolated or dimeric silicates were found, which is reasonable because the SiO_2 loading was responsible for ca. 80% of full monolayer coverage (**Figure 6-8**). Considering the structure of TMA-Si that consists of small polymeric clusters (i.e. cubic octamer nuclei, dependent on solvent and concentration [251-252, 259]), monomeric and dimeric Si units are unlikely to be formed. An increase of the aging temperature to 600 and 650°C resulted in increased Q^4 species and decreased Q^3 and Q^2 contributions. The increase of Q^4 species originates from the condensation of Si-OH groups to Si-O-Si bonds thus suggesting the formation of an extended network, which may coincide with the observation of the SiO_2 agglomerates in TEM.

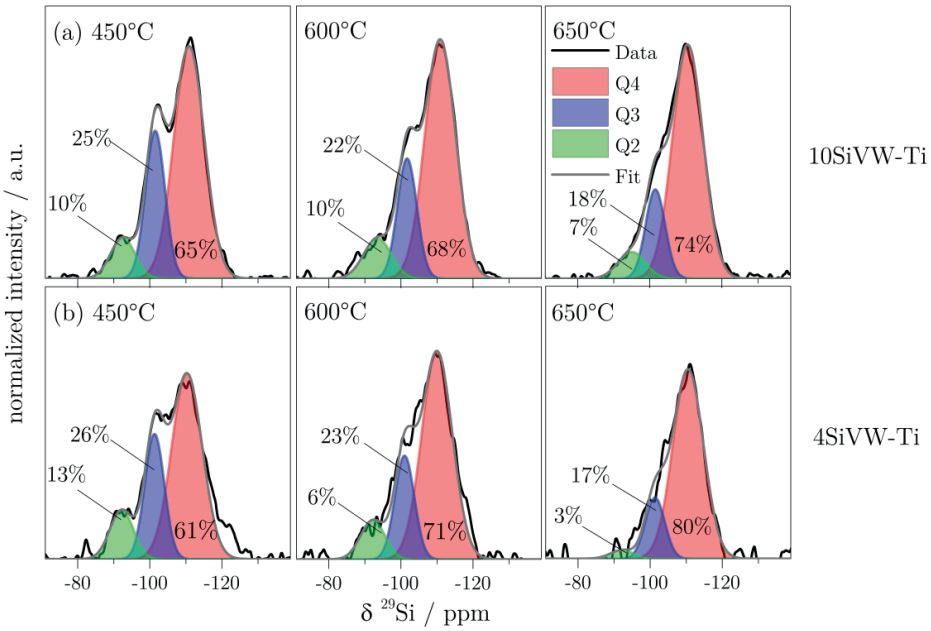

Figure 6-13. ^{29}Si MAS NMR of (a) 10SiVW-Ti and (b) 4 SiVW-Ti calcined at 450, 600 and 650°C, respectively.

The same behavior was observed for 4SiVW-Ti (**Figure 6-13b**) with increasing aging temperature but due to the overall lower SiO_2 concentration, the signal-to-noise ratio of the spectra was lower than in the 10SiVW-Ti sample. The deconvolution revealed that the Q^3 and Q^2 silicate fractions in the fresh state

were slightly larger compared to 10Si-VWT, suggesting that the amorphous silicate particles were more dispersed, possibly due to their lower SiO_2 content [259]. It is plausible that Q^3 and Q^2, accounting for ca. 30 - 40% of the SiO_2 units, play an important role in the stabilization of Si-VWT catalysts. The combination of STEM and ^{29}Si NMR results suggests that small and dispersed SiO_2 units play a role in hindering the TiO_2 particle sintering. It is clear that overall understanding of the Si stabilization effect could be improved with a different combination and other methods and more work is needed to fully disentangle its impact.

6.5 Conclusions

This chapter showed that a VWT catalyst synthesized via co-impregnation exhibited an improved low temperature activity to an analogous catalyst obtained by impregnation of V on a commercial tungsta-titania support (see Chapter 3 and 4). Because the hydrothermal stability of the co-impregnated sample was however poor, its stability was increased by co-impregnating TiO_2 with precursors of V, W and varying amounts of Si, a known stabilizing agent of SCR catalysts. With the right choice of the SiO_2 precursor, the co-impregnated catalyst endured aging up to 650°C and remained highly active between 250°C and 500°C. This is of particular importance because it contributes to overcome the unfavorable trade-off between low temperature activity and high temperature stability of V-based SCR catalysts. Because of the systematic SiO_2 loading study, it could be shown that the addition of 2 - 4 wt % SiO_2 was sufficient to stabilize the catalyst where a full surface coverage was reached. The physico-chemical characterization revealed that SiO_2 promoted the agglomeration of WO_3 owing to the excess of the total surface coverage. Moreover, the silicates formed an amorphous phase that prevented most likely the TiO_2 particles from sintering, which is the main driving force for aging. SiO_2 was present as large and smaller polymeric SiO_2 entities, both contributing to inhibit the inter-particle contact of the anatase TiO_2 crystallites by modification of the surface of the support in the form of localized agglomerates and of small well dispersed domains.

Chapter 7

Introducing metal vanadate-based SCR catalysts

7.1 Introduction

In the previous Chapter 6 was shown that SiO_2 is a valuable candidate for introducing stability to a V-based VWT catalyst. Using a co-impregnation method, the Si-stabilized VWT catalysts were more low-temperature active compared to reference catalysts using a Si-stabilized support material. The applied preparation method, however, also showed limitation because the catalysts heavily deactivated at aging temperature above 650°C. On the contrary, V-based reference catalysts using Si-stabilized support material were stable up to 700°C but were lacking low temperature activity. This is of importance because mobile SCR applications demand more efficient catalysts which fulfil new and different requirements (see section 1.6). The SCR catalyst has to operate under dynamic conditions and has to work properly in extreme cases, such as low temperature due to cold starts or short city driving. It can also be exposed to high temperature (> 650°C) due to the coupled particulate filter which is often located upstream of the SCR catalyst that undergoes periodical regeneration. Therefore, future catalysts will have to exhibit both high N_2 selectivity and high-temperature stability over a broader operation temperature window [8, 64, 167-168].

Chapters 3, 4 and 6 have shown that it is difficult to generate catalyst which are highly active and withstand temperatures above 650°C. As described in

This chapter is based on the postprint version of the publication: A. Marberger, M. Elsener, D. Ferri, A. Sagar, K. Schermanz, O. Kröcher, Generation of NH_3 Selective Catalytic Reduction Active Catalysts from Decomposition of Supported $FeVO_4$, *ACS Catal.* **2015**, 4180-4188. A. Marberger performed the experiments, analyzed and interpreted the data together with the co-authors and wrote the manuscript.

section 1.5, a potential solution was presented by Casanova et al. by using a Si-stabilized support (SiWTi) and metal vanadate as the SCR active redox center [169]. More recent studies show that various metal vanadates ($MeVO_4$), such as $FeVO_4$, $ErVO_4$ or $TbVO_4$ demonstrate promising NH_3-SCR activity when supported on SiWTi [170, 178, 182]. The higher melting point of e.g. $FeVO_4$ (ca. 850°C) compared to V_2O_5 (ca. 690°C) makes them attractive as high temperature stable SCR catalysts [168, 173]. It is reported that metal vanadates and mixtures thereof such as $Fe_xEr_{1-x}VO_4$ ($0 \leq x \leq 1$) supported on SiWTi, exhibit excellent temperature stability and good SCR activity [167, 182, 260]. The origin of the temperature stability was interpreted as a result of the lack of free vanadia species on the surface of the catalyst, which is responsible for the undesired anatase to rutile phase transformation above 700°C. Liu et al. [168] investigated $FeVO_4$ deposited by co-impregnation from $Fe(NO_3)_3$ and NH_4VO_3 on TiO_2. The catalyst with 9 wt% $FeVO_4/TiO_2$ showed an excellent NO_x conversion for calcination temperatures below 600°C. Above this temperature, a severe NH_3-SCR activity loss was observed. The deactivation was correlated to the phase transformation of TiO_2, leading to a loss of surface area. The $FeVO_4$ phase was identified by extended X-ray absorption fine structure (EXAFS) and was stable up to 800°C.

In this chapter, metal vanadates of the type $Fe_xAl_{1-x}VO_4$ ($0 \leq x \leq 1$, $MeVO_4$) were investigated as potential SCR catalysts after loading on SiWTi. The composition of the catalysts was varied upon addition of an Al source since not only $FeVO_4$ but also Al exhibits a promising effect on temperature stability [261]. Upon optimization of composition and loading, the catalyst showed an enhanced performance compared to a reference V_2O_5/SiWTi but only after calcination at elevated temperature. A range of characterization techniques was used to provide an interpretation of the nature of the activation.

7.2 Experimental section

The general preparation of V-based catalysts is described in detail in the section 2.1. For this investigation, a commercial $SiO_2/WO_3/TiO_2$ (SiWTi, **Table 1-1**) was used as support material. The vanadium was introduced with either ammonium vanadate (NH_4VO_3, Sigma Aldrich) for the reference materi-

al or with $Fe_xAl_{1-x}VO_4$ ($0 \leq x \leq 1$, Treibacher Industrie AG). For the loading studies, 3 - 8 wt% $Fe_{0.8}Al_{0.2}VO_4$ supported on SiWTi was used. In order to compare the various $MeVO_4$, various catalysts were prepared with 4.4 wt% $FeVO_4$, 4.2 wt% $Fe_{0.8}Al_{0.2}VO_4$, 3.9 wt% $Fe_{0.5}Al_{0.5}VO_4$ and 3.5 wt% $AlVO_4$ on SiWTi. This corresponds to the same molar amount of vanadium used in the reference material V-SiWTi with ca. 2.3 wt% V_2O_5 which was prepared by wet impregnation of NH_4VO_3 on SiWTi and calcined at the same temperatures as the vanadate samples [75]. The coated monoliths and the remaining slurry were dried overnight (120°C) and calcined at 650°C for 10 h.

7.3 Results and discussion

7.3.1 Loading dependent catalytic activity

The catalytic activity of the fresh and hydrothermally aged catalysts is reported in **Figure 7-1a-c** and in **Figure 7-1d-f**, respectively.

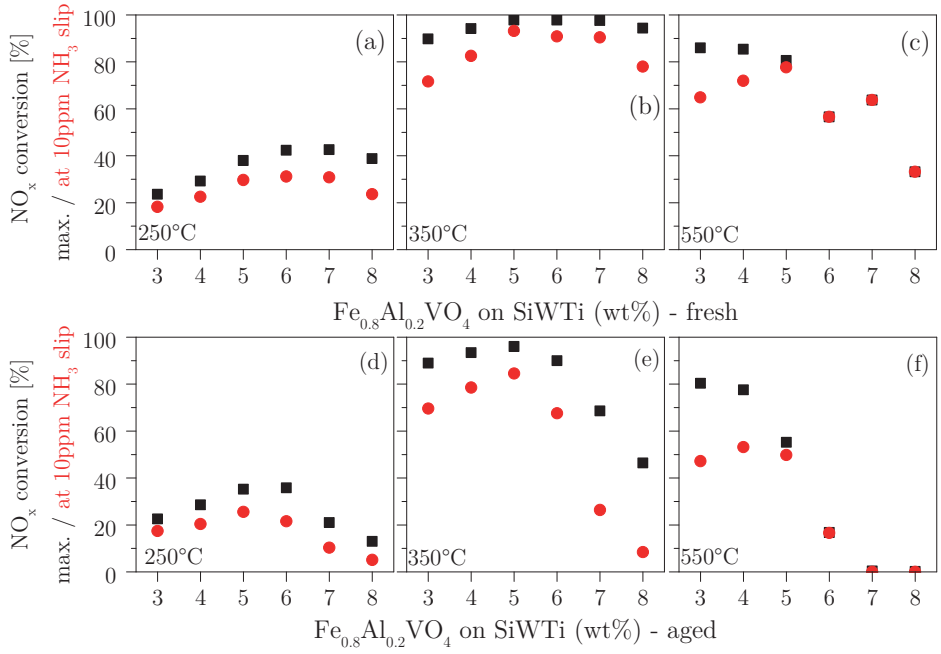

Figure 7-1. NO_x conversion of 3 - 8 wt% $Fe_{0.8}Al_{0.2}VO_4$/SiWTi at 250, 350 and 550°C a-c) in the fresh state (calcined at 650°C for 10 h) and d-f) in the aged state (hydrothermal aging at 700°C for 16 h). Black squares: Maximum NO_x conversion with $NH_3/NO = 1.2$. Red circles: NO_x conversion at 10 ppm NH_3 slip.

Figure 7-1a shows that at 250°C, the NO_x conversion reached a maximum for 6 wt% $Fe_{0.8}Al_{0.2}VO_4$/SiWTi whereas at 550°C the maximum was observed for a

loading of 4 wt% $Fe_{0.8}Al_{0.2}VO_4$ (**Figure 7-1c**). For the intermediate temperature (350°C), the optimal loading was observed with 5 wt% $Fe_{0.8}Al_{0.2}VO_4$. The aged samples exhibited the same behavior at 250 and 350°C whereas the catalysts with higher $Fe_{0.8}Al_{0.2}VO_4$ loading than 5 wt% deactivated at 550°C (**Figure 7-1f**). The optimal loading of 4 - 5 wt% metal vanadate determined from the data of **Figure 7-1** corresponds to a V_2O_5 content of 2.2 - 2.5 wt%. A similar behavior was already described in Chapter 3 and in earlier studies for V_2O_5/WTi, where an optimal V loading was observed between 2.0 - 2.6 wt% V_2O_5 [46, 75]. Therefore, the reference material chosen for this study is 2.3 wt% V_2O_5/TiO_2-WO_3-SiO_2 (V-SiWTi). While a low V loading is beneficial for the temperature stability of the catalyst, a higher V loading is advantageous for the activity in the low temperature regime [75]. Hence, a $Fe_{0.8}Al_{0.2}VO_4$ content of 4 - 5 wt% is a good compromise between low temperature activity and high temperature stability. The SCR activity of the reference material V-SiWTi shown in **Figure 7-2** is comparable with that of 4 - 5 wt% $Fe_{0.8}Al_{0.2}VO_4$/SiWTi. Despite some deactivation at 550°C after aging at 700°C, it can be concluded that the optimal $Fe_{0.8}Al_{0.2}VO_4$ loading is 4 - 5 wt%. The practice-oriented NO_x conversion at 10 ppm NH_3 slip also shows a maximum at 4 - 5 wt% $Fe_{0.8}Al_{0.2}VO_4$ (**Figure 7-1**). This loading is lower compared to the values reported in recent work on supported $FeVO_4$ as SCR catalysts [168, 170, 182].

7.3.2 Composition dependent catalytic activity

In order to investigate the influence of Al in $Fe_xAl_{1-x}VO_4$ on the catalytic activity, four different metal vanadates, namely $FeVO_4$, $Fe_{0.8}Al_{0.2}VO_4$, $Fe_{0.5}Al_{0.5}VO_4$ and $AlVO_4$ were loaded on SiWTi. Based on the considerations above, the vanadate loading was calculated based on one equivalent of V_2O_5 in V-SiWTi (2.3 wt%).

The catalytic activity of the different vanadates is compared in **Figure 7-2a** - **Figure 7-2c** and in **Figure 7-2d** - **Figure 7-2f** for the fresh and the aged monoliths, respectively. In case of the fresh catalysts, the maximum NO_x conversion at 250°C (42%, **Figure 7-2a**) and 550°C (85%, **Figure 7-2c**) was found for $FeVO_4$/SiWTi, whereas at 350°C (**Figure 7-2b**) $Fe_{0.8}Al_{0.2}VO_4$/SiWTi

was the most active catalyst (98%). Both $FeVO_4$/SiWTi and $Fe_{0.8}Al_{0.2}VO_4$/SiWTi exhibited a comparable activity to the V-SiWTi reference. The NO_x conversion at 10 ppm NH_3 slip dropped significantly for $Fe_{0.5}Al_{0.5}VO_4$/SiWTi and $AlVO_4$ at 350 and 550°C.

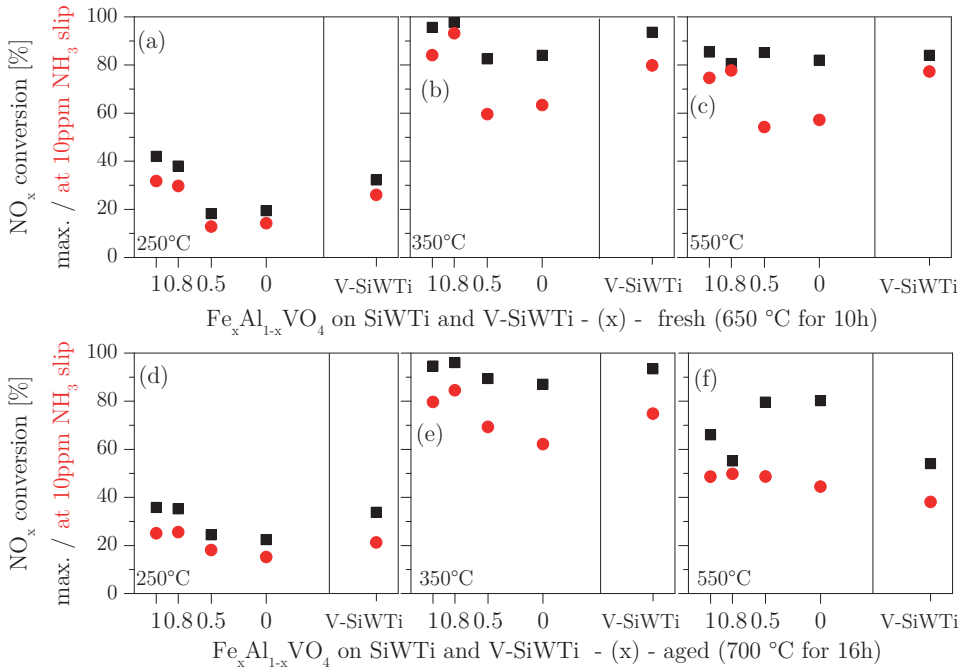

Figure 7-2. NO_x conversion of $MeVO_4$/SiWTi (= 2.3 wt% V_2O_5) at 250, 350 and 550°C a-c) in the fresh state (calcined at 650°C for 10 h) and d-f) in the aged state (hydrothermal aging at 700°C for 16 h). Black squares: Maximum NO_x conversion with NH_3/NO = 1.2. Red circles: NO_x conversion at 10 ppm NH_3 slip. V loading of V-SiWTi = 2.3 wt% V_2O_5.

The high temperature stability was tested by hydrothermally aging the catalysts at 700°C for 16 h. The aging did not influence substantially the catalyst performance at 250 and 350°C (**Figure 7-2d** and **Figure 7-2e**). At 550°C (**Figure 7-2f**), however, aging caused deactivation of $FeVO_4$/SiWTi, $Fe_{0.8}Al_{0.2}VO_4$/SiWTi and V-SiWTi with maximum NO_x conversion of 66%, 55% and 53%, respectively. $FeVO_4$/SiWTi and $Fe_{0.8}Al_{0.2}VO_4$/SiWTi behaved very similar with the exception of the high temperature, where the $FeVO_4$/SiWTi performed slightly better and appeared more stable against high temperature aging.

By comparing the catalysts with the NO_x conversion at 10 ppm NH_3 slip, it is obvious that high Al/Fe ratio ($x \geq 0.5$) is detrimental for the performance at all temperatures in the fresh and aged states. Furthermore, the NO_x conversion at 10 ppm NH_3 slip is always lower for catalysts with high Al content, confirming that Al in $Fe_xAl_{1-x}VO_4$ does not favor NH_3 adsorption.

The results of the loading and composition experiments indicate that for 4 - 5 wt% $FeVO_4$/SiWTi and $Fe_{0.8}Al_{0.2}VO_4$/SiWTi, an optimal compromise is found between low temperature activity and high temperature stability. It must be noted that the performance is enhanced compared to the reference V-SiWTi material for all temperatures in the fresh and aged states (**Figure 7-2a** - **Figure 7-2f**). The largest NO_x conversion difference was found for the aged state of $FeVO_4$ and V-SiWTi at 550°C with 66% and 54%, respectively. Because of the high activity of the Al-free catalyst and the apparent negative effect of Al on the activity of supported $MeVO_4$, $FeVO_4$/SiWTi with 4.5 wt% $FeVO_4$ was selected for a detailed characterization.

7.3.3 Calcination dependent catalytic activity

The calcination study was performed on the catalyst optimized from composition and loading experiments. Therefore, 4.5 wt% $FeVO_4$/SiWTi was washcoated on four identical monoliths and calcined in air at 550°C (4.5FeV-SiWTi-550), 600°C (4.5FeV-SiWTi-600), 650°C (4.5FeV-SiWTi-650) and 700°C (4.5FeV-SiWTi-700) for 10 h. The catalytic activity of these catalysts is shown in **Figure 7-3**. V-SiWTi was treated under identical conditions (**Figure 7-4**). It is evident, that activation occurs for calcination temperature higher than 550°C (**Figure 7-3**). After calcination at 600°C, the NO_x conversion is equal to that of V-SiWTi, whereas 4.5 wt% $FeVO_4$/SiWTi was superior to V-SiWTi at 650°C. The activation through calcination is noticeable since V-based catalysts supported on SiWTi are generally activated at lower temperature (about 400 - 600°C) and do not improve at higher temperature [64, 102]. For the reference material V-SiWTi, the different calcination temperatures (550 - 700°C) did not affect the overall performance (**Figure 7-4**). For the sake of comparison, **Figure 7-3a** shows the NO_x conversion of V-SiWTi calcined at 650°C, which is inferior compared to that of 4.5FeV-SiWTi-650 and 4.5FeV-SiWTi-700.

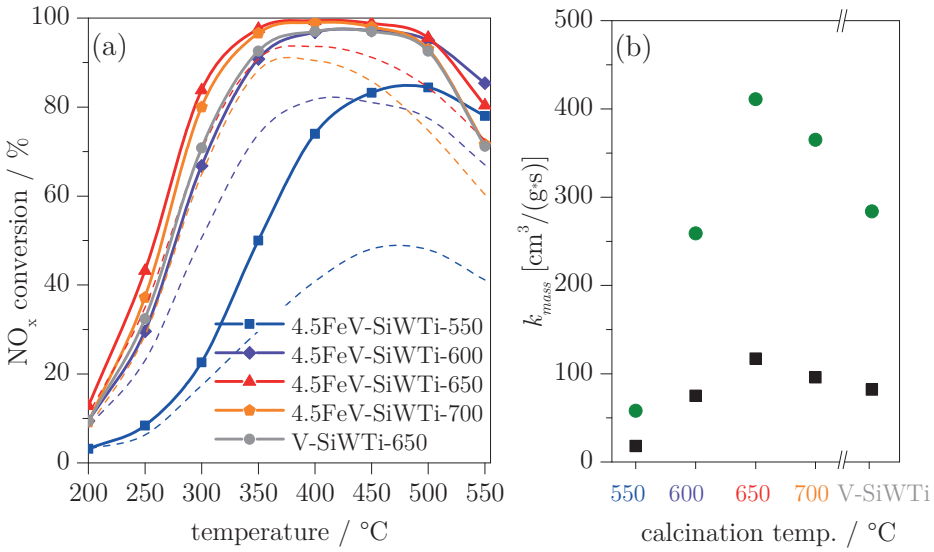

Figure 7-3. (a) NO_x conversion of 4.5 wt% $FeVO_4$/SiWTi (calcined at 550, 600°C, 650 and 700°C) and V-SiWTi - 650. Reaction conditions: 0 - 600 ppm NH_3, 500 ppm NO, 10 vol% O_2, 5 vol% H_2O (bal. N_2), GHSV: 50'000 h^{-1}. Solid lines for maximum NO_x conversion with NH_3/NO =1.2; Dashed lines for NO_x conversion at 10 ppm NH_3 slip. (b) Mass specific rate constants (k_{mass}) at 250°C (■) and 300°C (●) as function of calcination temperature of 4.5FeV-SiWTi.

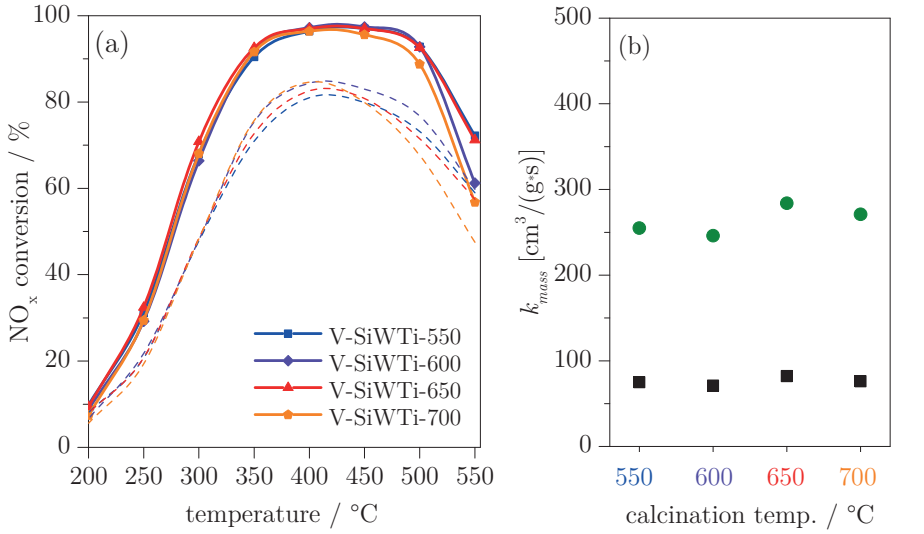

Figure 7-4. (a) NO_x conversion of 2.3 wt% V_2O_5/SiWTi calcined at 550, 600, 650 and 700°C. Reaction conditions: 0 - 600 ppm NH_3, 500 ppm NO, 10 vol% O_2, 5 vol% H_2O (bal. N_2), GHSV: 50'000 h^{-1}. Solid lines for maximum NO_x conversion with NH_3/NO =1.2; Dashed lines for NO_x conversion at 10 ppm NH_3 slip. (b) Mass specific rate constants (k_{mass}) at 250°C (■) and 300°C (●) as function of calcination temperature of V-SiWTi.

4.5FeV-SiWTi-700 showed deactivation tendencies compared to 4.5FeV-SiWTi-650. The deactivation is associated with the sintering of the support material [64], which was confirmed by the BET surface area measurements (**Table 7-1**). The surface area of 4.5FeV-SiWTi-650 decreased from 77 to 68 m^2g^{-1} after calcination at 700°C. The mass specific rate constants (k_{mass}) of **Figure 7-3b** also demonstrate that the highest conversion rates (120 $cm^3g^{-1}s^{-1}$ at 250°C and 420 $cm^3g^{-1}s^{-1}$ at 300°C) are obtained at the calcination temperature of 650°C. The k_{mass} shown in **Figure 7-3b** was determined at 250 and 300°C. These temperatures were chosen because the corresponding Arrhenius plots of FeV-SiWTi-550, FeV-SiWTi-650 and V-SiWTi-650 remain linear (**Figure 7-5**). Above 300°C, various effects such as internal and external mass transfer limitations prevent the use of these k_{mass} values for a linear regression.

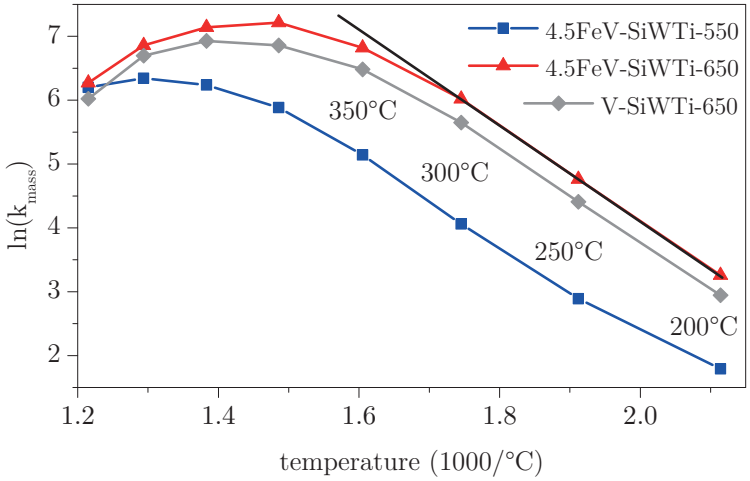

Figure 7-5. Arrhenius plot of the k_{mass} values at 200, 250 and 300°C of FeV-SiWTi-550, FeV-SiWTi-650 and V-SiWTi-650.

Additionally, 4.5FeV-SiWTi becomes increasingly unselective with increasing temperature, which is reflected by the increased N_2O production (**Figure 7-6**) of 4.5FeV-SiWTi. With k_{BET} (**Table 7-1**), the catalytic activity can be compared independent of surface area and active component loading. The rate constants k_{BET} for 4.5FeV-SiWTi-650 and 4.5FeV-SiWTi-700 (1.8 and 1.7, respectively) are significantly higher compared to that of V-SiWTi-700 (1.0). The results obtained upon prolonged treatment of the material at 650 and 700°C (10 h) prove that supported $FeVO_4$ is a suitable material for high temperature

stability. The remarkable effect of the calcination temperature on the catalytic activity of $FeVO_4$/SiWTi has been subject of a detailed physico-chemical characterization.

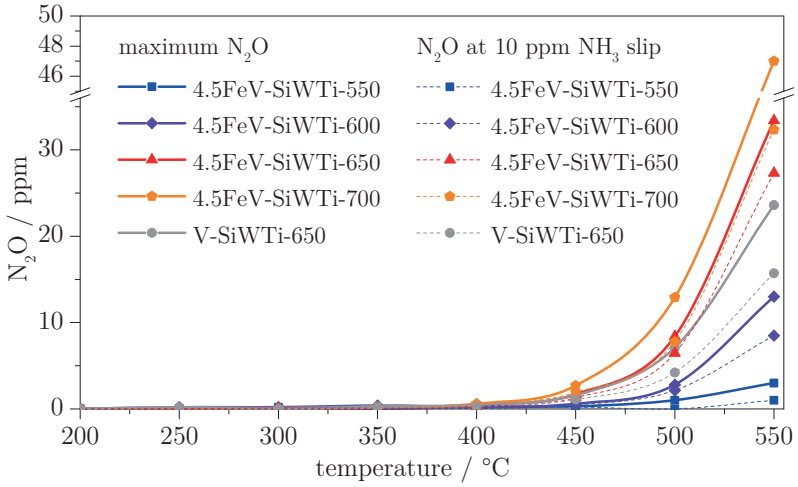

Figure 7-6. N_2O production of 4.5FeV-SiWTi calcined at 550, 600, 650 and 700°C for 10 h. Reaction conditions: 0 - 600 ppm NH_3, 500 ppm NO, 10 vol% O_2, 5 vol% H_2O (bal. N_2), GHSV: 50'000 h^{-1}.

The most active catalyst obtained from loading and composition optimization was characterized in greater detail in order to gather insight into the origin of the activation effect observed in **Figure 7-3**. To this end, the slurry of the 4.5 wt% $FeVO_4$/SiWTi washcoat was dried, calcined at different temperatures, analyzed with XRD, BET, DRIFT spectroscopy and XANES spectroscopy and was systematically compared to the reference material V-SiWTi.

7.3.4 Physico-chemical characterization - BET and XRD

Figure 7-7 shows the XRD patterns of 4.5 wt% $FeVO_4$/SiWTi calcined in the temperature range 550 - 700°C, V-SiWTi and unsupported $FeVO_4$ both calcined at 700°C. For all SiWTi supported catalysts, the patterns of the anatase phase are clearly visible. The main peaks at 25.4 and at 48.0° were used for determining the crystallite size listed in **Table 7-1**. No anatase to rutile phase transformation was observed at any calcination temperature. This needs to be attributed to the presence of Si, since Si as a structural promoter stabilizes the thermodynamically unfavored anatase phase [101].

Table 7-1. Textural and structural properties of the support material and the catalysts.

Catalyst abbreviation	V loading (wt%)	Calc. temp. (°C)	BET SSA (m^2)	k_{BET}[a]	TiO_2 crystal. size (nm)
4.5FeV-SiWTi-550	4.5 wt% $FeVO_4$	550	109	0.2	12.6 ± 0.2
4.5FeV-SiWTi-600	4.5 wt% $FeVO_4$	600	96	0.9	13.5 ± 0.2
4.5FeV-SiWTi-650	4.5 wt% $FeVO_4$	650	77	1.8	16.1 ± 0.5
4.5FeV-SiWTi-700	4.5 wt% $FeVO_4$	700	68	1.7	18.9 ± 0.7
V-SiWTi-700	2.3 wt% V_2O_5	700	90	1.0	15.0 ± 0.6
$FeVO_4$	-	700	6	-	-
SiWTi	-	700	94	-	12.6 ± 0.3
SiWTi	-	550	110	-	15.0 ± 0.7

[a] $k_{BET} = k_{mass}$/BET SSA, V-SiWTi - 700 set to 1.0.

The calcination temperature linearly increases the crystallite size thus lowering the surface area from 4.5FeV-SiWTi-550 to 4.5FeV-SiWTi-700. Despite the equal total vanadium content in 4.5FeV-SiWTi-700 and V-SiWTi-700, the TiO_2 crystallite size differed with 18.9 ± 0.7 and 15.0 ± 0.6, respectively. This corresponds to the low surface area of 4.5FeV-SiWTi-700 (68 m^2g^{-1}) compared to V-SiWTi-700 (90 m^2g^{-1}). The lower surface area and the bigger anatase crystallites of the supported $FeVO_4$ catalyst compared to the V-SiWTi-700 suggest a strong interaction between the active material and the support material. The unsupported $FeVO_4$ calcined at 700°C has a triclinic $FeVO_4$ phase (space group P -1, main reflections at 27.2 and 27.8° 2Θ) and consists of three distinct isolated VO_4 units [262-263]. The $FeVO_4$ phase is clearly still present in the catalyst calcined at 550°C, but it is diminished by elevating the temperature to 575°C and vanishes above 575°C. A weak reflection at 32.9° appears in the temperature range 600 - 650°C, which was tentatively assigned to the rhombohedral V_2O_3 phase (karelianite, space group R-3c, main reflections at 32.9 and 35.8° 2Θ) [264]. This phase also vanishes by increasing the temperature to 700°C. Simultaneously to the V_2O_3 phase, a reflection at 33.2°, assigned to rhombohedral Fe_2O_3 (hematite, space group R-3c, main reflections at 33.2 and 35.7° 2Θ, [265]) appears after calcination at 600°C and is more evident at 700°C.

The presence of Fe_2O_3 clearly reveals that decomposition of $FeVO_4$ occurred on SiWTi already above 575°C, whereas the unsupported $FeVO_4$ is stable at 700°C. As a consequence, V-species are also set free from $FeVO_4$ decomposition. Mixed phases of V, Fe, W or Ti could not be observed at any temperature indicating that if they ever formed, they were on the nanoscale. Similarly, the absence of any feature related to V-containing phases in the XRD at 700°C suggests that they are well dispersed over the surface so that they are invisible to XRD. In contrast, the iron species seem to sinter with increasing temperature to form bulk Fe_2O_3 particles.

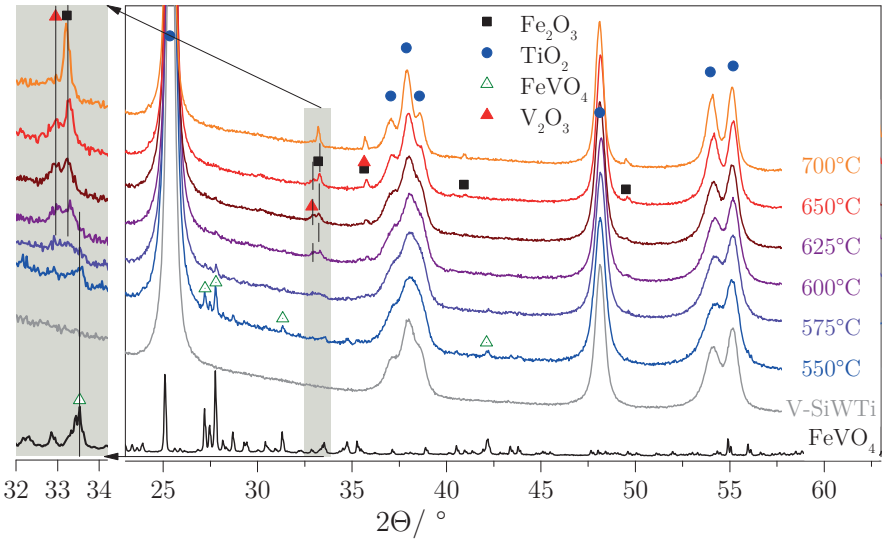

Figure 7-7. XRD patterns of 4.5 wt% $FeVO_4$/SiWTi calcined at the indicated temperatures, unsupported $FeVO_4$ (scaled 1:5) and V-SiWTi calcined at 700°C. The diffractograms are normalized using the anatase peak at 25.4° for 2Θ.

The mobility of the V-containing species (in the following, VO_x) could be rationalized on the base of the Tamman temperature, the half melting point of the oxides that is listed in **Table 1-2**. While it is below 250°C for V_2O_5, the Tamman temperature for the Fe_2O_3 is ca. 650°C. Therefore, the VO_x-species are more readily prone to difference on the support compared to other oxide phases present in the catalysts. The Tamman temperature of $FeVO_4$ (ca. 300°C) is further giving a theoretical explanation why the $FeVO_4$ already decomposes at above 550°C as it is indirectly confirmed in the XRD patterns.

Another aspect of the early decomposition is the likely crucial interactions of V with SiO_2, WO_3 or TiO_2.

The V_2O_3 phase has not often been observed in a V-based SCR system. Habel et al. have analyzed a system of 5 - 15 wt% V_2O_x/TiO_2 in oxidizing and reducing conditions [266]. V_2O_3 was detected in a CO_2 rich atmosphere, whereas the vanadium was immediately oxidized to V_2O_5 in presence of O_2. In the present system, all treatments and measurements were conducted in air. A feasible interpretation of the presence of V_2O_3 is the structural similarity to Fe_2O_3. The two phases not only have the same crystal system but possess also the same space group and very similar lattice parameters. With the decomposition of $FeVO_4$ and the rearrangement of VO_x and FeO_x species, a VO_x layer is formed which has the same crystal structure of the substrate on which it grows (Fe_2O_3) [267]. Therefore, the XRD data were interpreted with an epitaxial growth of V_2O_3 on the Fe_2O_3 phase which generated small V_2O_3 particles. It is likely that above 650°C, the system becomes increasingly mobile and VO_x species start to migrate further towards the support material, as suggested by XRD where the small V_2O_3 crystallites are not detectable anymore for 4.5FeV-SiWTi-700.

7.3.5 DRIFT and XANES

Figure 7-8 displays the DRIFT spectra collected after the samples were exposed to 200 ppm NH_3 at 350°C for 30 min in the regions of (a) N-H and O-H stretch, (b) M=O overtone and (c) N-H deformation modes. The assignments of the various signals were performed according to literature [39, 78, 123, 135, 216-217, 240]. Unsupported $FeVO_4$ exhibits the least signal intensity among the selected samples, indicating a weak interaction with NH_3. Even though the very low surface area compared to the supported samples contributing to the low intensity (**Table 7-1**), NH_3 adsorption does not appear favored as the very weak signals below 2000 cm^{-1} suggest. A signal at 3641 cm^{-1} reveals that V-OH groups are present and perturbed by interaction with NH_3 [268]. The signal intensity increases from 4.5FeV-SiWTi-550 to 4.5FeV-SiWTi-700. Therefore, both uptake and surface acidity increase with increasing calci-

nation temperature, supporting the evolution of the catalyst surface in agreement with the structural changes observed by XRD.

All samples containing SiWTi show two types of adsorbed NH_3 species. In a first set of signals, NH_3 adsorption on Lewis acid sites shows features at ca. 3350, 3257 and 3164 cm^{-1} (ν(N-H)) and the corresponding asymmetric deformation mode at 1600 cm^{-1} (δ_{as}(N-H)). The symmetric deformation mode at ca. 1200 cm^{-1} (δ_s(N-H)) is obscured by the fundamental modes of the material. The signals of Lewis acid sites origin from W^{6+}, Ti^{4+} and $V^{4+/5+}$ adsorption sites, which are present in the SiWTi support material as well as in the pure $FeVO_4$, though to a lesser extent. The signal at ca. 3350 cm^{-1} provides a qualitative indication of the presence of Lewis sites. While SiWTi has a main feature at 3350 cm^{-1} with a shoulder at high energy that becomes the dominant contribution at 3377 cm^{-1} in V-SiWTi and 4.5FeV-SiWTi-600 - 4.5FeV-SiWTi-700. This observation suggests that in the V-containing samples, except for 4.5FeV-SiWTi-550, Lewis sites origin from similarly dispersed $V^{4+/5+}$ species. The same signal is found at 3339 cm^{-1} in unsupported $FeVO_4$, likely indicating the presence of a third type of Lewis acid site characteristic of bulk $FeVO_4$.

The second set of signals is characteristic of protonated NH_4^+ species corresponding to the coordination of NH_3 on Brønsted acid sites. This species is characterized by signals at 2999 and 2776 cm^{-1} (ν(N-H)) and at 1672 and 1427 cm^{-1} (δ_s(N-H) and (δ_{as}(N-H)), respectively). The latter one presents an evident shoulder at ca. 1480 cm^{-1} in agreement with the formation of different multibonded NH_4^+ species [269]. NH_3 adsorption on terminal OH group causes the appearance of negative signals in the O-H region (**Figure 7-8a**) [270]. The signal is present on all materials, except $FeVO_4$. The signals at ca. 3690 and 3647 cm^{-1} were assigned to W-OH and Ti-OH groups of SiWTi. The former is absent on all other samples suggesting that it may be a contribution of NH_3 coordinated to W-OH groups. The negative (ν(V-OH)) signal at 3640 cm^{-1} attenuates (becomes increasingly less negative) with increasing calcination temperature and this behavior is accompanied by the loss of a signal at 3587 cm^{-1} that is most negative for 4.5FeV-SiWTi-700. Because of the XRD data of **Figure 7-7**, showing appearance of Fe_2O_3 with increasing calcination temperature,

the signal was tentatively assigned to coordination of NH_3 to Fe-OH groups. Finally, a weak feature at ca. 3745 cm^{-1} in SiWTi and 4.5FeV-SiWTi-550 indicates coordination to Ti-OH. That the signal is visible specifically on these two samples has to be related to their structure. Being V missing (SiWTi) or bound to Fe in $FeVO_4$ (4.5FeV-SiWTi-550), W-OH and Ti-OH groups become more accessible. The negative signal at ca. 1620 cm^{-1} is due to removal of physisorbed water.

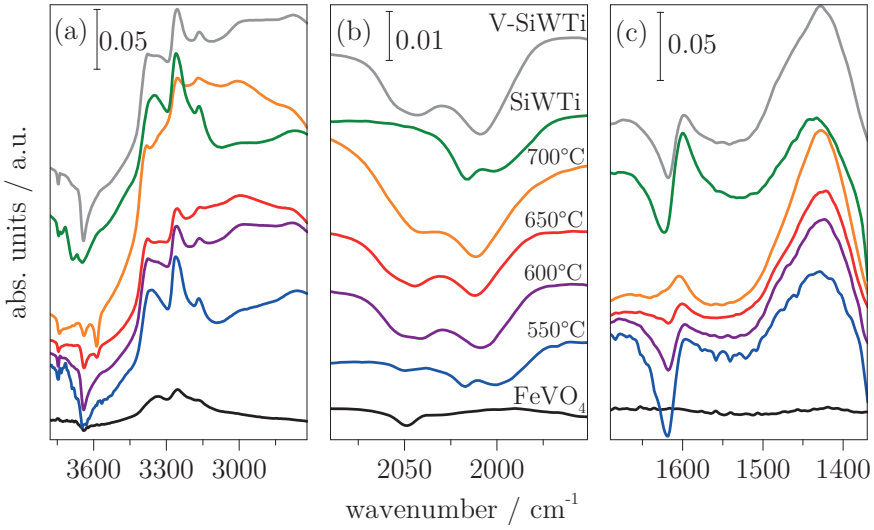

Figure 7-8. DRIFT spectra of 4.5 wt% $FeVO_4$/SiWTi calcined at the indicated temperatures, unsupported $FeVO_4$, SiWTi and V-SiWTi calcined at 700°C. The samples were exposed to 200 ppm NH_3 for 30 min at 350°C.

Figure 7-8b displays the spectral region of the overtones of fundamental modes of metal oxides [240, 271]. The 2060 - 2030 cm^{-1} range corresponds to the first overtone of surface vanadyl species (2ν(V=O)) and is dependent on the specific oxide support and the surface vanadia coverage [61, 242]. The 2020 - 2000 cm^{-1} region represents the first overtone of surface wolframyl species (2ν(W=O)) [61]. The signals are negative because the terminal oxo groups are consumed upon NH_3 adsorption. Therefore, NH_3 adsorption is potentially able to interrogate the various V and W species of unsupported $FeVO_4$, supported $FeVO_4$ and V-SiWTi obtained after calcination at increasing temperature. The gradual decomposition of the $FeVO_4$ in the 550 - 700°C temperature range into the XRD-visible Fe_2O_3 phase likely affects the type and coordination of the neighboring atoms of vanadium. The spectra of unsupported $FeVO_4$ and

4.5FeV-SiWTi-550 are characterized by the 2ν(V=O) mode at 2049 cm^{-1}. Hence, the V-containing species of supported $FeVO_4$ are not altered by the calcination at 550°C. Routary et al. observed, that $FeVO_4$ possesses distinct and isolated VO_4 units that are linked to an Fe(III) via an oxygen atom [263]. However, the surface termination of $FeVO_4$ was found to be an amorphous VO_x layer (**Figure 7-9a**). Upon calcination at 600°C, the signal at 2049 cm^{-1} splits in two distinct features at 2053 and 2041 cm^{-1}, suggesting that at least two V=O species are present with different bond length. The split of the 2ν(V=O) mode was associated to the variation of electronic environment experienced by interaction with new neighboring atoms and different oxidation states as shown in **Figure 7-9b** that is probably created upon $FeVO_4$ decomposition. The formation of the signal at 2042 cm^{-1} can be tentatively interpreted with the formation of vanadyl species lacking interaction with Fe atoms above 600°C that is otherwise providing electron density into the V−O bond (**Figure 7-9**).

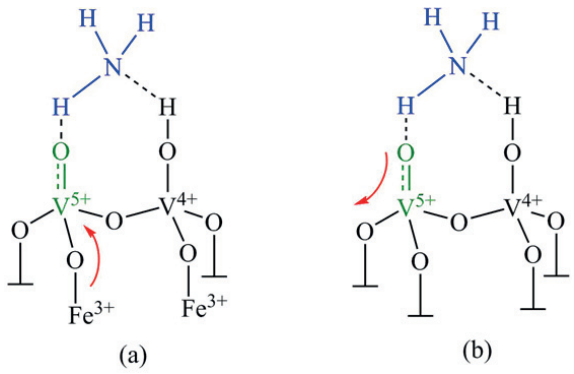

Figure 7-9. (a) Representation of a vanadyl species of $FeVO_4$ with adsorbed NH_3. (b) Representation of a vanadyl species on SiWTi with adsorbed NH_3. The arrows indicate a plausible shift of electron density in the V=O bond.

However, precise assignment of the two 2ν(V=O) signals based solely on the presented data is not possible. The temperature increase to 650 and 700°C does not influence further the 2ν(V=O) signals, which closely resemble the signals observed in the case of V-SiWTi. Contrary to V-SiWTi, 4.5FeV-SiWTi-700 appears to experience a partial loss of the species affording the signal at high energy that could be taken as a possible indication of the initial effects of thermal aging and aggregation of VO_x species [141, 272]. Based on the interpretation of the DRIFT data, it was concluded that the VO_x-species responsi-

ble for NH_3 adsorption in 4.5FeV-SiWTi-600 - 4.5FeV-SiWTi-700 are likely finely dispersed and exhibit a very similar geometry to that of the VO_x-species in V-SiWTi. This VO_x species is believed to be composed of one terminal V=O mono-oxo species and three bridging V-O-V bonds as depicted in **Figure 7-9** [273]. The observation of free VO_x-species on the surface of $FeVO_4$/SiWTi is in agreement with observations by Casanova et al. [179].

The features corresponding to the 2ν(W=O) mode of the SiWTi support are at 2017 and 2002 cm^{-1} and are also present in 4.5FeV-SiWTi-550. Hence, the presence of $FeVO_4$ particles does not interfere with the adsorption properties of the wolframyl groups of SiWTi. This information is in agreement with the presence of negative signals of Ti-OH in these two samples, confirming the weak interaction of $FeVO_4$ with NH_3 and with the support. The two 2ν(W−O) modes can be attributed to monomeric tungsten mono-oxo species and to polymeric mono-oxo wolframyl species, respectively [61]. In contrast, only one feature appears at 2008 cm^{-1} (4.5FeV-SiWTi-600 and V-SiWTi) and 2012 cm^{-1} (4.5FeV-SiWTi-650), indicating that the environment of the wolframyl species changed upon calcination and by contact with VO_x-species. The fact that no change was found for SiWTi calcined at different temperatures (not shown) reveals that VO_x-species, obtained from thermal decomposition of $FeVO_4$, interact with the wolframyl sites on 4.5FeV-SiWTi-600 - 4.5FeV-SiWTi-700.

The changes in both the V and W regions strongly support the interpretation that upon decomposition of $FeVO_4$ above 600°C, the released V atoms interact with the SiWTi support more strongly than in the original material (supported $FeVO_4$, 4.5FeV-SiWTi-550). The role and the interaction of Fe_2O_3 with the support or the VO_x at elevated temperature could not be defined within this system. The close resemblance of the IR spectrum of SiWTi in the vanadyl and wolframyl regions with that of supported $FeVO_4$ calcined at elevated temperature and V-SiWTi, however, convincingly indicates that a similar degree of interaction with SiWTi and similar VO_x-species are observed after $FeVO_4$ decomposition.

The evolution of the bulk $FeVO_4$ species supported on SiWTi upon increasing calcination has been followed also by X-ray absorption spectroscopy in order to

evaluate the local environment of the VO_x-species. The normalized XANES spectra recorded at the V K-edge are shown in **Figure 7-10a** for the catalysts and **Figure 7-10b** for the references. Without attempting a quantitative assessment of both oxidation state and coordination of the VO_x-species represented by these spectra, a qualitative discussion is sufficient to support the interpretation of the observed phenomena. Two major changes are observed in the XANES spectra with increasing calcination temperature.

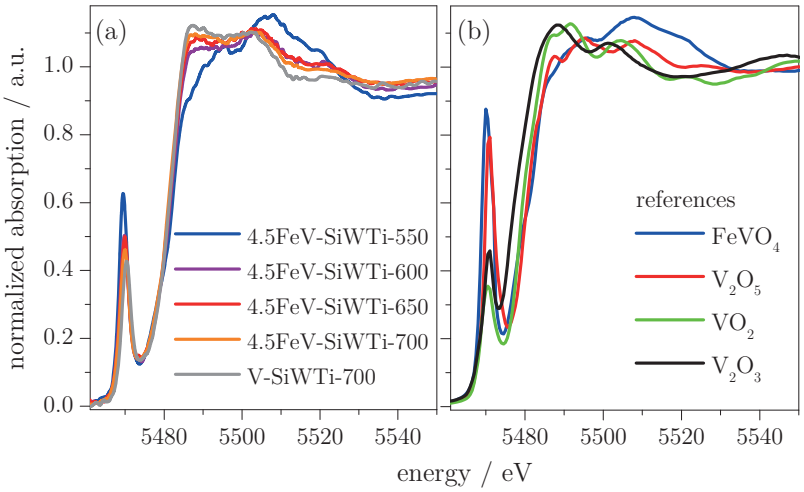

Figure 7-10. Normalized V- K-edge XANES spectra of (a) selected catalysts and (b) unsupported $FeVO_4$ as well as various V_xO_y reference materials.

The pre-edge peak (1s-3d dipole transition) loses intensity and shifts to higher energy, especially when changing from 4.5FeV-SiWTi-550 to 4.5FeV-SiWTi-600, while the edge position shifts to lower energy suggesting V reduction. The decrease of the oxidation state can also be intrinsic to the loss of intensity of the pre-edge [274]. Importantly, it is evident that the shape of the rising edge changes from that characteristic of $FeVO_4$ in favor of a species strongly reminding the coordination found for V-SiWTi. The increasing resemblance of the rising edge also to that of V_2O_3 (**Figure 7-10b**) rather than V_2O_5 suggest that a fraction of V is in this coordination environment which is supported by the XRD observation in **Figure 7-7**. The evolution of the pre-edge energy to that found in V-SiWTi could reflect the change of coordination geometry from the tetrahedral VO_4 units of $FeVO_4$ to the trigonal units of V_2O_3 or the square pyramidal units of and VO_x [274]. Precise assignment is complicated by the

additional effect of distortion of the V-O bonds [106]. These observations clearly strengthen the perception of the phase transformation of VO_4 units from $FeVO_4$ to a similar structure of dispersed VO_x species in the reference V-SiWTi catalyst. Further characterization is required to assess the geometry of the VO_x species and their interaction with the support. Given the activity of V-SiWTi at the various temperatures (**Figure 7-4**) it is fair to propose that such species are likely the ones responsible for SCR activity.

7.4 Conclusion

SCR catalysts with metal vanadates of the type $Fe_xAl_{x-1}VO_4$ ($0 \leq x \leq 1$, $MeVO_4$) supported on SiO_2-WO_3-TiO_2 were prepared with different loadings, compositions and at different calcination temperatures. The loading experiments showed that a low $FeVO_4$ loading is beneficial for the thermal stability whereas a high loading improves catalytic activity. Additionally, it was found that incorporation of Al in $MeVO_4$ does neither improve the catalyst performance nor its thermal stability. The optimized catalyst with respect to V loading and composition, containing 4.5 wt% $FeVO_4$/SiWTi, shows an enhanced performance compared to 2.3 wt% V_2O_5/SiWTi. Remarkable catalyst activation was observed above 600°C that was investigated by means of XRD, BET, DRIFT and XANES. The activation and formation of active species directly correlates with the calcination temperature and NO_x conversion. Supported intact $FeVO_4$, present at low temperature, is hardly SCR active. However, after decomposition of $FeVO_4$, dispersed VO_x species are present, which are beneficial for high SCR activity. At elevated temperature, all VO_x species are finely dispersed on the SiWTi surface and migrate towards WO_3, while the iron species sinter to Fe_2O_3 particles. Thus, $FeVO_4$ is not the active phase for catalyst prepared with this protocol, rather it acts as the catalyst precursor. This Chapter provided strong evidences that the phase transformation of VO_x species from $FeVO_4$ leads to very similar VO_x species to that of the reference V-SiWTi catalyst. Despite this phase decomposition, the VO_x species are likely the active ones responsible for NH_3-SCR and a very active and thermally stable SCR catalyst can be obtained after thermal activation.

Chapter 8

Supported rare earth metal vanadates as SCR catalysts

8.1 Introduction

In the previous Chapter 7 was shown that supported $FeVO_4$ obtained from mixing $FeVO_4$ and SiWTi is not stable and decomposes into Fe_2O_3 and VO_x species above 600°C. Below this temperature, the intrinsic activity of $FeVO_4$-based SCR catalysts was rather low and was only enhanced by its thermal decomposition into VO_x species. Using XANES, it was shown that these species resembled those obtained on classic V_2O_5-based SCR catalysts. In order to clarify the benefits of $MeVO_4$ on SiWTi, this chapter is dedicated to compare the activity and stability of $FeVO_4$, $CeVO_4$ and $ErVO_4$ on SiWTi, aiming at unraveling the origin of their controversial SCR activity.

In literature, the enhanced thermal stability of catalysts based on rare earth vanadates supported on SiWTi is associated mainly with the ability of the rare earth metals to suppress the undesired anatase to rutile phase transition of the support [167, 182]. This consequently hinders the sintering and shifts the loss of surface area to higher calcination temperatures. Since vanadium is locked in the vanadate structure, no free V_2O_5 that would promote sintering is dispersed on the catalyst surface [167]. Except for $LaVO_4$, a broad range of rare earth vanadate based SCR catalysts exhibit high thermal stability. Especially $ErVO_4$ and $TbVO_4$ were found the most active and temperature stable compositions [167, 169]. However, the catalysts were previously compared with a V_2O_5-based

This chapter is based on the postprint version of the publication: A. Marberger, M. Elsener, D. Ferri, A. Sagar, C. Artner, K. Schermanz, O. Kröcher, Relationship Between Structures and Activities of Supported Metal Vanadates for the Selective Catalytic Reduction of NO by NH_3, *Appl. Catal. B*, **2017**, 218, 731-742 A. Marberger performed the experiments, analyzed and interpreted the data together with the co-authors and wrote the manuscript.

one whose high loading is not suitable for high temperature treatment [75]. The best compromise between low-temperature activity and thermal stability was found for mixed $Fe_{0.5}Er_{0.5}VO_4$/SiWTi [182], which was interpreted to originate from both Fe and Er, the former promoting the low temperature activity because of the $FeVO_4$ decomposition to Fe_2O_3 and VO_x species and the latter increasing the structural stability of the system.

Cerium is widely considered as SCR active component due to its redox ability and promotional effects such as increased acidity and enhanced oxygen storage capacity. The redox properties of the Ce^{4+}/Ce^{3+} pair and the propensity of Ce to form solid solutions with other oxides thus increasing the amount of active sites and improving the (hydro)-thermal stability represent relevant benefits of CeO_2 [59, 116-122]. Ce-modified V_2O_5-based SCR catalysts showed enhanced thermal stability because the formation of cerium vanadate decreased sintering tendencies [123]. Supported rare earth vanadate catalysts, among which $CeVO_4$, were found to be more thermally stable compared to a V_2O_5-based reference catalyst [167, 169]. Finally, it was shown that unsupported $CeVO_4$ and transition metal vanadates can exhibit some SCR activity [175-177].

In order to elucidate the discrepancy from literature and the findings of Chapter 7, this chapter is dedicated to study the origin of the SCR activity of supported $FeVO_4$, $CeVO_4$ and $ErVO_4$ on SiWTi.

8.2 Experimental section

8.2.1 Catalyst preparation

The general preparation of V-based catalysts is described in detail in the section 2.1. The preparation of $MeVO_4$-based materials is described in Chapter 7. Bulk metal vanadates ($CeVO_4$, $FeVO_4$, $ErVO_4$, **Table 8-1**) were provided by Treibacher Industrie AG and were obtained from co-precipitation of metals and vanadium precursors. For the sake of comparison, the metal vanadate loading was chosen on the amount of nominal V_2O_5, e.g. 5.6 wt% $CeVO_4$-SiWTi is equivalent to 2.0 wt% V_2O_5. Calcination of powders and monoliths was carried out in a muffle oven at 650, 700, 750 and 800°C for 10 h. The catalysts

composition, V content and abbreviations are summarized in **Table 8-2** and **Table 8-3**.

Table 8-1. Calcination temperature, color, XRD crystallite size an particle size of bulk metal vanadates utilized to prepare metal vanadate based catalysts.

	Calcination t. (°C)	color	crystallite size (nm)	mps[(a)] (µm)
$FeVO_4$	120	orange-brown	12 ± 2	4.0
$FeVO_4$	700	orange	103 ± 1	3.4
$CeVO_4$	120	red-gray	14 ± 2	7.3
$CeVO_4$	700	vinous	80 ± 1	9.6
$ErVO_4$	700	pale pink	24 ± 1	3.4
SiWTi	700	white	16 ± 1	1.7

[(a)] mps (median particle size) measured on a particle size analyzer, H_2O as solvent

8.2.2 Catalytic Measurements

The catalytic measurements were performed on a dedicated laboratory test reactor described in section 2.2.

8.2.3 Characterization methods

Temperature programmed reduction with H_2 (H_2-TPR) was conducted on a bench top TPDRO-1100 (ThermoElectron) instrument equipped with a thermal conductivity detector. The calcined powder samples (ca. 100 mg) were loaded into the quartz reactor tube and heated under constant flow of 20 vol% O_2 to 500°C. After cooling to room temperature, H_2-TPR profiles were recorded in 10 vol% H_2/Ar (20 mL/min) at 5°C/min. XRD, BET, DRIFT and DRUV spectroscopy were also used and their experimental detail are described in section 2.3.3 and 2.3.4.

8.3 Results and discussion

8.3.1 Catalytic activity

The NO_x conversion of 5.6 wt% $CeVO_4$-SiWTi (6CeV-SiWTi, equivalent to 2.0 wt% V_2O_5, **Table 8-2**) and 9.1 wt% $CeVO_4$-SiWTi (9CeV-SiWTi, 3.3 wt%

V_2O_5) calcined at various temperatures is presented in **Figure 8-1a** and **Figure 8-1b**, respectively.

The activity of samples calcined at 450°C (hereafter defined as the fresh state) and at 650°C was similar and rather modest (maximum at 450 - 500°C with ca. 80% conversion). The intrinsic activity of CeV-SiWTi is evident after comparison with the activity of SiWTi (**Figure 8-2b**). Especially for 9CeV-SiWTi, the NO_x conversion increased after calcination at 700 and 750°C and 90% conversion was obtained. This effect is more clearly visible in the k_{mass} values obtained at the reaction temperature of 300°C (**Figure 8-1c**) showing that calcination at 700 and 750°C resulted in higher reaction rates. The k_{mass} values of fresh 6CeV-SiWTi and 9CeV-SiWTi were comparable, but the k_{mass} of 9CeV-SiWTi was nearly twice that of 6CeV-SiWTi after calcination at 700 and at 750°C. The NO_x conversion declined above 400°C for both catalysts after calcination at 800°C signifying the propensity of the material towards thermal aging and selectivity loss that can be verified by the characterization data presented below.

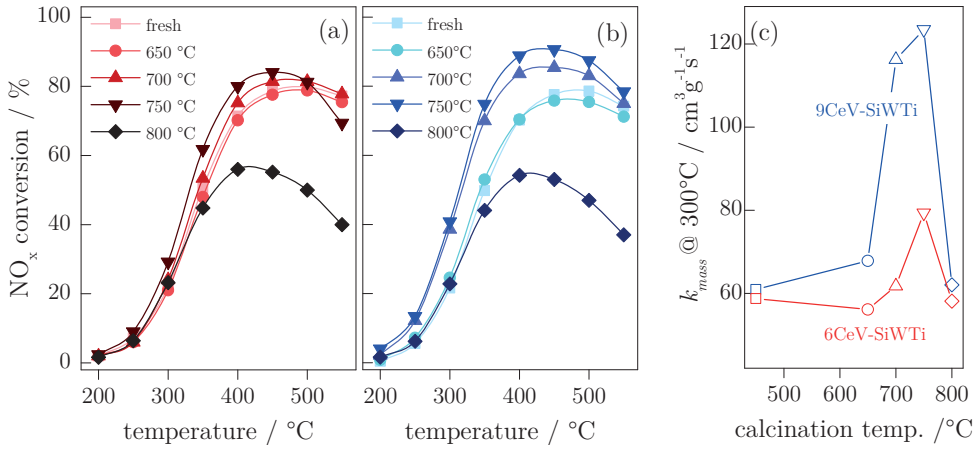

Figure 8-1. SCR activity of (a) 6CeV-SiWTi, (b) 9CeV-SiWTi calcined at various temperatures and (c) the corresponding mass normalized rate constants k_{mass}.

Because the highest NO_x conversion was obtained after calcination at 750°C, the effect of $CeVO_4$ loading was studied with catalysts calcined at this temperature (**Figure 8-2b**). The loading of 9 wt% $CeVO_4$ was found to be optimal and a maximum of ca. 90% NO_x conversion was reached between 350 and 450°C (**Figure 8-2a**). The overall SCR activity of the $CeVO_4$-based catalysts

and their corresponding k_{mass} values (**Table 8-2**) were rather low compared to those of a $FeVO_4$ catalyst based on the same SiWTi support (see Chapter 7).

In view of the further discussion, the activity of CeV-SiWTi was also compared with that of a vanadia and CeO_2-based catalyst (**Figure 8-2b**). The activity for the vanadia-based reference catalysts increased with increasing V content from 0.0 wt% V_2O_5 (0V-SiWTi) to 0.5 wt% V_2O_5/SiWTi (0.5V-SiWTi) and to 1.0 wt% V_2O_5/SiWTi (1V-SiWTi) after calcination at 750°C. For a V_2O_5 loading of 2 wt% (2V-SiWTi), the catalyst showed similar activity for all calcination temperatures (**Figure 8-3**) but deactivated after calcination at 750°C (drop of NO_x conversion above 400°C and maximum NO_x conversion of 80%). A lower V content causes an activity decrease of V_2O_5-WO_3-TiO_2 catalysts (no SiO_2) but also an increase in their thermal stability (see Chapter 3). Therefore, a compromise between V content and calcination temperature is a requirement for active and stable V_2O_5-based catalysts.

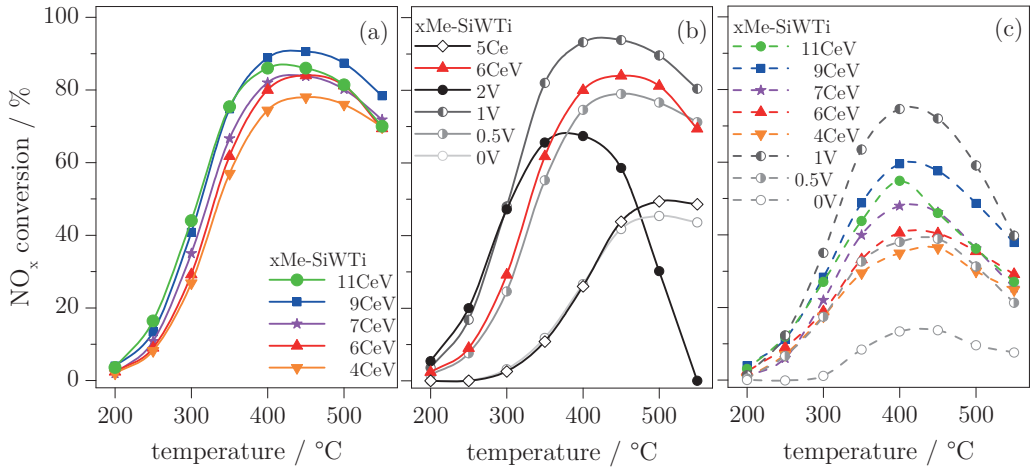

Figure 8-2. SCR activity of (a) $CeVO_4$-based catalysts and (b) reference V_2O_5 and CeO_2-based catalysts. (c) Corresponding SCR activity at 10 ppm NH_3 slip. All materials were calcined at 750°C for 10 h. xMe-SiWTi: "x" represents the loading and "Me" the metal(vanadate) that was mixed with SiWTi.

9CeV-SiWTi was at best as active as 1V-SiWTi calcined at 750°C (**Figure 8-2a** and **2b**) but was more active than 2V-SiWTi calcined at 750°C. Following the analogy with V-SiWTi, the NO_x conversion of 6CeV-SiWTi was between that of 0.5V-SiWTi and 1V-SiWTi (**Figure 8-2b**). No significant aging tendencies were observed for 6CeV-SiWTi after calcination at 750°C. Increas-

ing the loading of $CeVO_4$ to 11 wt% (11CeV-SiWTi, 4.0 wt% V_2O_5) was no longer beneficial for the activity. Finally, the activity of 9CeV-SiWTi calcined at 750°C was not dictated by the CeO_2 possibly present because of the high calcination temperature as demonstrated with 5.0 wt% CeO_2-SiWTi (5Ce-SiWTi, equimolar amount of Ce as 9CeV-SiWTi; **Figure 8-2b**). The reason to select CeO_2 will become clear with the characterization data.

Table 8-2. Nominal V_2O_5 content, estimated *r(V₂O₅)*, TiO_2 crystallite size, k_{mass}, BET surface area, calculated V surface coverage (Υ) of FeV-SiWTi, CeV-SiWTi and ErV-SiWTi after calcination at 750°C.

				After calcination at 750°C for 10h				
	Me	$MeVO_4$ loading (wt%)	Nom. V_2O_5 (wt%)[a]	Released V_2O_5 (wt%)[b]	TiO_2 size (nm)[b]	k_{mass} (cm^3 $g^{-1}s^{-1}$)	BET SSA (m^2g^{-1})	Υ[c] (%)
4CeV-SiWTi	Ce	4.2	1.5	0.6 ± 0.1	20	71	71	7
6CeV-SiWTi	Ce	5.6	2.0	0.7 ± 0.1	19	79	69	9
7CeV-SiWTi	Ce	7.0	2.5	0.8 ± 0.2	20	101	69	10
9CeV-SiWTi	Ce	9.1	3.3	1.1 ± 0.2	19	123	67	14
11CeV-SiWTi	Ce	11.2	4.0	1.2 ± 0.2	23	141	53	20
4FeV-SiWTi	Fe	3.75	2.0	2.0	26	299	49	34
5FeV-SiWTi	Fe	5.0	2.7	2.7	36	198	33	69
6ErV-SiWTi	Er	6.1	2.0	0.2 ± 0.2	21	30	70	2
10ErV-SiWTi	Er	10	3.3	0.1 ± 0.3	19	33	69	1
6CeV-dried-SiWTi	Ce[d]	5.6	2.0	1.1 ± 0.1	25	137	57	16

[a] based on V_2O_5 equivalents, [b] estimated from XRD, [c] determined from theoretical saturation value (7.9 VO_x nm^{-2} [135]) for monolayer coverage and the BET surface area, [d] $CeVO_4$ dried at 120°C.

The NO_x conversion at 10 ppm NH_3 slip (**Figure 8-2c**) delivers additional useful information since it is a qualitative indication of surface acidity deviations, e.g. upon sintering of the support or poisoning of acid sites [192]. A high surface acidity is beneficial for the NH_3 storage property and delays the NH_3 slip (see chapter 3). In **Figure 8-2c**, this parameter was lower in all CeV-SiWTi catalysts compared to that of 1V-SiWTi, despite the overall higher equivalent V content (**Table 8-2**). This indicates that the acidity of CeV-SiWTi was low-

er than that of the V_2O_5-based catalyst and the catalyst was not able to store the needed amount of NH_3 for the reaction. After calcination at 750°C, the CeV-SiWTi catalysts exhibited higher NO_x conversion above 400°C than 2V-SiWTi, indicating a lower deactivation effect (lower competing NH_3 oxidation reaction).

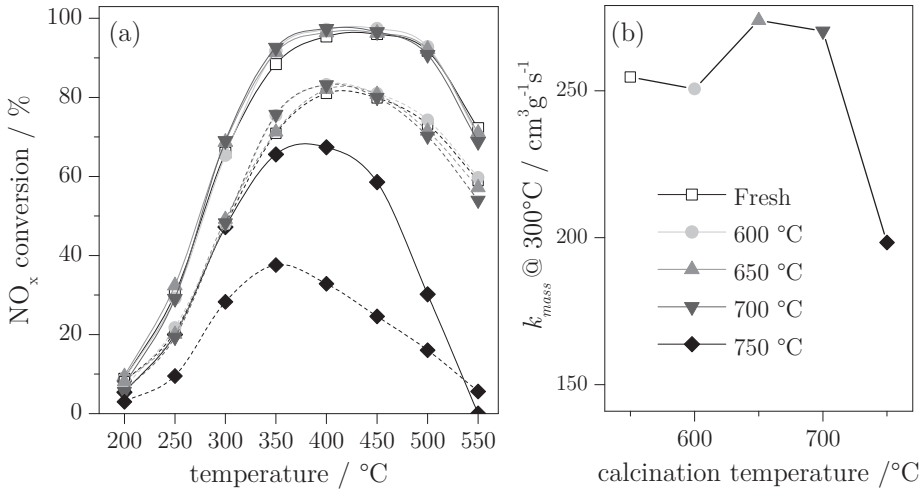

Figure 8-3. (a) NO_x conversion (solid lines) and activity at 10 ppm NH_3 slip (dashed lines) of 2V-SiWTi calcined at various temperatures and (b) the corresponding mass normalized rate constants k_{mass} at 300°C.

The high activity and the increased thermal stability have been interpreted previously as the intrinsic properties of rare earth metal vanadates and the result of a stabilization effect of the support by the vanadate [167, 169]. Hence, this chapter is dedicated to investigate the origin of the activity and resistance to deactivation of $MeVO_4$ based SCR catalysts using XRD, BET, *in situ* DRIFT and *ex situ* DRUV spectroscopy.

8.4 Material characterization

8.4.1 XRD results

Figure 8-4a shows the X-ray diffractograms of 6CeV-SiWTi calcined at increasing temperature, unsupported $CeVO_4$ calcined at 700 and 750°C and SiWTi calcined at 750°C. The XRD diffractograms of all the other CeV-SiWTi catalysts with different CeO_4 content calcined at 750°C as well as the reference V-SiWTi catalysts are presented in **Figure 8-5**.

The prominent TiO_2 anatase reflections were visible in all SiWTi-containing samples. The anatase TiO_2 crystallite size increased with increasing calcination temperature but was similar for SiWTi (20 nm) and 6CeV-SiWTi (19 nm) after calcination at 750°C indicating that indeed $CeVO_4$ did not promote sintering. While the main peak of $CeVO_4$ at 32.4° (**Figure 8-4c**) decreased with increasing calcination temperature, the reflection at 28.6° (**Figure 8-4b**) assigned to CeO_2 appeared clearly at 650°C and intensified with increasing calcination temperature.

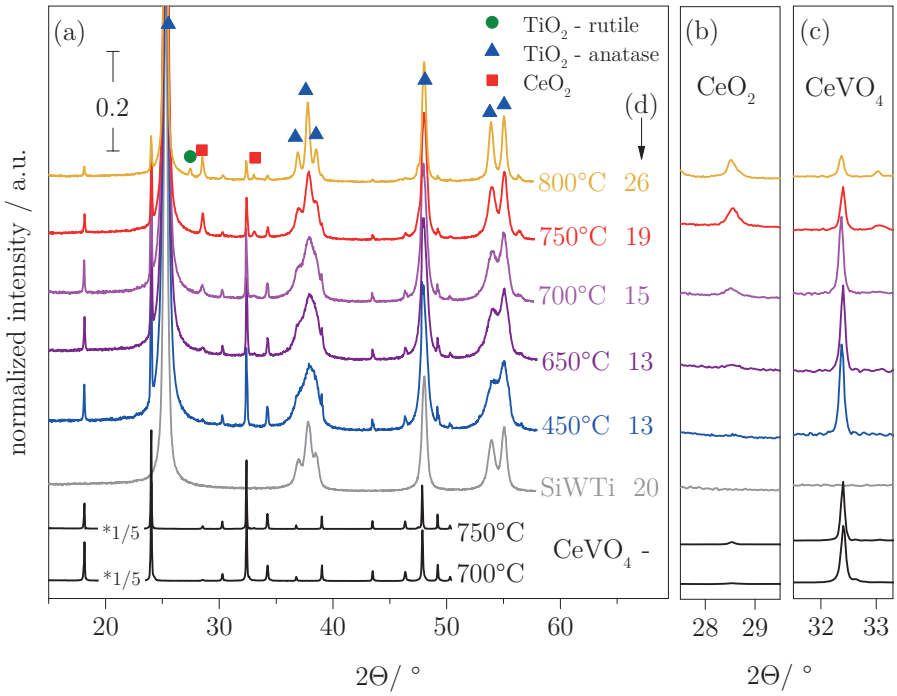

Figure 8-4. (a) XRD patterns of unsupported $CeVO_4$, SiWTi and 6CeV-SiWTi calcined at various temperatures. TiO_2 anatase crystallite sizes (d) were determined from the Scherrer equation. The 2Θ regions (b) around 28.5° ($CeVO_4$) and (c) 32.4° (CeO_2) are enlarged.

The XRD data suggests that supported $CeVO_4$ is not as stable as unsupported $CeVO_4$ and decomposed in analogy to Chapter 7 for supported $FeVO_4$. CeO_2 was the only visible decomposition product from the $CeVO_4$ phase. The corresponding amount of vanadium made available by $CeVO_4$ decomposition did not form a phase that was detectable by XRD, suggesting that the amount of V was low and/or that the new V-containing phase was highly dispersed. The

fraction of released VO_x species was estimated from the peak area of the $CeVO_4$ reflection at 32.4°:

$$r(V_2O_5) = n(V_2O_5) * \left(1 - \frac{A_{CeVO4(x°C)}}{A_{CeV-TWS(450°C)}}\right) \quad \textbf{(8.1)}$$

where $r(V_2O_5)$ is the released fraction of VO_x species expressed in wt% V_2O_5, $n(V_2O_5)$ the equivalent V_2O_5 content (in wt%) for each catalyst according to **Table 8-2** and **Table 8-3**, $A_{CeVO4(x°C)}$ the $CeVO_4$ peak integral area in the diffractograms obtained at the selected calcination temperature x, and $A_{CeVO4(450°C)}$ the same integral area for the fresh sample in which $CeVO_4$ is still intact (taken as 100%). This assumption is valid because the areas of the $CeVO_4$ and CeO_2 reflections were similar at 450 and 650°C, indicating that the metal vanadate remained unchanged after calcination at 450°C. The error on $r(V_2O_5)$ was calculated by including a peak area of $CeVO_4$ at 18.1° and an additional measurement and integration error (10%). Differences in structure and coordination of the released VO_x species could not be distinguished with this estimation and were investigated by diffuse reflectance spectroscopy in the sections below. It is important to note that $r(V_2O_5)$ does not necessarily reflect the accurate amount of free VO_x. Since small $CeVO_4$ crystallites below the detection limit of XRD, amorphous $CeVO_4$ phases or decomposed $CeVO_4$ during the washcoating procedure are not included, $r(V_2O_5)$ is only an estimate for the sake of this discussion. It was also assumed here that the extent of vanadium loss due to volatilization is negligible by using SiWTi (ca. 50 ng / g V_2O_5 for 2 wt% V_2O_5-SiWTi calcined at 750°C) [64].

Table 8-3. TiO_2 crystallite size, k_{mass}, BET surface area, calculated V surface coverage (Υ) of V_2O_5-based catalysts after calcination at 750°C.

	V_2O_5 loading (wt%)	TiO_2 size (nm) [(a)]	k_{mass} ($cm^3g^{-1}s^{-1}$)	BET SSA (m^2g^{-1})	Υ (%)[(b)]
0V-SiWTi	0	20	10	78	0
0.5V-SiWTi	0.5	19	67	72	6
1V-SiWTi	1	21	148	61	14
2V-SiWTi	2	55	198	21	80

[(a)] estimated from XRD in Figure 8-5, [(b)] determined from theoretical saturation value (7.9 VO_x nm^{-2} [135]) for monolayer coverage and the BET surface area

Figure 8-6 shows the calcination temperature dependence of the structural changes expressed in terms of the integral areas of the $CeVO_4$ and CeO_2 peaks (**Figure 8-6b**, data from **Figure 8-4b** and **Figure 8-4c**), of the corresponding $r(V_2O_5)$ (**Figure 8-6c**, eq. (8.1)) and of the catalytic performance expressed in terms of k_{mass} (**Figure 8-6a**, data from **Figure 8-1**). The appearance of the CeO_2 reflections, the decrease of those of $CeVO_4$ and the increase of the k_{mass} after calcination at 700°C revealed that decomposition of supported $CeVO_4$ started between 650 and 700°C. The catalytic activity (k_{mass}) passed through a maximum value after calcination at 750°C, which matched with the maximum of CeO_2 formation.

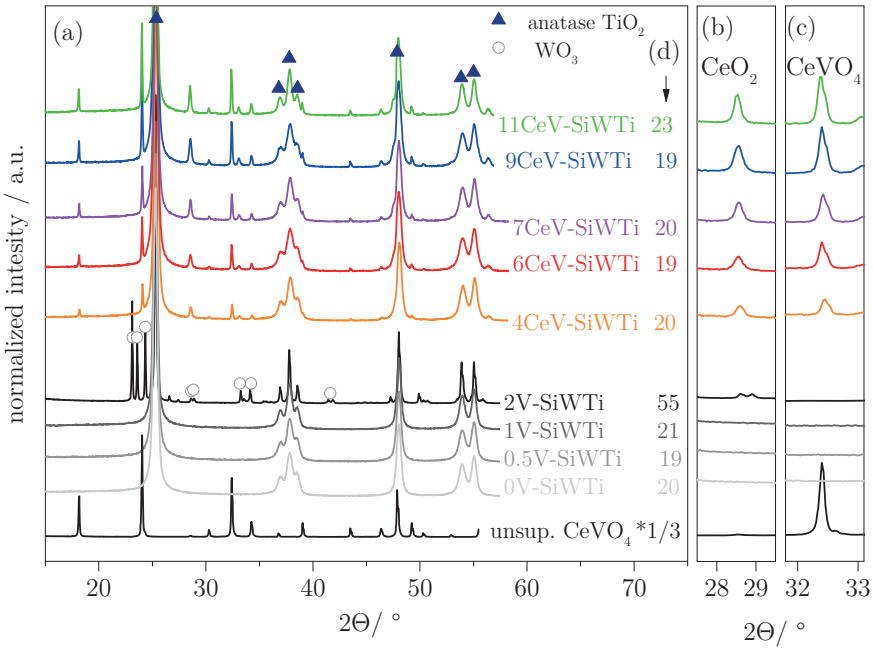

Figure 8-5. (a) XRD patterns of unsupported $CeVO_4$ (×1/3), SiWTi, 0.5V-SiWTi, 1V-SiWTi and 2V-SiWTi and 4, 6, 7, 9, and 11CeV-SiWTi calcined at 750°C. TiO_2 anatase crystallite sizes (d) were determined from the Scherrer equation. (b, c) Enlarged 2Θ regions correspond to selected reflections of CeO_2 and $CeVO_4$.

The increase in $r(V_2O_5)$, which is responsible for the SCR reaction on V_2O_5-based catalysts (see Chapter 3 and 4), also became measurable after calcination at 700°C and increased continuously with increasing calcination temperature. The k_{mass} value of 6CeV-SiWTi-750°C (79 $cm^3g^{-1}s^{-1}$, **Table 8-2**) was between those of 0.5V-SiWTi (67 $cm^3g^{-1}s^{-1}$, **Table 8-3**) and 1V-SiWTi (148 $cm^3g^{-1}s^{-1}$)

and the NO_x conversion was intermediate between those of the two V_2O_5-based catalysts (**Figure 8-2b**). Accordingly, *r(V₂O₅)* of 6CeV-SiWTi-750°C (ca. 0.7 wt%) was intermediate between the nominal V_2O_5 loadings of 0.5V-SiWTi and 1V-SiWTi. Therefore, the activity of 6CeV-SiWTi was closely related to the evolution of SCR-active VO_x species and to the decomposition of $CeVO_4$.

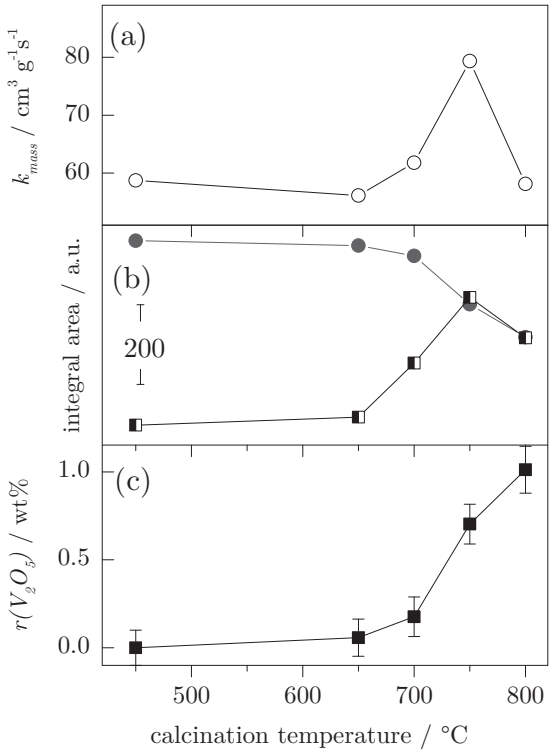

Figure 8-6. (a) k_{mass} values obtained at 300°C for 6CeV-SiWTi calcined at the indicated temperatures. (b) XRD peak integral areas of 6CeV-SiWTi ((●) $CeVO_4$, 32.4°; (◧) CeO_2, 28.6°, data from Figure 8-4). (c) Released VO_x (calculated and displayed as V_2O_5 (*r(V₂O₅)*).

In **Figure 8-7**, the catalysts with the highest NO_x conversion for each metal vanadate, namely 5FeV-SiWTi (**Figure 8-7a-c**), 9CeV-SiWTi (**Figure 8-7d-f**) and 10ErV-SiWTi (**Figure 8-7g-i**) were compared with each other with respect to k_{mass}, the relevant XRD peak integrals and the estimated *r(V₂O₅)* for each composition. The k_{mass} of the fresh catalysts was rather modest. Similar to **Figure 8-6**, calcination at higher temperature produced increasingly active catalysts which is evident at 600°C for 5FeV-SiWTi (**Figure 8-7a**), at 700°C for 9CeV-SiWTi (**Figure 8-7d**) and only limited above 700°C for 10ErV-

SiWTi (**Figure 8-7g**). Moreover, the activity of 5FeV-SiWTi and 9CeV-SiWTi decreased sharply after calcination at 700 and 800°C, respectively. The integrals of selected XRD reflections of the corresponding vanadate and oxide phases closely followed this behavior (**Figure 8-7b**, **Figure 8-7e** and **Figure 8-7h**). The decrease of the $FeVO_4$ reflection and the appearance of Fe_2O_3 (**Figure 8-7b**) started to be noticeable at around the same temperature as the change in k_{mass}. $FeVO_4$ vanished completely above 650°C. Fe_2O_3 still slightly increased after calcination at 700°C before passing through a minimum at 750°C that was concomitant to the appearance and decomposition of Fe_2WO_6. This observation suggests that iron released from $FeVO_4$ decomposition reacted with WO_3 of SiWTi. The formation of Fe_2WO_6 above 650°C is plausible because a metastable α-Fe_2WO_6 can form at 650 - 750°C [275].

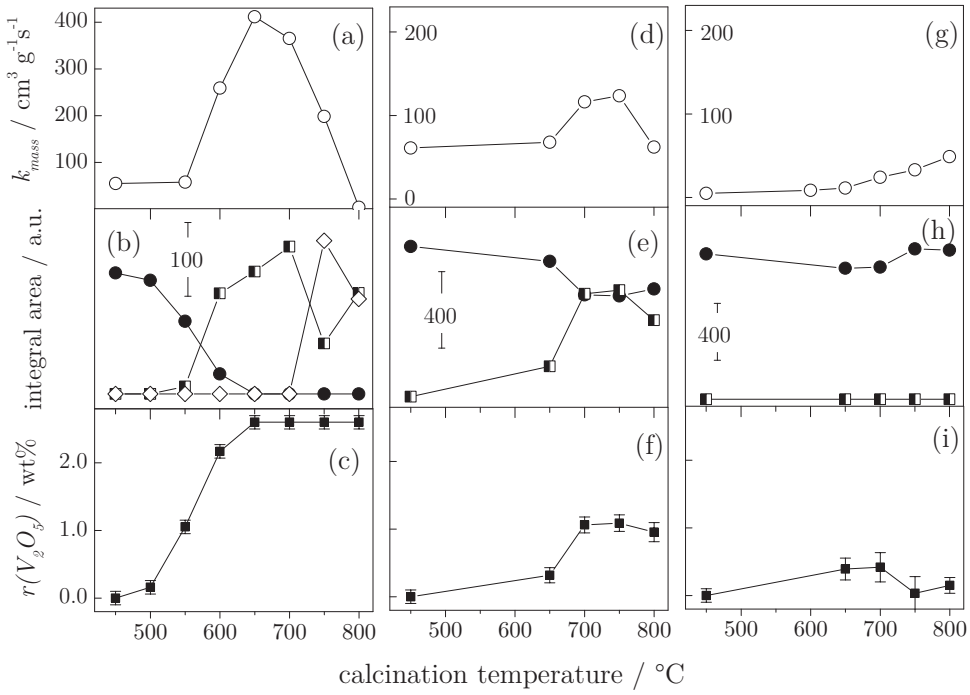

Figure 8-7. k_{mass} values obtained at 300°C for (a) 5FeV-SiWTi, (d) 9CeV-SiWTi and (g) 10ErV-SiWTi calcined at the indicated temperatures. (b) XRD peak integral areas of 5FeV-SiWTi (● $FeVO_4$, 27.2°; ◧ Fe_2O_3, 33.1°; ◇ Fe_2WO_6, 31.0°, data from Figure 8-9). (e) XRD peak integral areas of 9CeV-SiWTi (● $CeVO_4$, 32.4°; ◧ CeO_2, 28.6°). (h) XRD peak integral areas of 10ErV-SiWTi (● $ErVO_4$, 33.6°; ◧ Er_2O_3, 29.3°, data from Figure 8-8). (c,f,i) Corresponding estimated released fractions of V_2O_5 ($r(V_2O_5)$).

9CeV-SiWTi progressed similarly exhibiting an increase of CeO_2 content and a decrease of $CeVO_4$ after calcination at 700°C. Complete disappearance of the $CeVO_4$ phase never occurred and the extent of decomposition did not change considerably above 700°C. Finally, in marked contrast to FeV-SiWTi and CeV-SiWTi, the $ErVO_4$ phase in 10ErV-SiWTi remained almost unperturbed at all calcination temperatures and no Er_2O_3 could be detected by XRD (**Figure 8-7h**). The data of **Figure 8-7** indicates that the supported metal vanadates underwent decomposition to different extents. The propensity to decomposition was in the order $FeVO_4$>$CeVO_4$>$ErVO_4$ and followed the stability order of the unsupported counterparts, $FeVO_4$<$CeVO_4$<$ErVO_4$ [173, 276-277]. $FeVO_4$ is the least stable vanadate and decomposes consistently at lower temperature once it is supported on SiWTi.

The decomposition of supported $FeVO_4$ and $CeVO_4$ generated the corresponding single oxides and free VO_x species on the catalyst. The estimated amounts of $r(V_2O_5)$ are displayed in **Figure 8-7c**, **Figure 8-7f** and **Figure 8-7i** for 5FeV-SiWTi, 9CeV-SiWTi and 10ErV-SiWTi, respectively. It is remarkable that, similar to 6CeV-SiWTi (**Figure 8-6**), the changes of $r(V_2O_5)$ and k_{mass} are closely correlated. **Figure 8-7e** demonstrates that complete $FeVO_4$ decomposition into VO_x and oxide/tungstate species occurred after calcination above 600°C. 5FeV-SiWTi was the most active SCR catalyst in the series shown in this work and exhibited the largest fraction of released VO_x. A remaining vanadate phase was detected at all calcination temperatures in 9CeV-SiWTi and 10ErV-SiWTi and the maximum $r(V_2O_5)$ was ca. 1.1 wt% and 0.4 wt%, respectively. As a consequence, 9CeV-SiWTi exhibited moderate SCR activity above the calcination temperature of 700°C. The SCR activity of this sample matched that of 1V-SiWTi (**Figure 8-2b**), a strong evidence for the direct correlation between $r(V_2O_5)$ and NO_x conversion for this type of catalysts.

To this end, 10ErV-SiWTi barely showed any SCR activity in agreement with the negligible value of $r(V_2O_5)$. Therefore, the poor reactivity of ErV-SiWTi catalysts can be attributed to the high thermal stability of $ErVO_4$ and to its inability to decompose on SiWTi (**Figure 8-8**). The three metal vanadate-

based catalysts exhibited improved SCR activity only after calcination at temperatures where the vanadate phases decomposed.

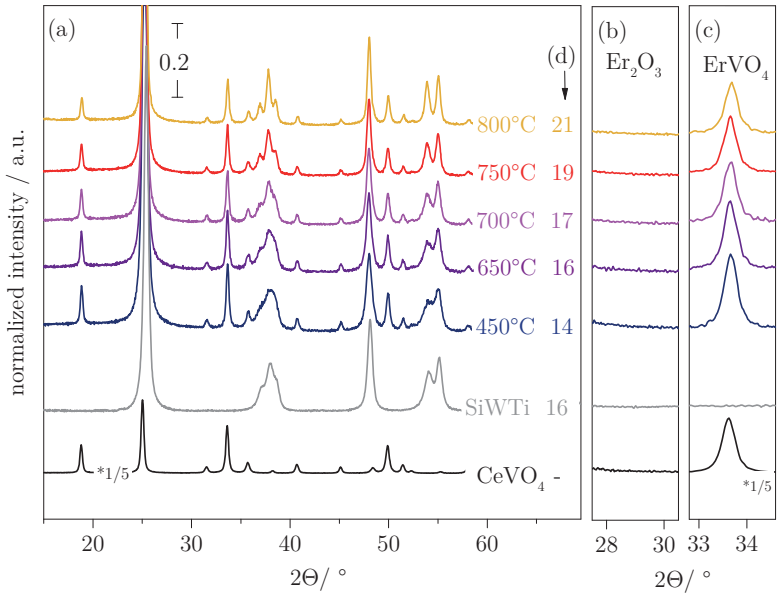

Figure 8-8. (a) XRD patterns of unsupported $ErVO_4$ (*1/5), SiWTi-700°C and of 10ErV-SiWTi calcined at the indicated temperatures. TiO_2 anatase crystallite sizes (d) were determined from the Scherrer equation. (b, c) Enlarged 2Θ regions correspond to selected Er_2O_3 and $ErVO_4$ reflections.

The decomposition of the vanadates also affected the thermal stability of the catalysts. 5FeV-SiWTi, which displayed the largest fraction of released V_2O_5, experienced the largest extent of phase transition from anatase to rutile after calcination at 800°C (**Figure 8-9**), followed by 9CeV-SiWTi and 10ErV-SiWTi. The extent of sintering of the support is thus dependent on the amount of VO_x that is made available from decomposition of the vanadate, in agreement with the role of vanadium in promoting the phase transition of TiO_2 in SCR catalysts [75, 278]. The lower the temperature of vanadate decomposition, the earlier SiWTi sintered.

It has to be mentioned that the V content of 5FeV-SiWTi (2.7 wt% V_2O_5) was lower compared to that of 9CeV-SiWTi (3.3 wt% V_2O_5) and 10ErV-SiWTi (3.3 wt% V_2O_5). The 5 wt% $FeVO_4$ loading of 5FeV-SiWTi was selected based on its optimal performance and after the consideration that a high loading accelerates the sintering of the support (see Chapter 7). In this respect, FeV-SiWTi

with a $FeVO_4$ loading equivalent to the 3.3 wt% V_2O_5 of 9CeV-SiWTi and ErV-SiWTi would cause severe aging already at moderate calcination temperatures. The effect of sintering was already evident in the XRD patterns (**Figure 8-9**) and in the decreasing k_{mass} values (**Figure 8-6a**) of 5FeV-SiWTi calcined at 700 - 800°C.

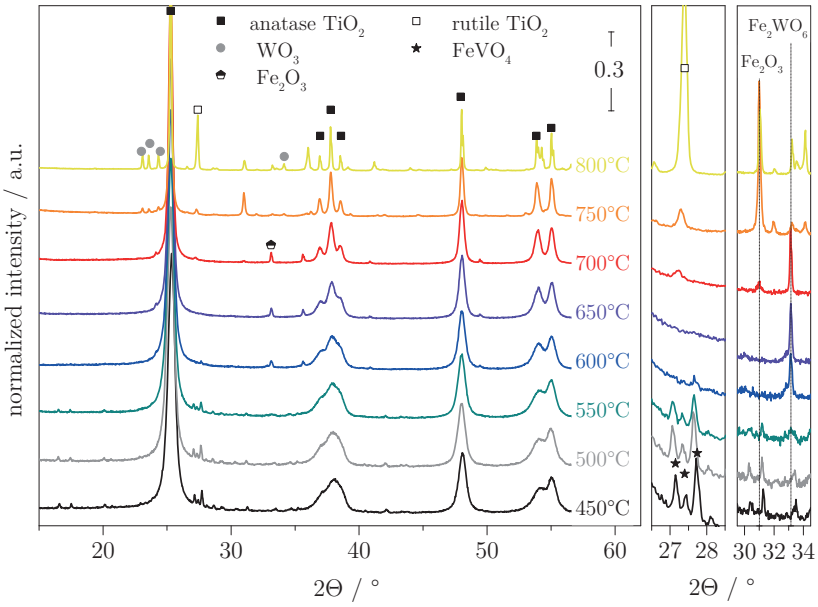

Figure 8-9. (a) XRD patterns of supported 5FeV-SiWTi calcined at the indicated temperatures. (b, c) Enlarged 2Θ regions correspond to selected reflections of $FeVO_4$ and Fe_2WO_6 / Fe_2O_3.

Compared to 5FeV-SiWTi, $r(V_2O_5)$ of 9CeV-SiWTi and 10ErV-SiWTi was lower at all calcination temperatures (**Figure 8-6c**, **Figure 8-6f** and **Figure 8-6i**, respectively) and the SiWTi support was not affected by sintering or by phase transitions. This is also evident by comparison of the k_{mass} values after calcination at 750°C in **Table 8-2** and **Table 8-3**. CeV-SiWTi catalysts exhibited increasing NO_x conversion with increasing $CeVO_4$ loading and increasing amount of released $r(V_2O_5)$, which however never exceeded values higher than ca. 1 wt%. Hence, a direct correlation between $r(V_2O_5)$ and SCR activity (k_{mass}) can be obtained only when VO_x species are not yet initiating the SiWTi sintering. The vanadates were therefore compared at lower but identical V_2O_5 content ($MeVO_4$ loading corresponding to 2 wt% V_2O_5, **Figure 8-10**) and the

same set of experiments was conducted as in **Figure 8-6**. This guaranteed a retarded sintering of the support and thus a more careful comparison. Although small differences in the onset of temperature of decomposition and formation of metal oxides were found, the correlation between catalytic activity and $r(V_2O_5)$ remained valid. The increase in NO_x conversion upon calcination can be conclusively linked to the partial or complete decomposition of the metal vanadates into single metal oxides and VO_x species. Despite the activation through calcination at high temperature, the rare earth metal based catalysts were not as active as conventional V_2O_5-based catalysts because only a fraction of the metal vanadate decomposed.

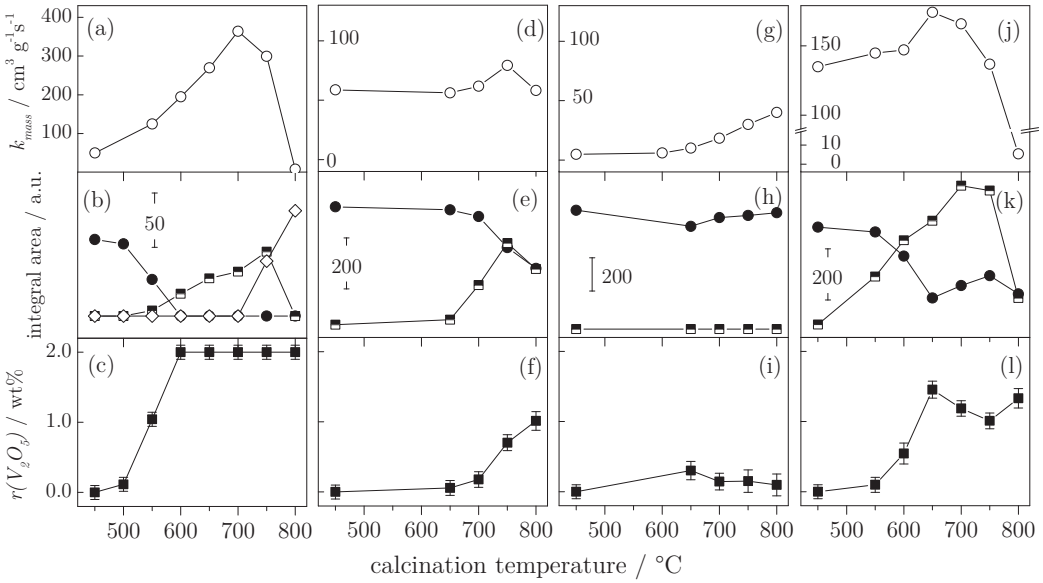

Figure 8-10. k_{mass} values obtained at 300°C for (a) 4FeV-SiWTi, (d) 6CeV-SiWTi, (g) 6ErV-SiWTi and (j) 6CeV-dried-SiWTi calcined at the indicated temperatures. (b) XRD peak integral areas of 4FeV-SiWTi ((●) $FeVO_4$, 27.2°; (◧) Fe_2O_3, 33.1°; (◇) Fe_2WO_6, 31.0°), (e) 6CeV-SiWTi ((●) $CeVO_4$, 32.4°; (◧) CeO_2, 28.6°), (h) 6ErV-SiWTi ((●) $ErVO_4$, 33.6°; (◧) Er_2O_3, 29.3°) and (k) 6CeV-dried-SiWTi ((●) $CeVO_4$, 32.4°; ◧ CeO_2, 28.6°). (c, f, i and l) Corresponding estimated released fractions of V_2O_5 ($r(V_2O_5)$).

Reference catalysts with the similar V_2O_5 loading as the $r(V_2O_5)$ of $MeVO_4$ demonstrated the validity of the correlation between activity and $r(V_2O_5)$. It has to be mentioned that the correlation was not anymore valid after severe aging of the catalyst at 800°C. While the $MeVO_4$ decomposition still occurs,

the catalyst starts sintering (phase transformation of TiO_2 and crystallite growth of WO_3, **Figure 8-4**) and the surface area decreases, factor that are responsible for the drop in the catalytic activity. This phenomenon is initiated at lower calcination temperature with increasing V content.

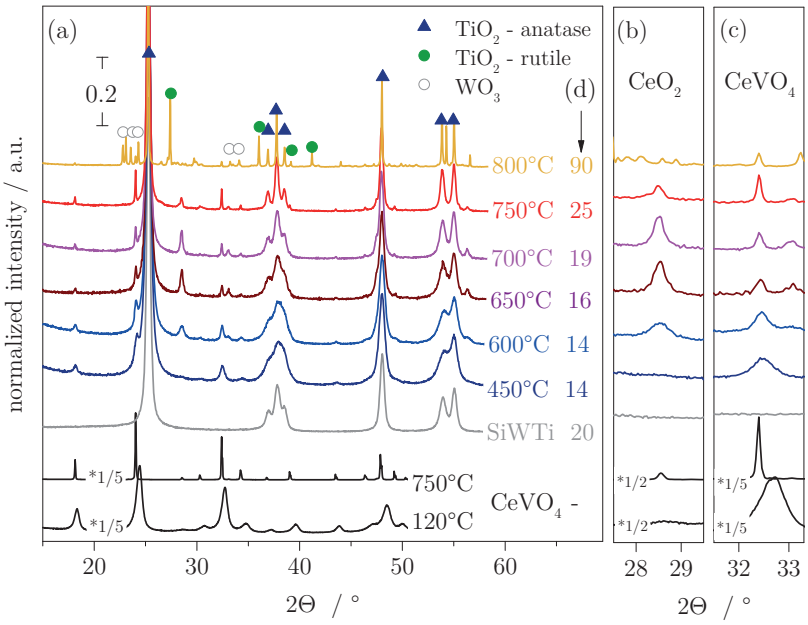

Figure 8-11. (a) XRD patterns of unsupported $CeVO_4$ (dried at 120°C and calcined at 750°C), SiWTi and 6CeV-dried-SiWTi calcined at the indicated temperatures. (b, c) Enlarged 2Θ regions correspond to CeO_2 and $CeVO_4$ reflections.

The selection of an alternative source of $CeVO_4$ may represent an option to improve the performance of a vanadate-based catalyst. $CeVO_4$ used to produce the CeV-SiWTi series so far was pre-treated at 700°C and was thus already a crystalline material (crystallite size: 80 ± 1 nm according to XRD, **Figure 8-4**). The pre-treatment of $CeVO_4$ was beneficial for the characterization of the catalysts by XRD because the $CeVO_4$ reflections were clearly visible. However, the initial physico-chemical properties of the material may influence the NO_x conversion. Smaller crystallites (14 ± 2 nm, **Table 8-1**) were measured when $CeVO_4$ was only dried after precipitation from the Ce and V precursors. A catalyst identical to 6CeV-SiWTi was then prepared with 5.6 wt% of dried $CeVO_4$ (6CeV-dried-SiWTi, 2.0 wt% V_2O_5). The behavior of this material (**Figure 8-10j-l**) in terms of changes in phase composition with increasing calcination temperature was similar to that of 6CeV-SiWTi (**Figure 8-10d-f**, see also

Figure 8-6). The *r(V_2O_5)* value (calculated from data in **Figure 8-11**) and k_{mass} increased with increasing temperature, while $CeVO_4$ progressively decomposed to CeO_2, but 6CeV-dried-SiWTi exhibited twofold values of k_{mass} and *r(V_2O_5)* (174 $cm^3g^{-1}s^{-1}$ and 1.5 wt%) compared to 6CeV-SiWTi (79 $cm^3g^{-1}s^{-1}$ and 0.7 wt%). Therefore, around twice as much $CeVO_4$ decomposed in the case of 6CeV-dried-SiWTi in agreement with the twofold increase in NO_x conversion. Moreover, the highest k_{mass} of CeV-dried-SiWTi was obtained already after calcination at 650°C, i.e. 100°C lower than in the case of CeV-SiWTi (750°C), which was accompanied by aging effects after calcination at 800°C.

Based on the above observations on the various vanadate catalysts, it was concluded that the higher activity at lower calcination temperature was caused by an easier $CeVO_4$ decomposition as a result of the smaller particle size and the partially amorphous state of $CeVO_4$. However, this also implies that deactivation occurred at lower temperature and that it was caused by an early and accelerated sintering induced by the free VO_x species according to the mechanisms known for V_2O_5-based catalysts. Hence, small $MeVO_4$ particles are beneficial for the activity of vanadate-based catalysts, not because $MeVO_4$ is more active but because the onset of its decomposition is shifted to lower temperature.

8.4.2 BET surface area and surface coverage of V

The BET surface area of the catalysts (**Table 8-2** and **Table 8-3**) provided precious information about the sintering of the support material and was a crucial parameter to estimate the V surface coverage. The surface area of SiWTi (78 m^2/g) decreased with increasing V content to 72 m^2/g (0.5V-SiWTi), 61 m^2/g (1V-SiWTi) and to 21 m^2/g (2V-SiWTi) after calcination at 750°C, thus reflecting the influence of V content on the stability of the support material (see Chapter 3). It decreased only slightly up to 1 wt% V_2O_5, indicating that SiWTi withstands calcination at 750°C within a certain threshold of V content. In contrast, the surface area of the CeV-SiWTi catalysts did not change up to 9 wt% $CeVO_4$ (ca. 70 m^2/g) after calcination at 750°C, while it decreased to 53 m^2/g in the case of 11CeV-SiWTi, presumably because *r(V_2O_5)* exceeded 1 wt% (**Table 8-2**). This is also evident in the case of FeV-SiWTi,

where the surface area dropped below 50 m^2/g in both materials used in this study.

The nominal V surface coverage (Υ) was calculated from the BET surface area assuming a theoretical value of 7.9 VO_x nm^{-2} for a monolayer coverage (**Table 8-2** and **Table 8-3**) [135]. In Chapter 3 it was shown that ideal V_2O_5-WO_3-TiO_2 catalysts in terms of activity and stability possess Υ values comprised between 25% and 50%. Below 25%, the V content is too low and/or the surface area too high accounting for their modest catalytic activity but also for their resistance to thermal aging. Higher NO_x conversion can be achieved by increasing the loading of the active phase or by decreasing the surface area upon increasing the calcination temperature. However, the stability of the catalyst is not guaranteed above Υ = 50% and the NO_x conversion decreases after exposure to high calcination temperature. This argument holds also for the V-SiWTi catalysts of this work.

0.5V-SiWTi and 1V-SiWTi displayed Υ values of 6% and 14%, respectively (**Table 8-3**). By increasing the V content to 2 wt% (2V-SiWTi) and the calcination temperature to 750°C, Υ increased to 80% and the sintering of SiWTi was evident in XRD (**Figure 8-5**). **Table 8-2** demonstrates that the estimated Υ values of all CeV-SiWTi and ErV-SiWTi catalysts were never above 20% after calcination at 750°C thus matching the low activity levels of these catalysts. The increase in $CeVO_4$ loading resulted in higher Υ because of the increasing $r(V_2O_5)$ value. This was also the fate of 5FeV-SiWTi (Υ = 69%) because of the complete decomposition of $FeVO_4$. On the contrary, the value of Υ obtained for 4FeV-SiWTi was within the 25 - 50% range (34%) and lead to the highest k_{mass} value among all the catalysts after calcination at 750°C (**Table 8-2** and **Table 8-3**).

8.4.3 H_2-TPR

The surface redox properties of selected catalysts were characterized by H_2-TPR (**Figure 8-12**). While XRD cannot deliver evidence for the presence of VO_x species, H_2-TPR is sensitive to reduction of V^{5+} species irrespective of

their crystallinity degree. This is demonstrated in **Figure 8-12a** and **Figure 8-12d** for 1V-SiWTi.

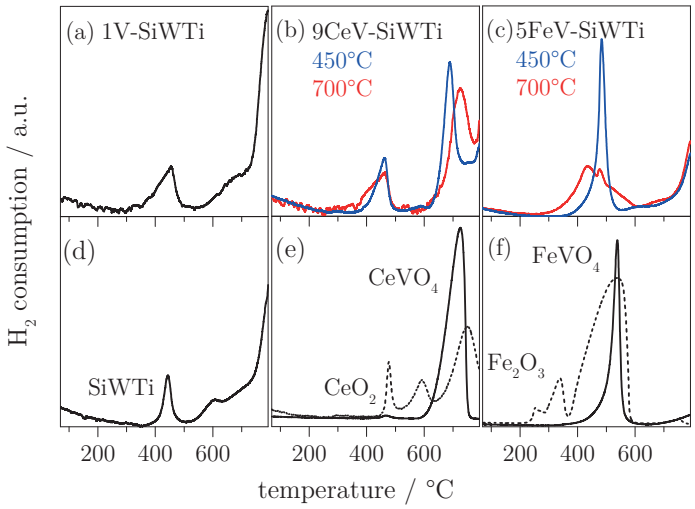

Figure 8-12. H_2-TPR profiles of (a-c) selected SCR catalysts and (d-f) corresponding reference materials.

The symmetric H_2 consumption peak of SiWTi at ca. 440°C (**Figure 8-12d**) corresponding to the $W^{6+} \rightarrow W^{4+}$ reduction broadened towards low temperature (380 - 460°C) because of the overlap with the $V^{5+} \rightarrow V^{3+}$ reduction [62] in 1V-SiWTi (**Figure 8-12a**). Further reduction events at ca. 600 and 800°C belong to complete reduction of the WO_3 component [279]. Unsupported $CeVO_4$ (**Figure 8-12e**) and $FeVO_4$ (**Figure 8-12f**) reduced in a single event at 725 and 540°C, respectively demonstrating the ease of reducibility of the latter vanadate. These reduction events shifted to lower temperature in fresh 9CeV-SiWTi (**Figure 8-12b**) and fresh 5FeV-SiWTi (**Figure 8-12c**) as a result of the presence of SiWTi, while the reduction peak of WO_3 was evident only in 9CeV-SiWTi. The H_2-TPR profiles changed significantly upon calcination at 750°C.

The thermogram of 9CeV-SiWTi is complex and presents two H_2 consumption events at 460 and 725°C. The latter reduction peak may be associated with the reduction of $CeVO_4$, the XRD data of **Figure 8-4**, however, showed that only a portion of $CeVO_4$ survived calcination at 750°C. Comparison with the H_2-TPR of CeO_2 reveals that the high temperature reduction needs to be associated to reduction of both the remaining $CeVO_4$ and the CeO_2 [280] produced up-

on $CeVO_4$ decomposition. The increased H_2 consumption at ca. 400°C is attributed to reduction of the corresponding fraction of VO_x species released from decomposed $CeVO_4$ at 750°C. While $CeVO_4$ was still partly available in CeV-SiWTi, $FeVO_4$ decomposition was extensive in 5FeV-SiWTi calcined at 700°C (**Figure 8-12c**). The sharp reduction peak of bulk $FeVO_4$ was replaced almost completely by a broad feature at 300 - 600°C after calcination at 700°C that was assigned to the simultaneous reduction of Fe and V oxides formed upon $FeVO_4$ decomposition and of W^{6+} in SiWTi. The remarkable difference between the two thermograms of 5FeV-SiWTi clearly suggests that $FeVO_4$ present in the fresh sample disappears after calcination above 700°C, in agreement with the data of **Figure 8-7**.

8.4.4 Diffuse reflectance UV-vis spectroscopy

In order to verify the presence of VO_x species from decomposition of the supported metal vanadates, DRUV spectra of CeV-SiWTi (**Figure 8-14a** and **Figure 8-14b**) and FeV-SiWTi (**Figure 8-14c** and **Figure 8-14d**). All supported metal vanadate samples were background corrected with a spectrum of SiWTi in order to visualize surface species which would otherwise be invisible due to the high absorbance of TiO_2 (**Figure 8-13**). Despite the awareness of the impact of drying the samples prior to spectroscopic investigations [281], no substantial difference between the spectra of selected ambient and dehydrated samples was found (**Figure 8-15**), thus the catalysts were analyzed without drying.

The spectra in **Figure 8-14** were dominated by a signal at ca. 388 nm that was accompanied by a weaker and broad feature extending to ca. 700 nm. In the case of CeV-SiWTi and 0.5V-SiWTi, a second sharp signal at 355 nm was also present. The 355 and 388 nm signals intensified not only with increasing $CeVO_4$ loading (**Figure 8-14a**) but also with increasing calcination temperature (**Figure 8-14b**). While it could be argued from **Figure 8-14a** that the stronger absorbance is a loading effect, **Figure 8-14b** gives a clear indication that these two features derive from increasing amounts of VO_x species. An increase in the calcination temperature of 9CeV-SiWTi promoted $CeVO_4$ decomposition into CeO_2 and VO_x species (**Figure 8-7**). Because CeO_2 mainly ab-

sorbs below 300 nm (**Figure 8-16a**), the signals between 300 and 400 nm were assigned to signatures of VO_x species. The increased intensity of these two signals with increasing $CeVO_4$ loading (**Figure 8-14a**) is the result of an increased amount of released vanadium (**Table 8-2**). Identical features between 300 and 400 nm were also found in 0.5V-SiWTi (**Figure 8-14a**), indicating that similar VO_x species to those obtained from $CeVO_4$ decomposition cover the SiWTi surface.

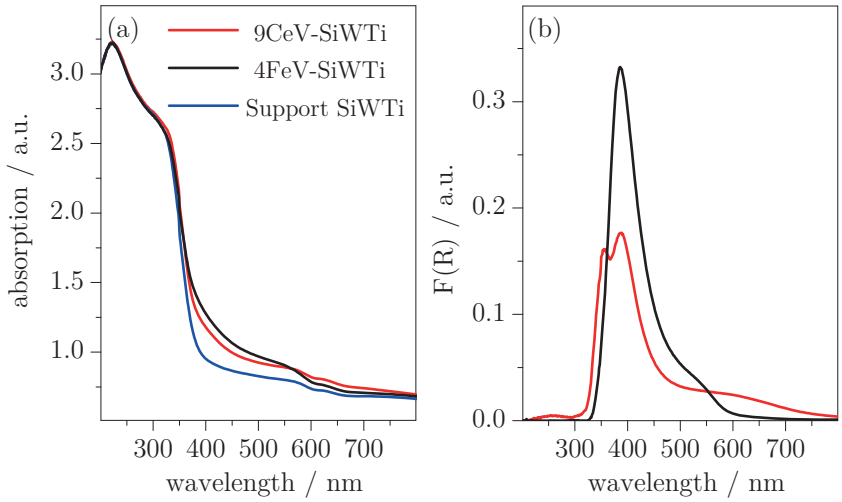

Figure 8-13. (a) Raw and (b) SiWTi background corrected DRUV spectra of 9CeV-SiWTi calcined at 750°C and 4FeV-SiWTi calcined at 650°C.

In the case of 5FeV-SiWTi (**Figure 8-14d**) only one main feature at 389 nm was visible above a calcination temperature of 550°C in correspondence to the $FeVO_4$ decomposition occurring at around this temperature. This feature was not visible in the fresh state, supporting the findings that $FeVO_4$ did not decompose at this temperature (**Figure 8-7b**, see also Chapter 7). The spectra did not change significantly after calcination at 700°C, suggesting that no further change occurred in the VO_x population. This is in agreement with the observation that at this temperature supported $FeVO_4$ mostly decomposed to Fe_2O_3 (**Figure 8-7b** and **Figure 8-14c**) and that $r(V_2O_5)$ remained constant at the maximum value (**Figure 8-7c**). After calcination above 650°C, 5FeV-SiWTi showed stronger signals compared to those of 4FeV-SiWTi (**Figure 8-14c**) as a consequence of the higher $r(V_2O_5)$ value at the equivalent temperatures.

The decomposition of the supported metal vanadates could also be followed by DRUV. The signature of bulk $CeVO_4$ in **Figure 8-14b** was centered at ca. 550 nm extending to 700 nm (see also **Figure 8-16** and **Figure 8-17a**). This signal attenuated steadily with increasing calcination temperature but never disappeared suggesting that a fraction of $CeVO_4$ survived above 700°C in agreement with the trends observed in the XRD data. The same signal increased with increasing $CeVO_4$ loading after calcination at 750°C suggesting that the remaining fraction of $CeVO_4$ was proportional to the $CeVO_4$ loading (**Figure 8-14a**). A similar behavior was observed also for the FeV-SiWTi catalysts (**Figure 8-14c** and **Figure 8-14d**). $FeVO_4$, identified by the broad absorption from 400 to 500 nm, was only visible in fresh FeV-SiWTi (**Figure 8-17b**). By increasing the calcination temperature, a feature at ca. 525 nm appeared and intensified that was assigned to the growth of the Fe_2O_3 phase (**Figure 8-16a** and **Figure 8-17d**) in agreement with the XRD results.

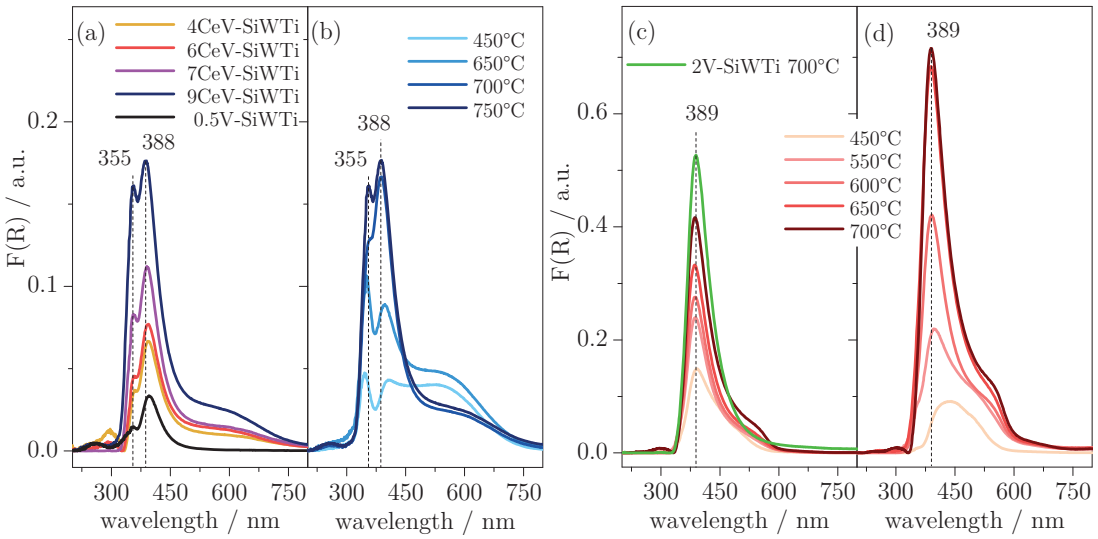

Figure 8-14. Diffuse reflectance UV-vis spectra of (a) CeV-SiWTi and 0.5V-SiWTi calcined at 750°C, (b) 9CeV-SiWTi, (c) 4FeV-SiWTi (and 2V-SiWTi) and (d) 5FeV-SiWTi calcined at various temperatures.

A more detailed assignment of the features observed in the DRUV spectra to specific VO_x species is not straightforward. The available literature is ambiguous on the nuclearity of the VO_x species. For the purpose of this discussion and according to the trends visible in the spectra presented, it was referred to VO_x species organized in small and large domains to avoid speculations. It is evi-

dent from the presented spectra that with higher V_2O_5 loading (e.g. 2V-SiWTi) or large *r(V_2O_5)* (FeV-SiWTi, **Figure 8-14c** and **Figure 8-14d**), only the 389 nm feature was detected. Because the calculated VO_x surface coverage was higher for 2V-SiWTi and FeV-SiWTi compared to CeV-SiWTi samples (**Table 8-2** and **Table 8-3**), it was concluded that the 389 nm feature could origin from extended domains of VO_x. This is further strengthened by the attribution of a transition at ca. 400 nm to polymerized VO_5/VO_6 species on SiO_2 in both ambient and dehydrated conditions [282-283] and to polymeric distorted tetrahedral VO_4 units on TiO_2 [284-285]. The DRUV spectrum of 0.5V-SiWTi-750 in **Figure 8-14a** exhibited a similar signal at 389 nm but of lower intensity because of the lower equivalent V content of 0.5V-SiWTi than in all CeV-SiWTi catalysts. It can also be assumed that the impregnation of SiWTi to obtain 0.5V-SiWTi produced a better V_2O_5 dispersion thus leading to a lower extent of agglomeration. The contribution of the VO_x species in the large domains increased upon increasing the calcination temperature of 9CeV-SiWTi (**Figure 8-14b**), 4FeV-SiWTi (**Figure 8-14c**) and 5FeV-SiWTi (**Figure 8-14d**), suggesting that the released fraction of VO_x from decomposition of the metal vanadate produced a high degree of polymerization.

The signal at 355 nm was present only in catalysts with low *r(V_2O_5)* (CeV-SiWTi, affording between 0.5 and 1.1 wt% V_2O_5, **Table 8-2**) and in 0.5V-SiWTi (**Figure 8-14a**). It is therefore plausible that this feature origins from small VO_x domains. Also the reference materials $Zn_3(VO_4)_2$ or Na_3VO_4 (isolated monomeric tetrahedral units; 349 and 352 nm, respectively) and $Ba_2V_2O_7$ or $Sr_2V_2O_7$ (dimeric tetrahedral units; 336 and 343 nm, respectively) exhibited a similar $O \rightarrow V^{5+}$ charge transfer transition [286-287]. The V_2O_5 loading was linked to the presence of this transition: the signal vanished by increasing the V_2O_5 loading to 2 wt% (2V-SiWTi, **Figure 8-14c**) indicating that all VO_x units agglomerated to form the domains characterized by the signal at 388 nm. The transition from small to large VO_x domains at higher V_2O_5 loading can also be followed during the decomposition of supported $FeVO_4$. The shoulder at 355 nm was still visible in the spectrum of 5FeV-SiWTi calcined at 550°C (**Figure 8-14d**), suggesting a partial population of small VO_x domains. This is reasonable because the estimated *r(V_2O_5)* was ca. 1.0 wt% (**Figure 8-7c**).

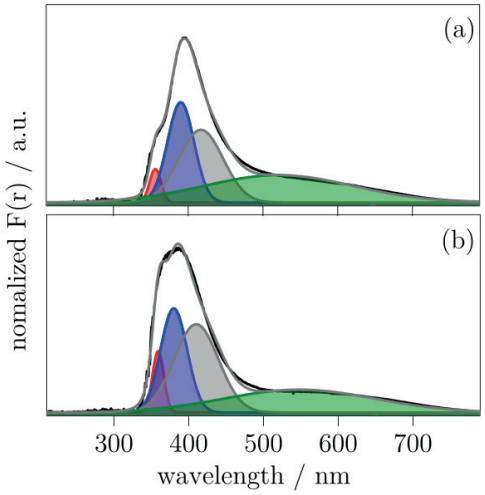

Figure 8-15. Deconvoluted *in situ* DRUV spectra of 9CeV-SiWTi calcined at 750°C. The sample was measured in O_2/N_2 (a) at RT and (b) after dehydration at 250°C for 1 h. The deconvolution revealed that the ambient and dehydrated exhibit the same absorption features. Small differences were only found in the intensity of individual contributions. Differences were also found by comparing the spectra to that of 9CeV-SiWTi (Figure 8-17c) which can be explained from the differences in the set up (presence/absence of CaF_2 window and gas flow).

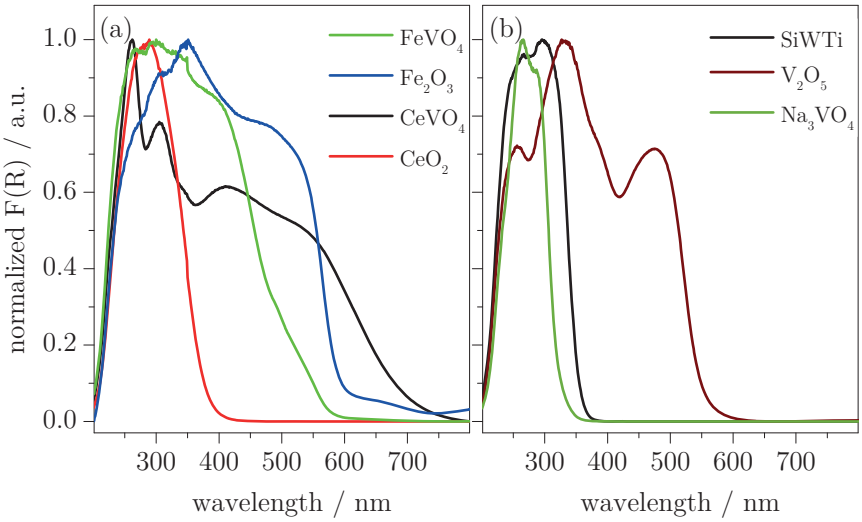

Figure 8-16. DRUV spectra of reference materials.

At higher calcination temperature, $FeVO_4$ decomposed completely into Fe_2O_3 and VO_x, thus increasing the surface VO_x concentration and causing the disap-

pearance of the signal at 355 nm at lower calcination temperature than in the case of CeV-SiWTi.

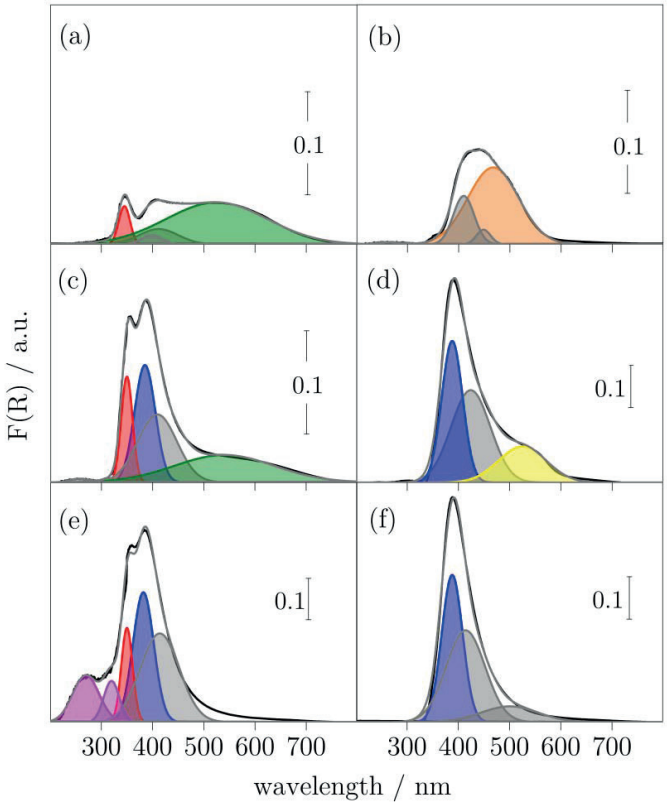

Figure 8-17. Deconvoluted *ex situ* DRUV spectra of (a) fresh 9CeV-SiWTi, (b) fresh 5FeV-SiWTi, (c) 9CeV-SiWTi-750, (e) 1V-SiWTi-750, (d) 5FeV-SiWTi-700 and (f) 2V-SiWTi-700. Red – ca. 350 nm: small domains of VO_x units; Blue – ca. 385 nm: extended domains of VO_x units; Grey – 400 - 450 nm: bulk-like V_2O_5; Green – ca. 550 nm: $CeVO_4$; Orange – ca. 465 nm: $FeVO_4$; Yellow – ca. 525 nm: Fe_2O_3; Pink – ca. 270 - 320 nm: isolated domains of VO_x units.

Finally, the low energy shoulder in the DRUV spectra of FeV-SiWTi indicates an additional feature that was isolated by fitting the spectra using a signal at ca. 400 - 450 nm (**Figure 8-17**). This signal was attributed to bulk-like V_2O_5 species [285] that were most prominent in 2V-SiWTi-700 and 5FeV-SiWTi-700. The same feature was also observed in 9CeV-SiWTi and indicates that the VO_x species represented by the peak at 389 nm further aggregated to a bulk-like V_2O_5 phase of amorphous character since they remain XRD invisible. Only 0.5V-SiWTi exhibited high energy signatures that was assigned to isolated species (**Figure 8-14a**) [283, 288]. The synthesis method used to prepare V-

SiWTi (impregnation with ammonium metavanadate) is probably beneficial to obtain more uniformly distributed VO_x species.

The deconvolution of CeV-SiWTi, FeV-SiWTi and V-SiWTi at different calcination temperatures in **Figure 8-17** was useful for distinguishing the different VO_x species more precisely. Fresh 9CeV-SiWTi (**Figure 8-17a**) featured a minor fraction of small VO_x domains (ca. 350 nm) but the absorption from $CeVO_4$ at ca. 550 nm was dominant. A third species at ca. 400 - 440 nm could be attributed to bulk-like V_2O_5 species. After calcination at 750°C (**Figure 8-17c**), the absorption from small domain VO_x units increased and the band from $CeVO_4$ absorption decreased. The most prominent new phase at ca. 385 nm was assigned to extended domains of VO_x units. A comparison with 1V-SiWTi-750 (**Figure 8-17e**), which roughly comprises one equivalent of surface V_2O_5 species, suggests that the same domains of VO_x species cover the surface. An additional feature at 270 nm suggests the presence of other V_2O_5 units, which was assigned to isolated domains.

The deconvolution was repeated for fresh 5FeV-SiWTi (**Figure 8-17b**) and after calcination at 700°C (**Figure 8-17d**) and compared to 2V-SiWTi-700 (**Figure 8-17f**). The lower calcination temperature of 5FeV-SiWTi than 9CeV-SiWTi was chosen due to the higher fraction of released VO_x species, which would induce severe catalyst aging upon calcination at 750°C. In the fresh sample (calcination at 450°C), the spectra mainly originated from $FeVO_4$ and only small contributions of bulk-like V_2O_5 were found. Calcination at 700°C revealed the presence of extended domains (385 nm) and bulk-like (400 - 450 nm) V_2O_5 species, similar to the spectra of CeV-SiWTi (**Figure 8-17c**). The feature at ca. 525 nm was assigned to Fe_2O_3, which formed upon decomposition of $FeVO_4$. Small domains of VO_x units were not detected, which is in agreement with the high V surface coverage of FeV-SiWTi. These species were also absent in the spectra of 2V-SiWTi-700 (**Figure 8-17f**), presumably due to the same reason. The signals of extended domains were also very similar to those of 5FeV-SiWTi. Especially the most prominent feature at ca. 380 nm was equal and is therefore a strong indication that the metal vanadate decomposi-

tion gives rise to VO_x species that are indistinguishable from those of V-SiWTi catalysts.

8.4.5 NH_3 adsorption - DRIFT spectroscopy

Specific surface features such as acid sites, hydroxy and terminal oxo-groups possess characteristic fingerprints that are strongly perturbed upon titration with NH_3, making infrared spectroscopy an ideal tool for the characterization of non-crystalline surface species. DRIFT spectra of adsorbed NH_3 were recorded after exposing unsupported $CeVO_4$, 6CeV-SiWTi, 9CeV-SiWTi, 1V-SiWTi and SiWTi to 500 ppm of NH_3 at 250°C for 15 min in 5 vol% O_2/N_2. The spectra of the catalysts in their fresh state (**Figure 8-18a-c**) and after calcination at 750°C (**Figure 8-18e-f**) are divided into the region of the N—H and O—H stretch modes, the overtone of the M=O stretch and the N—H deformation modes. The signals were assigned according to literature [71, 78, 123, 135, 216-218, 289].

NH_3 did not interact with unsupported $CeVO_4$ (**Figure 8-18a - Figure 8-18c**) indicating that either $CeVO_4$ did not contain surface acid sites or that the surface area (below 3 m^2/g) was too low for infrared experimentation. In the case of SiWTi supported samples calcined at 450°C, the three spectral regions showed specific features of adsorbed NH_3. The largest perturbation in the O—H stretch region was observed in the spectrum of SiWTi (**Figure 8-18a**). Negative bands appeared that were due to the consumption of surface hydroxyl groups by NH_3. The signals at 3745 and 3733 cm^{-1} corresponded to the perturbation of terminal Si-OH groups [290]. Two types of Ti-OH and one W-OH groups were visible at 3690 and 3661 cm^{-1} and at 3650 cm^{-1}, respectively. The Si-OH and Ti-OH features were less prominent in 1V-SiWTi due to the presence of VO_x species and to the overlap with the ν(V-OH) that was reported at 3645 cm^{-1} [219]. The V-OH group was most pronounced in 1V-SiWTi and less distinct in the two $CeVO_4$ containing catalysts in agreement with the limited release of VO_x in CeV-SiWTi detected in the DRUV spectra (**Figure 8-14a**).

It is possible that the Ti-OH group (shoulder at 3660 cm^{-1}) was therefore still visible in the spectrum of CeV-SiWTi. NH_3 coordinated to Lewis acid sites (δ_{as},

1603 cm^{-1}) and NH_4^+ bound to Brønsted acid sites (δ_s, 1670 cm^{-1}; δ_{as}, 1423 cm^{-1}) were visible in the region of the δ(N-H) modes (**Figure 8-18c**). These signals were of similar intensity in 1V-SiWTi, 6CeV-SiWTi and 9CeV-SiWTi. The negative feature at 1365 cm^{-1} belonged to residual sulfate species (ν_{as}(S=O)) whose presence was influenced by the addition of $CeVO_4$ and V_2O_5 in the corresponding materials [220]. The general absorption decrease in this region for the three V-containing catalysts reflects the disappearance of surface sulfate species.

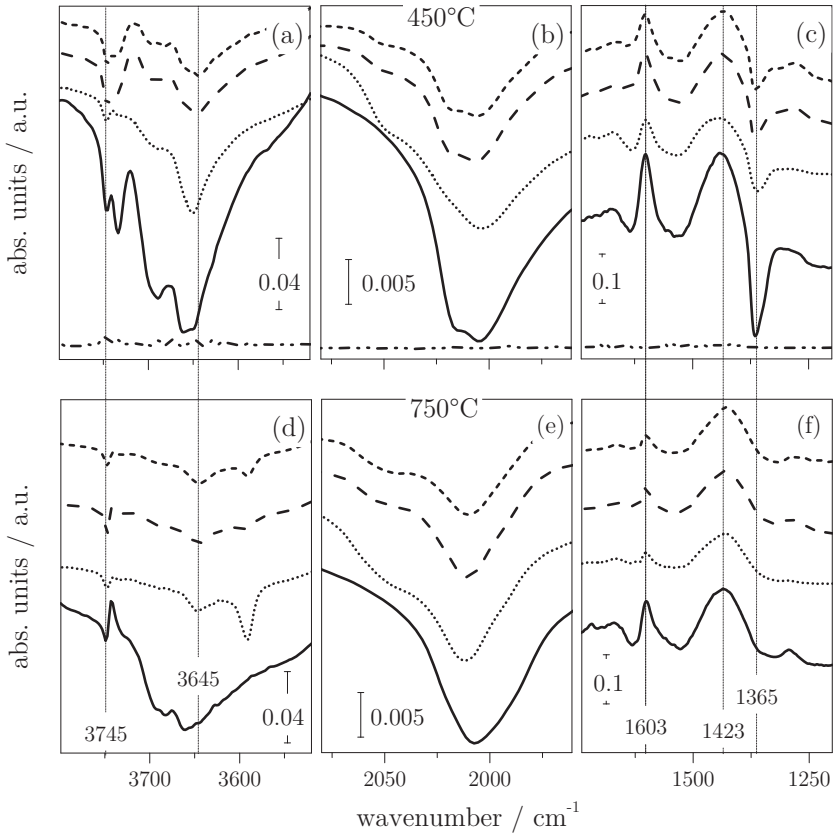

Figure 8-18. DRIFT spectra of NH_3 adsorption in the region of the OH and NH stretch (a and d), the overtone of M=O stretch (b and e) and the N−H deformation mode (c and f) on 9CeV-SiWTi (---), 6CeV-SiWTi (– – –), 1V-SiWTi (·····), SiWTi (——) and of unsupported $CeVO_4$ (–···–···) calcined at 450°C (a - c) and 750°C (e - f). The samples were exposed to 500 ppm of NH_3 for 15 min at 250°C after dehydration at 400°C for 1 h in O_2-N_2.

The extent of perturbation of the hydroxyl groups was different after calcination at 750°C (**Figure 8-18d**). Only the Si-OH signal at 3745 cm^{-1} was visible

in all materials. The intensity of the V-OH signal perturbed by NH_3 was comparable in CeV-SiWTi and 1V-SiWTi suggesting a similar level of VO_x on the surface in agreement with the corresponding V surface coverage values (for both $\Upsilon = 14\%$, **Table 8-2** and **Table 8-3**). The most prominent change in the δ(N-H) region caused by calcination at 750°C (**Figure 8-18f**) is the loss of the sulfate species [220], evident from the absence of the signal at 1365 cm^{-1}. The overall low intensity of the NH_3 signals coordinated to Brønsted and Lewis acid sites further indicates the loss of surface area after calcination at 750°C. To that end, the Brønsted and Lewis acid sites signals in 1V-SiWTi and $CeVO_4$-SiWTi were no longer of similar intensity but intensified in favor of the Brønsted acid sites whereas they were of similar intensity after 450°C calcination (**Figure 8-18c**).

Table 8-4. Contributions of the W=O (WO_A and WO_B) and V=O (VO_A and VO_B) overtone stretch modes calculated from the deconvoluted NH_3-DRIFT spectra of Figure 8-19.

	Calcination	WO_A[a] (%)	WO_B[b] (%)	VO_A[c] (%)	VO_B[d] (%)	VO_{tot} (%)
SiWTi	450	93	7	0	0	0
SiWTi	750	97	3	0	0	0
6CeV-SiWTi	450	90	0	7	3	10
6CeV-SiWTi	750	88	0	8	4	12
9CeV-SiWTi	450	85	5	8	1	9
9CeV-SiWTi	750	81	0	15	3	18
1V-SiWTi	450	77	3	17	3	20
1V-SiWTi	750	82	0	15	3	18

[a] ca. 2010 cm^{-1}; [b] ca 2020 cm^{-1}; [c] ca. 2050 cm^{-1}; [d] ca. 2040 cm^{-1}

After calcining the catalysts at 450°C (**Figure 8-18b**), the V=O overtone around 2049 cm^{-1} was visible in the CeV-SiWTi samples and most prominent in 1V-SiWTi. The presence of two W=O overtone features at ca. 2018 and 2005 cm^{-1} suggests two kinds of terminal W=O surface WO_x species. It has been proposed that a W=O signal shift to higher frequencies origins from an oligomerization of the WO_x species because of the dipole coupling between neighboring oxo-groups [224, 291-292]. It can therefore be argued that WO_x

species in different degrees of polymerization (different nuclearity of the domains) are present. After calcination at 750°C (**Figure 8-18e**), the signal at 2005 cm^{-1} shifted to 2011 cm^{-1}, indicating a growth of larger WO_x domains.

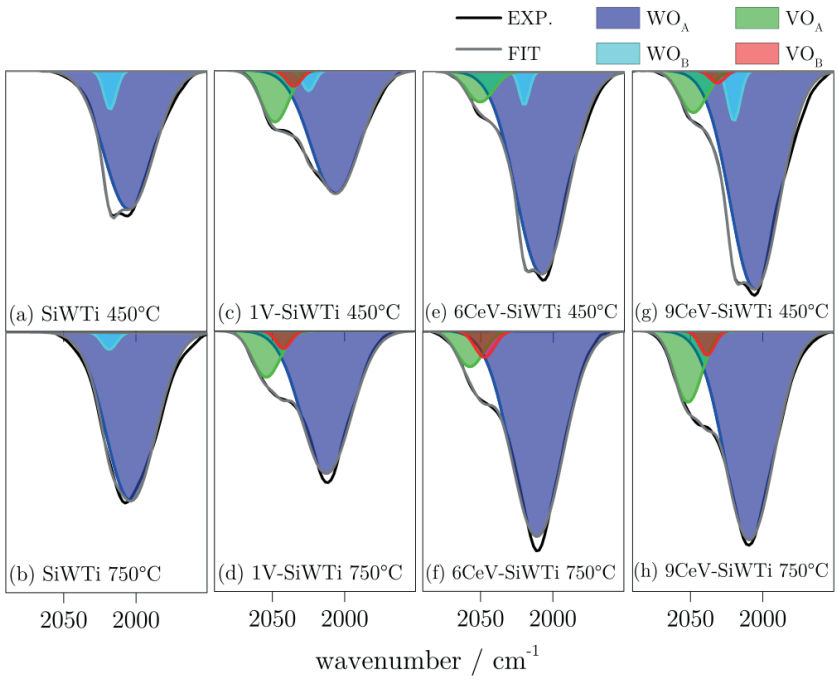

Figure 8-19. Deconvoluted DRIFT spectra of in the 2ν(W=O) and 2ν(V=O) overtone region of selected catalysts. Spectra were obtained after adsorption of NH_3 at 250°C.

For the purpose of investigating the VO_x and WO_x species more precisely, the spectral region of the overtones of the stretch modes of vanadyl (V=O) and wolframyl (W=O) groups at 2050 - 2000 cm^{-1} is represented in **Figure 8-19**. The relative intensity of these signals can also deliver information on changes of W and V surface coverage (**Table 8-4**) [293]. Because of the strong overlap of signals associated with both functional groups perturbed by NH_3 adsorption (**Figure 8-18**), the 2100 - 1950 cm^{-1} spectral region of 6CeV-SiWTi, 9CeV-SiWTi, 1V-SiWTi and SiWTi was background corrected, normalized and deconvoluted (**Figure 8-19**). This exercise clearly evidenced 2ν(W=O) features at ca. 2000 - 2020 cm^{-1} [293] for all samples and 2ν(V=O) features at ca. 2030 - 2055 cm^{-1} [271] in the vanadium containing catalysts (**Figure 8-19c** - **Figure 8-19h**). A feature was found at ca. 2050 cm^{-1} (VO_A) in the fresh catalyst and after calcination at 750°C. A second component (VO_B) at ca. 2035 cm^{-1} (fresh

state) and 2040 cm^{-1} (after calcination at 750°C) was necessary to fit the spectra satisfactorily. Association of the different degrees of nuclearity of VO_x and the corresponding energy shifts is rather ambiguous in the available literature [71, 219, 224, 282, 294-295], making the assessment of the precise nature of these signals difficult. The present data reveals that already the fresh CeV-SiWTi catalyst exhibit a limited amount of free VO_x species which were possibly formed during the washcoat procedure. It can therefore be assumed that intrinsic activity of the fresh CeV-SiWTi catalysts in **Figure 8-1** origin from small amounts of VO_x species.

The DRIFT data further showed that calcination at 750°C did not affect the V=O signals of 1V-SiWTi (**Figure 8-19c** and **Figure 8-19d**) because the VO_x content does not change and the support sintering was not initiated. However, the intensity of the V=O features in 9CeV-SiWTi increased from 9% to 18% relative to the WO_B signal after calcination at 750°C (**Figure 8-19g** and **Figure 8-19h**, **Table 8-4**). This observation agrees well with the increase in $r(V_2O_5)$, the increased value of k_{mass} (**Figure 8-7**) and the increased VO_x absorption signals in the DRUV spectra (**Figure 8-14**) and confirms the presence of an increased amount of VO_x species with increasing calcination temperature. The same accounts for 6CeV-SiWTi (**Figure 8-19e** and **Figure 8-19f**), but the V=O contribution increased only from 10% to 12%. Since 6CeV- and 9CeV-SiWTi do not show any aging tendency at 750°C (same TiO_2 crystallite sizes and BET surface area, **Table 8-2**) and did not exhibit any crystalline V- or W-containing phase in the XRD (**Figure 8-5**), it was concluded that the larger V=O contribution in 9CeV-SiWTi is related to the correspondingly higher $r(V_2O_5)$ values of **Table 8-2**. It is further notable that an identical fraction of VO_x species was estimated for 1V-SiWTi and 9CeV-SiWTi after calcination at 750°C (**Table 8-4**), in agreement with the calculated $r(V_2O_5)$ for 9CeV-SiWTi (1.1 wt%) and the V_2O_5 loading in 1V-SiWTi (1.0 wt%). The VO_B component was of lower intensity for both catalysts than VO_A. Identically to VO_A, VO_B intensified after calcination of 9CeV-SiWTi at 750°C but remained similar in the case of 1V-SiWTi. Tentatively, this signal was assigned to vanadyl species of limited nuclearity, similar to the conclusion from the DRUV data.

Finally, the deconvolution of 1V-SiWTi, 9CeV-SiWTi and SiWTi confirmed that the fresh samples comprised two wolframyl species with 2ν(W=O) at ca. 2010 cm^{-1} (WO_A) and ca. 2020 cm^{-1} (WO_B), which were both perturbed by NH_3 addition (**Figure 8-19a**, **Figure 8-19c** and **Figure 8-19e**). These two features remained unchanged in SiWTi after calcination at 750°C (**Figure 8-19f**). However, the WO_B signal disappeared in the CeV-SiWTi and 1V-SiWTi spectra, possibly due to the presence of VO_x units covering the mentioned wolframyl species. This assumption is strengthened by the fact that fresh 1V-SiWTi exhibited a lower fraction of WO_B due to the larger V_2O_5 content compared to fresh 9CeV-SiWTi. The diffuse reflectance spectroscopy experiments unambiguously unveiled the presence of VO_x species from decomposed $MeVO_4$. They were therefore an essential complement to the XRD and H_2-TPR data, where the formation of VO_x species could only be followed indirectly.

8.5 Conclusions

In this Chapter, the nature of active species and the dependence of calcination temperature of $CeVO_4$, $FeVO_4$ and $ErVO_4$ catalysts on SiO_2-WO_3-TiO_2 were investigated. It was shown that the catalysts became more active after the metal vanadate started to decompose into metal oxides and freed VO_x species. While the $FeVO_4$-based catalyst completely decomposed into Fe_2O_3 and VO_x species, the rare earth metal based catalysts only decomposed partially which could be directly correlated to their lower activity but high stability. This correlation could be verified by preparing vanadia-based catalysts of similar loading as the amount of released VO_x species from the metal vanadate, which resulted in identical activity and stability. The limited decomposition of the rare earth metal vanadates generated low levels of released VO_x species dispersed on the support, which in turn was responsible for the high temperature stability of the catalysts. The decomposition and consequently the activity of $MeVO_4$ based catalysts could be improved using vanadates of lower crystallinity, which however accelerated the aging of the catalyst. It was shown that a released fraction of ca. 1 wt% V_2O_5 is sufficient to induce catalyst aging at a calcination temperature above 750°C. The evidence of the presence of released VO_x species was obtained from H_2-TPR, DRUV and DRIFT spectroscopy.

Similar vanadyl species to those of vanadia-based catalysts were found. At elevated calcination temperature, VO_x migrates towards WO_3 surface species which is a potential initiation step for the sintering of the support material. The decomposed metal vanadates predominantly form extended VO_x domains while the impregnated vanadia-based catalysts feature also VO_x domains of lower nuclearity. Due to the generation of VO_x species at elevated temperatures, $MeVO_4$ can be envisaged as precursor materials for active phases for various reaction catalyzed by vanadium.

Chapter 9

Summary and Outlook

9.1 Summary

The motivation for this work was to explore the potential and development of vanadium-based SCR catalysts. The focus was set on the optimization and in-depth characterization of $V_2O_5/WO_3/TiO_2$ (VWT) catalysts, the capability of SiO_2 as a promoter to enhance their stability and the exploration of supported metal vanadates as potential alternative SCR active materials.

The emphasis of the first part of the thesis was set on the extensive understanding and optimization of a typical VWT catalyst and to investigate its limitations regarding its stability at elevated temperatures. The systematic variation of the vanadium content revealed that only V_2O_5 loadings up to 2.6 wt% withstood hydrothermal aging at 600°C for 16 h. Loadings below 2.0 wt% did not guarantee sufficient activity and above 2.6 wt%, deactivation tendencies were associated to support material sintering, the loss of selectivity and lower overall surface acidity. Exposure to various aging procedures of the V-loading optimized VWT catalyst revealed that a hydrothermal environment affects the aging more severely compared to a dry environment. The VWT catalyst was activated at moderate hydrothermal aging temperatures and only showed deactivation tendencies at ca. 600°C. For a dry aging environment, deactivation was observed at higher temperature (650°C). The activation was correlated to changes in V and W surface coverage, the fraction of Lewis and Brønsted acid sites and the amount of redox active vanadyl sites. The accelerated aging in presence of water was related to formation of volatile V and W species which resulted in a greater amount of released V. It could be concluded

that VWT catalysts without stabilizing additives are not suitable for temperature surges above 600°C.

Due to the availability of cutting-edge spectroscopic instrumentation, the VWT catalysts were able to be investigated in greater depth. Together with transient experimentation it was possible to differentiate between active, intermediate and spectator species, which solved mechanistic ambiguities of the SCR reaction. It was shown that NO predominantly reacts with NH_3 adsorbed on Lewis acid sites at low temperature. Despite their abundance, Brønsted acid sites hardly contribute to the SCR activity and mainly serve as a NH_3 pool to replenish the Lewis sites. The active Lewis acid site consists of mono-oxo V^{5+}, which reduces only in presence of both NO and NH_3. By exploiting the time-resolved multiple transient experimental approach, it was also possible to verify the formation of the nitrosamide intermediate, which is formed simultaneously to V^{5+} reduction. Once consumed, the active Lewis sites must be regenerated upon re-oxidation, which was shown to be the rate determining step. Conclusively, the results presented in Chapter 5 add a new perspective to the SCR mechanism of V-based catalysts and possibly assist in the generation of advanced catalytic SCR material.

In the second part of the thesis, the emphasis was set on gaining thermal stability of the VWT catalyst by modification of the composition. In Chapter 6, the benefit of SiO_2 addition was shown for co-impregnated VWT. Co-impregnation of V and W on TiO_2 produces highly active SCR catalysts at low temperature and with additional Si, this low temperature activity could be preserved up to a hydrothermal aging temperature of 650°C. It was concluded that 2 - 4 wt% SiO_2 was sufficient for the stabilization because of an amorphous SiO_2 phase formation that prevented anatase particles from sintering upon inhibition of their inter-particle contact.

The potential of $FeVO_4$ as a new source of active redox center was tested after supporting it on a SiO_2 stabilized WO_3-TiO_2 support material. A loading study in Chapter 7 revealed ca. 4.5 wt% $FeVO_4$ to be the optimum trade-off between stability and activity. Remarkable catalyst activation was observed after calcination at ca. 600°C and it was possible to show that this activation is relat-

ed to the decomposition of $FeVO_4$, which generates dispersed VO_x species. Consequently, $FeVO_4$ is not the active phase for $FeVO_4$-based SCR catalyst and acts rather as the catalyst precursor. This is in contradiction with literature where bulk and supported metal vanadates are considered to impart more stability to the catalyst because of the lack of free VO_x species. Supported $CeVO_4$, $AlVO_4$ and $ErVO_4$ on SiO_2-WO_3-TiO_2 were also tested as potential high temperature stable SCR catalysts in Chapter 8. Similar to $FeVO_4$, it was proven that the catalytic activity of these materials is closely correlated to their degree of decomposition. Metal vanadates with limited stability generated active SCR catalysts already at moderate calcination temperature while more stable metal vanadates needed a higher temperature for activation. The limited decomposition of especially the rare earth metal vanadates generated low levels of dispersed VO_x species on the support, which in turn were responsible for the high temperature stability of the catalysts. It was shown that a V amount corresponding to ca. 1 wt% V_2O_5 is sufficient to induce catalyst aging at a calcination temperature above 750°C. The decomposed metal vanadates predominantly form VO_x domains that are very similar to those obtained in impregnated vanadia-based catalysts.

9.2 Outlook

The findings in this thesis demonstrate that advances in V-based SCR catalyst research can be achieved despite the intensive activity over the last four decades. The methodology used for mechanistic investigation of vanadium-based SCR catalyst presented in Chapter 5 can also be applied for copper- and iron-exchanged zeolite SCR catalysts. These types of SCR catalysts have been heavily discussed within the SCR community in the last five years and it would be interesting to mechanistically investigate them accordingly. The DRIFT set-up is now being upgraded with a Raman spectrometer with the goal to gain decisive insights on mechanistic details of various SCR catalysts. First preliminary measurements are very promising and it is plausible that this diversified set-up can markedly enhance the visibility of structural changes of metal oxides when exposed to working conditions. Raman spectroscopy, together with modulation excitation spectroscopy, is capable to visualize small

variations occurring on the support, the promoters as well as the actives sites when exposed to different conditions. The methodology is not limited to SCR catalysts but could be used for a wide range of heterogeneous catalysts.

The studies with supported metal vanadates as an alternative source of vanadium for SCR catalysts showed the active phase is generated by their decomposition. One can envisage that metal vanadates can, however, be used as precursors of active vanadium species thus prolonging the lifetime of a catalyst due to the replenishment of new active material. To prove this hypothesis, a systematic study is, however, needed. The decomposition of supported metal vanadates not only generated dispersed VO_x active sites but also the corresponding metal oxides. Especially from the study with supported $FeVO_4$ in Chapter 7 it was shown that the generation of Fe_2O_3 could be a reason for the enhanced stability compared to its V_2O_5-based reference catalyst. Based on these findings, the stabilization effect of the oxides of iron, cerium or even erbium could be studied more thoroughly.

References

[1] R. Stone, in *Introduction to Internal Combustion Engines*, Macmillan Education UK, London, **1999**, pp. 1-21.

[2] R. C. Flagan, J. H. Seinfeld, *Fundamentals of air pollution engineering*, Dover Publications Inc, Mineola New York, **2012**.

[3] G. A. Karim, in *Dual-Fuel Diesel Engines*, CRC Press, **2015**, pp. 195-214.

[4] R. N. Colvile, E. J. Hutchinson, J. S. Mindell, R. F. Warren, *Atmos. Environ.* **2001**, *35*, 1537-1565.

[5] G. J. K. Acres, *Stud. Environ. Sci.* **1991**, *44*, 376-396.

[6] S. C. Anenberg, J. Miller, R. Minjares, L. Du, D. K. Henze, F. Lacey, C. S. Malley, L. Emberson, V. Franco, Z. Klimont, C. Heyes, *Nature* **2017**, *545*, 467-471.

[7] M. J. Nunney, *Light and Heavy Vehicle Technology, Vol. 4th ed*, Routledge, Oxford, **2007**.

[8] I. Nova, E. Tronconi, *Urea-SCR Technology for DeNOx After Treatment of Diesel Exhausts*, Springer New York, **2014**.

[9] P. Brimblecombe, in *Urban Air Pollution - European Aspects* (Eds.: J. Fenger, O. Hertel, F. Palmgren), Springer Netherlands, Dordrecht, **1998**, pp. 7-20.

[10] A. W. Reitze, *Air Pollution Control Law: Compliance and Enforcement*, Environmental Law Institute, Washington, D.C., **2001**.

[11] A. Faiz, C. S. Weaver, M. P. Walsh, *Air Pollution from Motor Vehicles*, The Word Bank, Washington, D.C., **1996**.

[12] M. Nesbit, M. Fergusson, A. Colsa, J. Ohlensdorf, C. Hayes, K. Paaquel, J.-P. Schweitzer, *Comparative study on the differences between the EU and US legislation on emissions in the automotive sector*, Policy Department A: Economic and Scientific Policy, Eurpean Union, **2016**.

[13] M. Masiol, S. Squizzato, G. Formenton, R. M. Harrison, C. Agostinelli, *Sci. Total Environ.* **2017**, *576*, 210-224.

[14] Z. Shao, T. Dallmann, *European Stage V non-road emission standards*, icct -International council on clean transportation, **2016**.

[15] R. Isermann, in *Engine Modeling and Control: Modeling and Electronic Management of Internal Combustion Engines*, Springer, Berlin, Heidelberg, **2014**, pp. 1-27.

[16] T. Maunula, *Combust. Engin.* **2014**, *53*, 60-63.

[17] A. Russell, W. S. Epling, *Catal. Rev.* **2011**, *53*, 337-423.

[18] W. A. Majewski, **2011**, *09.08.2017*, dieselnet.com/tech/cat_doc.php.
[19] G. Corro, *React. Kinet. Catal. Lett.* **2002**, *75*, 89-106.
[20] I. P. Kandylas, G. C. Koltsakis, *Ind. Eng. Chem. Res.* **2002**, *41*, 2115-2123.
[21] T. V. Johnson, *Int. J. Engine Res.* **2009**, *10*, 275-285.
[22] N. Takahashi, H. Shinjoh, T. Iijima, T. Suzuki, K. Yamazaki, K. Yokota, H. Suzuki, N. Miyoshi, S.-i. Matsumoto, T. Tanizawa, T. Tanaka, S.-s. Tateishi, K. Kasahara, *Catal. Today* **1996**, *27*, 63-69.
[23] L. Chmielarz, A. Węgrzyn, M. Wojciechowska, S. Witkowski, M. Michalik, *Catal. Lett.* **2011**, *141*, 1345-1354.
[24] M. Colombo, I. Nova, E. Tronconi, G. Koltsakis, *Top. Catal.* **2013**, *56*, 177-181.
[25] Q. Schiermeier, in *Nature*, Nature News, Nature News, **2015**.
[26] D. Carder, M. Besch, A. Thiruvengadam, H. Kappanna, G. Thompson, in *6th International PEMS Conference & Workshop* Riverside, US, **2016**.
[27] D. Morgan, *West Virginia engineer proves to be a David to VW's Goliath*, Reuters, Thomson Reuters, **2015**.
[28] V. Franco, F. P. Sánchez, J. German, P. Mock, icct - The international council on clean transportation, Berlin, **2014**.
[29] G. Gates, J. Ewing, K. Russell, D. Watkins, *How Volkswagen's 'Defeat Devices' Worked*, The New York Times, New York, **2017**.
[30] J. C. Jung, A. Park, S. Bin, *Thunderbird Int. Bus. Rev.* **2017**, *59*, 127-137.
[31] J. Ando, H. Tohata, G. A. Isaacs, *NOx Abatement for Stationary Sources in Japan*, U.S. Environmental Protection Agency, Cincinnati, Ohio, **1976**.
[32] M. Takagi, T. Kowai, M. Soma, I. Onishi, K. Tamaru, *J. Catal.* **1977**, *250*, 441-446.
[33] W. E. Bowers, US4719092 A, **1988**.
[34] W. Held, A. König, T. Richter, L. Puppe, SAE International, **1990**.
[35] N. Yadav Indrajit, *Int. J. Environ. Sci. Technol.* **2010**, *2*, 766-773.
[36] P. L. T. Gabrielsson, *Top. Catal.* **2004**, *28*, 177-184.
[37] D. Peitz, *Investigations on the catalytic decomposition of guanidinium formate, ammonium formate and methanamide as NH-precursors for the selective catalytic reduction of NOx*, Type thesis, ETH Zurich, Zurich - Switzerland, **2012**.
[38] A. Kato, S. Matsuda, T. Kamo, F. Nakajima, H. Kuroda, T. Narita, *J. Phys. Chem.* **1981**, *85*, 4099-4102.
[39] P. Forzatti, *Appl. Catal. A Gen.* **2001**, *222*, 221-236.

[40] M. Koebel, M. Elsener, M. Kleemann, *Catal. Today* **2000**, *59*, 335-345.
[41] M. Koebel, M. Elsener, G. Madia, *Ind. Eng. Chem. Res.* **2001**, *40*, 52-59.
[42] L. Lietti, I. Nova, P. Forzatti, *Top. Catal.* **2000**, *11*, 111-122.
[43] G. Madia, M. Koebel, M. Elsener, A. Wokaun, *Ind. Eng. Chem. Res.* **2002**, *41*, 4008-4015.
[44] S. Solomon, D. Qin, M. Manning, *Climate Change 2007: The Physical Science Basis.*, IPCC, New York, **2007**.
[45] M. Koebel, G. Madia, M. Elsener, *Catal. Today* **2002**, *73*, 239-247.
[46] P. Forzatti, L. Lietti, *Heterogen. Chem. Rev.* **1996**, *3*, 33-51.
[47] T. Dallmann, A. Menon, *Technology Pathways for Diesel Engines Used in Non-Road Vehicles and Equipment*, Washington, DC, **2016**.
[48] J. A. Sullivan, J. Cunningham, M. A. Morris, K. Keneavey, *Appl. Catal. B: Environ.* **1995**, *7*, 137-151.
[49] T. Komatsu, M. Nunokawa, I. S. Moon, T. Takahara, S. Namba, T. Yashima, *J. Catal.* **1994**, *148*, 427-437.
[50] T. Seiyama, T. Arakawa, T. Matsuda, Y. Takita, N. Yamazoe, *J. Catal.* **1977**, *48*, 1-7.
[51] L. Singoredjo, R. Korver, F. Kapteijn, J. Moulijn, *Appl. Catal. B: Environ.* **1992**, *1*, 297-316.
[52] M. Piumetti, S. Bensaid, D. Fino, N. Russo, *Catal. Struct. React.* **2015**, *1*, 155-173.
[53] J. Li, H. Chang, L. Ma, J. Hao, R. T. Yang, *Catal. Today* **2011**, *175*, 147-156.
[54] K. Kamasamudram, N. W. Currier, X. Chen, A. Yezerets, *Catal. Today* **2010**, *151*, 212-222.
[55] A.-Z. Ma, W. Grunert, *Chem. Commun.* **1999**, 71-72.
[56] S. Djerad, L. Tifouti, M. Crocoll, W. Weisweiler, *J. Mol. Catal. A: Chem.* **2004**, *208*, 257-265.
[57] L. Lietti, I. Nova, G. Ramis, L. Dall'Acqua, G. Busca, E. Giamello, P. Forzatti, F. Bregani, *J. Catal.* **1999**, *187*, 419-435.
[58] M. Casanova, A. Sagar, K. Schermanz, A. Trovarelli, *Top. Catal.* **2016**, *59*, 996-1001.
[59] L. Chen, J. Li, M. Ge, *J. Phys. Chem. C* **2009**, *113*, 21177-21184.
[60] Z. Liu, Y. Li, T. Zhu, H. Su, J. Zhu, *Ind. Eng. Chem. Res.* **2014**, *53*, 12964-12970.
[61] J. L. G. Fierro, *Metal Oxides: Chemistry and Applications*, CRC Press **2005**.
[62] P. G. W. A. Kompio, A. Brückner, F. Hipler, G. Auer, E. Löffler, W. Grünert, *J. Catal.* **2012**, *286*, 237-247.

[63] I. E. Wachs, *Catal. Today* **2005**, *100*, 79-94.
[64] D. M. Chapman, *Appl. Catal. A Gen.* **2011**, *392*, 143-150.
[65] X. Zhang, X. Li, J. Wu, R. Yang, Z. Zhang, *Catal. Lett.* **2009**, *130*, 235-238.
[66] I. Georgiadou, C. Papadopoulou, H. K. Matralis, G. A. Voyiatzis, A. Lycourghiotis, C. Kordulis, *J. Phys. Chem. B* **1998**, *102*, 8459-8468.
[67] M. Anstrom, N.-Y. Topsøe, J. A. Dumesic, *J. Catal.* **2003**, *213*, 115-125.
[68] M. Gruber, K. Hermann, *J. Chem. Phys.* **2013**, *139*, 244701- 244708.
[69] G. Ramis, L. Yi, G. Busca, *Catal. Today* **1996**, *28*, 373-380.
[70] N.-Y. Topsøe, *Science* **1994**, *265*, 1217-1219.
[71] N. Y. Topsøe, J. A. Dumesic, H. Topsøe, *J. Catal.* **1995**, *151*, 241-252.
[72] E. Tronconi, I. Nova, C. Ciardelli, D. Chatterjee, M. Weibel, *J. Catal.* **2007**, *245*, 1-10.
[73] A. Vittadini, M. Casarin, A. Selloni, *J. Phys. Chem. B* **2005**, *109*, 1652-1655.
[74] Y. Zheng, A. D. Jensen, J. E. Johnsson, J. R. Thøgersen, *Appl. Catal. B Environ.* **2008**, *83*, 186-194.
[75] G. Madia, M. Elsener, M. Koebel, F. Raimondi, A. Wokaun, *Appl. Catal. B Environ.* **2002**, *39*, 181-190.
[76] P. G. W. A. Kompio, A. Brückner, F. Hipler, O. Manoylova, G. Auer, G. Mestl, W. Grünert, *Appl. Catal. B Environ.* **2017**, *217*, 365-377.
[77] Z. Zhang, V. E. Henrich, *Surf. Sci.* **1992**, *277*, 263-272.
[78] D. Nicosia, M. Elsener, O. Kröcher, P. Jansohn, *Top. Catal.* **2007**, *42-43*, 333-336.
[79] X. Xie, J. Lu, E. Hums, Q. Huang, Z. Lu, *Energy Fuels* **2015**, *29*, 3890-3896.
[80] H. Kamata, K. Takahashi, C. U. I. Odenbrand, *J. Mol. Catal. A: Chem.* **1999**, *139*, 189-198.
[81] S. Bagheri, N. Muhd Julkapli, S. Bee Abd Hamid, *Sci. World J.* **2014**, *2014*, 1-21.
[82] J. R. H. Ross, in *Heterogeneous Catalysis*, Elsevier, Amsterdam, **2012**, pp. 65-96.
[83] D. A. H. Hanaor, C. C. Sorrell, *J. Mater. Sci.* **2011**, *46*, 855-874.
[84] K. I. Hadjiivanov, D. G. Klissurski, *Chem. Soc. Rev.* **1996**, *25*, 61-69.
[85] M. C. Paganini, L. Dall'Acqua, E. Giamello, L. Lietti, P. Forzatti, G. Busca, *J. Catal.* **1997**, *166*, 195-205.
[86] T. Baidya, A. Gayen, M. S. Hegde, N. Ravishankar, L. Dupont, *J. Phys. Chem. B* **2006**, *110*, 5262-5272.

[87] M. D. Amiridis, R. V. Duevel, I. E. Wachs, *Appl. Catal. B Environ.* **1999**, *20*, 111-122.

[88] W. Choi, A. Termin, M. R. Hoffmann, *Angew. Chem. Int. Ed.* **1994**, *33*, 1091-1092.

[89] P. Goya, P. Román, *Chem. Int.* **2005**, *27*, 26-28.

[90] C. Cristiani, M. Bellotto, P. Forzatti, F. Bregani, *J. Mater. Res.* **1993**, *8*, 2019-2025.

[91] X.-F. Yu, N.-Z. Wu, H.-Z. Huang, Y.-C. Xie, Y.-Q. Tang, *J. Mater. Chem.* **2001**, *11*, 3337-3342.

[92] G. Ramis, G. Busca, C. Cristiani, L. Lietti, P. Forzatti, F. Bregani, *Langmuir* **1992**, *8*, 1744-1749.

[93] Y. He, M. E. Ford, M. Zhu, Q. Liu, Z. Wu, I. E. Wachs, *Appl. Catal. B Environ.* **2016**, *188*, 123-133.

[94] G. D. Panagiotou, T. Petsi, K. Bourikas, C. Kordulis, A. Lycourghiotis, *J. Catal.* **2009**, *262*, 266-279.

[95] T. Yamaguchi, Y. Tanaka, K. Tanabe, *J. Catal.* **1980**, *65*, 442-447.

[96] G. Busca, *Chem. Rev.* **2007**, *107*, 5366-5410.

[97] T. Murayama, K. Nakajima, J. Hirata, K. Omata, E. J. M. Hensen, W. Ueda, *Catal. Sci. Technol.* **2017**, *7*, 243-250.

[98] K. Doura, *Tuning Bifunctional Surface Redox-Acid Sites for Enhanced Catalytic Performance*, Type thesis, Lehigh University, **2011**.

[99] L. J. Alemany, L. Lietti, N. Ferlazzo, P. Forzatti, G. Busca, E. Giamello, F. Bregani, *J. Catal.* **1995**, *155*, 117-130.

[100] J. P. Chen, R. T. Yang, *Appl. Catal. A Gen.* **1992**, *80*, 135-148.

[101] D. M. Chapman, US 8545796 B2, **2013**.

[102] D. M. Chapman, G. Fu, S. Augustine, J. Crouse, L. Zavalij, M. Watson, D. Perkins-Banks, *SAE Int. J. Fuels Lubr.* **2010**, *3*, 643-653.

[103] M. Kobayashi, R. Kuma, S. Masaki, N. Sugishima, *Appl. Catal. B Environ.* **2005**, *60*, 173-179.

[104] X. Liu, X. Wu, T. Xu, D. Weng, Z. Si, R. Ran, *Chin. J. Catal.* **2016**, *37*, 1340-1346.

[105] Y. Pan, W. Zhao, Q. Zhong, W. Cai, H. Li, *J. Environ. Sci.* **2013**, *25*, 1703-1711.

[106] A. M. Beale, I. Lezcano-Gonzalez, T. Maunula, R. G. Palgrave, *Catal. Struct. React.* **2015**, *1*, 25-34.

[107] R. Jossen, M. C. Heine, S. E. Pratsinis, S. M. Augustine, M. K. Akhtar, *Appl. Catal. B Environ.* **2007**, *69*, 181-188.

[108] Y. Peng, C. Liu, X. Zhang, J. Li, *Appl. Catal. B Environ.* **2013**, *140*, 276-282.

[109] M. A. Bañares, L. s. J. Alemany, M. C. Jiménez, M. A. Larrubia, F. Delgado, M. L. Granados, A. Martınez-Arias, J. M. Blasco, J. L. s. G. Fierro, *J. Solid State Chem.* **1996**, *124*, 69-76.

[110] M. Kobayashi, R. Kuma, A. Morita, *Catal. Lett.* **2006**, *112*, 37-44.

[111] G. Deo, I. E. Wachs, *J. Catal.* **1994**, *146*, 335-345.

[112] Cristal, **2016**, *17.11.2017*, cristal.com/products-and-services/ultrafine-and-specialty-tio2/ultrafine-and-specialty-tio2-products/Pages/default.aspx.

[113] E. Hums, *Res. Chem. Intermed.* **1993**, *19*, 419-441.

[114] W. Shan, F. Liu, H. He, X. Shi, C. Zhang, *Appl. Catal. B Environ.* **2012**, *115*, 100-106.

[115] W. Xu, Y. Yu, C. Zhang, H. He, *Chem. Commun.* **2008**, *9*, 1453-1457.

[116] K. A. Michalow-Mauke, Y. Lu, K. Kowalski, T. Graule, M. Nachtegaal, O. Kröcher, D. Ferri, *ACS Catal.* **2015**, *5*, 5657-5672.

[117] F. Liu, Y. Yu, H. He, *Chem. Commun.* **2014**, *50*, 8445-8463.

[118] W. Shan, F. Liu, Y. Yu, H. He, *Chin. J. Catal.* **2014**, *35*, 1251-1259.

[119] X. Wang, L. Zhang, S. Wu, W. Zou, S. Yu, Y. Shao, L. Dong, *Catalysts* **2016**, *6*, 112.

[120] C. Li, Q. Li, P. Lu, H. Cui, G. Zeng, *Front. Environ. Sci. Eng.* **2012**, *6*, 156-161.

[121] L. Chen, Z. Si, X. Wu, D. Weng, R. Ran, J. Yu, *J. Rare Earths* **2014**, *32*, 907-917.

[122] X. Zhao, L. Huang, S. Namuangruk, H. Hu, X. Hu, L. Shi, D. Zhang, *Catal. Sci. Technol.* **2016**, *6*, 5543-5553.

[123] M. A. L. Vargas, M. Casanova, A. Trovarelli, G. Busca, *Appl. Catal. B Environ.* **2007**, *75*, 303-311.

[124] P. R. Ettireddy, N. Ettireddy, S. Mamedov, P. Boolchand, P. G. Smirniotis, *Appl. Catal. B Environ.* **2007**, *76*, 123-134.

[125] Z. Wu, R. Jin, Y. Liu, H. Wang, *Chem. Commun.* **2008**, *9*, 2217-2220.

[126] F. Gao, X. Tang, H. Yi, S. Zhao, C. Li, J. Li, Y. Shi, X. Meng, *Catalysts* **2017**, *7*, 199.

[127] D. Rehder, in *Bioinorganic Vanadium Chemistry*, John Wiley & Sons, Ltd, **2008**, pp. 1-11.

[128] A. V. Fortunatov, V. N. Baranova, *Vanadium : Chemical Properties, Uses and Environmental Effects*, Nova Science Publishers, Inc, New York, **2012**.

[129] M. Rychcik, M. Skyllas-Kazacos, *J. Power Sources* **1988**, *22*, 59-67.

[130] S. Joshi Sunil, V. Ranade Vivek, in *Industrial Catalytic Processes for Fine and Specialty Chemicals*, Elsevier, , **2016**.

[131] C. Hess, R. Schlögl, in *Nanostructured Catalysts: Selective Oxidations*, Royal Society of Chemistry, **2012**.
[132] G. T. Went, L. J. Leu, R. R. Rosin, A. T. Bell, *J. Catal.* **1992**, *134*, 492-505.
[133] G. T. Went, L.-j. Leu, A. T. Bell, *J. Catal.* **1992**, *134*, 479-491.
[134] J. Haber, A. Kozlowska, R. Kozłowski, *J. Catal.* **1986**, *102*, 52-63.
[135] I. E. Wachs, *Catal. Today* **1996**, *27*, 437-455.
[136] P. Alotto, M. Guarnieri, F. Moro, *Renew. Sustainable Energy Rev.* **2014**, *29*, 325-335.
[137] M. Ek, Q. M. Ramasse, L. Arnarson, P. Georg Moses, S. Helveg, *Nat. Commun.* **2017**, *8*, 305.
[138] I. Giakoumelou, C. Fountzoula, C. Kordulis, S. Boghosian, *J. Catal.* **2006**, *239*, 1-12.
[139] I. E. Wachs, *J. Catal.* **1990**, *124*, 570-573.
[140] G. Busca, L. Lietti, G. Ramis, F. Berti, *Appl. Catal. B Environ.* **1998**, *18*, 1-36.
[141] M. A. Bañares, I. E. Wachs, *J. Raman Spectrosc.* **2002**, *33*, 359-380.
[142] I. E. Wachs, G. Deo, B. M. Weckhuysen, A. Andreini, M. A. Vuurman, M. d. Boer, M. D. Amiridis, *J. Catal.* **1996**, *161*, 211-221.
[143] A. Burkardt, W. Weisweiler, J. A. A. van den Tillaart, A. Schäfer-Sindlinger, E. S. Lox, *Top. Catal.* **2001**, *16-17*, 369-375.
[144] G. Busca, A. Zecchina, *Catal. Today* **1994**, *20*, 61-76.
[145] C. Cristiani, P. Forzatti, G. Busca, *J. Catal.* **1989**, *116*, 586-589.
[146] C. Femandez, M. Guelton, *Catal. Today* **1994**, *20*, 77-86.
[147] H. Eckert, I. E. Wachs, *J. Phys. Chem.* **1989**, *93*, 6796-6805.
[148] K. V. Chary, G. Kishan, T. Bhaskar, C. Sivaraj, *J. Phys. Chem. B* **1998**, *102*, 6792-6798.
[149] G. C. Bond, S. Flamerz, *Appl. Catal.* **1989**, *46*, 89-102.
[150] R. Gryboś, M. Witko, *J. Phys. Chem. C* **2007**, *111*, 4216-4225.
[151] M. Calatayud, C. Minot, *J. Phys. Chem. B* **2004**, *108*, 15679-15685.
[152] K. Alexopoulos, P. Hejduk, M. Witko, M.-F. Reyniers, G. B. Marin, *J. Phys. Chem. C* **2010**, *114*, 3115-3130.
[153] M. Gruber, *The selective catalytic reduction of NO by NH3 at Brønsted and Lewis acid sites of vanadium oxide surfaces: Density functional theory studies* Type thesis, Freie Universität Berlin, **2011**.
[154] S. Soyer, A. Uzun, S. Senkan, I. Onal, *Catal. Today* **2006**, *118*, 268-278.
[155] R.-M. Yuan, G. Fu, X. Xu, H.-L. Wan, *PCCP* **2011**, *13*, 453-460.
[156] M. Calatayud, B. Mguig, C. Minot, *Theor. Chem. Acc.* **2005**, *114*, 29-37.
[157] M. Calatayud, C. Minot, *Top. Catal.* **2006**, *41*, 17-26.

[158] M. Gruber, K. Hermann, *J. Chem. Phys.* **2013**, *138*, 094704.
[159] M. Inomata, A. Miyamoto, Y. Murakami, *J. Catal.* **1980**, *62*, 140-148.
[160] F. J. J. G. Janssen, F. M. G. Van den Kerkhof, H. Bosch, J. R. H. Ross, *J. Phys. Chem.* **1987**, *91*, 6633-6638.
[161] F. J. J. G. Janssen, F. M. G. Van den Kerkhof, H. Bosch, J. R. H. Ross, *J. Phys. Chem.* **1987**, *91*, 5921-5927.
[162] G. Ramis, G. Busca, F. Bregani, P. Forzatti, *Appl. Catal.* **1990**, *64*, 259-278.
[163] N. Y. Topsøe, H. Topsoe, J. A. Dumesic, *J. Catal.* **1995**, *151*, 226-240.
[164] F. Gilardoni, J. Weber, A. Baiker, *Int. J. Quantum Chem.* **1997**, *61*, 683-688.
[165] L. Arnarson, H. Falsig, S. B. Rasmussen, J. V. Lauritsen, P. G. Moses, *PCCP* **2016**, *18*, 17071-17080.
[166] M. Szaleniec, A. Drzewiecka-Matuszek, M. Witko, P. Hejduk, *J. Mol. Model.* **2013**, *19*, 4487-4501.
[167] M. Casanova, K. Schermanz, J. Llorca, A. Trovarelli, *Catal. Today* **2012**, *184*, 227-236.
[168] F. Liu, H. He, Z. Lian, W. Shan, L. Xie, K. Asakura, W. Yang, H. Deng, *J. Catal.* **2013**, *307*, 340-351.
[169] M. Casanova, E. Rocchini, A. Trovarelli, K. Schermanz, I. Begsteiger, *J. Alloys Compd.* **2006**, *408–412*, 1108-1112.
[170] A. Sagar, A. Trovarelli, M. Casanova, K. Schermanz, *SAE Int. J. Engines* **2011**, *4*, 1839-1849.
[171] M. A. Carreon, V. V. Guliants, *Eur. J. Inorg. Chem.* **2005**, *2005*, 27-43.
[172] U. Kolitsch, D. Holtstam, *Eur. J. Mineral.* **2004**, *16*, 117-126.
[173] J. Walczak, I. Rychłowska-Himmel, *Thermochim. Acta* **1994**, *239*, 269-274.
[174] R. Merkle, J. Maier, *Z. Anorg. Allg. Chem.* **2005**, *631*, 1163-1166.
[175] S. Gillot, J. P. Dacquin, C. Dujardin, P. Granger, *Top. Catal.* **2016**, *59*, 987-995.
[176] X. Zhao, L. Huang, H. Li, H. Hu, X. Hu, L. Shi, D. Zhang, *Appl. Catal. B Environ.* **2016**, *183*, 269-281.
[177] L. Huang, X. Zhao, L. Zhang, L. Shi, J. Zhang, D. Zhang, *Nanoscale* **2015**, *7*, 2743-2749.
[178] K. Schermanz, A. Sagar, A. Trovarelli, M. Casanova, WO 2010121280 A1, **2010**.
[179] M. Casanova, L. Nodari, A. Sagar, K. Schermanz, A. Trovarelli, *Appl. Catal. B Environ.* **2015**, *176–177*, 699-708.
[180] P. Zhang, D. Li, *Catal. Lett.* **2014**, *144*, 959-963.

[181] G. Wu, J. Li, Z. Fang, L. Lan, R. Wang, M. Gong, Y. Chen, *Chem. Commun.* **2015**, *64*, 75-79.

[182] M. Casanova, J. Llorca, A. Sagar, K. Schermanz, A. Trovarelli, *Catal. Today* **2015**, *241, Part A*, 159-168.

[183] Z. G. Liu, N. A. Ottinger, C. M. Cremeens, *Atmos. Environ.* **2015**, *104*, 154-161.

[184] J. Taylor, S. Keith, L. Cseh, L. Ingerman, L. Chappell, J. Rhoades, A. Hueber, *Toxicological profile for Vanadium*, U.S. Department of health and human services, Atlanta, **2012**.

[185] U. S. EPA, *IRIS Toxicological Review of Vanadium Pentoxide (External Review Draft)*, U.S. Environmental Protection Agency, Washington DC, **2011**.

[186] A. Marberger, M. Elsener, D. Ferri, O. Kröcher, *Catalysts* **2015**, *5*, 1704-1720.

[187] A. Marberger, D. Ferri, M. Elsener, O. Kröcher, *Angew. Chem. Int. Ed.* **2016**, *55*, 11989-11994.

[188] A. Marberger, M. Elsener, D. Ferri, O. Kröcher, *manuscript in preparation,* **2017**.

[189] A. Marberger, M. Elsener, D. Ferri, A. Sagar, K. Schermanz, O. Kröcher, *ACS Catal.* **2015**, *5*, 4180-4188.

[190] A. Marberger, D. Ferri, M. Elsener, A. Sagar, C. Artner, K. Schermanz, O. Kröcher, *Appl. Catal. B Environ.* **2017**, *218*, 731-742.

[191] A. Marberger, D. Ferri, D. Rentsch, F. Krumeich, M. Elsener, O. Kröcher, *Catal. Today,* **2017***, doi.org/10.1016/j.cattod.2017.11.037.*

[192] O. Kröcher, M. Devadas, M. Elsener, A. Wokaun, N. Söger, M. Pfeifer, Y. Demel, L. Mussmann, *Appl. Catal. B Environ.* **2006**, *66*, 208-216.

[193] M. Kleemann, M. Elsener, M. Koebel, A. Wokaun, *Appl. Catal. B Environ.* **2000**, *27*, 231-242.

[194] M. Casapu, O. Kröcher, M. Elsener, *Appl. Catal. B Environ.* **2009**, *88*, 413-419.

[195] M. Koebel, M. Elsener, *Chem. Eng. Sci.* **1998**, *53*, 657-669.

[196] Y. Zhao, J. Hu, L. Hua, S. Shuai, J. Wang, *Ind. Eng. Chem. Res.* **2011**, *50*, 11863-11871.

[197] P. Scherrer, *Nachr. Ges. Wiss. Göttingen* **1918**, *26*, 98-100.

[198] S. Brunauer, P. H. Emmett, E. Teller, *JACS* **1938**, *60*, 309-319.

[199] M. S. Wong, in *Metal Oxides: Chemistry and Applications* (Ed.: J. L. G. Fierro), CRC Press, **2005**, pp. 31-54.

[200] P. Kubelka, F. Munk, *Z. Tech. Phys.* **1931**, *12*, 593-601.

[201] M. Wojdyr, *J. Appl. Crystallogr.* **2010**, *43*, 1126-1128.

[202] B. Ravel, M. Newville, *J. Synchrotron Rad.* **2005**, *12*, 537-541.

[203] L. E. Briand, O. P. Tkachenko, M. Guraya, X. Gao, I. E. Wachs, W. Grünert, *J. Phys. Chem. B* **2004**, *108*, 4823-4830.

[204] B. W. Lee, H. Cho, D. W. Shin, *J. Ceram. Process. Res.* **2007**, *8*, 203-207.

[205] S. S. R. Putluru, L. Schill, D. Gardini, S. Mossin, J. B. Wagner, A. D. Jensen, R. Fehrmann, *J. Mater. Sci.* **2014**, *49*, 2705-2713.

[206] M. D. Amiridis, J. P. Solar, *Ind. Eng. Chem. Res.* **1996**, *35*, 978-981.

[207] D. W. Kwon, K. H. Park, S. C. Hong, *Appl. Catal. A Gen.* **2015**, *499*, 1-12.

[208] P. S. Metkar, V. Balakotaiah, M. P. Harold, *Catal. Today* **2012**, *184*, 115-128.

[209] M. Turco, L. Lisi, R. Pirone, P. Ciambelli, *Appl. Catal. B: Environ.* **1994**, *3*, 133-149.

[210] I. Nova, L. dall'Acqua, L. Lietti, E. Giamello, P. Forzatti, *Appl. Catal. B: Environ.* **2001**, *35*, 31-42.

[211] T. Maunula, T. Kinnunen, M. Iivonen, SAE International, **2011**.

[212] G. Cavataio, J. Girard, J. E. Patterson, C. Montreuil, Y. Cheng, C. K. Lambert, SAE International, **2007**.

[213] J. W. Girard, C. Montreuil, J. Kim, G. Cavataio, C. Lambert, *SAE Int. J. Fuels Lubr.* **2008**, *1*, 488-494.

[214] Y. Ma, J. Wang, *J. Dyn. Syst. Meas. Control.* **2016**, *139*, 021002-021002-021009.

[215] D. G. Barceloux, D. Barceloux, *J. Toxicol. Clin. Toxicol.* **1999**, *37*, 265-278.

[216] H. Kamata, K. Takahashi, C. U. I. Odenbrand, *Catal. Lett.* **1998**, *53*, 65-71.

[217] A. Shi, X. Wang, T. Yu, M. Shen, *Appl. Catal. B Environ.* **2011**, *106*, 359-369.

[218] F. Rainone, D. A. Bulushev, L. Kiwi-Minsker, A. Renken, *PCCP* **2003**, *5*, 4445-4449.

[219] G. Busca, G. Centi, L. Marchetti, F. Trifirò, *Langmuir* **1986**, *2*, 568-577.

[220] O. Saur, M. Bensitel, A. B. M. Saad, J. C. Lavalley, C. P. Tripp, B. A. Morrow, *J. Catal.* **1986**, *99*, 104-110.

[221] F. Giraud, C. Geantet, N. Guilhaume, S. Loridant, S. Gros, L. Porcheron, M. Kanniche, D. Bianchi, *J. Phys. Chem. C* **2014**, *118*, 15677-15692.

[222] S. T. Choo, Y. G. Lee, I.-S. Nam, S.-W. Ham, J.-B. Lee, *Appl. Catal. A Gen.* **2000**, *200*, 177-188.

[223] T. Ohsaka, F. Izumi, Y. Fujiki, *J. Raman Spectrosc.* **1978**, *7*, 321-324.

[224] Y. He, M. E. Ford, M. Zhu, Q. Liu, U. Tumuluri, Z. Wu, I. E. Wachs, *Appl. Catal. B Environ.* **2016**, *193*, 141-150.

[225] Y. T. Chua, P. C. Stair, I. E. Wachs, *J. Phys. Chem. B* **2001**, *105*, 8600-8606.

[226] M. F. Daniel, B. Desbat, J. C. Lassegues, B. Gerand, M. Figlarz, *J. Solid State Chem.* **1987**, *67*, 235-247.

[227] F. Roozeboom, M. C. Mittelmeijer-Hazeleger, J. A. Moulijn, J. Medema, V. H. J. De Beer, P. J. Gellings, *J. Phys. Chem.* **1980**, *84*, 2783-2791.

[228] M. A. Vuurman, I. E. Wachs, A. M. Hirt, *J. Phys. Chem.* **1991**, *95*, 9928-9937.

[229] N. Y. Topsoe, *Science* **1994**, *265*, 1217-1219.

[230] T. V. W. Janssens, H. Falsig, L. F. Lundegaard, P. N. R. Vennestrøm, S. B. Rasmussen, P. G. Moses, F. Giordanino, E. Borfecchia, K. A. Lomachenko, C. Lamberti, S. Bordiga, A. Godiksen, S. Mossin, P. Beato, *ACS Catal.* **2015**, *5*, 2832-2845.

[231] C. Sun, L. Dong, W. Yu, L. Liu, H. Li, F. Gao, L. Dong, Y. Chen, *J. Mol. Catal. A: Chem.* **2011**, *346*, 29-38.

[232] L. Lietti, J. L. Alemany, P. Forzatti, G. Busca, G. Ramis, E. Giamello, F. Bregani, *Catal. Today* **1996**, *29*, 143-148.

[233] F. Giraud, C. Geantet, N. Guilhaume, S. Loridant, S. Gros, L. Porcheron, M. Kanniche, D. Bianchi, *J. Phys. Chem. C* **2015**, *119*, 15401-15413.

[234] L. Lietti, I. Nova, S. Camurri, E. Tronconi, P. Forzatti, *AIChE J.* **1997**, *43*, 2559-2570.

[235] J. Sirita, S. Phanichphant, F. C. Meunier, *Anal. Chem.* **2007**, *79*, 3912-3918.

[236] D. Baurecht, U. P. Fringeli, *Rev. Sci. Instrum.* **2001**, *72*, 3782-3792.

[237] I. Nova, L. Lietti, E. Tronconi, P. Forzatti, *Chem. Eng. Sci.* **2001**, *56*, 1229-1237.

[238] I. Nova, L. Lietti, E. Tronconi, P. Forzatti, *Catal. Today* **2000**, *60*, 73-82.

[239] A. A. Tsyganenko, D. V. Pozdnyakov, V. N. Filimonov, *J. Mol. Struct.* **1975**, *29*, 299-318.

[240] N.-Y. Topsøe, *J. Catal.* **1991**, *128*, 499-511.

[241] A. Brückner, *Chem. Commun.* **2005**, 1761-1763.

[242] L. Burcham, G. Deo, X. Gao, I. E. Wachs, *Top. Catal.* **2000**, *11-12*, 85-100.

[243] I. E. Wachs, *Dalton Trans.* **2013**, *42*, 11762-11769.

[244] D. Ferri, M. A. Newton, M. DiMichiel, G. L. Chiarello, S. Yoon, Y. Lu, J. Andrieux, *Angew. Chem. Int. Ed.* **2014**, *53*, 8890-8894.

[245] A. Urakawa, T. Bürgi, A. Baiker, *Chem. Eng. Sci.* **2008**, *63*, 4902-4909.
[246] M. A. Reiche, P. Hug, A. Baiker, *J. Catal.* **2000**, *192*, 400-411.
[247] C. F. Lei Pang, Lina Shao, Junxia Yi, Xing Cai, Jian Wang, Ming Kang, Tao Li, *Chin. J. Catal.* **2014**, *35*, 2020-2028.
[248] L. Gan, F. Guo, J. Yu, G. Xu, *Catalysts* **2016**, *6*, 25.
[249] S. Yang, C. Wang, L. Ma, Y. Peng, Z. Qu, N. Yan, J. Chen, H. Chang, J. Li, *Catal. Sci. Technol.* **2013**, *3*, 161-168.
[250] B. Blümich, *Solid-State NMR II : Inorganic Matter*, Berlin; Heidelberg Springer, **1994**.
[251] R. K. Harris, C. T. G. Knight, *J. Mol. Struct.* **1982**, *78*, 273-278.
[252] D. Hoebbel, G. Garzó, G. Engelhardt, R. Ebert, E. Lippmaa, M. Alla, *Z. Anorg. Allg. Chem.* **1980**, *465*, 15-33.
[253] C. Fede, F. Selvestrel, C. Compagnin, M. Mognato, F. Mancin, E. Reddi, L. Celotti, *Anal. Bioanal. Chem.* **2012**, *404*, 1789-1802.
[254] P. M. Woodward, A. W. Sleight, T. Vogt, *J. Phys. Chem. Solids* **1995**, *56*, 1305-1315.
[255] A. Auroux, A. Gervasini, *J. Phys. Chem.* **1990**, *94*, 6371-6379.
[256] A. Gervasini, A. Auroux, *J. Catal.* **1991**, *131*, 190-198.
[257] S. N. Rashkeev, S. Dai, S. H. Overbury, *J. Phys. Chem. C* **2010**, *114*, 2996-3002.
[258] K. Okada, N. Yamamoto, Y. Kameshima, A. Yasumori, K. J. D. MacKenzie, *J. Am. Ceram. Soc.* **2001**, *84*, 1591-1596.
[259] C. T. G. Knight, *Zeolites* **1989**, *9*, 448-450.
[260] G. Wu, J. Li, Z. Fang, L. Lan, R. Wang, T. Lin, M. Gong, Y. Chen, *Chem. Eng. Sci.* **2015**, *271*, 1-13.
[261] K. Schermanz, C. Hamon, A. Sagar, WO 2014056698 A1, **2014**.
[262] B. Robertson, E. Kostiner, *J. Solid State Chem.* **1972**, *4*, 29-37.
[263] K. Routray, W. Zhou, C. J. Kiely, I. E. Wachs, *ACS Catal.* **2010**, *1*, 54-66.
[264] W. Robinson, *Acta Crystallogr., Sect. B: Struct. Sci* **1975**, *31*, 1153-1160.
[265] L. W. Finger, R. M. Hazen, *J. Appl. Phys.* **1980**, *51*, 5362-5367.
[266] D. Habel, O. Goerke, M. Tovar, E. Kondratenko, H. Schubert, *J. Phase Equilib. Diff.* **2008**, *29*, 482-487.
[267] J. Y. Tsao, *Materials fundamentals of molecular beam epitaxy*, Mass.: Academic Press, Boston, **1993**.
[268] G. Busca, L. Marchetti, G. Centi, F. Trifiro, *J. Chem. Soc., Faraday Trans.* **1985**, *81*, 1003-1014.
[269] A. Zecchina, L. Marchese, S. Bordiga, C. Paze, E. Gianotti, *J. Phys. Chem. B* **1997**, *101*, 10128-10135.

[270] M. Bevilacqua, T. Montanari, E. Finocchio, G. Busca, *Catal. Today* **2006**, *116*, 132-142.
[271] G. Busca, J. C. Lavalley, *Spectrochim. Acta, Part A* **1986**, *42*, 443-445.
[272] G. Busca, *J. Raman Spectrosc.* **2002**, *33*, 348-358.
[273] I. E. Wachs, L. E. Briand, J.-M. Jehng, L. Burcham, X. Gao, *Catal. Today* **2000**, *57*, 323-330.
[274] T. Yamamoto, *X-Ray Spectrom.* **2008**, *37*, 572-584.
[275] J. Walczak, I. Rychiowska-Himmel, P. Tabero, *J. Mater. Sci.* **1992**, *27*, 3680-3684.
[276] V. Panchal, S. López-Moreno, D. Santamaría-Pérez, D. Errandonea, F. J. Manjón, P. Rodríguez-Hernandez, A. Muñoz, S. N. Achary, A. K. Tyagi, *Phys. Rev. B* **2011**, *84*, 0241111-02411112.
[277] J. R. Gambino, C. J. Guare, *Nature* **1963**, *198*, 1084-1084.
[278] G. C. Bond, A. J. Sárkány, G. D. Parfitt, *J. Catal.* **1979**, *57*, 476-493.
[279] C. Wang, S. Yang, H. Chang, Y. Peng, J. Li, *Chem. Eng. Sci.* **2013**, *225*, 520-527.
[280] Z. Lian, F. Liu, H. He, *Catal. Sci. Technol.* **2015**, *5*, 389-396.
[281] X. Gao, S. R. Bare, B. M. Weckhuysen, I. E. Wachs, *J. Phys. Chem. B* **1998**, *102*, 10842-10852.
[282] D. Nitsche, C. Hess, *J. Phys. Chem. C* **2016**, *120*, 1025-1037.
[283] R. Bulánek, L. Čapek, M. Setnička, P. Čičmanec, *J. Phys. Chem. C* **2011**, *115*, 12430-12438.
[284] D. W. Kwon, K. H. Park, S. C. Hong, *J. Chem. Eng. Jpn.* **2016**, *49*, 526-533.
[285] D. Srinivas, W. F. Hölderich, S. Kujath, M. H. Valkenberg, T. Raja, L. Saikia, R. Hinze, V. Ramaswamy, *J. Catal.* **2008**, *259*, 165-173.
[286] Y. Matsushima, T. Koide, M. Hiro-Oka, M. Shida, A. Sato, S. Sugiyama, M. Ito, *J. Am. Ceram. Soc.* **2015**, *98*, 1236-1244.
[287] G. Catana, R. R. Rao, B. M. Weckhuysen, P. Van Der Voort, E. Vansant, R. A. Schoonheydt, *J. Phys. Chem. B* **1998**, *102*, 8005-8012.
[288] Z. Wu, H.-S. Kim, P. C. Stair, S. Rugmini, S. D. Jackson, *J. Phys. Chem. B* **2005**, *109*, 2793-2800.
[289] U. Scharf, M. Schraml-Marth, A. Wokaun, A. Baiker, *J. Chem. Soc., Faraday Trans.* **1991**, *87*, 3299-3307.
[290] J. P. Gallas, J. C. Lavalley, A. Burneau, O. Barres, *Langmuir* **1991**, *7*, 1235-1240.
[291] T. Kim, A. Burrows, C. J. Kiely, I. E. Wachs, *J. Catal.* **2007**, *246*, 370-381.
[292] D. S. Kim, M. Ostromecki, I. E. Wachs, *J. Mol. Catal. A: Chem.* **1996**, *106*, 93-102.

[293] G. Ramis, G. Busca, P. Forzatti, *Appl. Catal. B Environ.* **1992**, *1*, L9-L13.

[294] M. Baron, H. Abbott, O. Bondarchuk, D. Stacchiola, A. Uhl, S. Shaikhutdinov, H. J. Freund, C. Popa, M. V. Ganduglia-Pirovano, J. Sauer, *Angew. Chem. Int. Ed.* **2009**, *48*, 8006-8009.

[295] L. Kiwi-Minsker, D. A. Bulushev, F. Rainone, A. Renken, *J. Mol. Catal. A: Chem.* **2002**, *184*, 223-235.

List of publications

Peer reviewed papers

A. Marberger, M. Elsener, D. Ferri, O. Kröcher, VO_x Surface Coverage Optimization of $V_2O_5/WO_3/TiO_2$ Catalysts by Variation of the V Loading and by Aging, *Catalysts* **2015**, *5(4)*, 1704-1720.

A. Marberger, M. Elsener, D. Ferri, A. Sagar, K. Schermanz, O. Kröcher, Generation of NH_3 Selective Catalytic Reduction Active Catalysts from Decomposition of Supported $FeVO_4$, *ACS Catal.* **2015**, 4180-4188.

A. Marberger, D. Ferri, M. Elsener, O. Kröcher, The Significance of Lewis Acid Sites for the Selective Catalytic Reduction of Nitric Oxide on Vanadium-Based Catalysts, *Angew. Chem. Int. Ed.* **2016**, *55*, 11989-11994

A. Marberger, M. Elsener, D. Ferri, A. Sagar, C. Artner, K. Schermanz, O. Kröcher, Relationship Between Structures and Activities of Supported Metal Vanadates for the Selective Catalytic Reduction of NO by NH_3, *Appl. Catal. B*, **2017**, *218*, 731-742

A. Marberger, D. Ferri, D. Rentsch, F. Krumeich, M. Elsener, O. Kröcher, Effect of SiO_2 on Co-impregnated $V_2O_5/WO_3/TiO_2$ Catalysts for the Selective Catalytic Reduction of NO with NH_3, *Catal. Today*, **2017**, doi.org/10.1016/j.cattod.2017.11.037.

A. Marberger, D. Ferri, M. Elsener, O. Kröcher, The Influence of Water to the Aging of V-based Catalysts for the Selective Catalytic Reduction of NO with NH_3, *Manuscript in preparation,* **2017**

A. Marberger, A. W. Petrov, P. Steiger, M. Elsener, O. Kröcher, M. Nachtegaal, D. Ferri, The power of transient experimentation: Time-resolved copper speciation during selective catalytic reduction of NO on Cu-SSZ-13, *Submitted Manuscript,* **2017**

Talks

A. Marberger, Generation of NH_3-SCR active catalysts from decomposition of supported $FeVO_4$, *SCS Fall meeting*, Lausanne, Switzerland, September 4th **2015**

A. Marberger, Evidence for the involvement of Lewis acid sites in NH_3-SCR on $V_2O_5/WO_3/TiO_2$ by time-resolved operando DRIFT and DR-vis, *17th Nordic symposium*, Lund, Sweden, June 14th - 16th **2016**

A. Marberger, Structure-Activity Relations of Supported Metal Vanadates for the Selective Catalytic Reduction of NO with NH_3, *NAM 25*, Denver, USA, June 5th - 9th **2017**

Posters

A. Marberger, Generation of NH_3-SCR active catalysts from decomposition of supported $FeVO_4$, *Capoc10*, Brussels, Belgium, October 28th - 30th **2015**

A. Marberger, The Significance of Lewis Acid Sites for the Selective Catalytic Reduction of Nitric Oxide on Vanadium-Based Catalysts, *SCS Fall meeting*, Zurich, Switzerland, September 15th **2016**

A. Marberger, The Significance of Lewis Acid Sites for the Selective Catalytic Reduction of Nitric Oxide on Vanadium-Based Catalysts, *PSI Catalysis Seminar*, Villigen, Switzerland, May 16th **2017**

A. Marberger, Transient, time-resolved diffuse reflectance spectroscopy study of the SCR mechanism on V_2O_5-WO_3-TiO_2, *NAM 25*, Denver, USA, June 5th - 9th **2017**

Curriculum vitae

Name:	Adrian Marberger
Date of birth:	24.07.1984
Place of birth:	Luzern, Switzerland
Nationality:	Swiss

Professional education

02/2014 - 12/2017	PhD thesis in the Catalysis for Energy Group at Paul Scherrer Institute (PSI) in Villigen, Switzerland under the supervision of Prof. Dr. O. Kröcher (EPF Lausanne, Switzerland) and Dr. D. Ferri (PSI, Switzerland)
03/2013 - 11/2013	Master thesis in the group of Prof. R. Alberto (University of Zurich, Switzerland) and in the group of Prof. S. Ott (University of Uppsala, Sweden)
09/2012 - 11/2013	Master studies in Chemistry at the University of Zurich, Switzerland
09/2009 - 09/2012	Bachelor studies in Chemistry at the University of Zurich, Switzerland
09/2005 - 09/2008	Bachelor studies in Material Science at ETH Zurich, Switzerland